“SOME STUDIES ON THE SYNTHESIS AND CHARACTERI-ZATION OF NCD/UNCD THIN FILMS DEPOSITED OVER VARIOUS SUBSTRATES”

By

JAGANNATH DATTA

(CHEM01201004009)

Bhabha Atomic Research Centre

Mumbai 400085, India

A thesis submitted to the

Board of Studies in Chemical Sciences

In partial fulfillment of requirements

for the Degree of

DOCTOR OF PHILOSOPHY

of

HOMI BHABHA NATIONAL INSTITUTE

NOVEMBER, 2014

Homi Bhabha National Institute

Recommendations of the Viva Voce Committee

As members of the Viva Voce Committee, we certify that we have read the dissertation prepared by ***Jagannath Datta*** entitled "***Some studies on the synthesis and characterization of NCD/UNCD thin films deposited over various substrates***" and recommend that it may be accepted as fulfilling the thesis requirement for the award of Degree of Doctor of Philosophy.

Chairman - DR. S. BHATTACHARYA **Date:** S. Bhattacharya 7/5/15

Guide / Convener — **Date:** —

Co-guide - Dr. A.V.R. REDDY * Convener **Date:** 07.05.15

External Examiner - Dr. Achintya Singha **Date:** A Singha 07.05.15

Member - DR. P. BARAT **Date:** P. Barat 07/05/2015

Member - Dr. D. P. Chowdhury **Date:** D P Chowdhury 7.5.2015

Final approval and acceptance of this thesis is contingent upon the candidate's submission of the final copies of the thesis to HBNI. I/We hereby certify that I/we have read this thesis prepared under my/our direction and recommend that it may be accepted as fulfilling the thesis requirement.

Guide **Date:**

Co-guide **Date:**

* as Prof N.R. Ray superannuated more than two years back, I have convened the meeting.

STATEMENT BY AUTHOR

This dissertation has been submitted in partial fulfillment of requirements for an advanced degree at Homi Bhabha National Institute (HBNI) and is deposited in the Library to be made available to borrowers under rules of the HBNI.

Brief quotations from this dissertation are allowable without special permission, provided that accurate acknowledgement of source is made. Requests for permission for extended quotation from or reproduction of this manuscript in whole or in part may be granted by the Competent Authority of HBNI when in his or her judgment the proposed use of the material is in the interests of scholarship. In all other instances, however, permission must be obtained from the author.

(JAGANNATH DATTA)

DECLARATION

I, hereby declare that the investigation presented in the thesis has been carried out by me. The work is original and has not been submitted earlier as a whole or in part for a degree / diploma at this or any other Institution / University.

(JAGANNATH DATTA)

List of Publications arising from the thesis

Journal

1. "Structure of Hydrogenated diamond like carbon by Micro-Raman Spectroscopy″, **Jagannath Datta**, Nihar R Ray, Pintu Sen, Hari S Biswas, and Erwin A Vogler, *Materials Letters*, **2012**, Vol. 71, Pages 131–133 (DOI : 10.1016/j.matlet.2011.12.041).

2. "Study of depth profile of hydrogen in hydrogenated diamond like carbon thin film by ion beam analysis techniques″, **J. Datta**, H.S. Biswas, P. Rao, G.L.N. Reddy, S. Kumar, N.R. Ray, D.P. Chowdhury, and A.V.R. Reddy, *Nuclear Instruments and Methods in Physics Research B,* **2014**, Vol. 328, 27-32 (DOI : 10.1016/j.nimb.2014.02.127).

3. "Signature of Misoriented Bilayer Graphenelike and Graphanelike Structure in the Hydrogenated Diamond-Like Carbon Film″, Nihar R. Ray, **Jagannath Datta**, Hari S. Biswas and Someswar Datta, *IEEE Transactions on Plasma Science*, **2012,** Vol. 40, Issue 7, Pages 1789-1793 (DOI: 10.1109/TPS.2012.2201176).

Conferences

1. "Formation of Atomically Thin Film of Coherent Domains of sp^2 C=C and sp^3 C-H carbons at the surface of Hydrogenated Diamond like Carbon Substrate″, N.R. Ray, **J. Datta**, P. Sen, H.S. Biswas, E.A. Vogler, *XXX International Conference on Phenomena in Ionized Gases (ICPIG),* August 28^{th} – September 2^{nd} **2011**, Belfast, Northern Ireland, UK.

2. "On the Thin Film of Nanocrytalline Graphite Clusters″; N.R. Ray, **J. Datta**, H. S. Biswas, and S Datta, *4^{th} International Symposium on Advanced Plasma Science and*

its Applications for Nitrides and Nanomaterials (ISPlasma 2012), March 04 - 08, **2012**, Aichi, Japan.

3. "Formation of Continuous Thin Film of Nanocrytalline Graphite Clusters", H. S. Biswas, **J. Datta**, N.R. Ray, S Datta, and U.C. Ghosh, *International Conference on Nanoscience and Technology (ICONSAT - 2012)* January 20 - 23, **2012,** Hyderabad, India.

4. "Development of Hydrogenated Diamond like Carbon as Hydrogen Storage Material" Jagannath Datta, Sanjiv Kumar, D.P. Chowdhury, A.V.R. Reddy and Nihar Ranjan Ray, *Satellite Conference on 100 Years of Science in India*, during January 9 – 10, 2013 at SINP, Kolkata.

5. "Study of depth profile of Hydrogen in Hydrogenated Diamond like Carbon thin film by Ion Beam Analysis techniques", **J. Datta**, H.S. Biswas, S. Kumar, D.P. Chowdhury, N.R. Ray, A.V.R. Reddy, *In the proceedings of DAE-BRNS Fifth Symposium on Nuclear Analytical Chemistry (NAC-V)* during January 20-24, **2014**, at Bhabha Atomic Research Centre, Trombay, Mumbai, India.

(JAGANNATH DATTA)

Journal contributions NOT included in this thesis

1. Covalent Immobilization of Protein onto a functionalized Hydrogenated Diamond Like Carbon substrate; Hari Shankar Biswas, **Jagannath Datta**, D.P. Chowdhury, A.V.R. Reddy, Uday Chand Ghosh and Nihar Ranjan Ray, *Langmuir,* **2010**, Vol. 26 (22), Pages 17413–17418.

2. Ceria associated manganese oxide nanoparticles: synthesis, characterization and arsenic (V) sorption behavior, Kaushik Gupta, Sayan Bhattacharya, Aniruddha Mukhopadhyay, Harishankar Biswas, **Jagannath Dutta**, Nihar Ranjan Roy, Uday Chand Ghosh, *Chemical Engineering Journal, **2**011*, Vol. 172, Pages 219-229.

3. Raman spectra of electrochemically hydrogenated diamond like carbon surface; Hari Shankar Biswas, **Jagannath Datta**, Pintu Sen, Uday Chand Ghosh, Nihar Ranjan Ray, *Chemical Physics Letters* **2014**, Vol. 600, Pages 10-14.

4. Covalently bound Bovine Serum Albumin (BSA) protein modified Hydrogenated Diamond Like Carbon (HDLC) surface as biosensor application; Hari Shankar Biswas, Kausik Gupta, **Jagannath Datta**, Uday Chand Ghosh, Nihar Ranjan Ray, *preprint arXiv*:1404.0553 (**2014**).

Dedicated to my

mother

ACKNOWLEDGEMENTS

It is a great pleasure to express my deep sense of gratitude and regards to Professor N. R. Ray, Plasma Physics Division, Saha Institute of Nuclear Physics, Kolkata, for giving me the opportunity of doing this research work under his constant guidance. I sincerely thank him for his encouragement and useful suggestions.

I am grateful to Dr. A.V.R. Reddy, Head, Analytical Chemistry Division, Bhabha Atomic Research Centre (BARC), Mumbai for granting me the official permission to get myself registered under HBNI for the Ph.D. thesis.

I am extremely grateful to Professor D.K. Srivastava, Director, Variable Energy Cyclotron Centre (VECC), Kolkata for allowing me to carry out my research work using the Cyclotron machine and other experimental facilities.

I sincerely express my thanks to Director, Saha Institute of Nuclear Physics for his support and guidance in performing this thesis work in SINP, Kolkata.

I am especially thankful to Dr. S.K. Das and Dr. R. Guin, Radiochemistry Division (RCD), BARC, Dr. M. K. Das, Board of Radiation and Isotope Technology (BRIT), Dr. S. K. Bandyopadhyay, Dr. P. Sen, VECC, Kolkata for their valuable suggestions and encouragement during the course of my work.

Grateful thanks are due to Dr. R. Verma, Dr. (Mrs.) S. D. Kumar, Analytical Chemistry Division, BARC, Mumbai and Dr. S. Kumar, and his team, National Centre for Compositional Characterization of Materials (NCCCM), Hyderabad with whom a part of the experimental work was successfully carried out.

I owe my thanks to Professor S. Datta, Bio-ceramic and Coating Division, CSIR-Centre for Glass and Ceramic Research Institute (CSIR-CGCRI), Kolkata for their collaboration and help in providing me with some valuable samples.

I would like to thank S.S. Sil, U.S. Sil, and A.A. Mallick for their technical help during the experimental works.

I sincerely express my thanks to Dr. D.P. Chowdhury, my mentor, and Head, Nuclear Method Group, ACD, BARC, at VECC, Kolkata for his encouragement and inspiration.

I owe my thanks to Mr. H.S. Biswas, Co-worker and friends, SINP, Kolkata for their help in providing me during the sample imaging and analysis.

I wish to thanks all my colleagues and friends of VECC, Kolkata, and Analytical Chemistry Division, BARC, Mumbai for their help and co-operation at various stages of my work.

Finally, I wish to express my deep sense of gratitude to my family and relatives who have sacrificed immensely in their own ways and had been a constant source of my inspiration and moral support throughout the tenure of this study.

NOV, 2014 (JAGANNATH DATTA)

CONTENTS

CHAPTER – 1

Introduction

CHAPTER – 2

Experimental set-up for the synthesis of HDLC films on various substrates at room temperature

CHAPTER – 3

Characterization Tools

CHAPTER – 4

Results and Discussions

CHAPTER – 5

Summary and Conclusions

Abbreviations:

DLC – Diamond Like Carbon

HDLC –Hydrogenated Diamond Like Carbon

HD - Hydrogenated Diamond

ND - NanoDiamond

NCD – Nano-Crystralline Diamond

UNCD – Ultra Nano-crystalline Diamond

a-C - Amorphous carbon

a-C:H - Hydrogenated amorphous carbon

N-UNCD – Nitrogen-incorporated ultrananocrystalline diamond

B-NCD- Boron-doped NCD

SCCM – Standard Cubic Centimeter per minute

MFC – Mass flow controller

CVD – Chemical Vapor Deposition

PECVD - Plasma Enhanced Chemical Vapor Deposition

MPCVD – Microwave Plasma Chemical Vapor Deposition

MPACVD – Microwave Plasma Assisted Chemical Vapor Deposition

HFCVD – Hot Filament Chemical Vapor Deposition

HOPG – Highly Oriented Pyrolytic Graphite

S.S – Stainless Steel

RT – Room Temperature

BEN – Biased Enhanced Nucleation

BEG – Biased Enhanced Growth

RF – Radio Frequency

RH- Relative Humidity

COF-Coefficient of friction

TCR - Temperature Coefficient of Resistivity

TEC-Thermal Expansion Coefficient

RMS - Root Mean Square

mRS – micro-Raman Spectroscopy

HRTEM - High Resolution Transmission Electron Microscope

AFM - Atomic Force Microscope

STM - Scanning Tunneling Microscope

SEM - Scanning Electron Microscope

XPS – X-ray Photoelectron Spectroscopy

XANES - X-ray absorption near-edge spectroscopy

ESCA - Electron Spectroscopy for Chemical Analysis

SIMS – Secondary Ionization Mass Spectroscopy

Vac FTIR – Vacuum Fourier Transform Infra-red

UV-Vis – Ultra Violet Visible

IBA – Ion Beam Analysis

NRA –Nuclear Reaction Analysis

RBS –Rutherford Back Scattering

ERDA - Elastic Recoil Detection Analysis

EELS- Electron Energy Loss Spectroscopy

NMR - Nuclear Magnetic Resonance

NEMS /MEMS – Nano-Electro Mechanical System/ Micro-Electro Mechanical System

SET – Single Electron Transistor

CB - Coulomb blockade

TB - Tunneling barrier

2-D - Two Dimension

Units :

Speed of light (c) = 3×10^{10} cm/s

Planck Constant (h) = 6.67×10^{-27} erg.s

Electron charge (e) = 1.602×10^{-19} coulomb= 4.803×10^{-10} esu

Avogadro Number (NA)=6.02×10^{23} mol^{-1}

Molar gas constant (R)= 8.314×10^{7} erg $mol^{-1}K^{-1}$

Conductance quantum (G_0) = ($2e^2/h$)= 7.748×10^{-5} S

Farad (F)= 1×10^{21} Zeptofarad (zF)= 10^{12} Picofarad (pF)

1 Radians (rad) =57.295 degrees (deg)= 63.662 grad

1 atm. =760 Torr =1.013 Bar=1.013×10^{6} dynes/cm^2

Temp (^oC) = 273 K

1 nm =10^{-3} μm =10^{-9} met =10^{-7} cm

1 g =10^{6} μg

1 MeV =10^{6} eV =1.602×10^{-13} J

1 A^0 = 10^{-8} cm

1 fm= 10^{-13} cm

1 cal = 4.2 J

Title of the Thesis:

Some studies on the synthesis and characterization of NCD/UNCD thin films deposited over various substrates

Preamble

The interest in the chemical vapor deposition (CVD) of diamond films is due to diamond's unique mechanical, thermal and electronic properties [1]. The dissociation of carbon containing gas precursor onto solid substrate is the key technique involved in the CVD of diamond films. The substrate can be either bulk diamond (natural or synthetic) or a non-diamond substrate. The resulting films, in the first case, are said to be homoepitaxial or single crystalline, in opposition to heteroepitaxial or polycrystalline films in the latter case. The technological challenges, issues, achievements of depositing CVD diamond films onto foreign substrates are the major areas of research worldwide since the early 1980's [2]. In spite of remarkable properties of diamond, the high surface roughness of CVD diamond films is not suitable for their widespread use in various applications such as machining and wear, field-emission or optical applications, transistor applications etc. [3, 4]. The reduction of the film grain size (from micrometres to nanometres) by means of the growth chemistry, and the surface temperature is one, out of different approaches followed to overcome the problem of high surface roughness of CVD diamond films [2, 5]. These diamond films, commonly referred to as nanocrystalline diamond (NCD) films are grown in hydrogen-rich CVD environments, and have grain size 30-100 nm (increasing with the film thickness). A second category of NCD, known as ultra-nanocrystalline diamond (UNCD) films, are grown in argon-rich, hydrogen poor CVD environments, and have a typical grain size of 3–5 nm, independent of the film thickness. The nanograins are embedded in a non-diamond matrix,

and the films show a significant content of sp^2-bonded carbon (up to 5%) [6]. NCD and UNCD films have, in general, high Young's modulus, high hardness and a low macroscopic friction coefficient, due to their low surface roughness, and are optically transparent. The UNCD films are also electrically conductive, due to the non-diamond matrix. Both NCD and UNCD films are usually deposited on non-diamond substrates, such as silicon wafers. Other materials like SiC, SiO_2 can also be used as substrates.

The growth of NCD/UNCD films from the vapor phase on non-diamond substrates at practical rates was accomplished with the development of thermal- and plasma-enhanced CVD methods [7-10] in which a hydrocarbon gas (usually methane) mixed in low concentrations with hydrogen is energized thermally or in a plasma, prior to contact with a heated substrate.

In order to achieve good adhesion of NCD/UNCD films onto foreign substrate, heat-assisted bias-enhanced nucleation (BEN)/ bias enhanced growth (BEG) technique, was found to be very successful in terms of achieving diamond nanograins (3–5 nm), with smoother surfaces (6 nm rms) and higher growth rate (1 m/h) of the film [11]. In the BEN/BEG technique, there is a speculative atomic model of possible diamond/graphite/Si interface, causing a very good adhesion of the film onto the Si substrate due to minimum lattice mismatch [12].

While the technology of diamond deposition develops, interest turned to related materials such as Diamond like Carbon (DLC). DLC is a dense, metastable form of amorphous carbon (a-C) or hydrogenated amorphous carbon (a-C:H) containing a significant sp^3 C-H bonding. The sp^3 bonding confers valuable 'diamond-like' properties such as mechanical hardness, low friction, optical transparency, and chemical inertness. Although DLC films have poorer properties than

diamond films, they have some advantages, notably deposition at room temperature, deposition onto Fe or plastic substrates and superior surface smoothness.

Using asymmetrically coupled RF (13.56 MHz) discharge, a dc negative self-bias can be produced continuously during deposition of Hydrogenated Diamond like Carbon (HDLC) thin film onto substrates like Si(100), steel etc. at room temperature, with ultrasmooth surface (~ 0.0175 nm rms) [13, 14]. The sp^3 C-H contents and presence of NCD in the HDLC films depend on the ratio of flow rates of hydrogen (H_2) and methane (CH_4) for a given deposition conditions like pressure, dc negative bias, deposition time etc. [15]. A high resolution transmission electron microscope (HRTEM) image of MeV nitrogen ion irradiated HDLC film, clearly shows existence of crystalline graphite with lattice spacing of 0.34 nm in the HDLC film, although the crystallographic planes are somewhat distorted compared to the perfect graphite structure [16].

All these properties of HDLC films in the early works [13-16], motivated me, for PhD thesis works, to investigate the structural composition of HDLC films by Micro-Raman spectroscopy and High Resolution Transmission Electron Microscope (HRTEM), depth profile of hydrogen in the HDLC film by ion beam analysis (IBA) techniques, surface smoothness by Atomic Force Microscope (AFM) and Scanning Electron Microscope (SEM), surface conductance property of HDLC film from the current (I) vs. voltage (V) characteristics by Keithley source meter. By these investigations on HDLC films, I have addressed the key issues like ultrasmoothness of HDLC surface, compatibility of BEN model [12] in the structural composition of HDLC, new information about the surface conductance of HDLC in comparison to that of hydrogenated diamond (HD) film.

The thesis has been organized into five chapters, elaborating on the work carried out on the above-mentioned themes.

Chapter 1: Introduction

Chapter 1 gives an introduction on the growing role of various new forms of NCD/UNCD films as tribological coating, electrochemical devices, coatings for MEMS devices, and in modern electronics industry. In this part, we shall subdivide the nanocrystalline diamond into two broad categories based on their microstructure, growth chemistries, and properties. The controlled synthesis of nanocrystalline diamond film to overcome and minimize the non-diamond carbon or amorphous carbon is discussed. A brief overview of various types of DLC thin films containing NCD, their classifications and properties are given. The basic differences between the various deposition methods of DLC thin film using modern technology are discussed. This chapter describes some unique advantage of the in situ BEN-BEG mechanism using plasma enhanced CVD (PECVD) deposition onto substrate at room temperature for the synthesis of HDLC films. The unique characterization techniques of HDLC films for its various parameters used in the literature are described. This chapter also provides a short introduction on: (i) Visible Micro-Raman spectroscopy for the estimation of sp^2 and sp^3 carbons and their structure in the HDLC thin films (ii) Nuclear Reaction Analysis, Rutherford backscattering spectrometry for measurement of depth profile of hydrogen in the HDLC films (ii) Measurement of current vs. voltage characteristics of the HDLC surface to address the issue of surface conductance property.

Chapter 2: Experimental set-up for the synthesis of HDLC films on various substrates at room temperature

Chapter 2 describes schematic and picture for the synthesis of HDLC thin film in details with introduction, experimental, and results and discussion. The introduction gives the potentiality of Plasma Enhanced Chemical Vapor deposition (PECVD) technique for the synthesis of hydrogenated diamond like carbon thin films. The 'experimental' gives the description of production of dc negative self bias in asymmetrically coupled RF (13.56 MHz) discharge and their role in depositing thin films onto substrate at room temperature. That the dc negative self bias in a controlled manner, a biased enhanced nucleation/growth (BEN/BEG), plays the key role in depositing the thin films is described in the 'results and discussion'.

Chapter 3: Description of Characterization tools used in the present works

3.1 High resolution transmission electron microscope (HRTEM)

The methodology for the cross sectional view and the morphology of the HDLC surface by HRTEM have been described. The cross sectional/planer views of the samples prepared by the TEM sample preparation equipments are described.

3.2. Micro Raman spectrometer:

The acquisition and analysis of Raman spectra of HDLC samples by Micro-Raman spectrometer (LabRAM HR vis. Horiba Jobin Yvon SAS France) are described herein.

3.3. Atomic Force Microscope (AFM)

The morphology of HDLC surface from the atomic force microscope (AFM) image and height profile along a given line of the AFM image using multimode scanning probe microscope (Agilent AFM 5500 series) is described herein.

3.4. Scanning Electron Microscope (SEM)

The measurement of surface continuity and ultra smoothness of the HDLC film, as obtained from AFM results, by Scanning Electron Microscopy (SEM) (FEI Quanta 200f), is described herein.

3.5. Pelletron Accelerator:

The acquisition and analysis of data for the interaction of ion beam of Pelletron accelerator (National Center for Compositional Characterization of Materials (NCCCM), Hyderabad, India) with thin film samples, in general, are described herein. Necessarily of using Nuclear reaction analysis (NRA) and Rutherford backscattering spectroscopy (RBS) techniques for studying HDLC samples (as-prepared and annealed) is also described, in particular, herein.

3.5.1. Nuclear Reaction Analysis

Nuclear reaction analysis (NRA) technique for depth profiling of hydrogen in the as prepared and annealed HDLC samples is described herein.

3.5.2. Rutherford Backscattering Spectroscopy

Rutherford backscattering spectroscopy (RBS) technique to measure the thickness of HDLC films (as prepared and annealed) is described herein.

3.6. Keithley Source Meter:

The acquisition and analysis of I-V characteristics on the HDLC surface at RT (295K) ambient condition using a Keithley 2635 source meter is described herein.

Chapter 4 : Results and Discussions

4.1. The typical results on HDLC films obtained by HRTEM, AFM, and SEM are displayed and critical discussions are made based upon the results herein.

4.2. The typical results on HDLC films obtained by Micro-Raman spectrometer are displayed and critical discussions are made based upon the results herein.

4.3. The typical results on HDLC films (as-prepared and annealed) obtained by NRA and RBS techniques are displayed and critical discussions are made based upon the results herein.

4.4. The typical results on HDLC films (as-prepared and annealed) obtained by current (I) vs. (V) characteristics onto the HDLC surface are displayed and critical discussions are made about the surface conductance mechanisms, based upon the results herein.

4.5. Taken all the results together, described in sec. 4.1. to sec. 4.4., a discussion is made herein, in order to arrive a plausible conclusion about our HDLC thin films.

Chapter 5 : Summary and Conclusions

Summary and conclusions are described herein based upon the following key results in the investigation of HDLC films:

1. Coherency of sp^3 C-H and sp^2 C=C carbons in the HDLC film can produce a continuous, non-porous thin film having atomically smooth surface, instead of discrete uniform grains as in the case of UNCD films, is a new result [17].
2. The depth profiles of hydrogen in the as-prepared and annealed HDLC thin films are indicative of the prevalence of graphitic carbon near the film-substrate interface and supporting experimentally for the first time, the theoretical model of diamond-graphite-Si structure under BEN deposition at room temperature [18].

3. Current (I) vs. Voltage (V) characteristics between two ohmic Cu contacts onto the HDLC surface is controllable via a third ohmic Cu contact in between, indicating possible quantum effects viz., quantum confinement, electron tunneling and coulomb blockade, in the nanostructure HDLC thin film composed of coherently coupled sp^2 C=C and sp^3C-H carbons [19,20].

The following SCI journal publications cover the present thesis works :

(1) Structure of hydrogenated diamond like carbon by Micro-Raman spectroscopy; **Jagannath Datta**, Nihar R. Ray, Pintu Sen, Hari S. Biswas, and Erwin A. Vogler; Materials Letters, 71 (2012) Pages 131–133 (DOI : 10.1016/j.matlet.2011.12.041).

(2) Study of depth profile of hydrogen in hydrogenated diamond like carbon thin film using ion beam analysis techniques; **J. Datta**, H.S. Biswas, P. Rao, G.L.N. Reddy, S. Kumar, N.R. Ray, D.P. Chowdhury, and A.V.R. Reddy; 'Nuclear Instruments and Methods in Physics Research, B, 328 (2014) Pages 27-32 (DOI :10.1016/j.nimb.2014.02.127) .

(3) Signature of Misoriented Bilayer Graphenelike and Graphanelike Structure in the Hydrogenated Diamond-Like Carbon Film; Nihar R. Ray, **Jagannath Datta**, Hari S. Biswas, and Someswar Datta; IEEE Transactions on Plasma Science, 40(7) (2012) Pages 1789-1793 (DOI: 10.1109/TPS.2012.2201176).

References

1. J. C. Angus, A. Argoitia, R. Gat, Z. Li, M. Sunkara, L. Wang, and Y. Wang, *Philos. Trans. R. Soc. London Ser. A* **342** (1993) 195 - 208

2. J. J. Gracio, Q. H. Fan, and J. C. Madalenol, *J. Phys. D: Appl. Phys.* **43** (2010) 374017 - 22.

3. M. Kamo, Y. Sato, S. Matsumoto, and N. Setaka, *J. Cryst. Growth* **62** (1983) 642 - 644

4. A. K. Gangopadhyay and M. A. Tamor, *Wear* **169** (1993) 221 - 229.

5. J. E. Butler and A. V. Sumant, *J. Chem. Vapor Depos.* **14** (2008) 145-160.

6. D. M. Gruen, *Annu. Rev. Mater. Sci.* **29** (1999) 211 - 259.

7. S. Matsumoto, Y. Sato, M. Kamo, and N. Setaka, *Japan. J. Appl. Phys.* **21(4)** (1982) L183 - L185.

8. S. Matsumoto, Y. Sato, M. Tsutsumi, and N. Setaka, *J. Mater. Sci.* **17** (1982) 3106 - 3112

9. H. Yoshikawa, C. Morel, and Y. Koga, *Diam Relat Mater*. **10** (2001) 1588 - 1591.

10. S. Matsumoto, *J. Mater. Sci. Lett.* **4** (1985) 600 - 602.

11. Y. C. Chen, X. Y. Zhong, A. R. Konicek, D. S. Grierson, N. H. Tai, I. N. Lin, B. Kabius, J. M. Hiller, A. V. Sumant, R. W. Carpick, and O. Auciello, *Appl. Phys. Lett.* **92** (2008) 133113-3.

12. J. Robertson, J. Gerber, S. Sattel, M. Weiler, K. Jung, and H. Ehrhardt, *Appl. Phys. Lett.* **66**(**24**) (1995) 3287 - 3289.

13. N. R. Ray and A. N. S. Iyengar, Proceedings of the Sixth International Conference on Reactive Plasmas and 23rd Symposium on Plasma Processing, 24–27 January 2006, Matshushima/Sendai, Japan, 2006, edited by R. Hatakeyama and S. Samukawa (ICRP-6/SPP-23), p. 583

14. K. Kumari, S. Benerjee, T. K. Chini, and N. R. Ray, *Bull. Mater. Sci.*, Vol. 32, No. 6, December 2009, 563–567.

15. A. Singha, A. Ghosh, A. Roy, and N. R. Ray, *J. Appl. Phys.* **100** (2006) 044910-8.

16. S. Mathew, U. M. Bhatta, A. K. M. M. Islam, M. Mukherjee, N. R. Ray, and B. N. Dev, *Appl. Surf. Sci.* **225**(**9**) (2009) 4796-4800.

17. J. Datta, N. R Ray, P. Sen, H. S. Biswas, and E. A. Vogler, *Materials Letters* **71** (2012) 131–133.

18. J. Datta, H.S. Biswas, P. Rao, G. L. N. Reddy, S. Kumar, N. R. Ray, D. P. Chowdhury, and A. V. R. Reddy, *Nucl. Inst. and Meth. in Phys. Res. B* **328** (2014) 27-32.

19. N. R. Ray, J. Datta, H. S. Biswas, and S. Datta, *IEEE Trans. on Plasma Sci.* **40**(**7**) (2012) 1789-1793.

20. N. R. Ray, J. Datta, H. S. Biswas, P. Sen, and K. Bagani, *preprint arXiv*:**1306.6477** (2013).

List of Figures

Page No.

Chapter 1

Chapter 2

Chapter 3

Chapter 4

List of Tables Page No.

Chapter 1

Introduction

1.0 Introduction

Today's, nanotechnology is an interdisciplinary technique, employed to interlink a wide range of exploration, preparation and application of these nanostructures. Additionally, nano technology is not straightforwardly functioning at just nanometer range dimensions. It preferably operates at the nano scale empowering scientists to take advantage of the unique physical, chemical, mechanical, optical, and electrical properties of materials which are observed at the nanometer dimensions. Nanotechnology is the understanding and control of matter at the nanoscale. When the materials are grown with the dimensions of about 1 to 100 nanometers (one millionth of a meter), the materials properties change significantly from those at bulk materials. It is now established that in the nanometer dimensions where so-called 'quantum effects' dominate the behavior and characteristic properties of the particles and other physical effects viz. large surface area. The properties of the materials are function of size of the particle when its sizes are brought down to nanometer dimension, viz. color, melting point, fluorescence, optical transparency, electrical conductivity, magnetic permeability, and chemical reactivity. Earlier, it was believed that all the biological events occur at the smallest dimension that is now taken into the consideration for developing and betterment of functioning of chemical catalysis, targeted drugs, materials synthesis, computing, imaging, printing, and other fields. The intention of the scientist leading to the tunability of properties of the material of interest viz. by changing the size of the particle is the attractive result of quantum effect.

1.1 Literature reviews on NCD and UNCD

1.1.1 Classification of NCD and UNCD

We shall divide the nanocrystalline diamond into two main categories : (1) Ultrananocrystalline Diamond (UNCD) (2) Nanocrystalline Diamond (NCD). According to

cluster model [1], tetrahedral carbon clusters based on the diamond lattice is called NCD; wherein boundary carbon atoms are saturated with hydrogen atoms for each cluster; a typical example of such cluster is shown below:

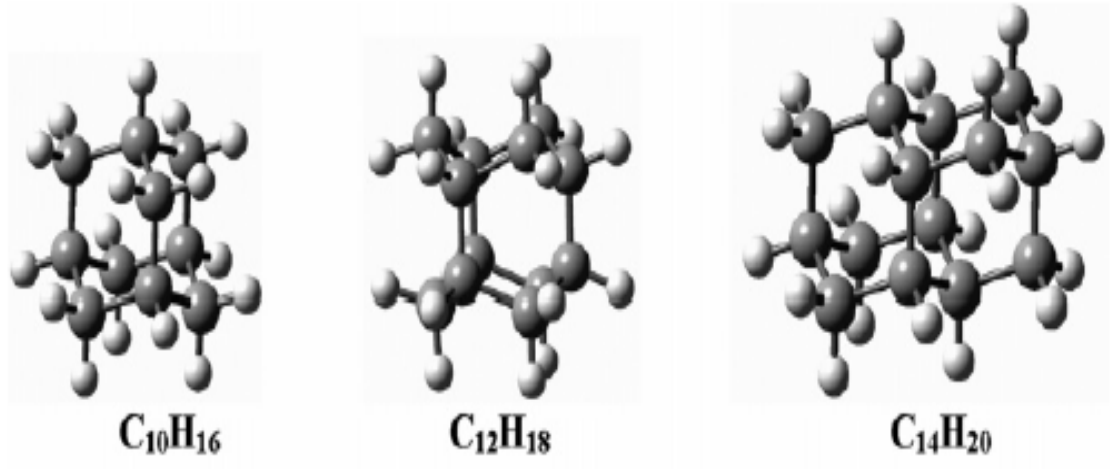

Figure 1.1 Tetrahedral carbon clusters for nanocrystalline diamond. The boundary carbon atoms were saturated with hydrogen atoms.

These classifications are based on their microstructure, growth chemistries, and properties. Based on microstructure, UNCD is generally having crystalline size of the order of 2-5 nm grains, surface roughness 5-25 nm surrounded by a layer of non-diamond carbons bounding the grains and the nature of these carbon is found to be significantly sp^3 bonded (95-98%) and (~5%) sp^2 bonded. UNCD is a very fine-grained material grown with Ar rich hydrogen poor plasmas/gas phase reaction. The UNCD has very different structure due to the Ar-rich plasmas growth chemistry, very high re-nucleation density, and controlling the re-nucleation of diamond during the deposition. The surface roughness 5-25 nm is independent of film thickness as there are no columnar structures. Consequently, UNCD can be grown to any thickness with no appreciable increase in roughness.

NCD thin film has grain sizes ranging from 10-100 nm, surface roughness 5-100 nm with very low to moderate amount of non-diamond carbon remained in the grain boundaries. The highest quality of NCD is having ~0.1% sp^2 but the sp^2 carbon content sometimes may rise to ~50% with the high methane input during the deposition. NCD films are grown mainly in hydrogen rich carbon poor CVD gas/plasmas environment. NCD film grown with a very high initial nucleation density and its grain size and hence roughness increases with film thickness due to their columnar growth. Consequently, the roughness increases with the film thickness for NCD films. There may be a little or no re-nucleation and above a certain thickness (~1 μm) the film becomes microcrystalline. The difference between the micro- or poly-crystalline diamond films is related to the grain size and thickness of the films. Therefore, the smaller grains are most preferable and grain sizes of NCD are generally quoted below 500 nm. The conventional microcrystalline diamond is generated from the NCD after a certain thickness during growth and roughness of microcrystalline is proportional to its thickness. The grain size of polycrystalline diamond is generally in the range of 0.5-1 μm.

1.1.2 Applications of NCD and UNCD

The two very different forms of diamond namely Nanocrystalline Diamond (NCD) and Ultrananocrystalline Diamond (UNCD) are having unique properties and applications. They not only render unique characteristics of diamond, viz., high hardness, chemical stability, stiffness and strength, but also have the advantages of nanomaterials, viz., large surface to volume ratio and high adsorption capacity. Over the last three decades the NCD and UNCD thin films have found enormous applications. NCD finds suitable applications for X-ray window, X-ray lithography. The bio-compatibility of nano-diamonds and their application in the drug delivery systems have been shown by Y Zhu and co-workers [2] from their in vitro and in vivo safety assessments. The various functional groups of drugs, targeting molecules, bio-imaging, protein mimics, and tissue engineering, loaded onto the Nanodiamonds (ND)

through assembly mechanism, help to build ND based versatile drug delivery system [3]. This type of drug delivery system would serve as the principal for modeling and developing of ND based drug delivery systems with efficient treatment for various cancers leaving behind lesser level of toxicity. The high performance Microelectromechanical systems based on silicon (MEMS) devices are not ideally robust, reliable, and suitable as MEMS components especially in harsh environmental condition. Panda and co-worker [4] has studied the tribological properties of UNCD in nitrogen and ambient atmosphere and reported the decrease in coefficient of friction (COF) with the decrease of relative humidity (RH) for understanding the environmental dependency of tribological properties. Liang et al. [5] have studied the Microwave Plasma Assisted Chemical Vapor Deposition (MPACVD) for undoped and Boron-doped nanocrystalline diamond in ambient air. It was reported that wear rate of B-doped NCD is ~10 times higher than that of undoped films and COF decreases with increasing normal loads. A major disadvantage of Si-based MEMS devices is due to poor flexural strength, fracture toughness, mechanical and tribological properties of silicon compared to diamond and NCD/UNCD films. The potential of NCD/UNCD have been employed [6-8] at both macro and micro/nanometer range as a structural materials due to its excellent mechanical, chemical and electrical properties for tribological applications. These are use as a coating materials in the seals of rotating shafts [9], as structural material for inkjets for corrosive liquids, micromechanical switches, and MEMS/NEMS as higher frequency high Q mechanical resonator. The diamond-based MEMS technology could be extended for applications in the field of bio-medicine, sensors, actuators for space applications. F. Buja [10] fabricated and tested the nitrogen incorporated UNCD for the development of next generation micro-actuators. The highly stable and sensitive platform for sensing biologically active molecules and DNA onto biologically or chemically modified NCD and UNCD diamond surfaces is now established. Yang et al. [11] showed the

covalently immobilization of the DNA molecules to the nanocrystalline diamond surface grown on silicon substrate via an amine group which serve as sites for DNA attachment. Comparison of biologically modified UNCD/NCD surfaces [12-13] with commonly used surface for the same purpose suggests that diamond films may be an ideal substrate for integration of microelectronics with biological modification and sensing.

1.1.3 Synthesis of NCD and UNCD

NCD/UNCD films are grown mostly on silicon wafer, silicon dioxide, silicon carbide, silicon nitride, metals or even sometime refractory materials. The high quality NCD materials start with a high areal density of diamond seeds, or nucleating sites where nanometer (nm) size diamond region growth starts in a columnar manner. NCD deposited on silicon or other refractory materials are treated or seeded to increase diamond nucleation density. The seeding or treatment is carried out to initiate and also to enhance the nucleation sites to diamond. Few typical methods are polishing of the substrate with diamond powder, ultrasonic treatment of the substrate with the slurry of nm sized diamond, coating of the wafer with diamond like substrate (ex-situ nucleation processes). Rotter and co-workers [14-15] developed a two stage nucleation method towards seeding of UNCD/NCD films. First stage was the deposition of amorphous carbon layer. Secondly, the ultrasonic treatment of amorphous carbon layer using nanodiamond powders which enables the nm size particles stick at to the carbon layer. Sharda and co-worker [16-17] utilized the bias enhanced nucleation (BEN) and bias enhanced growth (BEG) methods for growing NCD films with a steady DC bias (200-260 V) during the Microwave plasma chemical vapor deposition (MPCVD) processes (in-situ nucleation processes). Noticeably, they have used moderate (2-6%) CH_4 percent compared to 0.1-0.5% CH_4 in H_2 used by other groups [18-19] The unique advantages of this technique are that it does not require any pretreatment or pronunciation stage with the suitability of wide range of substrates. The mechanism behind this is believed to be an extension of Rotter's multistage

deposition process, due to the bombardment of highly energetic carbon ions. Consequently, the film having good adhesion properties and high hardness. Corvin and co-workers [20] introduce N_2 with CH_4/H_2 reactants helps to reduce the grain size of NCD, via increased stacking faults in the NCD structure due to higher CN concentrations. Zhang et al. [21] studied the effect of direct ion beam deposition technique with $Ar/H_2/CH_4$ as the reactant gases to induce nucleation on mirror-polished Si substrates on diamond nucleation. This detailed investigation were found very helpful for the evaluation of the mechanism of bias-enhanced nucleation

One of the most important nucleation techniques that can be widely utilized by several groups around the world is the in-situ biased enhanced nucleation (BEN). We have also purposefully performed the deposition of HDLC films onto substrate at room temperature due to the unique advantages of the in-situ BEN-BEG mechanism using plasma enhanced CVD (PECVD) technique. During BEN, the substrate is negatively biased by 100-300 V DC with respect to the ground (chamber or other internal electrode). The nanocrystalline diamond films are produced by biased enhanced nucleation-biased enhanced growth (BEN-BEG) using microwave plasma chemical vapor deposition method [17, 22], hot filament CVD (HFCVD) [23]. A different regime of growth process typical for growth by energetic species reveals in the films deposited by BEN-BEG technique which may be a combination of surface and subsurface processes. The maximum concentration of nanocrystalline diamond with the hardness approaching towards the hardness of natural diamond thus grown at various conditions using BEN-BEG in MPCVD are well reported. The advantages of in-situ BEN process over the other commonly used ex-situ processes for nucleation are (i) completely consolidated dry nucleation and growth technique using plasma processing, (ii) stronger adhesion towards substrate, (iii) enhanced efficiency.

1.1.4 Growth chemistry and mechanism of NCD and UNCD synthesis

To predict and correlate the nature of the deposits, with the chemical environment that the substrate is exposed during the deposition process; characterization of plasma species is needed. However, in low pressure plasma CVD process, the gas phase chemistry is negligible or limited to a few precursors. It has been found that hydrogen specifically atomic hydrogen plays a crucial role [24] in the various diamond CVD processes in typical hydrogen (99%) hydrocarbon (1%) mixtures. The growth of diamond from a mixture of radicals, ions, and molecules impinging on the substrate despite the fact that may depend on the nature and composition of reactants. Hydrogen is produced homogeneously in the plasma mixture of the plasma-enhanced systems viz. microwave, RF, or DC-arc plasmas. The electrons in the plasma gets energized from external input energy

$$H_2 + e^- \rightarrow H + H + e^-$$

However, the homogeneous recombination of hydrogen is slow process and neglected under typical low pressure CVD diamond conditions [25]. However, recombination of hydrogen is affected by the presence of few percent of hydrocarbons. Like many reaction mechanisms, the growth mechanisms of diamond films from various hydrocarbons remain mysterious. Many of the postulates focus on one or more principal species viz. C_2H_2, CH_3, CH_4, and C_2H_4. These species were detected in a simple system with methane in H_2 (0.1%) and with various gases mixtures by measurements of the gas phases during the depositions diamond films. The species responsible for the growth of the films, were suggested based upon the emission spectra on plasma environments during diamond growth. The most abundant species (CH_3, C_2H_2) have no prominent visible emission bands whereas few of the other less

abundant radicals viz. C_2, CH may have visible emission. Therefore, it is quite difficult to predict convincingly about the responsible species for the film growth from the emission spectra only. In the system of CVD diamond CH_3 and C_2H_2 were believed to be the principal growth species. However, the optical emission spectra suggest the observation of C_2 as dominant species during UNCD synthesis [26]. The synthesis of UNCD from C_{60} and Ar precursors in microwave or high methane concentration may lead to the production of C_2 radical viz. the following reactants.

$C_{60} + Ar^+ \rightarrow C_{60}^+ + Ar$

$C_{60}^+ + e^- \rightarrow C_{58} + C_2$

$2CH_4 \rightarrow C_2H_2 + 3H_2$

$C_2H_2 \rightarrow C_2 + H_2$

The measurements of the absolute concentration of C_2 species were performed using cavity ring down spectroscopy in $Ar/CH_4/H_2$ and $He/CH_4/H_2$ plasmas [27]. The C_2 radical can directly insert into C-H bonds of pre-existing diamond seeding due to low activation barrier (~ 5 $Kcal.mol^{-1}$) making very high heterogeneous re-nucleation rates in UNCD synthesis. Moreover, the dominant additive species was found to be C_2H_2 under typical diamond CVD conditions [25] based on first order kinetic model. However, the ^{13}C labelled hydrocarbon suggests the methane-based growth chemistry were in consistent with the deposited diamond film than acetylene-based mechanism. The rate determining step for diamond nucleation was the breaking of C-H bonds by C_2 which has been confirmed by deuterium substitution using emission spectroscopy during the diamond synthesis in microwave plasma system.

The role of atomic hydrogen is rationalized based on the facts that diamond is more stable towards atomic hydrogen than graphite in a typical CVD deposition from the source of volatile hydrocarbon and an abundant source of hydrogen. Therefore, if we consider the replacement of two neighboring carbons from diamond structure the resulting structure is still sp^3 hybridized, whereas the similar replacement from the graphite structure changes the ring structure. Thus, the growth of diamond from carbon containing hydrocarbons/sources diluted in hydrogen involves two processes. (1) Atomic hydrogen guides the hydrogen abstraction reactions and arranges for the CH_3 adsorption site by removing a hydrogen atom from the hydrogen terminated diamond surface; and (2) also remove the atomic hydrogen from the adsorbed CH_3. Consequently, carbon atom move into the position corresponding to an addition of the diamond network. Moreover, the atomic hydrogen preferentially etches the graphitic phase. Therefore, it is sufficiently promising to grow diamond films free from non-diamond phases by using a plasma conditioning of 98-99% H_2. The grain size can be reduced to 50-100 nm and the film roughness is correspondingly reduced, by increasing the CH_4/H_2 ratio in the plasma. Unfortunately, atomic hydrogen also etches the diamond phase and resulting non-diamond carbon phases or intergranular voids.

Table 1.1 list for outstanding properties and possible applications of CVD diamond due to the extreme properties of diamond (i) strong C-C covalent bond, and (ii) short range bonds of smaller carbon atoms.

Table 1.1 List for outstanding properties and possible applications of CVD diamond [25, 28]

Properties	Value	Applications
Hardness	100 GPa	Coatings for cutting and drilling tools
Coefficient of friction	0.1 in air	Wear resistant abrasive coatings on windows and bearing under vacuum
Thermal conductivity	20 W $cm^{-1}K^{-1}$	Heat sink for electronic devices, laser packages, heat spreading films in RF systems
Electrical Resistivity	$10^{16}\,\Omega$.cm	Good electrical insulator
Acid Resistant	Inert	Coating for reactor vessel, diamond electrode
Radiation resistant	-	High power microwave devices
Young's Modulus	1.2×10^{12} Nm^{-1}	MEMS components, stiff membrane for lithography
Band Gap	5.45 eV	Solid state detectors, High temperature devices, High power devices
Reflective index	2.41	Optical wave guide, optical filters, Windows for lens materials in UV-Vis-IR and microwave system
Thermal expansion coefficient	0.8×10^{-6} K^{-1}	Thermally stable substrates, X-ray lithography masks
Work function	-Ve	Light emitters, display

Table 1.2 Comparison of growth conditions and properties of various forms of carbon thin films [25, 29-53]

Properties	DLC	NCD	UNCD	Diamond (CVD)	Graphite
Reactants	C_nH_y/H_2	CH_4/H_2	CH_4/Ar	CH_4/H_2	allotropes of carbon
Deposition Temp (^{0}C)	25-800	450-950	400-800	700-1000	-
Bonding Character	80 % sp^3	50 % sp^2	2-5% sp^2 (grain boundary)	100% sp^3	100% sp^2
H content	<1%-60%	<1%	<1%	<0.25%	0
Growth Species	C	CH_3	C_2	C	C
Density (g/cm^3)	1.5-2.5	3.3-3.52	3.05	3.0-3.51	2.27
Grain Size (nm)	variable	5-100	5-25 nm depends on nucleation density & thickness	Variable	-
Surface Roughness (nm)@	0.05-100	5-100	5-25	Depends on preparation conditions	~ 0.3
Band Gap (eV)	1.0-4.0	3.2-4.3	5-5-5.65	5.45	~0.04
Hardness (GPa)	1-80	20-80	98	30-110	~0.01
Flexural strength (MPa)	-	3-4 GPa	5.4 GPa	2944	6.9-100
Fracture Toughness (MPa.m$^{1/2}$)	4.4-10.1	-	4.7-7.2	5.3	0.4-2.4
Poisson's ratio	0.22	0.12	0.057	0.1-0.3	0.17-0.23
Young's Modulus (GPa)	60-850	500-1120 depends on nucleation density	790	250-1050	1050 (in-plane) 36 (z-axis)
Macroscopic Friction Coefficient	0.01-0.5	0.02-0.05	0.02-0.05	0.05-0.15	0.1
Thermal expansion coefficient ($\times 10^{-6}K^{-1}$)	1.5-7.0	1.0-2.25	-	0.7-1	~1 (in-plane) 29 (z-axis)
UV-Vis Transmissions	Transparent/ Opaque	Transparent	Semi-opaque	Transparent	Opaque
Crystallinity	Mixed diamond &/or amorphous	Mixed diamond & non-diamond	Equiaxed diamond	Columnar	Hexagonal layer structure
Thermal Conductivity (W.m^{-1}.K^{-1})	0.56-3.5	1370	10-20	900-2200	25-470
Resistivity (Ω.cm)	10^6-10^8	1×10^{-2}	143-3 $\times10^{-2}$ (N-UNCD)	10^{13}	(40-80)$\times10^{-6}$
Adhesion Energy (mj.m^{-2})	48.5	10	10-59.2	40–45	40-150

Table 1.3 Comparison of deposition techniques, properties, and applications of different forms of NCD and UNCD films

NCD/UNCD Films [Ref]	Deposition technique and conditions	Properties	Applications
Diamond [9. 28]	HFCVD technique; filament temp. 2200-2500 ^{0}C; CH_4(1%)/H_2, Pressure 5.3-12 kPa; Temperature 950-1050 ^{0}C;	Density 3.515; Hardness 98; Reflective Index 2.42; Band gap 5.45 eV; Thermal conductivity 20 W $cm^{-1}K^{-1}$; Dielectric Constant 5.5; Resistivity 10^{13} Ω.Cm; COF 0.05-0.15†;TEC $1.1\times10^{-6}/^0$C; Young's Modulus 1200 GPa; Hardness 100 GPa; Fracture Toughness 5.3, Wear rate 1.8×10^{-7} $mm^3/Nm^{\ddagger}$	High power and high temp. devices, Diamond - MEMS
NCD [54]	HFCVD, filament temp. 2200 ^{0}C; Nucleation in-situ BEN; R-CH_4(0.3%)/H_2/N_2; S-Si(100); T-740 ^{0}C; P-1.5 kPa;	Thickness 2.0-8.0 μm; Grain size 60 nm; $^{\pm}$Roughness 50-60 nm;Young's Modulus 800-980 GPa; Fracture Strength 3 GPa;	MEMS devices
UNCD [9]	MPCVD; 2.45 GHz; CH_4(1%)/H_2, P 100 torr, T 350-800 ^{0}C; Growth species C_2 ;	Equiaxed diamond; Grain size 2-5 nm; Roughness 20-40 nm; 2-5% sp^2 ; H content <1%; COF 0.02-0.03; Hardness 88 GPa; Young's Modulus 980 GPa; Wear rate 0.02×10^{-6} mm^3	UNCD-MEMS moving mechanical assembly devices
UNCD [4]	MPECVD; Ultrasonication with nano diamond powder (5 nm) & titanium powders (325 nm) in methanol, Substrate Si(100), Reactants CH_4(6%)/ N_2, Temperature 550 ^{0}C, Pressure 50 torr; Power 1200 W	Thickness 1 μm; sp^2/sp^3 0.6; I(G)/I(G*) 1.92$^{\#}$; COF 0.52†;	MEMS/NEMS
UNCD [55]	MPCVD; Polishing & Ultrasonication with diamond nano powders (10 nm) in methanol, Substrate SiO_2, Reactants CH_4(1.6%)/Ar, Temperature 800 ^{0}C, Pressure 150 mbar; Power 800-1200 W, Duration 4 h;	Thickness 0.35 μm; Grain size 2-7 nm; Roughness 7-11 nm; Young's Modulus 980 GPa; Hardness 95 GPa;	Tribological applications
B-NCD [5]	MPCVD; ultrasonic agitation by diamond particle in water; Substrate Titanium alloy; Reactants $CH_4/H_2/N_2/B_2H_6$ (~0.03%); Temperature 780 ^{0}C; Pressure 4.67 KPa; Power 850 W; Duration 2.5 h;	Thickness 2.5-3.0 μm; Grain size 36 nm; $^{\pm}$Roughness 35 nm; COF 0.05; Wear rate ~ 2.45×10^{-9} mm^3/Nm	AFM probes, MEMS devices and biomedical sensors
N-UNCD [10]	MPCVD; 915 MHz, sputtering and ultrasonic agitation by diamond nano particle; Substrate tungsten; Reactants CH_4(1%)/Ar(79%)/N_2 (1-20%); Temperature 850 ^{0}C; Power 10 kW, Duration 10 h; Growth rate 0.3μm/h; growth species C-N and C_2;	Thickness 3.3 μm; Y-700 GPa; Internal Stress 17.5 GPa; Electrical Conductivity ~143 Ω^{-1} cm^{-1}; Thermal conductivity 8.6-16.6 $Wm^{-1}K^{-1}$; TCR (−)0.000345 $^0C^{-1}$; TEC $1.5\times10^{-6}/^0$C;	Bio-medicine, optics, sensors and actuators for space applications

MPECVD-Microwave plasma enhanced chemical vapor deposition; N-UNCD – Nitrogen-incorporated ultrananocrystalline diamond; **MPCVD**-Microwave plasma chemical vapor deposition; **B-NCD-** Boron-doped NCD;

S-substrate; **R**-reactants; **T**-deposition temperature; P- Pressure; **Pw**- Power input; t-deposition time;

d-Thickness; #using 632.8 nm laser, †in ambient air; COF-Coefficient of friction; ‡in humid air; **Y**-Young's Modulus; **H**-Hardness; **F**-Fracture Toughness; **IS**-Internal Stress; **EC**-Electrical Conductivity; **TC**-Thermal conductivity; **TCR** - temperature coefficient of resistivity; **TEC**-Thermal expansion coefficient; ±Surface RMS roughness;

1.1.5 Hydrogenated diamond like carbon (HDLC) and its characterization

Diamond Like Carbon (DLC) films can be defined as composites of amorphous carbon and/or nanocrystalline diamond with/without hydrogen which is required to passivate the dangling bonds of carbon. Some of the beneficial properties (viz., hardness) are like Diamond and hence this is called Diamond like carbon. The films with 20 - 50 % of hydrogen content are commonly known as hydrogenated DLC (HDLC) films. DLC films are usually composed of amorphous carbon with a significant amount of sp^3 bonds and sometime more than 85% sp^3 content are known as tetrahedral amorphous carbon (ta-C) rather than DLC. Again, the amorphous carbon can have sp^3 (diamond-like), sp^2 (graphite-like) and even sp^1 sites. Moreover, the presence of NCD in DLC/HDLC films results in a special characteristic of these materials compared to graphite or diamond. The unique characteristics of HDLC depends on various key parameters viz. sp^3 content, clustering of sp^2 phases, hydrogen content, bond disorder, sp^2/sp^3 ratio. A variety of techniques that can be used to distinguish the bonding in amorphous carbon (a-C) or hydrogenated amorphous carbon (a-C:H). The hydrogen content can be found by Nuclear reaction analysis (NRA) [56], Rutherford

Backscattering spectrometry (RBS) [57], Elastic recoil detection analysis (ERDA) [58], Nuclear magnetic resonance (NMR), combustion analysis, and sometimes using photoluminescence spectroscopy. The estimation of sp^3 fraction is carried out directly by NMR [59], EELS [60], XPS [55, 61], and RBS or indirectly from IR spectra or Raman spectroscopy [61]. A real time or in-situ measurements of the sp^3 fraction and thickness of the growing film is the spectroscopic Ellipsometry method. The mechanical properties of diamond like carbon viz. hardness, elastic modulus, friction, and wear stress yield are of great interest for its use as a coating. The strength and rigidity of these materials are because of their strong, directional σ-bond. Table 1.4 listed various routine methods to determine the sp^3 content and hydrogen content along with the advantages and disadvantages remaining with the methods [62].

Table 1.4 Methods to determine hydrogen and sp^3 content and its limitations

Method	Property/Limitation
NMR	Large sample needed, ^{13}C, dephasing
NRA & RBS	Widely used but special facility required
EELS	destructive and time consuming
ERDA	All atoms can be done, requires suitable detector and sophisticated system
Spectroscopic Ellipsometry	Useable in-situ, but spectra range
Diffraction	Time consuming
ESCA	Small peak shift due to homoplaner bonding
Vis-Raman	Non-destructive, but indirect and sp^3 sites are invisible

IR	Only sites bonded to hydrogen
UV-Raman	Future method of choice
XPS	Limited to near surface

1.1.5.1 Characterization using IR, NMR, XPS, and XANES

Thermal evolution method has difficulty to determine hydrogen content by the fact that hydrogen evolves from C-H bond not only in H_2 form but also sometime evolve specially as CH_4 or C_3H_8. The C-H bond stretching mode ~ 2900 cm^{-1} in IR spectrum is used to measure hydrogen content by using absorption strength (A). This method of estimation of hydrogen is not recommended now because of the wide variation of A (2×10^{20} cm^{-2} for poly a-C: H to 8.5×10^{20} cm^{-2} for diamond like a-C: H) in various types of C-H bonds. The proton decoupling is to separate the carbons bonded to carbon and hydrogen required in the NMR study for the determination of hydrogen content. This method has the unique ability to determine the each type of carbon elastic detection hydrogen site, number of bonded hydrogen and hybridization of carbon atoms. NMR has the advantages of determination of the areal density of both carbon and hydrogen and the ratio H/C simultaneously. However, this method requires special facility but widely used. It is also quite difficult to determine the hydrogen content in hydrogenated DLC from visible Raman spectra as C-H stretching lies above ~ 3000 cm^{-1} and C-H bending at 1290-1400 cm^{-1} which is masked by D-band. However, due to the recombination of electron hole pair with sp^2 bonded clusters in HDLC films, hydrogen content in films gives rise to a strong PL background. Casiraghi et al. [63] showed that the ratio of slope with the PL background to the fitted Gaussian intensity of the G-peak, increases exponentially with hydrogen content. The simple quantitative formula for the hydrogen content

$$H[at\%] = 21.7 + 16.6 \log\{\frac{m}{I(G)}\mu m\} \quad (1.1)$$

The sp^2 and sp^3 hybridized carbon ratio of is an important parameter in characterizing the quality of NCD, UNCD and DLC thin film, as the properties and quality of the films are the function of the ratio of hybridized carbon. Furthermore, the sp^2/sp^3 ratio varies depending on the deposition methodologies and conditions, ratio of the H_2 and other reactants and also with the other elements in the film. The quantification of the sp^3 fraction is more challenging. The sp^2 and sp^3hybrized carbons give distinct chemically shifted peaks in the solid state ^{13}C magic angle NMR spectrum measurements. It is possible to compare the relative contribution of sp^2 and sp^3 sites in the films from the intensities of the two peaks in the NMR spectra. Hydrogenated amorphous carbon film prepared by glow discharge and ion beam sputtering, is reported to give chemical shifts centered at ~130 ppm due to graphitic carbon atoms and ~40 ppm due to tetrahedral carbon atoms, relative to the carbon signal from tetramethylsilane [59]. These shifts are similar to those for diamond peak (sp^3) centered at 39 ppm and graphite peak (sp^2) centered at 158 ppm.

Ferrari et at. [60] showed that sp^3 content determined directly from NMR and EELS are in agreement with the sp^3 content derived from Raman spectroscopy. Thus Raman spectroscopy is a valuable method to obtain sp^3 content for the hydrogenated DLC films. An empirical relation obtained by [61] by fitting all experimental data of sp^3 content (as presented in ref 60 obtained by other measurements, viz. NMR, EELS) with ω_G (G peak position between 1515-1580 cm^{-1}) using a polynomial equation was given below.

$$sp^3 content = 0.24 - 48.9[\omega_G(\mu m^{-1}) - 0.1580] \quad (1.2)$$

For ω_G at 1580 cm^{-1} (i.e., 0.1580 μm^{-1}), the sp^3 fraction will be 0.24

The X-ray photoelectron spectroscopy (XPS) can also used to measure the sp^3 content. The high resolution XPS C 1s shows peak for C-H bonding at 284.85 eV, which is very close to

that of pure carbon C-C bonding at 284.7 eV, as obtained in high resolution photoemission study with single crystal diamond with and without H termination [55]. Moreover, high resolution C 1s spectrum shows C-C bond peak to be at 284.7 eV which is indicative of sp^2 hybridized carbon, such as graphite or amorphous carbon, is consistent with the XPS measurement reported in the literature [64]. However, the detecting the state of hybridization quantitatively using XPS is a controversial issue, because diamond and graphite show same binding energy (284.7 eV) [65]. The sample surface charging can also shift the peak position in XPS measurements. Therefore, rely on Auger electron spectroscopy (AES) or X-ray absorption near-edge spectroscopy (XANES) to detect small changes in the carbon hybridization is recommended. Singha et al. [61] reported the peak at around 284.3 eV and 285.3 eV correspond to sp^2 carbon atoms and sp^3 C-C bond, respectively of C 1s spectra of HDLC films. The presence of other features at 283 eV and 286.6 eV indicates that carbon atoms are bonded to Si and C-O formed on the film surface due to air exposure respectively [61]. The limitation on XPS technique while analyzing HDLC lies due to the fact that XPS is a surface sensitive probe [66]. Therefore, if the sample thickness is more than that of mean free path of electron (50 Å), it may results under estimation of sp^3 fraction in XPS measurement.

The X-ray absorption near-edge spectroscopy (XANES) is particularly useful for probing changes in hybridization in carbon based materials, as well as other chemical bonding states, because of their strong correlation with the unoccupied states on the local environment. It is equally sensitive to sp^3 and sp^2 bonded carbons as well as other bonding states, in contrast to Raman spectroscopy. XANES spectra for a single crystal diamond sample indicate distinct and well recognized spectral features that are commonly associated with crystalline sp^3 bonding including diamond excitation at 289.3 eV and the C 1s $\rightarrow$ σ^* transition starting at 289.5 eV which include the second band gap of diamond that produces a pronounced dip at

302 eV. The C 1s → π* transition peak at 285 eV is associated with sp^2 bonding. The UNCD spectra include exciton peak at 289.3 eV and is slightly broader and diminished intensity compared to that for single crystal diamond due to the confinement in the nanocrystalline grain of the exciton. The sp^2 fraction of UNCD is calculated from C 1s → π* transition. Sumant et al. [55] have estimated the sp^2 content of the top side (3%) and underside (7%) of a freestanding UNCD film. This reveals the increased presence of non-diamond carbon on the underside of a typical UNCD films.

1.1.5.2 Characterization using Raman spectroscopy

Raman spectroscopy is a routine and non destructive technique which is utilized to characterize and differentiate diamond, nanocrystalline diamond, diamond-like carbon, graphite, or polymer like carbon films. The origin and interpretation of the Raman features in the 1000-3000 cm^{-1} region of various carbon films deposited at room temperature is explored in this section. Visible Raman spectroscopy is 50-230 times more intense to sp^2 sites, as visible photons preferentially excite their π states. It is seen that the visible Raman spectrum depends fundamentally on the ordering of sp^2 sites and only indirectly on the fraction of sp^3 sites. The high photon energy of 5.1 eV, excites both σ and π states in UV-Raman spectroscopy. Consequently, UV-Raman spectroscopy is able to probe both sp^2 and sp^3 sites, providing a direct probe of the sp^3 bonds.

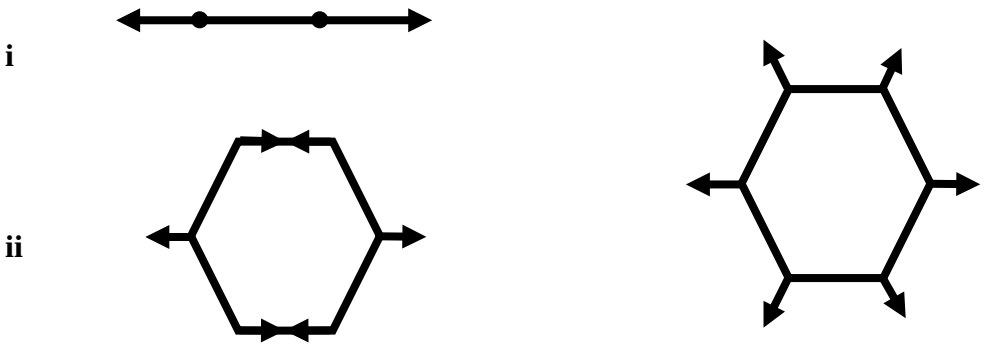

(a) (b)

Figure 1.2 Carbon motions in the (a) G mode and (b) D mode

The Raman spectra of single benzene ring exhibit peak at 1588 cm^{-1} and this feature is also seen in all aromatic rings, and condensed benzene rings. The G mode in the Raman spectra of graphite and other forms of carbon may be due to the stretching vibration of any pair of sp^2 sites, irrespective of the position/pair of sp^2 sites, viz. olefinic chains, or conjugated carbon chains or in aromatic rings at about 1620 cm^{-1}. This occurs in ethylene ($H_2C=CH_2$) as well as graphite (at higher wavenumber). Thus G does not only mean 'Graphite'. Moreover, the position of the G peak is complicated by the hydrogen content, local environment and sp^2 bonding and strongly depends on the stress in the film. The D mode is breathing mode of those sp^2 sites only in rings, not in chains. In the case of the interpretation of D peak, the interaction force constant effects have to be considered. If two or more oscillators in a molecule or solid are discrete from equilibrium, they may be able to affect each other's restoring forces to several degrees, due to changes in the electronic arrangement. The interaction force constant (is the second force constant and) can be either positive or negative. The presence of a peak at 1350 cm^{-1} proves the presence of aromatic or benzene clusters embedded in the amorphous (hydrogenated) carbon films. Moreover, if a Raman spectrum of a carbon film reveals a peak at 1350 cm^{-1} this peak may as well have its origin in the phonon DOS contribution of highly disordered graphite structure. The nomenclature of so called D peak for 'disordered' is not meaningful for a-C:H film because D peak is present in condensed benzene ring even a small as one benzene ring.

The visible Raman spectra of cubic diamond have a single sharp Raman active mode at 1332 cm^{-1}, which is the zone center mode of T_{2g} symmetry. This band is used as the characteristic signature of the diamond structure. Raman spectrum of hexagonal diamond (Lonsdaleite) is distinct from that of cubic diamond and allows it to be recognized. The hexagonal diamond

exhibits a single band at 1319 cm^{-1}. The Raman spectroscopy is more sensitive for graphitic carbon than that for diamond carbon. Consequently, the presence of sharp Raman lines allows effective means of detecting cubic diamond in the diamond film against a background/presence of graphitic carbon. Single crystal graphite or microcrystalline graphite has a single Raman active mode, which is the zone center mode at 1580 cm^{-1} of E_{2g} symmetry labelled as G band (there is a second Raman active E_{2g} mode at 42 cm^{-1} due to inter-planar vibrations). Disordered graphite has a second mode at around 1350 cm^{-1} of A_{1g} symmetry labeled "D″ for disorder. It is to be noted that stronger features at 1350 cm^{-1} in the spectra of glassy carbon is not observed in the spectra of large crystals.

The Raman line width and D/G intensity ratio both vary depending on the structure of carbon and have been related to the structural order. It was experimentally observed that the relative intensity of 1355 cm^{-1} mode with respect to the 1580 cm^{-1} mode varies as the inverse of the crystal flattened dominion size L_a. This observation can be used to determine the crystal planar domain size using Raman spectra data as shown by Nemanich et al. [67]. The Raman spectra of the sample from microcrystalline graphite to hydrogenated amorphous carbon (a-C:H) exhibit first order 1580 cm^{-1} and also the 1355 cm^{-1} line due to the small sp^2 domain size. Furthermore, the position of G peak is slightly dependent on domain size and may shift to higher frequency side by 10 cm^{-1} for the smallest L_a. The small shifts in the band wavenumber have been related to the stress of the deposited film onto the hard substrate viz. alumina, carbide. In addition to G band and D band, a zone-boundary phonon appears at 1620 cm^{-1} in some carbon and may affect the wavenumber of the G band. A peak at 1140 cm^{-1} was attributed to nanocrystalline diamond or hexagonal diamond or sp^3 rich phase [68]. Schwan et al. [69] showed that 1180 cm^{-1} line correlates to the sp^3 content in the film prepared by magnetron sputtering and can be attributed to sp^3 bonded carbon.

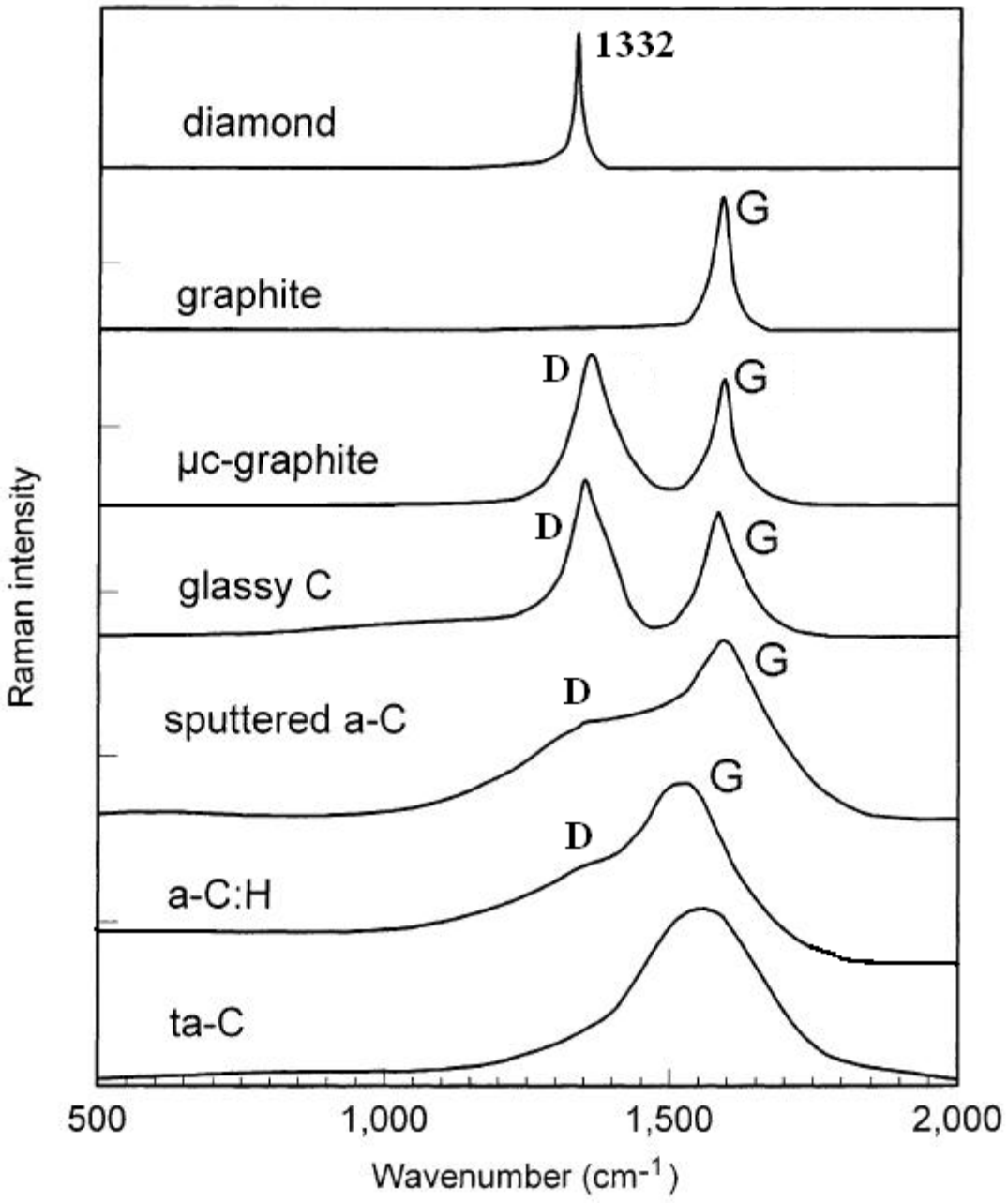

Figure 1.3 Comparison of typical first-order Raman spectra of different forms of carbon.

The other features observed by Raman spectroscopy in the 1000 – 1650 cm^{-1} region are considered to have their origin in sp^2 bonded carbon. Alternatively, Ferrari et al. [70] critically examined peaks near 1150 and 1450 cm^{-1} in the Raman spectra of low quality CVD diamond. They suggested that 1150 $cm^{-1}$and 1450 cm^{-1}peaks should not be assigned to

nanocrystalline diamond or other sp^3 bonded phase, as it disperses with excitation energy and its intensity decreases with increasing energy. The 1150 cm^{-1} peak is accompanied by 1450 cm^{-1} peak and these peaks are assigned to trans-polyacetylene (trans-PA) lying at grain boundaries and surface.

There is a sharp second order Raman line of diamond at 2450 cm^{-1} and its resonance scattering, line width and temperature dependency have been reported [71-73]. The second order spectrum of single crystal graphite shows several strong peaks in the frequency range 2450-3250 cm^{-1}. The second order spectra also exhibit interesting dependence on crystallite size. The features broaden as the crystalline domain size is decreased. All structural features are lost (at 2700 cm^{-1}) and single broad peak is observed; a new feature at 2950 cm^{-1} grows with decreasing crystal size. The interesting 2950 cm^{-1} feature has been reported by Wright et al. [74] and Tsu et al. [75]. They have reported that 2950 cm^{-1} mode was due to a combination of the zone-boundary 1355 cm^{-1} mode and zone-center 1580 cm^{-1} mode. Tsu et al. have suggested that 2950 cm^{-1} feature is due to the impurities. The origin of 2950 cm^{-1} is sometimes more complicated by the fact that sum of the 1355 cm^{-1} and 1620 cm^{-1} mode is very near to the 2950 cm^{-1} value of the new features in the second-order spectra. It is believed that strongest features at 2950 cm^{-1} arise from a combination of the strong density of states at 1350 cm^{-1} and 1600 cm^{-1}. Many times the features at 3248 cm^{-1} in the Raman spectra of single crystal graphite are observed which is a strong evidence for overtone scattering from highest frequency features at 1620 cm^{-1} in the density of states, and 2450 cm^{-1} features correspond to the overtone of Raman bands in the region of 1100-1300 cm^{-1}. The Raman features in the region of 500-3500 $cm^{-1}$are listed in Table 1.5.

Table 1.5 Raman features in the range between 500 - 3500 cm^{-1} are listed [61, 69-70]**.**

Possible interpretations of these features are given

Raman Features (cm^{-1})	Possible Interpretation (/Assigned to)
800	Hydrogen free carbon structure
1140-1180	Trans-polyacetylene (ν_1), Nanocrystalline diamond; hexagonal diamond; or sp^3 rich phase
1305-1320	Hexagonal diamond
1332	Cubic diamond
1350	D peak of microcrystalline graphite or glassy carbon, or alternating ring stretch vibration on benzene or condensed benzene rings
1450-1490	Trans-polyacetylene (ν_3), in case of a-C:H contribution of C-H vibration at 1500 cm^{-1}or contribution from the phonon density of state in finite size crystal of graphite or semicircle ring stretch vibration of benzene or condensed benzene rings
1580	G peak of graphite, sp^2 ring stretch vibration in benzene or condensed benzene rings, or sp^2 stretch vibration of olefinic/conjugated chains
1950	Second-order combination scattering of two main structures at 550 and 1550 cm^{-1}
2420	Two phonon excitation from the 1100 - 1300 cm^{-1} region
2710-2724	Two phonon band 2×1357 cm^{-1} that appears in the spectrum of natural graphite crystal, HOPG, Polycrystalline graphite
2930	Combination of the zone center 1580 cm^{-1} mode and the zone boundary 1355 cm^{-1} mode

The Raman spectrum can be correlated to the structure through (a) the wavenumber of G band (b) band width of G band (c) D/G intensity ratio and (d) band width of the second order phonon. It is generally observed that first order Raman lines relate to structure order within the carbon sheets whereas the second order lines relate to the stacking disorder along the crystallographic c-axis.

The Raman spectra of all types carbon films can be described with in a three stage model of increasing disorder [60]. As the hybridization, bond-angle, and bond-length disorder change from graphite structure to nanocrystalline graphite to amorphous carbon and finally to sp^3 bonded ta-C (or diamond), the sp^2 groups become first smaller, then topologically disordered and finally lost the ring structure. This amorphization trajectory consists of the following three stages as shown below by the schematic diagram.

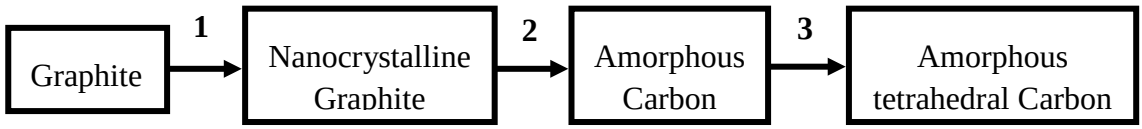

Figure 1.4 Schematic variation showing amorphization trajectory

The main effects on the Raman spectra in the first stage :

(i) The average G peak position changes from 1580 to 1600 cm^{-1}. (ii) The D peak takes shape and D/G intensity ratio increases according to Tuinstra and Koening relation $I_D/I_G \propto 1/L_a$. (iii) There is no dispersion of the G peak

The main effects of topological disorder into the graphite layer in the second stage :

(i) The average G peak position changes from 1600 to 1510 cm^{-1}. (ii) The D/G intensity ratio decreases towards low or zero value and the Tuinstra and Koening relation becomes invalid but $I_D/I_G \propto L_a^2$ i.e. is proportional to the number of aromatic rings. (iii) Increasing dispersion of the G peak occurs.

The main effects on the Raman spectra in the third stage :

In this stage, sp^3 content rises and sp^2 content gradually decreases as the configuration changes from ring structure to chain structure. (i) The G band rises from 1510 $cm^{-1}$to 1570 cm^{-1}. (ii) the D/G intensity ratio equal to zero as there is no ring structure. (iii) Dispersion of the G peak occurs. The detailed description of Micro-Raman spectrometer, data acquisition, and analysis of Raman spectra of HDLC samples by Micro-Raman spectrometer (LabRAM HR vis. Horiba Jobin Yvon SAS France) are described in chapter 3 (section 2). The typical results on HDLC films obtained by Micro-Raman spectrometer and critical discussions are made based upon the results are given in chapter 4 (section 2).

1.1.5.3 Characterization using NRA and RBS

There are few methods, such as nuclear based methods, Nuclear resonance reaction analysis (NRRA commonly known as NRA), and Elastic recoil detection analysis (ERDA), spectroscopic methods like Secondary ion mass spectroscopy (SIMS), and Auger electron spectroscopy (AES) have been reported for their effectiveness towards hydrogen depth profiling. The NRA method utilizes the nuclear resonance reaction between the element of interest and the chosen projectile. The isotope is produced having high energy gamma ray and or proton/alpha particles that are detected by the suitable detectors. Hydrogen depth profiling by ERDA through the bombardment with He ion [76] or heavy ions on the sample and the recoils were recorded in a detector. The depth scale can be generated in the recoil energy spectrum from the rate of energy loss of the incident and recoiled ions in the sample. These methods have some advantages and disadvantages with respect to the depth profiling of hydrogen. For example, SIMS suffers due to the mobility of hydrogen under high vacuum of the system, NRA has a minor problem of desorption under the impact of high energy of the beam. We have used NRA technique, which is easy, rapid, and sequential for the depth profiling of hydrogen in different types of sample, and standard.

The detection of hydrogen and its depth profiling is of wide interest. Indirect methods (like Infrared spectroscopy, Raman spectroscopy, etc.) of measuring hydrogen concentration exploit a standard calibrator for quantification. The conventional direct methods of hydrogen profiling are Secondary ionization mass spectroscopy (SIMS) [77-78], Nuclear reaction analysis (NRA) [79] and Elastic recoil detection analysis (ERDA) [76, 80]. This chapter mainly reports on the nuclear techniques of hydrogen profiling using the ion beams from Tandetron pelletron accelerator using resonance reaction. This method of hydrogen profiling has some advantages and disadvantages compared to other methods. Comparisons of different techniques of hydrogen depth profiling are reported in Table 1.6.

Table 1.6 Comparison of different techniques of hydrogen depth profiling

Techniques for Hydrogen depth profile	Destructive	Reference/ Standard	*Depth resolution (nm)	Sensitivity (at%)	Probing Depth (μm)	Multi-element detection
NRA	NO	NO	5-10	0.1	<3	NO
ERDA with He	NO	YES	30-40	0.1	~1	NO
ERDA with HI	NO	NO	30-40	<0.01	5-10	YES
SIMS	YES	YES	~3	0.01	~1	YES

*Depth resolution at surface; HI – Heavy Ions

SIMS is a very popular technique for depth profiling. The main drawback of SIMS is because of its destructive nature of analysis. The problems are the need of suitable reference standard having similar nature to that of the sample to be analyzed. The sensitivity for hydrogen (0.1 at% under ultra-high vacuum) is also dependent on ultimate vacuum in the SIMS apparatus. The rearrangement of hydrogen under the high vacuum of the system can't be ruled out in this method. The probing depth of this method is approximately ~ 1 μm and better depth resolution (~ 3 nm) than that of NRA (5-10 nm). It is also capable of multi-elemental detection. On contradictory, NRA is non destructive nature. The NRA has comparable

probing depth with ERDA, but the latter is having superior depth resolution (0.01 at%). However, both the methods are unable for multi-elemental detection.

Nuclear reaction analysis (NRA) is a non-destructive nuclear method for the quantitative determination and depth profiling of selected light elements and isotopes. Whereas Rutherford backscattering (RBS) is the method of choice for the detection, and depth profiling of medium to heavy elements. In case of depth profiling of light element in a substrate of heavy element, NRA prefers over RBS because of the complex spectra of RBS.

Table 1.7 Comparison of hydrogen depth profiling using nuclear reaction with different projectiles

Reaction	**$^{1}H(^{19}F,\alpha\gamma)^{16}O$**	**$^{1}H(^{15}N,\alpha\gamma)^{12}C$**
Resonance energy (E_R , MeV)	6.40	6.38
Peak cross section (σ_0 , mb)	88	1650
Resonance Width (Γ, keV)	44	1.8
$\sigma_0 \Gamma$ (mb.keV)	3870	2970
Energy of the Gamma (E_γ , MeV)	6.1, 6.9, and 7.1	4.43
Energy of the next resonance (MeV)	9.1	13.4

Therefore, the yield of the reaction $^{1}H(^{19}F,\alpha\gamma)^{16}O$ is superior than that of $^{1}H(^{15}N,\alpha\gamma)^{12}C$ reaction, and hence better sensitivity for the analysis of hydrogen. Nuclear reaction analysis (NRA) technique for depth profiling of hydrogen in the as prepared and annealed HDLC samples is described in chapter 3 (section 5.1). Rutherford backscattering spectroscopy

(RBS) technique to measure the thickness of HDLC films (as prepared and annealed) is described in chapter 3 (section 5.2). The typical results on HDLC films (as-prepared and annealed) obtained by NRA and RBS techniques and critical discussions are made based upon the results are given in chapter 4 (section 3).

1.1.5.4 Characterization using I-V measurement

The electrical properties of NCD and UNCD have been investigated due to unique applications, including electrochemical electrodes, conducting and insulating layers in MEMS devices etc. The electrical properties of NCD depend of pretreatment methods, deposition conditions and also impurity or doping concentration. The intrinsic NCD has electrical properties sometimes approaching toward single crystal diamond. The intrinsic conductivity after removal of surface conductivity due to hydrogen is $<10^{-11}$ $\Omega^{-1}cm^{-1}$, with breakdown voltage over 9×10^6 $V.cm^{-1}$ and dielectric less ~0.004 [18]. Boron doped NCD's (B conc. level $10^{15} - 10^{21}$ cm^{-3}) conductivity lies 0.1-1 $S.m^{-1}$. The electrical conductivity of UNCD was enhanced by more than four orders of magnitude with the addition of nitrogen doping agent. Four point probe and Hall measurement gave room temperature thermal conductivity of 140-260 $\Omega^{-1}.cm^{-1}$of a UNCD film containing ~0.2% nitrogen [18]. The electrical properties of UNCD driven by the properties of intragranular material and electronic states of the grain boundaries, whereas, the grain and grain boundary controls the electrical properties of NCD and are similar to the electrical properties of bulk or single crystal diamond.

The single electron transistor (SET) switches on and off every time an electron is added to conducting island, called coulomb blockade (CB), isolated from two metallic leads, called source (S) and drain (D), by insulator, called tunnel barrier (TB). In order to avoid thermally induced random tunneling events, the minimum size of CB has to be smaller than ~ 1 nm for

room temperature (RT) operation of SET [81]. The present conventional micro-fabrication process limits the size of CB within a few tens of nm [82-83]. The nature of the CB i.e. metallic nanostructures, semiconducting, or quantum dot – is irrelevant for creation of SET, in first order approximation. Hauf et al. [84] showed that although bulk diamond is a good electrical insulator, but may exhibits a high surface conductivity in air when the surface is hydrogen terminated. They experimentally demonstrated the two dimensional character of surface conductivity of diamond using in-plane gated FET in an nm sized device having laterally confined Source (S) - Drain (D) channel. They observed the CB effects of multiple quantity island varying size with gate voltage which is the direct result of the two dimensional character of the conductive channel formed by hydrogen terminated diamond surfaces. The electrical conductance properties of our HDLC film from current (I) vs. voltage (V) characteristics have been investigated using Keithley source meter. The acquisition and analysis of I-V characteristics on the HDLC surface at RT (300 K) in ambient condition using a Keithley 2635 source meter is described in chapter 3 (section 6) and the typical results on HDLC films obtained by current (I) vs. (V) characteristics onto the HDLC surface and critical discussions are made about the surface conductance mechanisms, based upon the results are given in chapter 4 (section 4).

1.2 Objectives

NCD and UNCD films have, in general, high Young's modulus, high hardness and a low macroscopic friction coefficient, and are also electrically conductive. Both NCD and UNCD films are usually deposited on non-diamond substrates, viz. silicon wafers, SiC, SiO_2. The growth of NCD/UNCD films from the vapor phase on non-diamond substrates at practical rates was accomplished with the development of thermal- and plasma-enhanced CVD methods [85-88] in which a hydrocarbon gas (usually methane) mixed in low concentrations with hydrogen is energized thermally or in a plasma, prior to contact with a heated substrate.

In order to achieve good adhesion of NCD/UNCD films onto foreign substrate, heat-assisted bias-enhanced nucleation (BEN)/bias enhanced growth (BEG) technique, was found to be very successful in terms of achieving diamond nano-grains (3–5 nm), with smoother surfaces (6 nm rms) and higher growth rate (1 m/h) of the film [22]. In the BEN/BEG technique, there is a speculative atomic model of possible diamond/graphite/Si interface, causing a very good adhesion of the film onto the Si substrate due to minimum lattice mismatch [89].

In my thesis works I have used asymmetrically capacitively coupled RF (13.56 MHz) discharge wherein a dc negative self-bias can be produced continuously during deposition of Hydrogenated Diamond like Carbon (HDLC) thin film onto substrates like Si(100), quartz, steel etc. at room temperature, with ultrasmooth surface (~ 0.0175 nm rms) [61, 90-91]. The sp^3 C-H contents and presence of NCD in the HDLC films depend on the ratio of flow rates of hydrogen (H_2) and methane (CH_4) for a given deposition conditions like pressure, dc negative bias, deposition time etc. [61]. A high resolution transmission electron microscope (HRTEM) image of MeV nitrogen ion irradiated HDLC film, clearly shows existence of crystalline graphite with lattice spacing of 0.34 nm in the HDLC film, although the crystallographic planes are somewhat distorted compared to the perfect graphite structure [92]. In the characterization of HDLC thin film by high resolution transmission electron microscope (HRTEM), it was observed that indexing of electron diffraction pattern with different orientation gives same hexagonal lattice parameters a=2.62 Å and c=6.752 Å (may be termed as Hexagonal HDLC, i.e. HHDLC), which are different from the hexagonal graphene/graphite structure [93]. These HRTEM characterization results do not reveal why the lattice parameters are different from the hexagonal graphene/graphite structure and if the nanocrystalline/ultra-nanocrystalline structures are embedded in the hexagonal HDLC film.

All these properties of HDLC films in the early works [61, 90-92], motivated me, for PhD thesis works, to investigate the structural composition of hexagonal HDLC films by

Micro-Raman spectroscopy and High resolution transmission electron microscope (HRTEM), depth profile of hydrogen in the HDLC film by ion beam analysis (IBA) techniques, morphology of HDLC surface by Atomic force microscope (AFM) and Scanning electron microscope (SEM), electrical conductance property of HDLC film from the current (I) vs. voltage (V) characteristics by Keithley source meter, optical property of HDLC surface by measuring the images of reflected light using Olympus digital camera, measurement of dielectric constant of HDLC film at frequency less than 1 Hz using Solartron 1296 dielectric interface instrument. By these investigations on HDLC films, I have addressed the key issues like ultrasmoothness of HDLC surface, compatibility of BEN model [89] in the structural composition of HDLC, electronic properties of HDLC film, new information about the surface conductance of HDLC in comparison to that of hydrogenated diamond (HD) film and applicability of HDLC as optical device.

My thesis works are arranged as follows: (i) chapter 1 describes literatures survey on the synthesis, characterization and applications of NCD/UNCD films (ii) chapter 2 describes experimental set-up for the synthesis of HDLC films onto various substrate at room temperature (iii) chapter 3 describes characterization tools (iv) chapter 4 describes results and discussions (v) chapter 5 describes summary and conclusions.

Chapter 2

Experimental set-up for the synthesis of HDLC films on various substrates at room temperature

2.0 Introduction

Over three decaeds of research in science and engineering technology have been performed into understanding, developing, and applying low pressure diamond deposition/coating onto the materials of immense interest for industrial, medical and technological fields. A unique method at low pressure diamond synthesis is designated to as the 'New Diamond Technology' to discriminate it from 'High Pressure and High Temperature' (HPHT) diamond synthesis. In new diamond technologoy, at low atomospheric pressure and at ordinary temperature, the typical sources of carbon, viz. methane, carbon monooxide, is changed by chemical vapor deposition of diamond. Technologically, the layers of diamond over large surface area can be synthesized. The deposited diamond layer on the wide variety of host materials is accompanied by the exceptional properties of diamond (viz. extreme hardness, high thermal conductivity, high corrosion resistant, low coefficient of friction, low infrared and microwave absorption, and wide band semiconductor) suitable for a particular applications. The deposition of diamond films using new technology is made possible by an improved scinetific knowledge and by the research and development of CVD systems espcially designed for the deposition of diamond. There are few efficient methods for making low pressure diamond depositions. To correlate the quality of the films and for better understanding of the characteristic properties of the films, the deposition conditions, methods of depositions, and the type of equipments are needed to be studied immensely [94].

Phase diagram of carbon is shown in Figure 2.1. From the diagram it is seen that diamond is the stable form of cabon at high pressure (thousands of atmospheres) and high temeratures (thousands of degree celsius). It may be seen that graphite is the stable form of carbon under ordinary temperature and pressure. The artificial synthesis of diamond from graphite is under the conditions of ~55000 atm. and temperature ~2000 ^{0}C was first reported by General

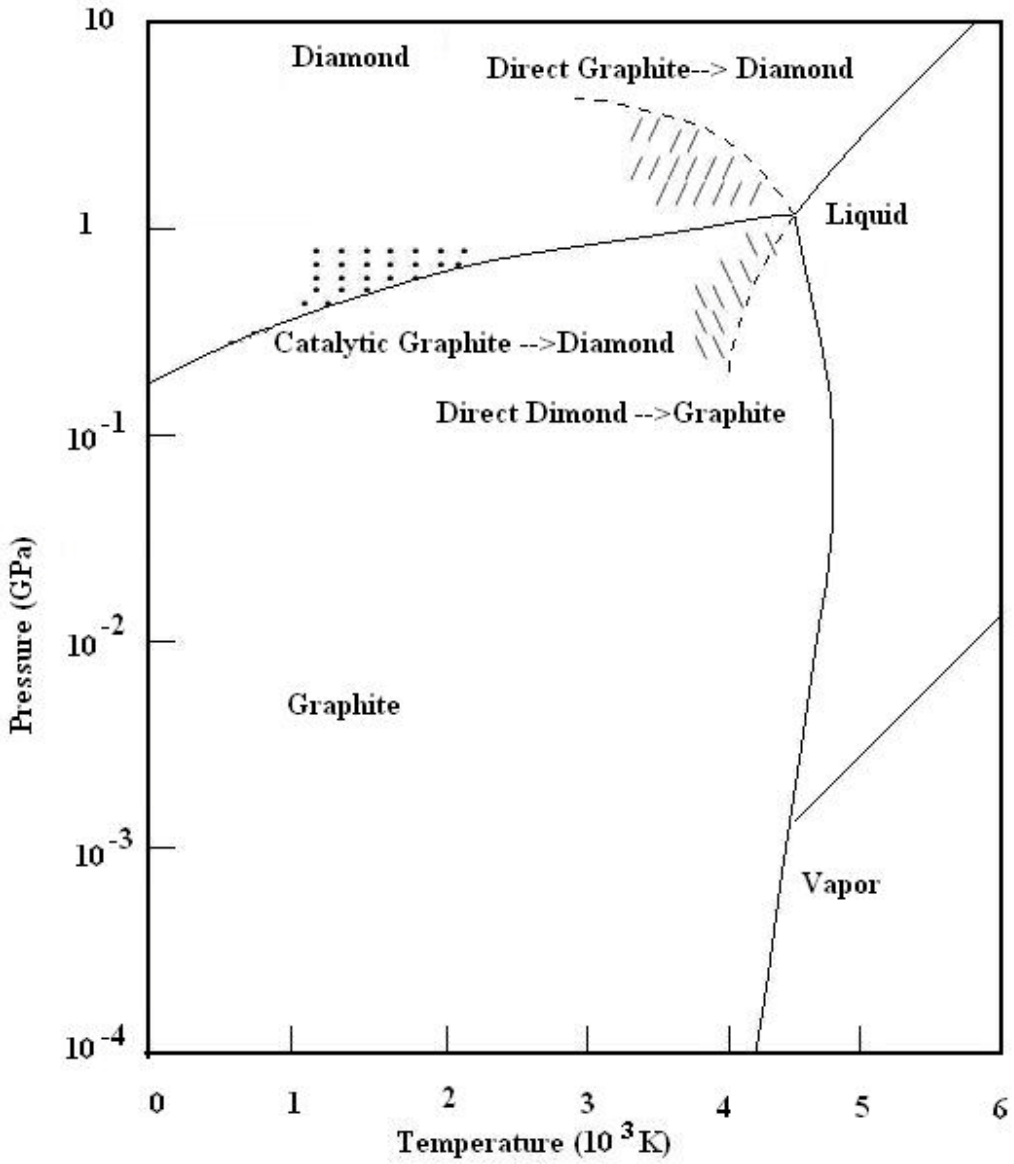

Figure 2.1 Phase diagram of carbon

Electric group viz. Bundy et at. in 1955 [95]. A metastable state is not the mimimum energy arrangement of the atoms. Diamond at ordinary temperature and pressure is metastable state of carbon. However, carbon atom in diamond lattice dose not spontaneously convert to graphite under low pressue and temperature. Therefore, under suitable deposition condition, synthesis of diamond seems to be feasible from nascent carbon containing species under metastable conditions and thus inviting the new era in the preparation of diamond film coatings. The possibility of new applications of diamond films are mainly due to the exceptional properties of diamond.

Table 2.1 Electronic Configuration of Elements

Element	Atomic Number	Electronic Configuration	Pictorial Representation
H	1	$1s^1$	$\frac{\uparrow}{1s}$
C	6	$1s^2\ 2s^2\ 2p^2$	$\frac{\uparrow\downarrow}{1s}\ \frac{\uparrow\downarrow}{2s}\ \frac{\uparrow}{2p}\ \frac{\uparrow}{2p}\ \frac{}{2p}$

In order to explain the formation of four equivalent covalent bonds by carbon it was assumed that prior to reactions, one of the two equivalent 2s electrons of carbon is promoted to the third 2p level giving the excited state configuration:

$$\frac{\uparrow\downarrow}{1s}\ \frac{\uparrow}{2s}\ \frac{\uparrow}{2p}\ \frac{\uparrow}{2p}\ \frac{\uparrow}{2p}$$

Then the mixing of one 2s and three 2p orbitals provide the four equivalent sp^3 hybrid orbitals with one electron in each. All the bond lengths and angles are equal when bonded to the same atoms.

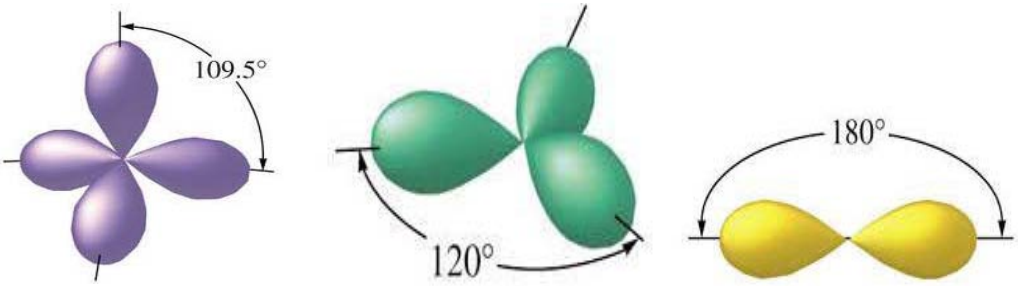

sp^3 sp^2 sp

Figure 2.2 Spatial arrangements of carbon sp^3, sp^2 and sp hybrid orbital (σ bonds)

Carbon forms variety of crystalline and disordered structures because it is able to exist in three hybridization states, viz. sp^3, sp^2, and sp (Fig. 2.2). In the sp^3 hybridization, as in diamond, a carbon atom forms four strong σ bonds along the tetrahedral directions using four valence electrons. In the three fold coordinated sp^2 hybridization, as in graphite; three valence

electrons forms trigonally directed planer sp^2 orbital's which forms σ–bonds in a plane. The fourth electron of the carbon atoms lies in a pπ orbital which forms a weaker π-bond with the neighboring atoms. This π bond lies normal to the σ–bonding plane. In sp hybridization, two of the four valence electrons enter σ–orbital's, each forming a σ–bond along the X-axis and other two electrons enter $p_y\pi$ and $p_z\pi$ orbital's in Y and Z direction make two π-bonding with orbital of neighboring atoms. The π-bonds are perpendicular to each other and also perpendicular to the σ–bond plane.

2.1 History of 'Diamond' and 'Low Pressure Diamond Synthesis'

The synthesis of 'Diamond' has been undertaken considering the two principal facts in the primary stage of diamond synthesis. They are (a) diamond and charcoal are made from same elemental carbon and (b) diamond is denser than charcoal. Therefore, compression at high pressure seems to be a viable route to achieveing diamond synthesis. Lewis and Randall [96] in 1915 showed that at room temperature and ~ 1 GPa pressure, diamond-graphite equilibrium exist. Soon after that, General Electric Corporation in 1955 first sucessfully synthesized diamond from graphite in molten metals at temperature 1700-2000 K and pressure from 7-10 GPa. Willam G. Eversole [97] for the first time proposed that the synthesis of diamond at low pressure from carbon monoxide on a diamond seed, considering the regions of metastability of diamond and graphite (Fig. 2.1 dashed line). Lander and Morrison et al. [98] crucially recognized the critical and significant role of hydrogen in epitaxial growth of diamond on diamond. Hydrogen creates a kinetic barrier to graphitization. Angus and his coworker [99] showed the role of hydrogen, the machanism for diamond growth, kinetics, and proposed the growth on surface sites. The numerous research established the unique and unmatched role of hydrogen which etched out the graphitic carbon structure preferentially than diamond and hence supress the nucleation and growth of

graphite. Consequently this results in the synthesis of diamond at low pressure inspite of its thermodynamic unstability.

2.2 General methods for Diamond Like Carbon Synthesis

2.2.1 Physical Vapor Deposition (PVD) :

Physical Vapor Deposition (PVD) is a general term used to describe variety of methods to deposit thin films by the condensation of a vaporized form of the desired film material onto various surfaces (e.g., onto semiconductor wafers). The coating process involves purely physical process for example high temperature vacuum evaporation. Few typical examples are given below

- **Cathodic Arc Deposition**:

  In which high power arc discharge at the target materials blasts away some into highly ionized vapor.

- **Pulsed Laser Deposition**:

  In which a high power laser ablates materials from the target into a vapor.

- **Sputter Deposition**:

  In which a glow discharge bombards the material sputtering some away as a vapor.

- **Electron Beam Physical Vapor Deposition**:

  In which material to be deposited is heated to a high vapor pressure by electron bombardment in high vacuum.

2.2.2 Chemical Vapor Deposition (CVD) :

Chemical Vapor Deposition (CVD) is a general term used to describe variety of methods [25-26, 85-88, 100-101] to deposit thin films from one or more volatile precursors, which react

and/or decompose to produce the desired deposit onto various surfaces (e.g., onto semiconductor wafers). Frequently, volatile by-products are also produced, which are removed by gas flow through the reaction chamber. Follwing are the different types of CVD methods

- **Atmospheric pressure CVD (APCVD)**

  Chemical vapor deposition at atmospheric pressure

- **Plasma Enhanced Chemical Vapour Deposition (PECVD)**

  CVD process that utlilize plasma to enhance chemical reaction rate of the precursors. PECVD process allows deposition at lower temperature (e.g., Room temperature).

- **Microwave Plasma-Assisted CVD (MPCVD)**

  Microwave is used to create the plasma

- **Metalorganic Chemical Vapor Deposition (MOCVD)**

  Metalorganic chemical vapor deposition based on metalo-organic precursors e.g., tri-methyl gallium

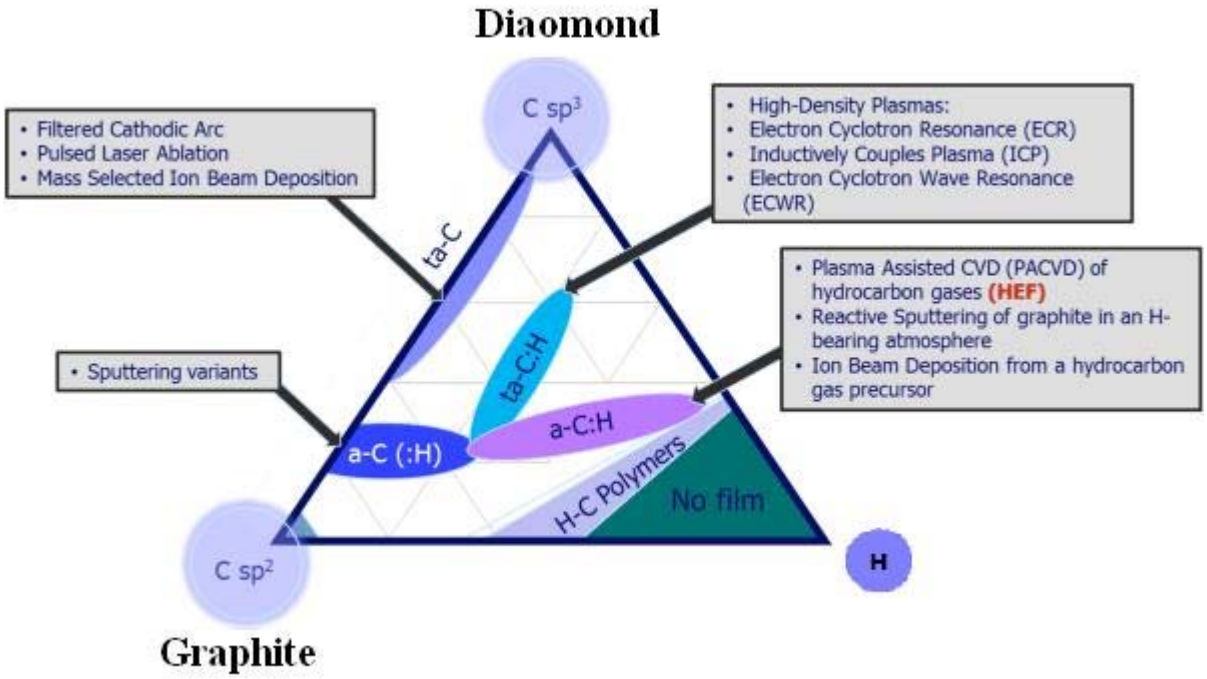

Figure 2.3 Ternary phase diagram of bonding of amorphous carbons. The corners represents to diamond (sp^3), graphite (sp^2) and hydrogen (H)

It is very convenient to display the composition of various forms of carbon films (C-H) on a ternary phase diagram as shown in Figure 2.3. The different deposition methods have been developed to produce carbon film with different degree of sp^3/sp^2 bonding. A range of deposition methods are able to reach in the different locations of the ternary phase diagram is also shown in Figure 2.3. For example, PECVD is able to reach into the interior of the triangle. In this chapter, brief introduction is given to HDLC film depositon using PECVD technique.

2.3 PECVD System

2.3.1 Description of the System

The experimental facility for synthesis of HDLC thin film at Saha Institute of Nuclear Physics is shown in Figure 2.4, and the schematic block diagram of the PECVD instrument is

shown in Figure 2.5 to explain the operation procedures. This instrument is a stat-of-art single chamber depostion system, which is indiginously designed and developed by my guide, Dr. Nihar Rajan Ray, to produce high quality PECVD films. Two major gas sources are available but we have used only one for our work which is methane (CH_4) for deposition of the film. The system also possesses other gases viz. Hydrogen (H_2), Helium (He), and Nitrogen (N_2). The hydrogen gas is used for both the pretreatment and deposition processes. The role of hydrogen and importance of hydrogen has been described in introduction part of chapter 1. The nitrogen is used as a purging gas and must be utilized during the deposition process to prevent the explosion. These gases are introduced into the chamber in a controlled manner using a Mass flow controller (MFC) units. The Si(100) substrates of ~10 mm diameter and 1 mm thick disc are always cleaned using isopropyl alcohol with a ultrasonic bath for 10 minutes, and then ultrasonically cleaned with milipore water and then used for deposition of the films. The loading and unloading of substrates can be done via a hinged door port located at the front of the deposition chamber. The other ports are provided in the chamber to view the substate and progress during the deposition. Those ports can be used in future for analysis of plasma emission spectra and electron temperature, electron density and electric potential of the plasma using a Langmuir probe. The substrates were always placed on the cathode (marked as 1 in Fig. 2.5). The cathode is 250 mm dia. of metallic electrode connected to the RF matching circuit and power supply. The substrate can be floated or biased, depending on bias requirement on the substrate. The system consists of two types of pumping systems. Mechanical pump is first, switched on for making the chamber pressure from atmospheric to ~ 0.1 mbar. Small traces of oil are absorbed by the chemical filter which prevents the contamination during the processes of deposition. Subsequently a Roots pump is switched on when the pressure is ~0.1 mbar and continued until the pressure reaches desired value (~10^{-4} mbar). The exhaust connection of the chamber rotary vane pump is connected to an effluent

scrubber system. As a safety feature, a diaphragm pump is used to ensure that air is never pumped into the gas scrubber system. The RF power is generated from a RF generator. There is a RF matching circuit that optimizes the input power on the deposition chamber. The sample, cathode plate and related RF electronic equipments are cooled with the help of the closed loop cooled water circulation system.

2.3.2 Description of System Operation

Our PECVD facility is a typical representation of deposition system with all components required for the synthesis of HDLC film is shown in Figure 2.4. The violet hydrogen plasma is clearly observed through the front glass view port of the system. For a typical deposition, we used the following gases : Helium (He, 1500 SCCM) (SCCM-Standard Cubic Centimeter Per Minute), hydrogen (H_2, 500 SCCM) and methane (CH_4, varying 90-10 SCCM). The substrate in most cases is Si(100) or sometime quartz, stainless steel, carbon foam etc. To run the system and deposit films, the chamber is evacuated through mechanical and roots pumps and cooled the substrate and electronic parts using closed loop cooled water circulation system. Then the gases are introduced into the chamber through MFC using a electronically controlled system. The chamber pressure is controlled by electronically adjusting the valves opening. The hydrogen gas is first introducd in the chamber for removal of any surface contamination and oxide layer onto the substrate. This etching of mirror polished Si(100) substrate of 10 mm diameter for 15 min is carried out in a pure hydrogen (H_2 flow rate ~ 500 SCCM) plasma (light pink in color), at a pressure of 0.193 mbar, produced by 30 W RF forward power producing dc self-negative bias (~ -200V) with a impedance matching circuit, to remove any oxide layer from the surface of Si(100). The in-situ biased enhanced nucleation (BEN) process using helium (He flow rate ~1500 SCCM) plasma is produced by 50 W RF power producing dc self-negative bias (~ -200 V), with H_2 (flow rate ~500 SCCM) and CH_4 (flow rate~50 SCCM) gases at a total pressure of 0.756 mbar and at substrate

temperature ~ 14 ^{0}C, for 30 min deposition time. Table 2.1 list the experimental parameters used for the deposition of various films.

Experimental facility for synthesis of HDLC at SINP :

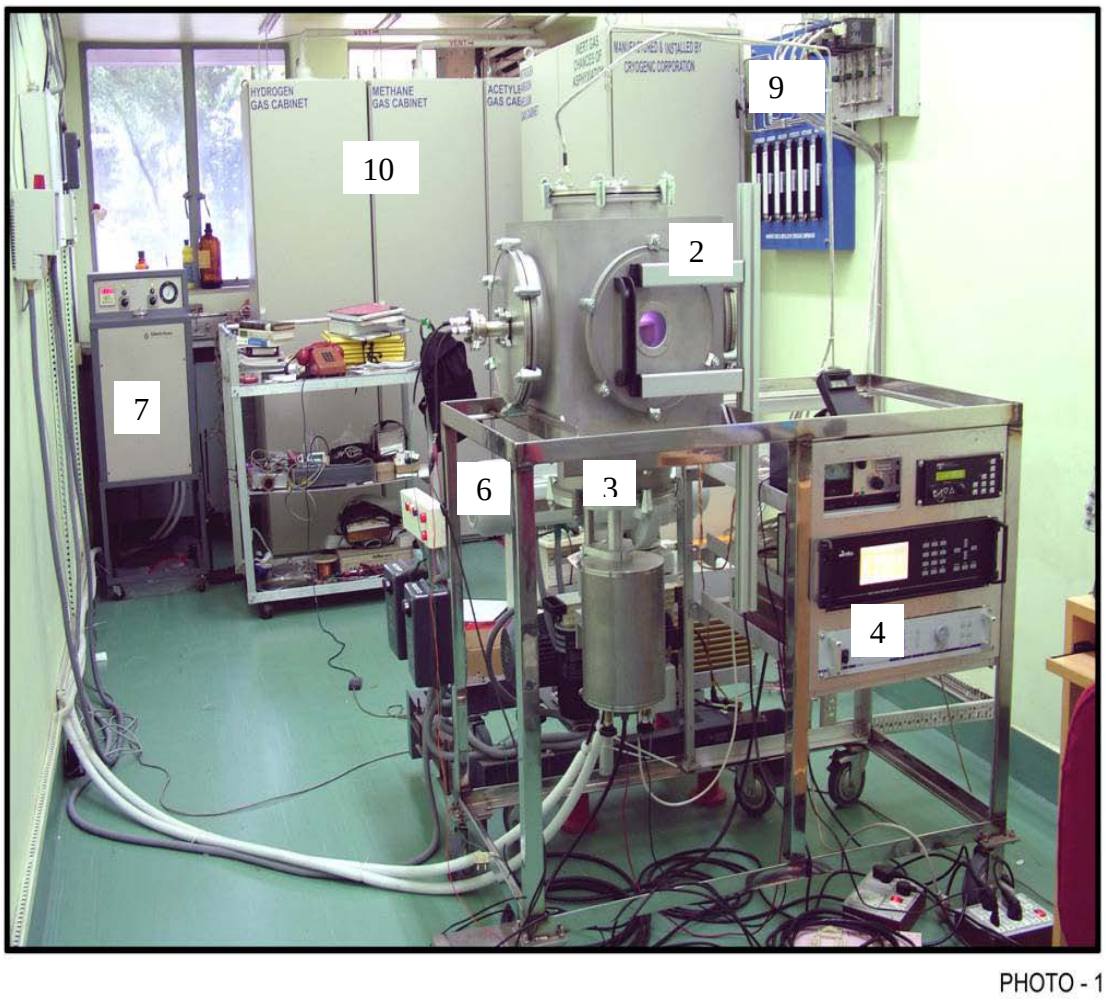

Figure 2.4 Experimental facility for synthesis of HDLC at Saha Institute of Nuclear Physics

Picture of our Plasma Enhanced Chemical Vapor Deposition (PECVD) Instruments for HDLC Synthesis. This instrument is indigenously developed by Prof. N. R. Ray, Plasma Physics Division, Saha Institute of Nuclear Physics. For this work, Prof. Ray got appreciation by Dr. A.P.J. Abdul Kalam, in the year of 2006.

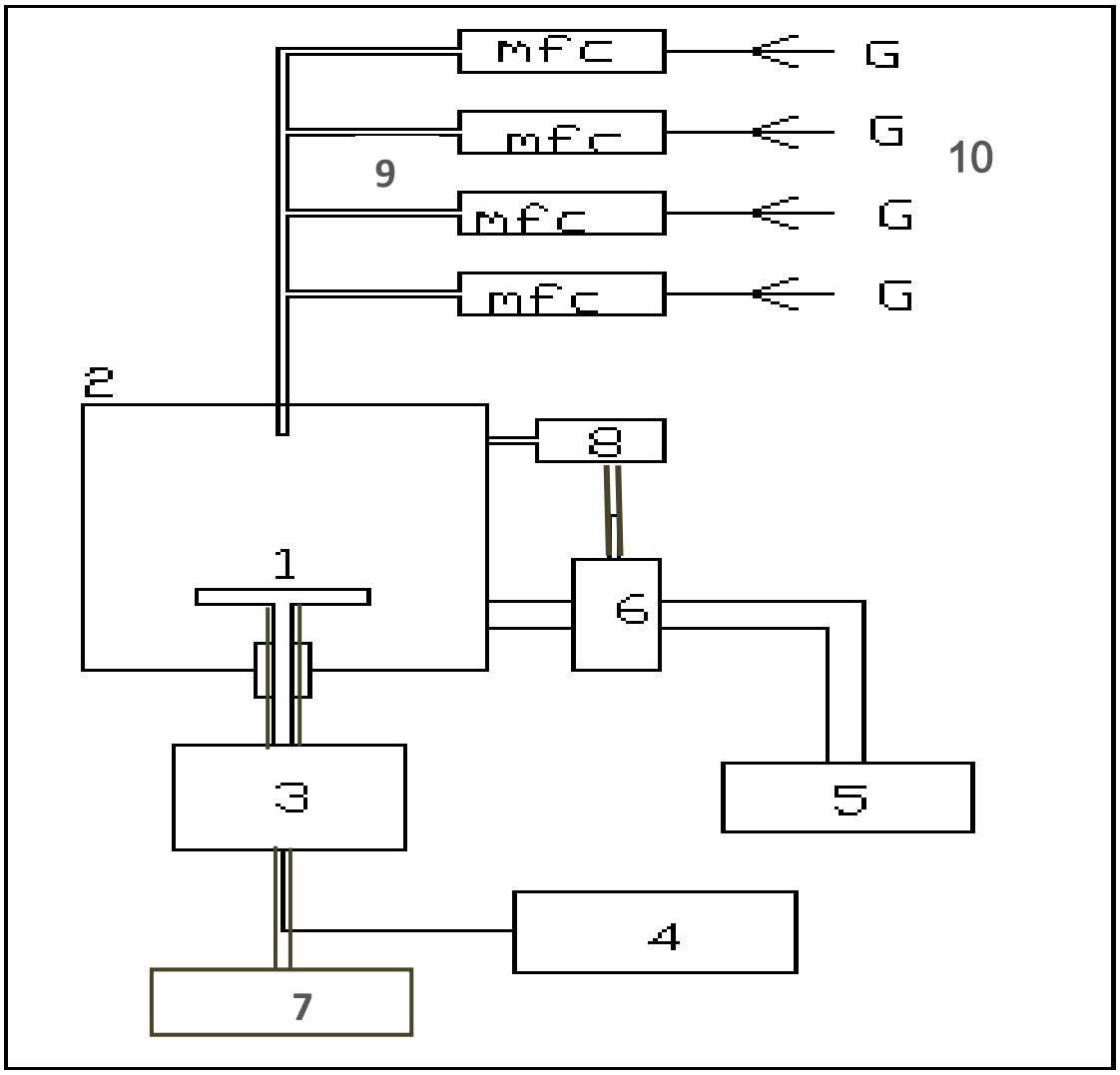

Figure 2.5 Schematic block diagram of the PECVD Instrument

Different parts of the System

1 – Cathode

2 – Anode

3 – RF-Matching Circuit

4 – RF Power Supply

5 –Drain (Collector)

6 – Vacuum Pumps (Mechanical and Roots pump)

7 – Cooled Water Circulation System

8 – Vacuum Gauge

9 – MFC (Mass Flow Controller)

10 – Gases (Hydrogen, Helium, Methane, Nitrogen, etc.)

The mechanism for plasma formation is discussed herein. In the beginning of the process, it is assumed that there are some electrons already exists inside the chamber. Under the acceleration of high voltage from the RF generator (13.56 MHz), they also oscillate very quickly among the gaseous atoms viz. He. Within very short time, they attain very high energy and momentum which are then trasferred to the atoms to ionize them. The resulting electrons then follow the same path, i.e. furthur ionize the atoms. This multiple ionization process proceeds very fast and resultant plasma is formed. The power supply from a RF generator is coupled through a capacitor to the cathode as shown in Figure 2.5. As a result, a negative dc self-bias is induced on the cathode and on an ungrounded substate Si(100). The bias on the cathode is controlled through RF impedence matching circuit and kept constant at ~ -200 V. The heavy and positive radicals/ions viz. C_2H_2, CH_3, CH_4, C_2H_4, C_2, and CH due to their low mobility, cannot be in phase with the RF power supply. However, due to the dc self-bias voltage on the target, make is possible the deposition of the film. Consequetly, the magnitude of the bias on the substrate has an important effect on the formation of thin film. It also affets the film composition and properties of the films.

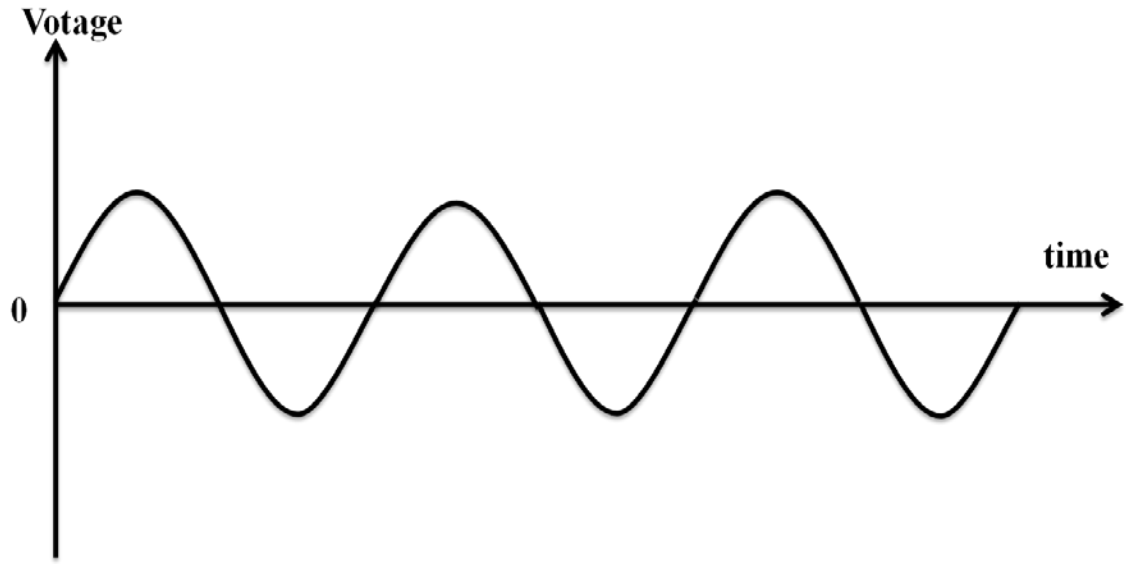

Figure 2.6 Original sine wave function of the RF power supply

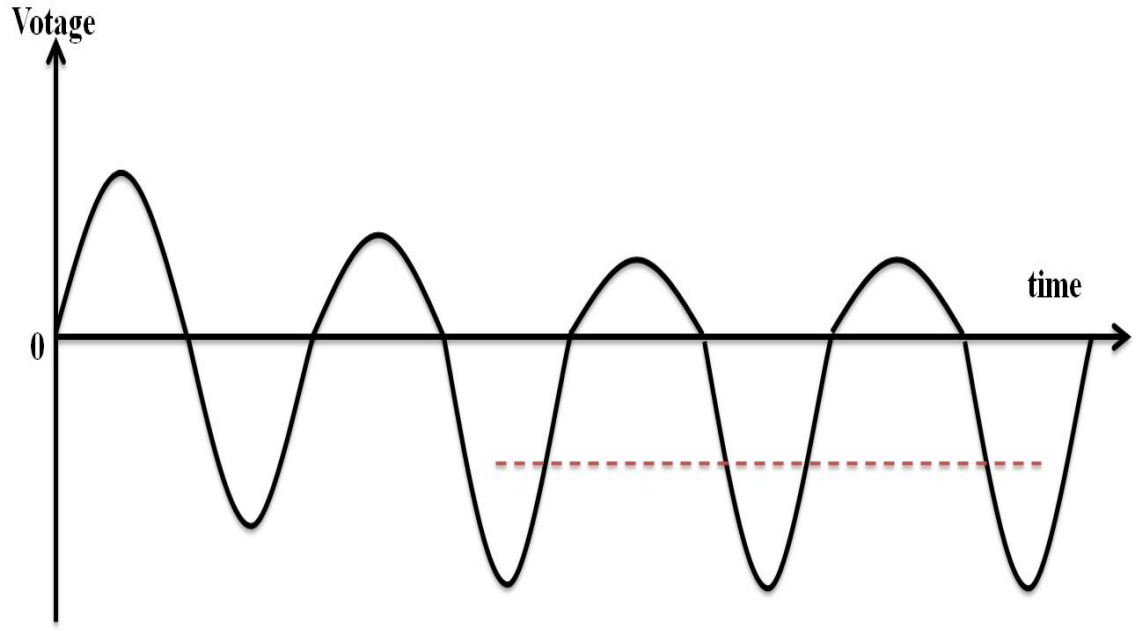

Figure 2.7 Resulting shape of the sine wave after application of RF power supply to the system

The frequency for the RF is 13.56 MHz and the original sine waveform output from the RF generator is shown in Figure 2.6. This AC voltage is applied onto the cathode through a capacitor between the cathode and the generator. After that the AC wavefunction will change from Figure 2.6 to Figure 2.7. In the first-half cycle, the cathode (substrate) is positive and

starts to accumulate electrons. During the next-half cycle the cathode is negative and begins to collect positive ions from the plasma. The number of electrons collected in first half cycle is very high compared to the number of positive ions collceted in the rest half cycle. Because of the higher mobility of the electrons (>10^2 times than that of positive ions), a net negative charge accumulates on the target as there is a capacitor between the target and the RF generator. The electrons collected on the target stay on the surface of the target for sometime. In the first half of the second cycle, the fewer number of electrons will accumulate, as prior gathered electrons still exist there. In the second half of the second cycle, the flux of positive ions will be larger than that of the first cycle. After few cycles, the elctron flux will be equal to the ion current, and the system reaches the state of equilibrium. After equilibrium state, most of the time the cathode voltage is negative, but remains positive for a short fraction of time of each cycle. Therefore, Figure 2.7 shows that the target is effectively biased by a negative dc potential with respect to ground. This bias enhanced nucleation (BEN) and bias enhanced growth (BEG) methods are very crutial for growing NCD films with a steady self-biased dc voltage (200-260 V) during the PECVD and MPCVD processes (in-situ nucleation processes). The unique advantages of this technique are that it does not require any pretreatment or pronunciation stage with the suitability of wide range of substrates. More detailed discussion are given in introduction part of chapter 1.

2.3.3 Synthesis of Hydrogenated Diamond Like Carbon thin film onto

2.3.3.1 (a) Silicon (b) Quartz substrates

PECVD is used to deposit thin films from a gas state to a solid state on a substrate. Chemical reactions are involved in the process, which occur after creation of plasma of reacting gases. The plasma is generally created by RF (AC) frequency discharge between two electrodes, the space between which is filled with the reacting gases.

The deposition process consists of two steps:

(1) Etching of mirror polished Si(100)/quartz substrate of 10 mm diameter for 15 min. in a pure hydrogen (H_2 flow rate ~ 500 SCCM) plasma (light pink in color), at a pressure of 0.193 mbar, by 30 W RF forward power producing dc self-negative bias (~ -200 V) with a impedance matching circuit, to remove any oxide layer from the surface of Si(100).

(2) in situ Biased Enhanced Nucleation (BEN) process using helium (He flow rate ~1500 SCCM) plasma by 50 W RF power generating dc self-negative bias (~ -200 V), with H_2 (flow rate ~500 SCCM) and CH_4 (flow rate ~ 50 SCCM) gases at a total pressure of 0.756 mbar and at substrate temperature ~ 14 ^{0}C, for 30 min. deposition time.

The reactive unexploited gases are taken out from the deposition chamber during the deposition process and purged out to the environment after mixing with nitrogen gas.

Experimental Parameters (Deposition Conditions) at a glance :

1. RF : RF-Frequency 13.56 MHz;
2. RF-Power : 30 ± 2 Watt during etching process and 50 ± 2 Watt during deposition process.
3. Pressure : 0.20 ± 0.02 mbar during etching and 0.75 ± 0.05 mbar during deposition
4. Substrate : Si(100)/Quartz
5. Pre-treatment : By hydrogen plasma for 15 min. at 0.2 mbar
6. Gas Mixture : CH_4 (50 SCCM), H_2 (500 SCCM) and He (1500 SCCM) (SCCM - Standard Cubic Centimeter Per Minute)
7. Deposition time : 30 min.
8. Temperature : 14 ^{0}C
9. Nitrogen Flow : 500 SCCM

2.3.3.2 Stainless steel

The stainless steel substrate (15 mm × 15 mm) was cleaned with NaOH followed by HNO_3 and then rinsed with millipore water. After cleaning, the argon ion sputtering was used to remove the passive chromium oxide layer for 15 minutes. The typical conditions used for sputtering were : flow rate of Ar gas 100 SCCM, total pressure 0·3 mbar, RF power 30 watts, dc self-bias –150 volts. After the sputtering, the steel surface was pre-treated with hydrogen plasma discharge. The typical conditions for this pre-treatment and deposition of HDLC over stainless steel substrate were tabulated in Table 2.1. Kumari et al. [91] have studied the HDLC coating over stainless steel using field effect and cross-sectional SEM (FESEM and XSEM) and energy dispersive X-ray analysis (EDX). They have reported the formation of a very smooth, continuous, non-poros, and homogeneous HDLC thin film coating with good adhesion properties. Therefore, i have not carried out any further study of HDLC film onto stainless steel substrate for my thesis work.

Table 2.2 Comparison of the PECVD deposition conditions on different substances

Parameters		Substrate		
		Silicon	**Quartz**	**Stainless Steel**
RF Frequency (MHz)		13.56	13.56	13.56
Pre-treatment	RF Power (Watt)	30	30	25
	Gases and Flow rate (SCCM)	H_2 (500)	H_2 (500)	*Ar (100) H_2 (500)
	Pressure (mbar)	0.19	0.20	0.30
	Time (min.)	15	15	15
Deposition	RF Power (Watt)	50	50	50

	Bias (V)	- 200	- 200	- 200
	Pressure (mbar)	0.75	0.75	0.70
	Time (min.)	30	30	25
	Gases and flow rate (SCCM)	He (1500), H_2 (500), CH_4 (50)	He (1500), H_2 (500), CH_4 (50)	He (1500), H_2 (500), CH_4 (50)
	Temp (^{0}C)	14	14	14
Nitrogen Flow (SCCM)		500	500	500

*****Sputtering condition : RF power 30 watts, dc self bias 150 volts, total pressure 0.3 mbar, time 15 min.

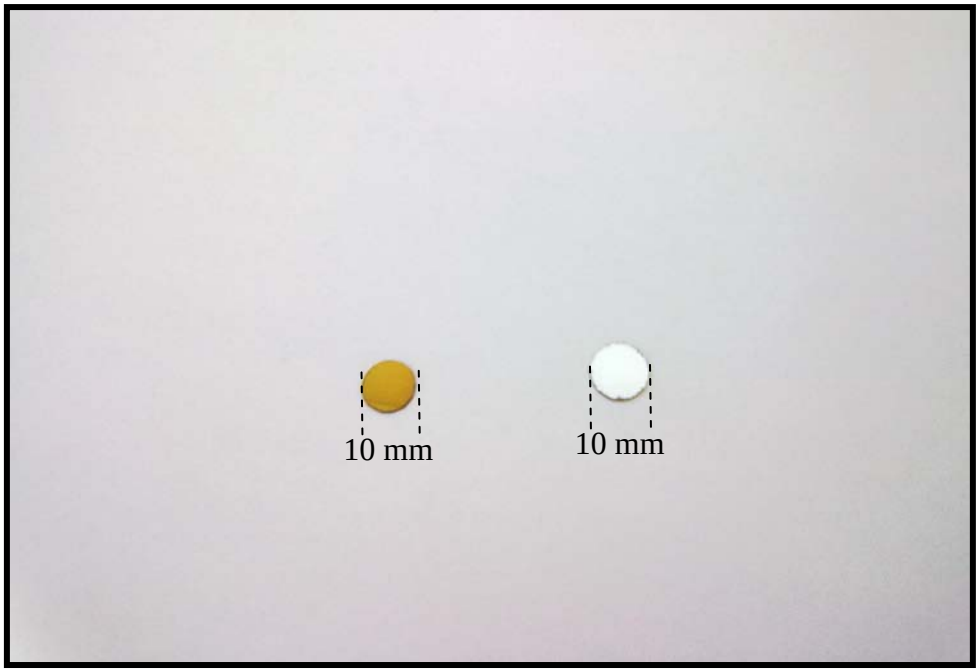

Figure 2.8 Picture of the film (golden color) deposited by PECVD method on 10 mm dia mirror polished silicon substrate

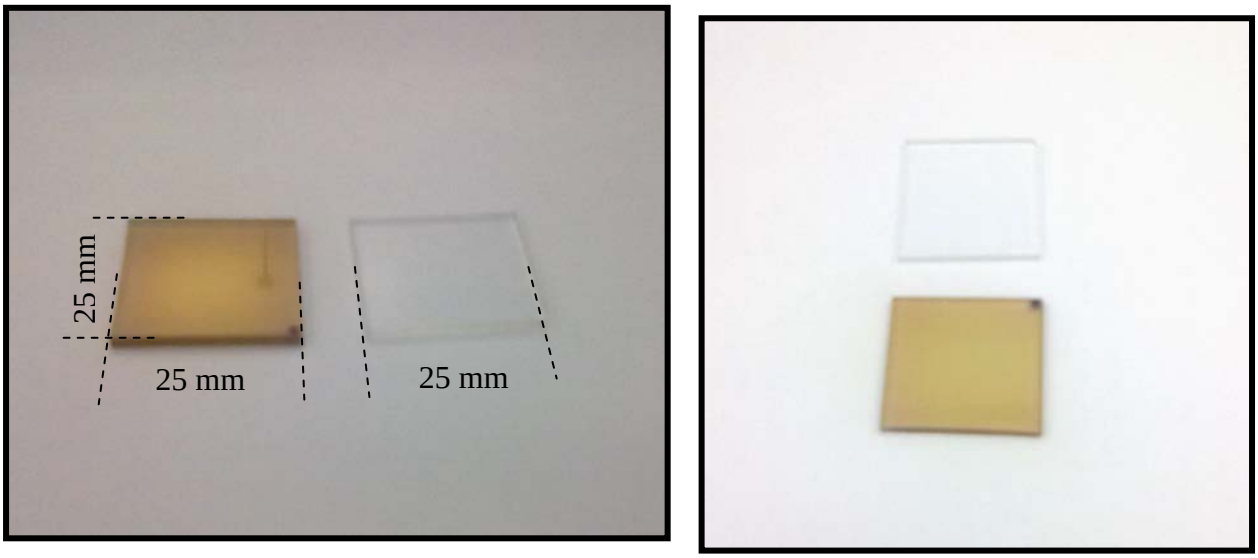

Figure 2.9 Pictures of the films (yellow color) deposited by PECVD method on 25 mm×25 mm quartz substrate

2.3.4 Description of the major parts of the System

Cathode : 250 mm dia. of metallic electrode connected to the RF matching circuit and power supply

Anode : Aluminum walled body connected to the ground as a anode and always at zero potential. Each wall side of the body is 50 cm × 50 cm.

RF-Matching Circuit : Contains an induction and capacitance circuit for matching the impedance between the input (RF circuit) and output (Plasma) systems

Vacuum pumps :

(a) Mechanical pump is switched on for making the chamber pressure from atmospheric to ~ 0.1 mbar. Small traces of oil are absorbed by the chemical filter which prevents the contamination during the processes of deposition.

(b) Roots pump is switched on when the pressure is ~0.1 mbar and continued until the pressure reaches desired value (~10^{-4} mbar)

Closed loop cooled water circulation system : Cooling of the substrate and cathode using a cooler maintained at 10 ^{0}C.

2.4 Annealing of HDLC samples

A few number of HDLC samples were prepared by PECVD method by varying the flow rate of methane 20, 30, 40, 50, 70, and 90 SCCM. Few sets of such HDLC samples were heated at a fixed temperature of 100, 250, 750, 900, and 1050 ^{0}C for 30 minutes in high vacuum ~1×10^{-6} torr and cooled to room temperature after heating in one set of experiment. The as prepared and annealed HDLC sample at 1050 ^{0}C were analyzed using confocal micro Raman spectra, current-voltage characteristics in ambient air, topographic image of the sample using AFM, and STM measurements under constant tunneling current mode. The results and discussion based upon the above measurements are given in chapter 4. The annealing experiments were carried out in Bioceramic and Coating Division, in CSIR-Centre of Glass and Ceramic Research Institute, Kolkata, India. The pictures of the HINDHIVAC instrument for annealing of HDLC samples at high temperature and high vacuum are shown below.

HINDHIVAC Instrument

Instrument Controller

Controlled Parameters at a glance

1) Temperature : 100 ^{0}C to 1050 ^{0}C (maximum)

2) Pressure : 1×10^{-6} torr

3) Annealing time : 30 minutes (for all samples)

4) Healing rate : 5 ^{0}C/min.

5) Cooling rate : 3 ^{0}C/min.

Figure 2.10 HINDHIVAC vacuum and sample heating control unit

Figure 2.11 HINDHIVAC Vacuum sample heating chamber

2.5 HDLC samples preparation for IBA study

Another few sets of samples were prepared by PECVD method at flow rate of methane 20, 30, 40, and 70 SCCM, by varying CH_4 to H_2 ratio at room temperature. One such set of samples was heated at a heating rate 5 ^{0}C/min under vacuum (1×10^{-7} torr) at temperature 750 ^{0}C and 1050 ^{0}C. These films are kept in the above desired target temperature for 30 minutes before cooling them to room temperature at a cooling rate of 3 ^{0}C/min. The as-prepared and annealed HDLC films have been depth profiled for hydrogen using the nuclear resonance at 6.44 MeV in $^1H(^{19}F,\alpha\gamma)^{16}O$ nuclear reaction by heavy ion beam. The Rutherford backscattering (RBS) on the as-prepared and annealed samples, with 1.0 MeV proton ion beam is carried out to measure the thickness of HDLC films. Both NRA and RBS measurements are carried out by a 3 MV Tandetron accelerator at the surface and profile measurement laboratory of the National Center for Compositional Characterization of Materials (NCCCM), Hyderabad, India. The results and discussion based upon the above measurement are given in chapter 4 (section 3). The picture of the NRA/RBS measurement instrument for depth profiling HDLC samples is shown below.

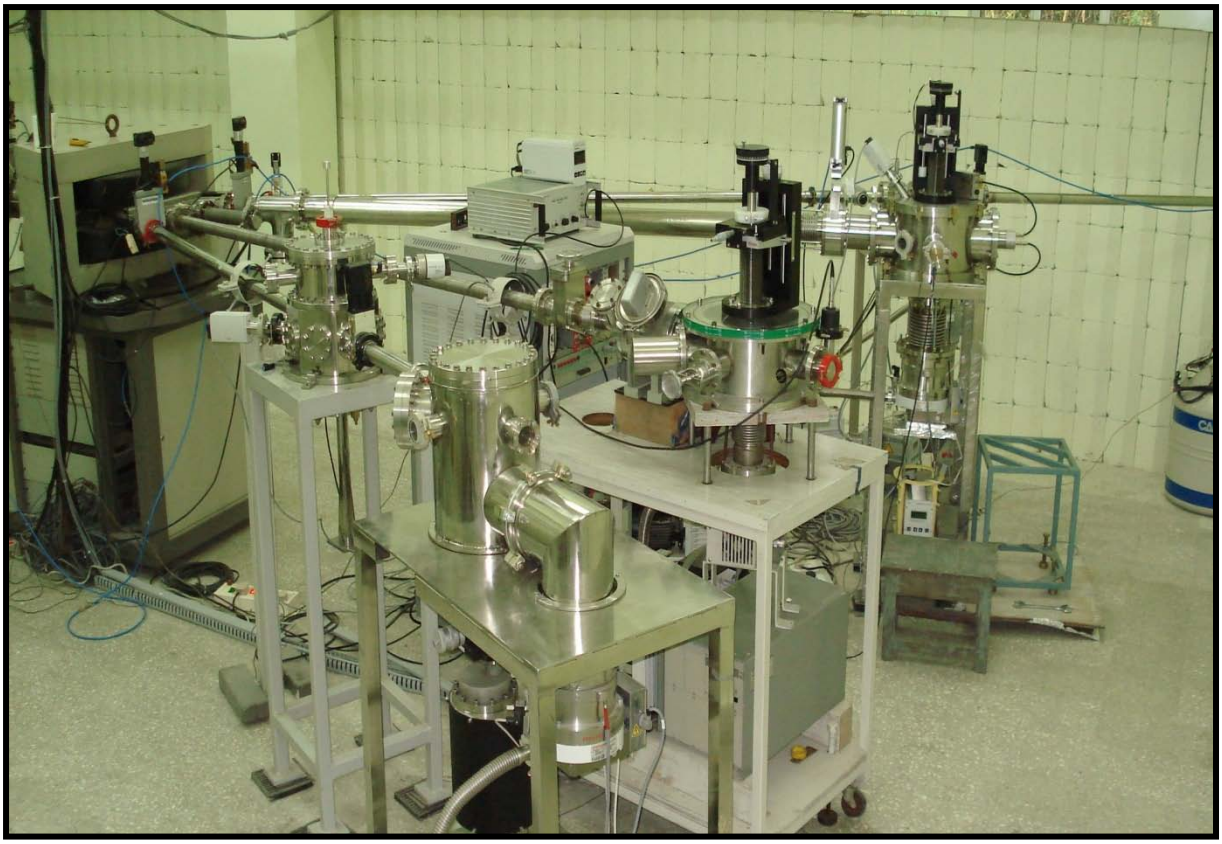

Figure 2.12 Picture of experimental arrangement for IBA study

Chapter 3

Characterization Tools

3.0 Introduction

The unique properties of diamond are expected to have many future applications due to the advancement of diamond coating technology developed various chemical vapor deposition (CVD) methods. These CVD methods of diamond like carbon deposition may result in different types of DLC films based on their inherent composition of the film, growth chemistry, structure, grain size, etc

The natural diamonds as well as the synthetic diamond are both highly precious. The coatings of the materials with these diamonds have been found to be not suitable from applications point of view. However, coating of the materials with diamond like carbon films have been found to be possesses unique properties that can be utilized in many applications. These DLC coatings are most commonly used as coating in cutting tools and wear resistant components because of its high hardness. The diamond and diamond like carbon coatings are suitable for bio-medical applications because of its chemical inertness, bio-compatibility, high melting point, and high thermal conductivity. These DLC coatings find its applications in heat sink. These coatings are well known to be optically transparent from the far infrared region to ultraviolet region and hence used in inert optical window. Therefore, the detailed understanding the film structure and the controlling parameters for their nucleation, growth, micro-structure of the films as needed for important applications to be implemented for practical uses.

3.1 High Resolution Transmission Electron Microscope

3.1.1. Imaging using HRTEM

The optical microscopy techniques are limited by diffraction effects, which depend approximately on the wavelength of light, and these techniques are used to obtain the exhaustive information on the physical environment of the surface. The one of the most important techniques is **T**ransmission **E**lectron **M**icroscopy (TEM) for much higher resolution and it is very rich to provide information of the surface of the specimen. TEM utilizes signal of elastically scattered electrons for re-construction of structural and defects image information. The imaging mode TEM provides real space information while diffraction mode of TEM gives reciprocal space almost simultaneously, and this is a major advantage of TEM over the other microscope. One of the powerful imaging modes of the transmission electron microscopy for studying the properties of material on the atomic dimension is called high resolution transmission electron microscope (HRTEM). HRTEM is commonly utilized to make quantitative measurements on nm scale features due to its excellent image resolution, high precision, and accuracy. In TEM, when a beam of electrons is transmitted through a film, it interacts with the electrons in a few nanometers thin films. A direct image of the atomic structure of the film is generated based on that interactions of the electrons transmitted through the film. The effect of electron beam interaction with the sample increases generally with the square root of the atomic number (Z) of the specimen. The nature of the type of interactions is distinctly different from that of neutron or X-Ray radiation. The image is stored in a suitable detector, e.g. CCD. With the development of high-end technology, improvements of TEM were implemented by different groups around the world. After the innovative modernization of cold field electron emission, Albert Crewe et al.

published a paper in Science journal in 1970 on “Visibility of Single atom”, which showed a single heavy atom on carbon substrate [102]. Meyer and co-workers elaborated the imaging and dynamics of light atoms on graphene for the first time using TEM in 2008 for visualization of carbon and hydrogen [103]. HRTEM can offer spatial resolution in general better than 0.2 nm, and it can go as high as 0.05 nm, as reported in 2008 by C. Kisielowki and co-workers [104] in “Microscopy Microanalysis”. The imaging of light atoms with the improved resolution of microscope is attainable due to the less efficient scattering of electron by the lighter atoms. Due to its resolving power in atomic scale, TEM therefore it finds applications in the field of nano-materials, semiconductors, material science, medical research, and sp^2 –bonded carbon such as nanotubes and graphene. Few classical highly useful applications of HRTEM are include the determination of particle size, shape distribution, structural defects, interface, grain boundaries, and crystallographic phases, diffusion, decompositions, and phase transformation in thermodynamic systems, characteristic features of nano-crystallinity in amorphous films.

The potentiality of the TEM can be furthermore widened by improving the stages, providing additional stages, and detectors that can be incorporated on the same microscope. A TEM system can be redesigned into a Scanning transmission electron microscope (STEM) by adding a raster system which helps the beam raster across the sample to form the image, with a suitable detector. In case of low voltage electron microscope (LVEM) [105-106] which is employed at relatively low electron accelerating voltage of 5 KV. The advantages of LVEM are the combination of TEM, SETM, and SEM in one instrument. This low voltage is especially essential for biological samples. Moreover, low voltage increases the image contrast. However, LVEM system requires thinner samples compared to that of general TEM system. Another modern TEM is the CryoTEM, which is an electron cryomicroscope capable of providing a facility to maintain the specimen at liquid nitrogen or helium temperatures.

The low temperature allows the proteins and macromolecules to remain unchanged, i.e. to protect the denaturation of protein and biomolecules. The finest TEM manufacturers incorporate incident monochromatic beams which reduce the energy spread of the incident electron beam. The modern TEM can also perform the aberration corrections to minimize the distortion in the image.

3.1.2 Transmission electron energy loss spectroscopy (TEELS)

Electron energy loss spectroscopy (EELS) is a complementary technique to energy dispersive X-ray spectroscopy (EDX) and it being available on many electron microscopes is commonly used for spectroscopic study. EDX is particularly sensitive to heavier elements for analyzing the atomic composition of materials, whereas EELS is, in principle, capable of measuring atomic composition, chemical bonding, valance and conduction band electronic properties for low Z elements. The excitation edges tend to be sharp, and well defined in EELS. With time EELS has been established as a most successful spectroscopic technique to study the chemical state of an element, particularly in the range from carbon to zinc. For carbon, its presence among diamond, graphite, amorphous carbon, and mineral carbon can be easily differentiated from fine features of their EELS spectra. The spectra of 3d transition metals can be probed to distinguish the oxidation states of the atoms. In the transmission electron microscope, most of the electrons generally pass through the sample without suffering an inelastic scattering event (i.e. no energy loss). However, when an electron beam transmits through solid, the incident electrons can inelastically scatter off the electrons bound to atom of solid material. Consequently, the inelastic scattered electrons have their path slightly and randomly deflected. The amount of energy loss can be measured via an electron spectrometer (which may be termed as transmission electron energy loss spectroscopy TEELS). A typical TEELS spectrum is shown in Figure 3.1.1.

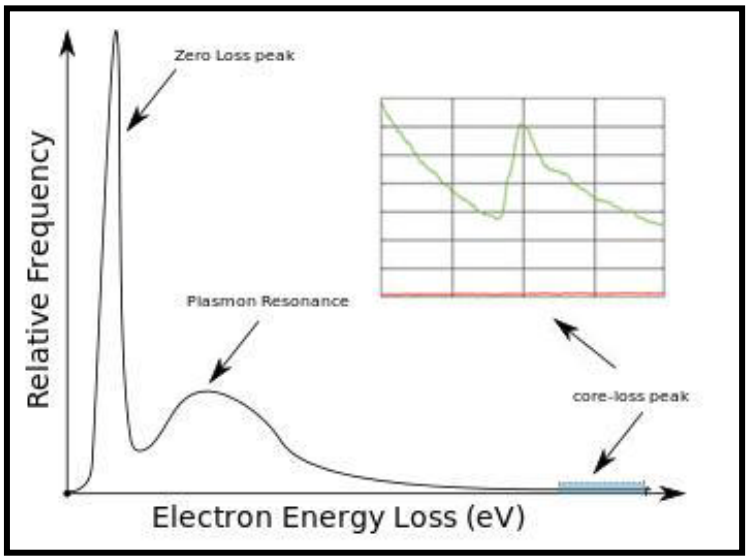

Figure 3.1.1 Schematic illustration of a TEELS profile

The inelastic interactions include phonon excitation, intra and inter band transition, plasmon excitations, inner shell ionizations, and Cherenkov radiation. The low loss region generally corresponds to roughly below 50 eV and the dominant features of the spectrum are zero loss peak (ZLP) and plasmon resonance. The remaining part of the spectrum is called as the core-loss regime. The ZLP region of the spectrum contains both electrons that are unscattered (vast majority of all electrons that pass through a thin specimen) and elastically scattered. The plasmon region contains electrons that have undergone loss of small amount of energy (< 50 eV). This energy loss includes interactions of the electrons in the beam with outer shell electrons to a bound atom in crystalline lattice (phonon effects) and with a compounds electronic band gap structure. The core-loss regime involves the ionization of inner shell electrons. The energy requirement in inner shell ionization depends on the type of atoms involved and its oxidation states. The distribution of electrons as a function of energy is measured using energy filters. The imaging mode is called “energy filtered transmission electron microscope” (EFTEM) and the spectroscopy mode is referred to as “electron energy

loss spectroscopy" (EELS). If the incident electrons have a kinetic energy of a few hundred electron volts and are reflected from the surface of the specimen, the technique is called high-resolution EELS (HREELS). In TEM, the energy of the electrons employed is generally in the range of 100-300 keV. Because of their high energy, electrons can pass completely through a specimen, provided its thickness is below 1 μm. The electromagnetic lenses of the TEM can be used to focus them into a very small diameter (~ 1 nm) and produce a transmitted-electron image of the specimen, with a spatial resolution down to atomic dimensions. As a result, EELS carried out in a TEM is capable of investigation with a very high spatial resolution. As, TEELS can be combined with transmission electron imaging, electron diffraction, and energy dispersive X-ray spectroscopy in the same instrument, this method has become very potential and versatile technique for studying the physical and chemical characteristics of materials. The energy resolution of EDXS is of the order of 150 eV, whereas EELS has a resolution of the order of 1 eV or better (0.1 eV) if an electron-beam monochromator is used.

The modern TEM instrument with EELS is capable of providing structural information and chemical bonding in the solids. Murooka et al. [107] studied the microscopic structure of the carbon film, prepared by electron cyclotron resonance (ECR) plasma sputtering by EELS using 200 kV TEM (JEM 2010) attached with an electron microscope. The TEELS spectra of the films and graphite show two charactistic peaks in low energy region. The broad peak at ~ 20 eV is the ($\pi+\sigma$) plasmon, i. e. the bulk plasmon, which is due to collective exication of all ($\pi+\sigma$) electrons. The peak positions are dependent on the density of ($\pi+\sigma$) electron in the films. Another peak is at ~ 4 eV which is due to the π plasmon. This corresponds to the $\pi \rightarrow \pi^*$ tranitions and its implies the presence of carbon clusters based on the sp^2 bonding. EELS spectra of diamond shows a broad peak centred at ~ 31 eV, whereas in graphite, two resonance peaks are observed at 7 eV and 27 eV [108]. Eberlein et al. [109] observed the π

and ($\pi+\sigma$) suface plasmon modes in free-standing single sheets graphene at 4.7 and 14.6 eV, which are red-shifted substantially from their values in graphite. Therefore, we can say that TEELS is a powerful analytical technique to distinguish between hydrogenated amorphous carbon (a-C) and hexagonal hydrogenated diamond like carbon (HHDLC) and one can analyze collective excitations of π and σ electrons in multilayered HHDLC films by this technique.

The high energy electrons from the HRTEM undergo elastic scattering as well as inelastic scattering. Elastically scattered electrons are used for imaging purposes like imaging of cross-sectional view of our HDLC film as carried out in the present thesis works. Energy loss upto 50 eV in the inelastically scattered electrons is dominated by collective excitations of valence electrons (plasmon) of samples like HDLC samples of the present thesis works. These results are given in chapter 4 (section 1). The measurements of HDLC samples were performed in a JEOL EM-2010 (with LaB_6 filament) at 200 kV accelerating voltage fitted with a Gatan Image Filter for parallel EELS of Materials Research Institute, The Pennsylvania State University, USA. The experimental conditions were :

(i) Ion-milled cross section sample

(ii) Accelerating voltage: 200 kV

(iii) Probe size: ~ 30 nm

(iv) Collection semi-angle: 12 mrad

(v) Convergence semi-angle: 6.4 mrad

3.2 Raman Spectroscopy

When beam of monochromatic light from the visible portion of the spectrum is passed through a substance under study, nearly all of it is transmitted and a portion of it is scattered in all directions. If the scattered light in a direction perpendicular to the direction of the incident beam is spectrographed, it is found that not only a line is contain corresponding to frequency of the incident light called Rayleigh line after the name of Lord Rayleigh, but also there is a pattern of relatively weak line on the low frequency side of the incident light and a similar part of still weak lines on the high frequency side called Raman lines after the name of C. V. Raman.

The phenomenon of inelastic scattering of light was first predicted by Adolf Smekal in 1923 and first observed experimentally by means of sun light in 1928 by C.V. Raman and Krishnan. Since then, the phenomenon has been referred to as Raman effect. In the original experiment sun light was focused by a telescope onto a sample. Raman got the Noble Prize in Physics in 1930 for this discovery.

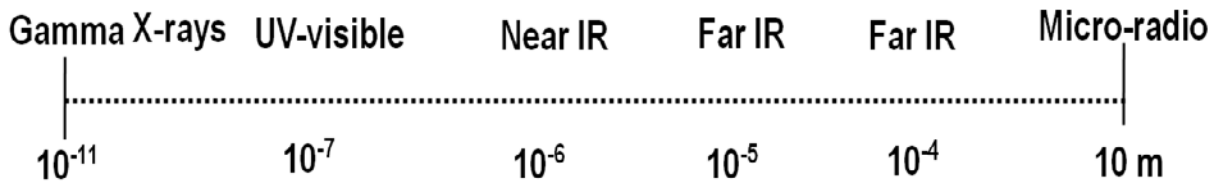

Figure 3.2.1 The electromagnetic spectrum on the wavelength scale in meters

3.2.1 Classical model for the interpretation of Raman lines

The Raman spectra are observed when there occurs a periodic change in the polarizability of molecule due to its vibrational or rotational oscillation. The above fact may be explained classically as follows.

In the presence of a static electric field, a molecule is polarized, i.e. the positively charged nuclei and the negatively charged electron cloud are attracted towards the respective oppositely charged pole of the electric field. Consequently, the molecule acquires an induced dipole moment which is given by

$$P_{ind} = \alpha E \tag{3.2.1}$$

where α is the polarizability of the molecule.

In the presence of a beam of radiation, the molecule also acquires an induced dipole moment due to the electrical component of the incident light/laser. This electrical component is not static but varies as per the sine (or cosine) wave according to the equation

$$E = E_0 \sin(2\pi\nu t) \tag{3.2.2}$$

where ν is the frequency of radiation and t is the time. Consequently, the induced dipole moment also oscillates according to the equation

$$P_{ind} = \alpha E = \alpha E_0 \sin(2\pi\nu t) \tag{3.2.3}$$

According to the electromagnetic theory, an oscillating dipole emits radiation of its frequency. This explains the occurrence of Rayleigh line in the light scattered by the substance. The presence of Raman lines is due to the periodic change in the value of α due to the internal vibrational or rotational motion according to the equation

$$\alpha = \alpha_0 + \left(\frac{\partial \alpha}{\partial \zeta}\right)\zeta \sin(2\pi\nu_i t) \tag{3.2.4}$$

where the $\partial\alpha/\partial\zeta$ is the change in polarizability with the displacement coordinate ζ, ν_i the frequency of internal motion, and α_0 is the polarizability in the equilibrium position ζ_0. The

periodic change in polarizability will also change periodically the induced dipole moment. Hence, equation 3.2.4, and 3.2.3 can be written as

$$P_{ind} = \left[\alpha_0 + \left(\frac{\partial \alpha}{\partial \zeta} \right) . \zeta_0 \sin(2\pi \nu_i t) \right] E_0 \sin(2\pi \nu t)$$

$$= \alpha_0 E_0 \sin(2\pi \nu t) + \left(\frac{\partial \alpha}{\partial \zeta} \right) \zeta_0 E_0 \sin(2\pi \nu_i t) \sin(2\pi \nu t)$$

$$= \alpha_0 E_0 \sin(2\pi \nu t) + \frac{1}{2} \left(\frac{\partial \alpha}{\partial \zeta} \right) \zeta_0 E_0 [\cos\{2\pi(\nu - \nu_i)t\} - \cos\{2\pi(\nu + \nu_i)t\}] \quad (3.2.5)$$

that is, the induced dipole moment of the molecule oscillates with the frequencies ν, $(\nu - \nu_i)$ and $(\nu + \nu_i)$. Therefore, the oscillating dipole will emit radiations of frequencies ν, $(\nu - \nu_i)$ and $(\nu + \nu_i)$. These frequencies appear as the Raman lines in the scattered light of a substance under study.

If there occurs no change in the polarizability during the vibrational or rotational motion, i.e. $\partial\alpha/\partial\zeta$ is zero, then the above equation 3.2.5 remains a single term. Hence the molecule will oscillate with one frequency related to the incident light. This frequency corresponds to the Rayleigh line (ν) and no other Raman lines are observed. Therefore the molecule is Raman inactive. Hence the Raman active molecules will emit three frequencies. Besides the Rayleigh line, $(\nu - \nu_i)$ frequency is known as Stokes line and ($\nu+\nu_i$) frequency is known as anti-Stokes line.

3.2.2 Quantum model for Raman lines

The photon from the light source collides with the molecule through elastic or inelastic mode. If the collision is elastic, the photon energy before and after collision remains unchanged. In other words, the molecule remains in the same energy state which it had before collision. This scattered photon is known as Rayleigh scattering (ν). Again, if the scattering is inelastic,

the photon energy as well as the energy of the molecule will alter. If the scattered photon is having lower energy than that of incident light, then the difference of energy is utilized to promote the molecule to one of the higher energy level as permitted by the selection rule. This scattered photon is known as Stokes scattering $(\nu - \nu_i)$ and they are at lower frequency side of Rayleigh scattering (ν). On the contrary, if the scattered photon is having higher energy than that of incident light then the difference of energy is obtained from the molecule has demotes to one of the lower energy level as permitted by the selection rule. This scattered photon is known as anti-Stokes scattering and they are at higher frequency side of Rayleigh scattering (ν).

Schematic representation of Raman Scattering

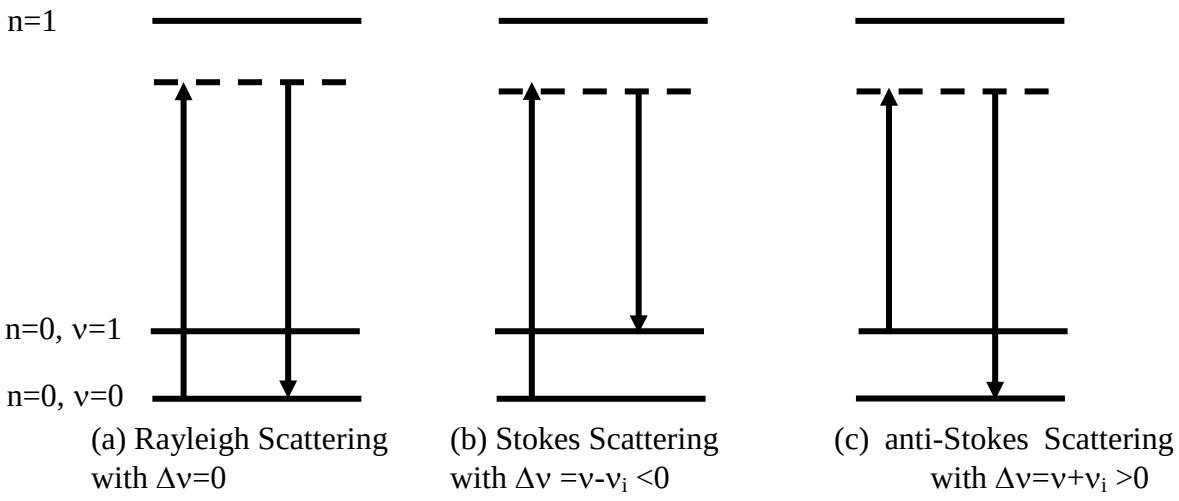

Figure 3.2.2 Schematic representation of Raman scattering

Since most of the photons undergo Rayleigh scattering process, hence Rayleigh lines will be the most intense. The intensities of the other lines will depend on the population of the initial energy level where from the molecules are promoted or demoted to the final level. According to the Boltzmann distribution law, the population of the lower energy level is more than that of the higher energy level. Therefore, out of the Stokes and anti-Stokes lines, the former will

be more intense than the latter. Consequently, the Stokes lines are recorded commonly in the Raman spectrometry.

The Raman effect, should not be confused with the absorption (e.g. fluorescence) process. Since Raman effect, is a light scattering phenomenon, molecules are excited to the virtual energy state. In contrast, molecules are excited to a discrete energy level (not virtual) in the absorption processes. Again, the difference between Raman and Infra-red absorption process is that Raman scattering requires a transitorily distortion of the electrons cloud distribution; the IR absorption requires a change of dipole moment during the vibrational or rotational motion of the molecule. Only then can be the radiation of same frequency to interact with the molecule and promotes it to an excited vibrational state.

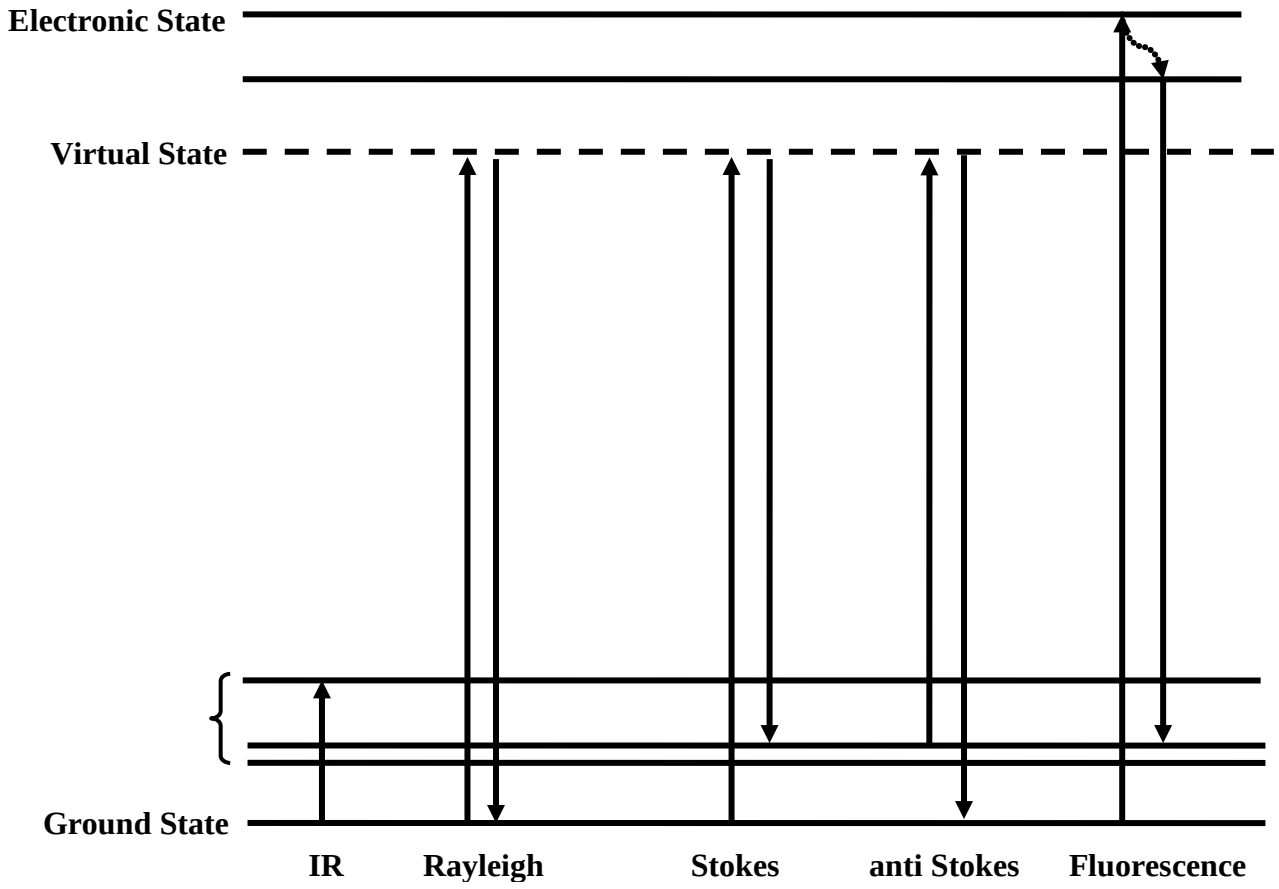

Figure 3.2.3 Schematic representation of electronic excitation

Typically, the intensity of Rayleigh line is 10^{-3} with respect to excitation radiation, whereas the intensity of Raman lines are 10^{-3} order less than Rayleigh line. Raman frequencies called as Raman shift are measured relative to that of excitation frequency. The excitation frequency can be imagined at the origin of the abscissa, the Raman shift will be on abscissa at $\pm\nu_0$

Raman scattering of gases at low pressure consists of vibrational-rotational line spectra. At higher pressure, Raman lines become broaden, similar to liquid. In solid having crystalline nature, the Raman bands are sharp and band width depends on anharmonicity of molecular vibration. Further broadening of Raman bands are due to other imperfections in the crystal lattice, vacancies, or other impurities. In general, the Raman spectra of amorphous substrates are characterized by broad spectral features. Classification of possible types Raman spectra is given in Table 3.2.1. The concept of group frequency is very important for the calculation of force constant and also for the interpretation of Raman vibration spectra of molecules. Some general principles apply on Raman vibrational modes generated from localized normal vibrations; a primary bond stretching band is more intense than for an angular deformation. The intensity increases with the bond orders and increases with the atomic number of the bonded atoms.

3.2.3 Second-order Raman Spectra

In all the above the scattering described in earlier paragraph is “first-order” scattering, i.e. the excitation of only one phonon. However, it can be also a “second-order” scattering, i.e. two phonons can be excited. According to the equation 3.2.4, the second-order derivative $\left(\frac{\partial^2\alpha}{\partial\zeta^2}\right)\zeta^2$ of the Taylor series expansion refers to the appearance of higher frequency bands to account for the polarizability in crystals. These bands are designated as second-order Raman bands. The second-order spectra of single crystals and highly oriented pyrolytic graphite are continuous and exhibit several well defined bands. The wavelength selection rule in this case

is that the two phonons must have equal wave vectors (or wavelength) but must be travelling in opposite directions. Second-order scattering is usually weak, but can be enhanced by various things. It is very difficult to distinguish between the overtones in the first-order Raman effect and the second-order Raman effect. In both cases, the polarization is proportional to the exciting field strength. Overtones appear when the system being excited is mechanically anharmonic and second-order Raman bands appear when it is electrically anharmonic. Second-order Raman bands, sometimes may be stronger than the first-order bands, and the two may be distinguished by the intensity of second-order bands due to its higher temperature sensitivity.

Table 3.2.1 Classification of possible types Raman spectra

Specimen	Possible types Raman spectra
Gases	Pure rotational
	Rotational-vibrational
	Overtones, combination tones, difference tones
Liquids	Vibrational
	Overtones, combination tones, difference tones
Crystals	Lattice
	Internal-vibrational
	Overtones, combination tones, difference tones
Amorphous	Mixed

3.2.4 Micro-Raman Spectrometer

The first experimental observation of the inelastic scattering of light was made by Raman and Krishnan (1928). The experimental setup consists of a light source-a focused, filtered beam of sunlight, a sample, a detector and a phototube or photographic plate. The basic experimental design of current Raman spectrometer has not been changed significantly. Presently, the micro Raman spectroscopic systems are designed with the capability of single point analysis, line analysis, Raman imaging (mapping) etc.

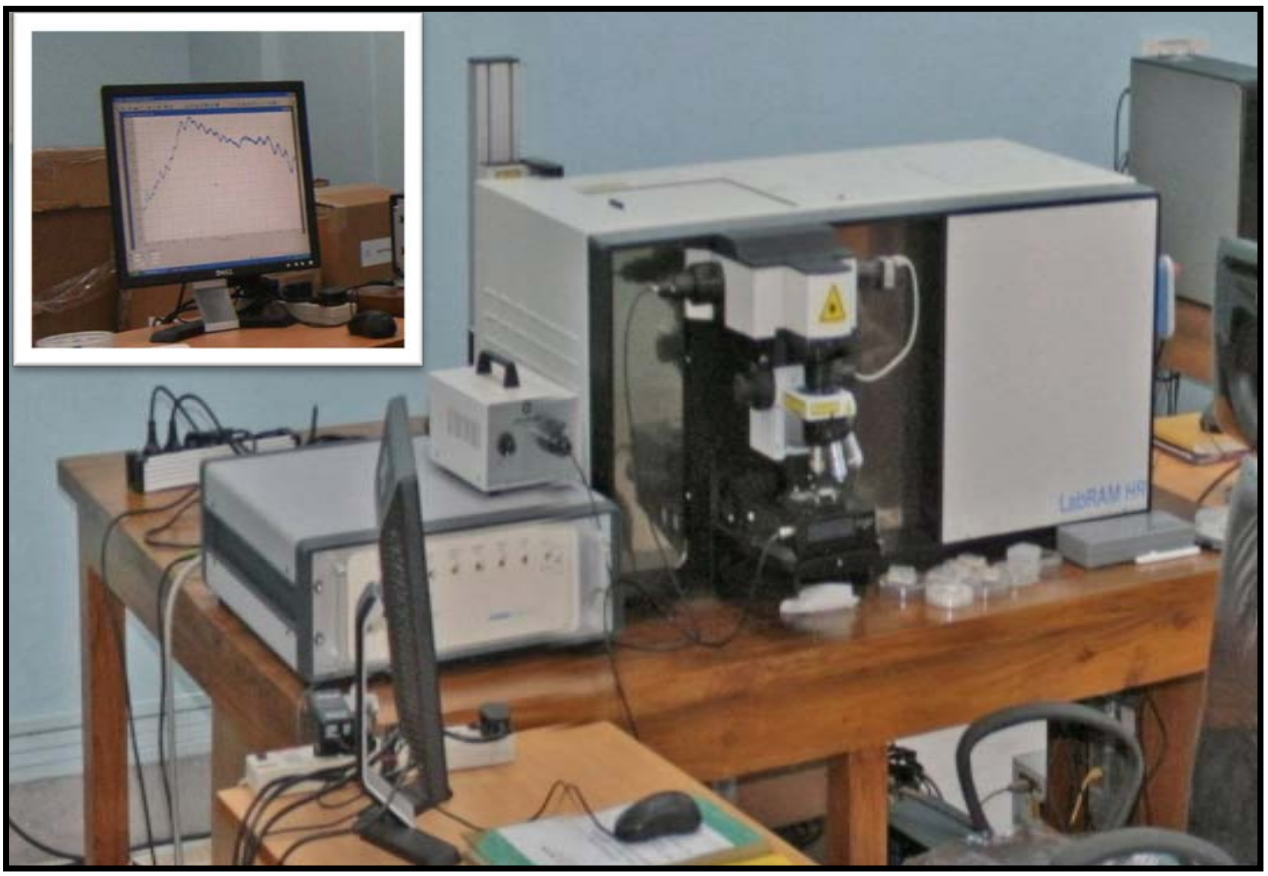

Figure 3.2.4 Image of Micro-Raman spectrometer LabRAM *HR800* Vis. Horiba Jobin Yvon SAS France

The HR800 is an integrated laser line scanning imaging Raman system. The instrument is capable of recording Raman spectra of solid, liquid, or even gaseous samples. It is recommended to use a microscope objective with a large depth of focus (for example a 10X, NA=0.25) so that it will collect the signal from a bigger volume of the sample in case of

homogeneous sample. On the contrary, it is better to use microscope objective with a high numerical aperture (100X, NA=0.9) so that the solid angle (NA=n.sinα where n is the refractive index of the medium between the object and the lens, and α is half the angular aperture) is bigger to obtain a maximum Raman signal. The microscope is coupled confocally to a 800 mm focal length spectrograph equipped with two switchable gratings viz. 1800 g/mm (scanning range 0-950 nm) and 600 g/mm (scanning range 0-2850 nm). Gratings are mounted on kinematically interchangeable holders driven by Sinus arm that is linear in wavelength. There is the provision for camera which is used for the observation of the sample.

The excitation wavelength 632.8 nm is supplied by an internal standard He-Ne laser (20 mW power, polarized 500 : 1) positioned at back side of the instrument. Another external laser of 488 nm Ar (max 50 W power) is also kept for analysis of various types of samples, at the back side of the instrument. Obviously, the changing of laser requires the change of the notch filter which is specific for one wavelength, which is necessary for filtering the exciting light. In the LabRam HR800 super notch plus is used as a dichroic mirror and the drop off stokes edge is <120 cm^{-1}. The laser is totally reflected by the notch filter towards the sample under microscope by a suitable objective viz. 10X (Numerical Aperture, NA= 0.25) 50X (NA= 0.7), and 100X (NA= 0.9). The scattering light is totally transmitted through the notch filter towards the confocal hole and entrance silt of the spectrograph. There is an adjustable confocal hole which can vary between the ranges of 0 to 1000 μm. The diverging beam coming from the slits is reflected by the two mirrors and then becomes parallel after the spherical mirror of 800 mm focal length. The spherical mirror reflects the parallel beam onto the grating. The diffracted first-order is collected by another spherical mirror of 800 mm focal length and focused onto the CCD detector. The spectrographic box contains the CCD detector that forms a spectrum. The CCD detector is having the pixel size of 1024×256 and

cooled by Peltier effect. The main advantage of our micro-Raman spectrometer is due to the confocal sampling which is responsible for considerable reduction of the signal from an inclusion against the signal coming from the surrounding medium and also able to separate the signal from each layer of a layered sample. Consequently, confocality reduces the depth of focus and thus an increased Z discrimination. The closing of confocal hole, however, while decreasing the depth of focus, decreases the Raman signal. Thus confocality is always a compromise between signal and resolution. With a NA = 0.9 100X objective, the confocality is ~ 2 μm and with a NA=0.25 10X objective, the best confocality is increased to 183 μm. In the range between 450 - 850 nm, the wavenumber accuracy is ± 1 $cm^{-1}$with 1800 g/mm grating. Under normal conditions of temperature stability (± 1 °C), the repeatability is 1 pixel with 1024×256 pixels of 26 microns CCD.

The instrument is always operated using standard operating procedures. The Raman microscope was kept ideal for 30 minutes before recording any data. Calibration is done most of the time using standard silicon sample whenever the instrument is started and the grating is changed. All the time standards and samples were focused using the objective 10X and position was set using joystick in X-Y directions. Coarse focus was done manually using the knob inside the microscope, only for the 10X objective. The instrument was focused at 10X, switched to 50X and then fine focused, then repeat was made at 100X. Silicon has a characteristic Raman shift at 520.7 cm^{-1}. The K_{oeff} parameter was adjusted until the peak on the display was at 520.7 cm^{-1}. After the calibration (Figure 3.2.5) instrument was ready to record the spectra. The LabSpec5 software provides a control of HORIBA Jobin-Yvon's Raman instruments, complete data acquisition, and analysis package using Windows 2000 or Windows XP-PRO operating software in a desktop computer. The control panel of the software contains information which is directly related to the system configuration and easy modification of the acquisition parameters. Real Time Display (RTD) acquisition mode

allows adjustment quickly the focusing and optimizing other experimental conditions to maximize the Raman signal. The exposure time in seconds to be used for the accumulation of sufficient counts of Raman signal and repetitions were performed to remove any spike of the cosmic line recorded during the acquisition. The spectra generally acquired with multiple accumulations covering the entire region 50-4000 cm^{-1} using extended spectral ranges acquisition, i.e. multi-window mode. Using motorized XY microscope sample stage for point by point Raman imaging, each spectrum was acquired with a particular varied parameter including the autofocus attachment for automatic Z-axis imaging (depth profiling)

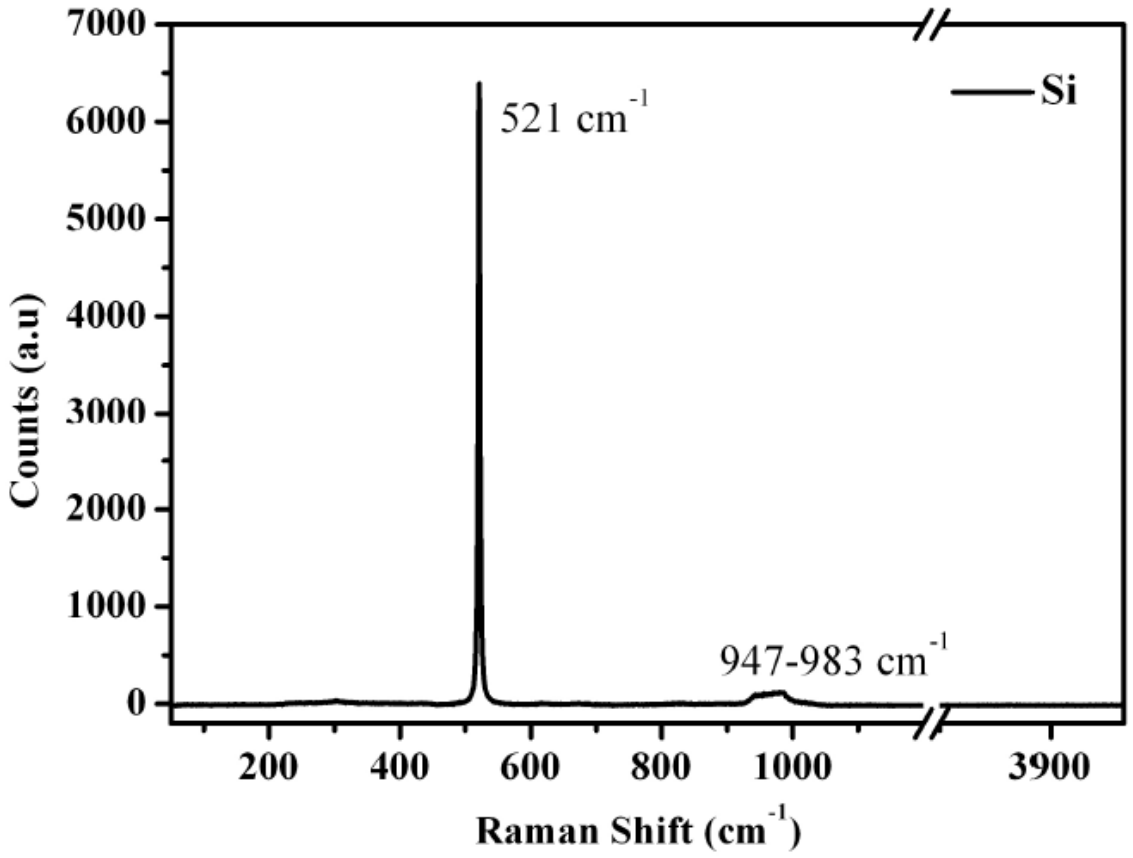

Figure 3.2.5 Calibration of micro-Raman spectrometer using standard silicon sample

3.2.5 Peak fitting and analysis

The typical Raman spectra of HDLC sample (Fig. 3.2.6) deposited onto the silicon substrate for the range from 50-4000 cm^{-1} and recorded using micro-Raman spectrometer, is described above. The increasing PL background of each spectrum is a typical signature of hydrogenated diamond like carbon films [61]. A broad peak first-order Raman spectra in the range 1000-2000 cm^{-1} was observed for all of the synthesized HDLC samples described in chapter 2. To know more information about the fine and inner structure of the carbon films, the Raman spectra should be deconvoluted. However, the fitting of the Raman spectra may leads to complex nature due to the manifold combination of the carbon and carbon-hydrogen structure in the films.

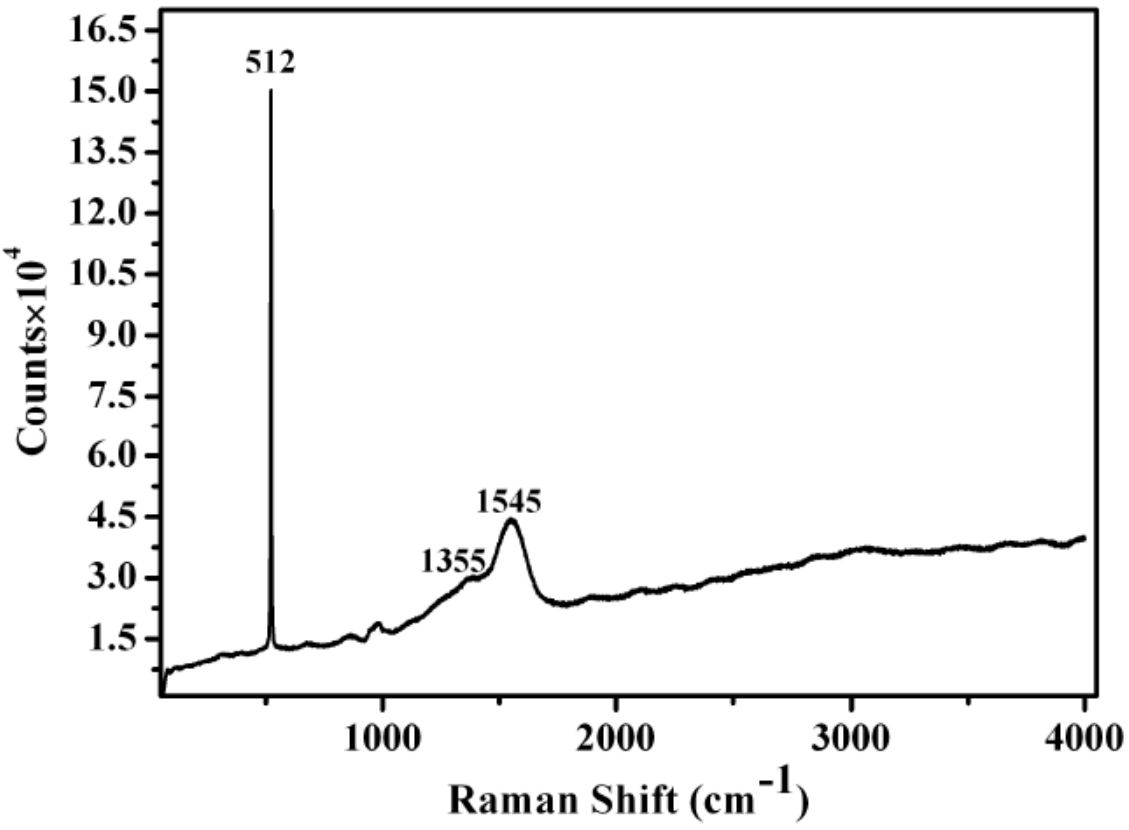

Figure 3.2.6 Typical Raman spectrum of HDLC film onto silicon substrate over the range 50-4000 cm^{-1}

The most widely used methods of Raman spectra fitting is to make use of two Gaussian peaks with linear/ non–linear background subtraction with the D peak centered at 1350 cm^{-1} and that of G peak centered at 1580 cm^{-1} [110]. This analysis is based on the assumption that the amorphous carbon films are composed of disordered sp^2 and sp^3 networks. This fittings lead to an estimate of the L_a that reflects the in-plane crystallite size from the ratio of the fitted peak intensity of D and G bands. In order to analyze the Raman spectra quantitatively, Prawer et al. [111] utilizes a Breit-Winger-Fano (BWF) line shape and linear background subtraction methods using a least squares computer programme. The BWF line shape is described by

$$I(\omega) = \frac{I_0 \left[1 + 2\frac{(\omega - \omega_0)}{Q\Gamma}\right]^2}{1 + \left[2\frac{(\omega - \omega_0)}{\Gamma}\right]^2} \qquad (3.2.6)$$

Where $I(\omega)$ is the intensity as a function of frequency, I_0 is the maximum peak intensity , ω_0 peak position, and Γ is the full width at half maximum (FWHM), Q is the BWF coupling coefficient. In the limit when 1/Q approaches to zero or negligible, the Lorentzian line shape is regained. Therefore, a total of six variables is essential to best fit the data, viz. I_0, ω_0, Q, and Γ and two parameters for the linear background. Prawer et al. [111] showed that Raman spectra of DLC films deposited at the carbon ion enerties 10-1000 eV is possible to fit with a single BWF lineshape, no need to include an extra peak at 1350 cm^{-1}, except for the films deposited at 200 keV for which it was necessary to include a two BWF line shpae in order to fit the data. To obtain a better fit, some other peaks are generally taken into consideration apart from G and D peaks.

Following aspects were considered during the deconvolution of Raman spectra using Lorentzian and Gaussian line profiles : (1) All molecules behaving in the same way results a

Lorentz line shape. Transit time broadening, pressure broadening, natural lifetime broadening are few typical examples. (2) All molecules behaving differently (resulting a distribution) results a Gaussian line shape. Few examples are Doppler broadening, power broadening etc. The Raman scattering is known to be due to the inelastic collisions between the light photons and the atoms. These inelastic collisions broaden the Lorentzian shape of spectra lines. The shift in peak frequency in elastic collisions to lower or higher values depending on the nature of the interaction potential. Hence, a Gaussian profile describes broadening effect due to randomly distributed Raman signals from the sample, with no associated shift, while a Lorentzian profile describes both effects- broadening and shift, due to the structure of the sample interacting coherently. Raman spectra are deconvolved in expectation of multiple chemical environments within the HDLC film, which is a graphite-based system [112]. Lorentzian peak shapes are used for all Raman modes, resulting in best fits of the broad spectral envelope. Keeping in mind the possibility of the presence of different phases of carbon, we have deconvoluted each spectrum with six Lorentzian functions (shown by solid lines in chapter 4) keeping intensities, width and peak positions as free fitting parameters. The asymmetric BWF line shape is usually used to fit the G-peak which appears due to asymmetry of the vibrational density of states of graphite towards lower wavenumber. The tail of BWF line takes into consideration the Raman modes between 1100 and 1400 cm^{-1}, without giving rise to extra peaks. It is to be noted that the intensities of the D-peak and other low frequency peaks are quite less than the intensity of the G-peak. Thus, if we deconvolute each spectrum with all low frequency components to obtain the information of individual modes, there is an inherent difficulty in using BWF line shape for the G-peak. For this reason, we have used Lorentzian line shapes for all modes to analyze our spectra. In chapter 4 we describe the details of experimental data, deconvoluted lines and net fitted spectrum for our HDLC sample and the properties of the films obtained from above Raman data

deconvolution. We have used origin software (v7.03) for deconvolution. The used Lorentzian equation and the fitting wizard are shown below.

$$y = y_0 + \frac{2.A}{\pi} \cdot \frac{w}{4(x - x_0)^2 + w^2} \qquad (4.2.7)$$

where, y_0 baseline offset, A total area under the curve from the baseline, X_0 center of the peak

w full width of the peak at half height

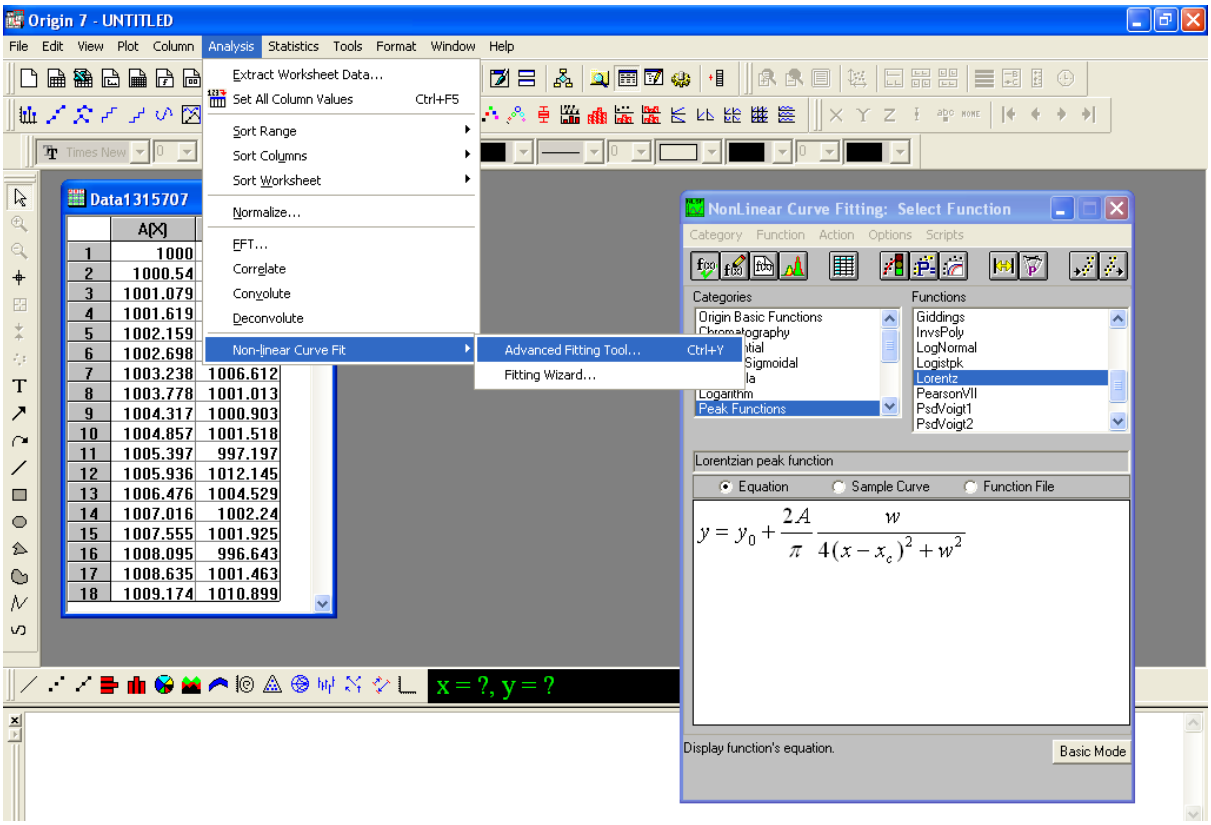

Figure 3.2.7 Fitting of Raman data using Origin software with a Lorentzian equation

3.3 Scanning Probe Microscopy

The two most popular and widely used scanning probe microscopy (SPM) techniques are viz. Scanning tunneling microscopy and Atomic force microscope for the scientists and researchers for the investigation of structural characterization of thin films. The discussion of each SPM is given below.

3.3.1 Scanning tunneling microscopy

Scanning tunneling microscopy, a novel technique based on quantum tunneling of current, has already become a useful tool in surface science due to its ability to characterize surfaces of metals and semiconductors [113-114]. As the name Scanning tunneling microscopy (STM) suggests that it is based on the concept of quantum tunneling. An object with a very small mass viz. electron has wavelike characteristic which permits it to pass through an impenetrable barrier. Such an event is referred to as tunneling. A STM is an instrument for topographic imaging of surfaces at atomic level in real space. A good STM (with lateral resolution 0.1 nm and depth resolution 0.01 nm) is capable of routinely imaging and mapping of individual atoms within the materials. STM inventors (G. Binning and H. Rohrer) got the Noble prize in 1986 for the development of this technique and its applications. When a conducting (metal) tip is brought closer to the surface of our interest, with a bias voltage applied between the two, can allow electrons to tunnel through the vacuum between them. This tunneling current is strongly dependent on the distance between the tip and sample surface, applied voltage, and the nature of the sample. The image is constructed from the measured tunneling current. There are two very popular modes of STM viz. constant current and constant height mode. In constant current mode, a feedback loop tries to keep the current between tip and sample constant while scanning viz. the Z-piezoelectric height control mechanism. This gives constant charge density i.e. contrast of the

image due to variations in charge density. In constant height mode, height is kept constant while current is measured during scanning over the surface. This leads to an image of current changes over the surface. STMs have already been operated in vacuum, air, oil, liquid nitrogen, and water. It can be operated in most gases and liquids and at temperatures ranging from few Kelvin to a few hundred Kelvin.

Using STM under the constant tunneling current mode, topographic image of the sample was obtained by multimode scanning probe microscope (Agilent AFM 5500 series system, USA) having multipurpose small scanner with scan range Z: 0-2 μm, noise level Z: < 0.02 nm RMS. In this instrument a feedback loop maintains a constant tunneling current during scanning by vertically moving the scanner at each (X-Y) data point until reaches a given set point value (0.5 nA). The computer stores the vertical position of the scanner at each (X-Y) data point to form the topographic image of the sample surface which is to be conductive or semiconductive in nature.

3.3.2 Atomic force microscope

The requirement of sample conductivity is one of the major limitations of STM. In 1986, G. Binnig, C. Quate, and Ch. Gerber have overcome this limitation and proposed a new type of microscope [115]. They have measured the forces on an atomic scale, instead of measuring tunneling currents between a probing tip and sample. Atomic force microscopy (AFM) is a very high-resolution type of scanning probe microscopy, with resolution (1000 times higher than the optical diffraction limit) in the order of fractions of a nanometer. The basic principle of this microscope is to measure forces or interactions between a sharp probing tip and sample surface. The AFM probe/cantilever having a sharp tip (mostly silicon or silicon nitride materials) at its end is used to scan the specimen surface. The cantilever is typically a tip with radius of curvature in the order of nanometers. When the tip is brought closer to a sample surface, in response to the force between tip and sample, the cantilever is

deflected. Typically, the deflection is measured using a laser spot reflected from the top surface of the cantilever into an array of photodiodes. Images are taken by scanning the sample relative to the probing tip and digitizing the deflection of the cantilever or the z-movement of the piezo as a function of the lateral position x, y. The AFM can be operated in different modes depending on the applications. In general, possible imaging modes are divided into contact modes and non-contact (tapping) modes. In contact mode, surface is scanned at a constant height, hence a risk would exist that the tip may collide with the surface, causing damage. A feedback mechanism is therefore employed to adjust the tip-sample distance to maintain a constant force between them using piezoelectric scanner. In non-contact mode, the tip of the cantilever oscillates either at its amplitude modulation (<10 nanometer - picometers) or at resonance frequency (frequency modulation). The decrease in resonance frequency, of the cantilever may be due to the van der Waals forces (acts in the range 1 - 10 nm) or any other long-range force above the surface [116]. This decrease in frequency combined with the feedback loop system, maintains a constant oscillation amplitude or frequency by adjusting the average tip-to sample distance. The scanning software thus constructs a topographic image of the sample surface after recording the tip-sample distance at each (x,y) data point.

An AFM topography image of our HDLC surface was obtained in contact and noncontact mode depending of the nature of sample surface by Agilent's open- and closed-loop scanners. The scanner provides (scan ranges : 90 μm x 90 μm, or 8 μm x 8 μm) excellent linearity, accuracy, and ease of use in air or liquid and also under controlled temperature and environmental conditions. The relative position of the laser spot was kept fixed in relation to the cantilever throughout the scan cycle in order to deliver high-resolution image. Our multimode scanning probe microscope (Agilent AFM 5500 series, U.S.A.) having a multipurpose small and large scanner are capable of scan range: XY: 8 μm x 8 μm; Z range :

2 μm, vertical noise level: Z<0.02 nm rms (root mean square) and scan range: XY: 90 μm x 90 μm; noise level XY<0.05 nm rms.

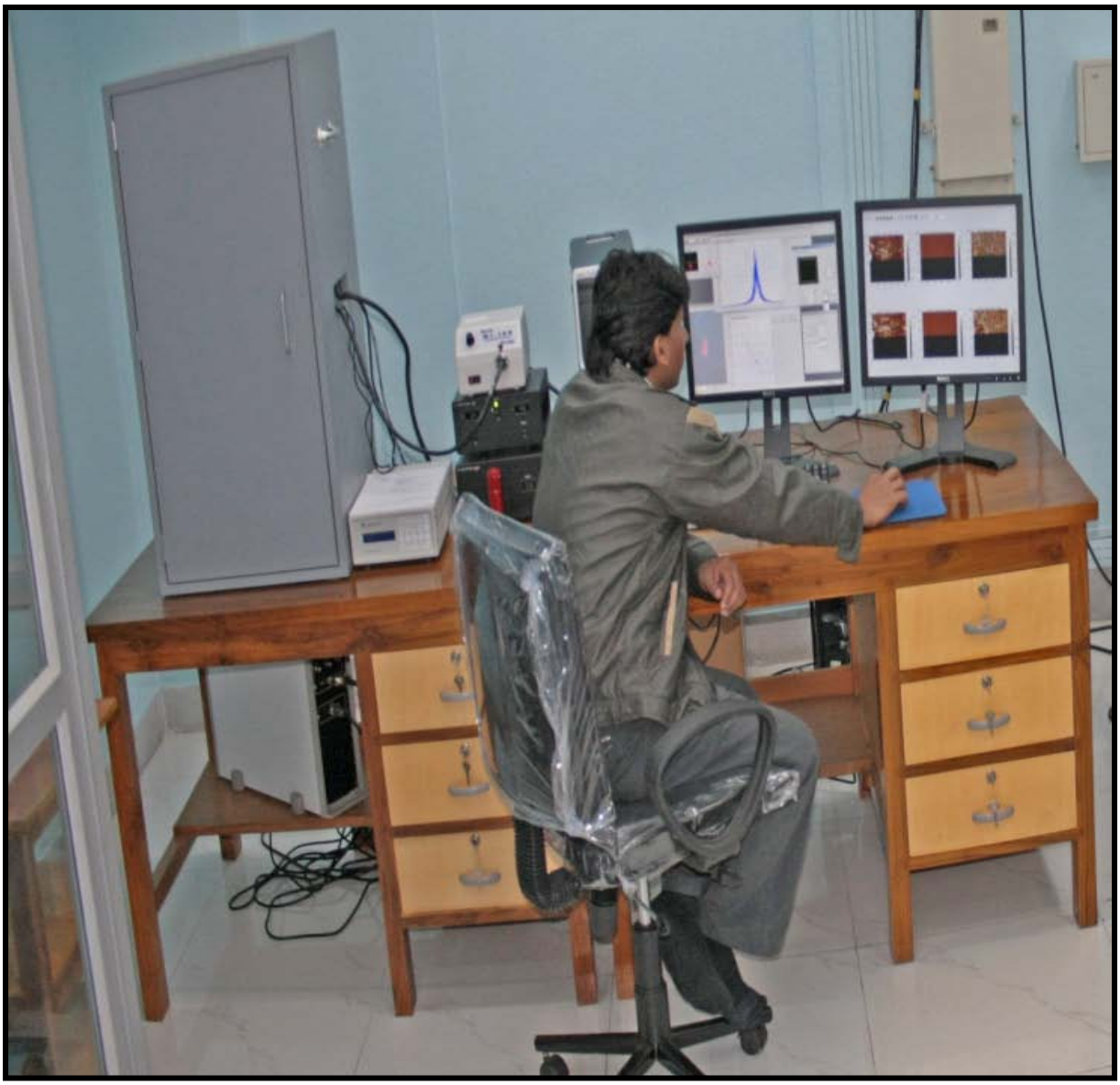

Figure 3.3.1 Image of Atomic Force Microscope (Agilent AFM 5500 series, U.S.A.)

3.4 Scanning Electron Microscopy

Like TEM, a scanning electron microscope (SEM) [117] is a type of electron microscope that scans the sample in a raster scan pattern by a focused beam of electrons and thus generates an image of the sample in combined with the detected signal. The electrons interact with the electrons of atoms in the sample and consequently produce various signals that can be detected. The types of signals produced by a SEM include secondary electrons (SE), back-scattered electrons (BSE), Auger electrons, characteristic X-rays, etc [118]. The most common mode of signal detection is by secondary electrons emitted by the host atoms excited by the electron beam. An image displaying the topography of the surface is created by detecting the secondary electrons during scanning the sample. SEM can provide resolution better than 1 nanometer. The conventional SEM operates under a vacuum of 10^{-6} torr or less. Specimens must be clean, dry and either electrically conductive or electrically grounded to prevent the accumulation of electrostatic charge at the non conductive surfaces. Schematic layout of SEM instrument is shown Figure 3.4.1

The surface continuity and ultra smoothness of our synthesized HDLC film have been analyzed by SEM. A typical SEM image of the HDLC film was recorded with a FEI Quanta 200f operating at 10 kV in low vacuum mode to avoid sample charging of the un-coated specimen.

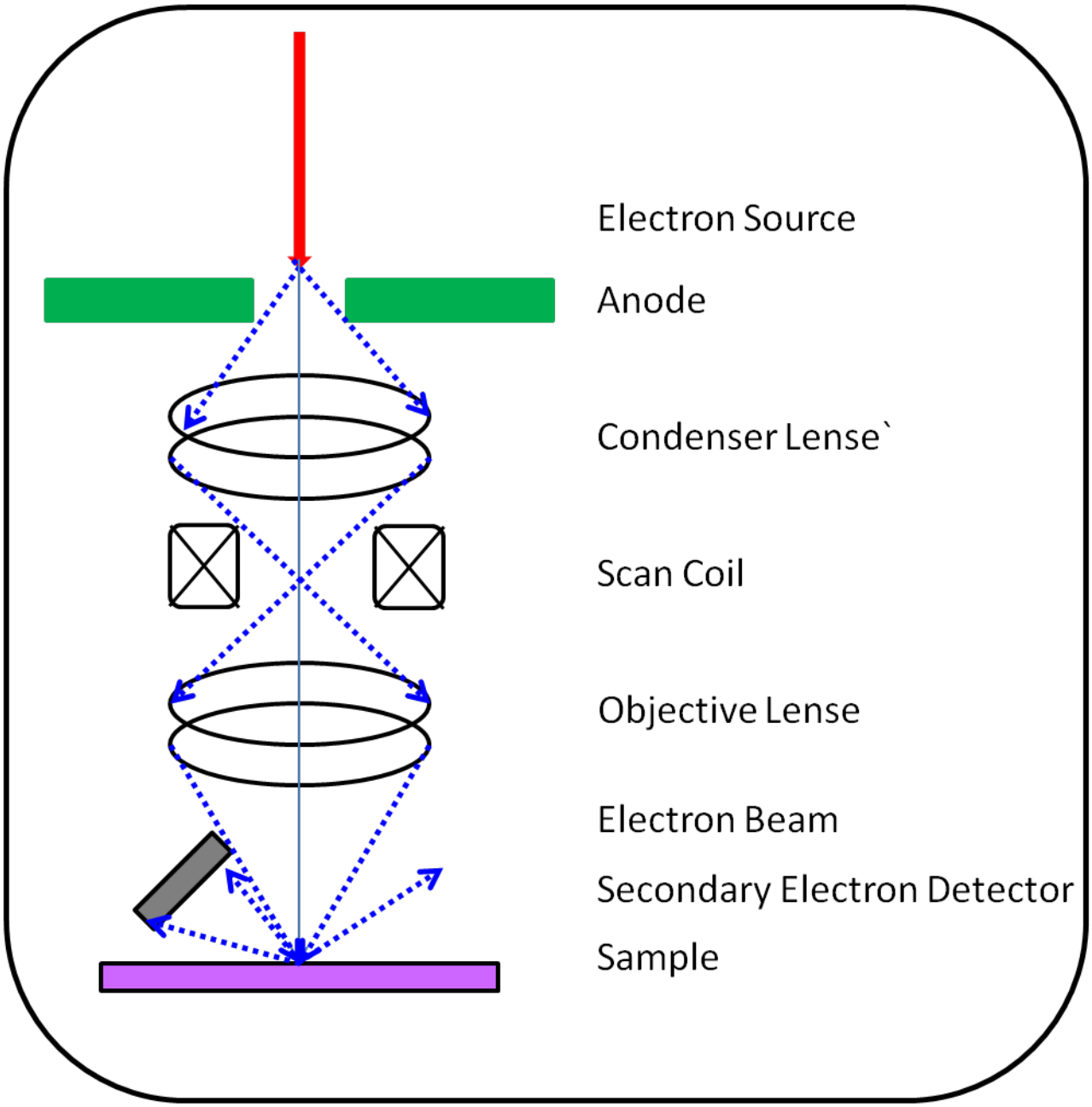

Figure 3.4.1 Schematic layout of Scanning Electron Microscope

3.5 Pelletron Accelerator

The accelerators are the machine to accelerate charged particles in high vacuum and high voltage potential system for million electron volts (MeV) to giga electron volts (GeV) energy range. The accelerating electrodes are arranged in a linear path called linear accelerator (LINAC), or repeated acceleration in a circular path called Cyclotrons / Synchrotrons. The very first machine used to produce high energy charged particles by accelerator is Van-de Graaff electrostatic accelerator by R. J. Van de Graaff, of Massachusetts Institute of Technology in 1929. The most recent and powerful one is the European Organization for Nuclear Research, known as CERN which is a network of six accelerators and a decelerator, for high-energy physics experiment in search of the origin of Universe.

In the past few decades, the research and development works based upon the accelerators were evolved enormously in the field of namely Archaeology, Engineering, Environment science, Geology, Material science, Physics, Forensic science, Biology, Biomedical etc. The research activities have been performed with tandem accelerator for the application of ion beam analysis to various disciplines of materials, medical sciences, and industrial applications. In the recent R&D study using ion beam include nuclear reactions, Rutherford Backscattering Spectroscopy (RBS), Particle Induced X-ray Emission (PIXE), Elastic Recoil Detection Analysis (ERDA), High Resolution X-ray Spectroscopy (HR XPS), Time of Flight (TOF) measurements, Ion Implantation, and Ion Microprobe studies.

A tandem accelerator accomplishes the acceleration of charged particle in two stages by converting their charge state on the high voltage terminal. Generally, a negative ion is accelerated more advantageously than that of the acceleration of positive ions. The maintenance work becomes very difficult, if a positive ion source is employed, because, the

ion source is to be placed within the high voltage terminal. In the two stage tandem Van de Graaff, negative ions are generated by electron bombardment, and are accelerated toward the positive high voltage terminal which is located near the center of the pressure tube. Inside the terminal the negative ions, having energy in the range of MeV, travel through the stripper foil or a gas-filled column, and are therefore stripped off electrons. The positive ions consequently produced, are further accelerated towards the ground potential in the usual way. The ion beams with current in the order of few milliamp's are produced in the two stage tandem which are commercially available.

In our tandem accelerator system, the negative ions with energy E_{EXT} (due to extraction voltage, here -3 kV) are extracted from an ion source, analyzed, and then injected into the accelerator, where it was accelerated in two steps. First, the injected negative ions are extracted due to the applied electrostatic field (+ voltage) on the terminal in the middle of accelerating tube. The Q-snout which is a pre-accelerating electrode mounted on the low energy side of the accelerator, acts with the same line of the first stage of the accelerator in order to collimate and the incoming negative particle is focused towards the center of accelerator. In the terminal, the injected monovalent negative ions are stripped off one or several electrons through charge exchange processes. The stripping off the ions is done using nitrogen gas, injected separately in the middle of the accelerating tube. The beam is now composed of positive ions with distribution of charge states and these ions are accelerated towards ground potential. The acceleration of each ion depends on its charge state z. The final energy E of the emerging positive ions with charge state z is given by equation

$$E = E_{EXTV} + (z+1)E_{TV} \qquad (4.5.1)$$

where E_{EXTV} is the energy of the injected negative ions from ion source, and E_{TV} is the energy of the charged particle by the terminal voltage. The above equation states that, the particle can be accelerated to the higher energy by charge conversion during the acceleration. A

focusing electrostatic quadrupole doublet is mounted at the end terminal in the high energy side of the accelerator system, for focusing of the positive ion beam onto the samples together with an analyzing magnet and proper X and Y steering system.

The schematic layout of the system is shown in Figure 3.5.1

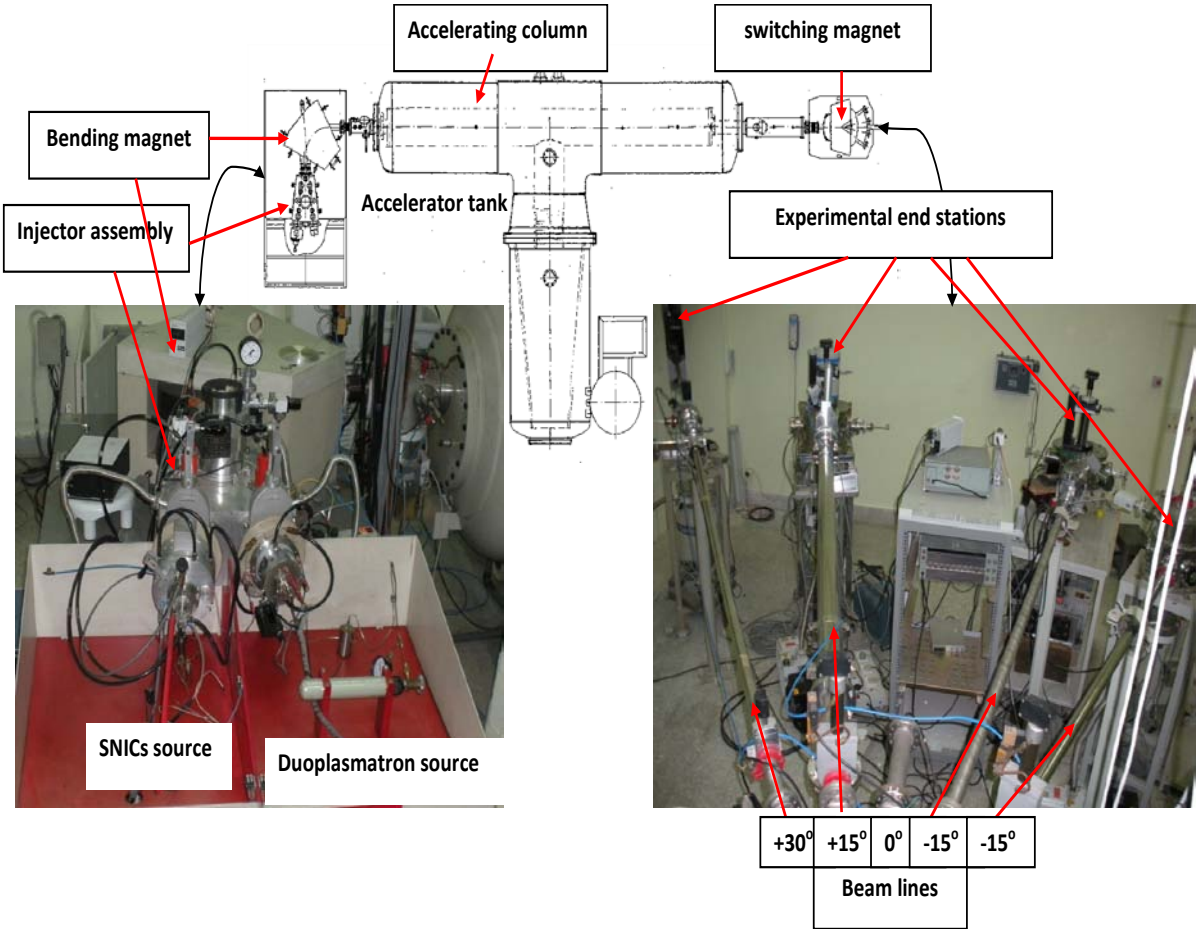

Figure 3.5.1 Schematic layout of Tandem Accelerator

(1) Ion Sources

(a) Source of Negative Ions by Cesium ion sputter (SNICS) : source of heavy ions viz. F, C, N, O, etc.

(b) Duoplasmatron ion source : Source of H, He ions for RBS study

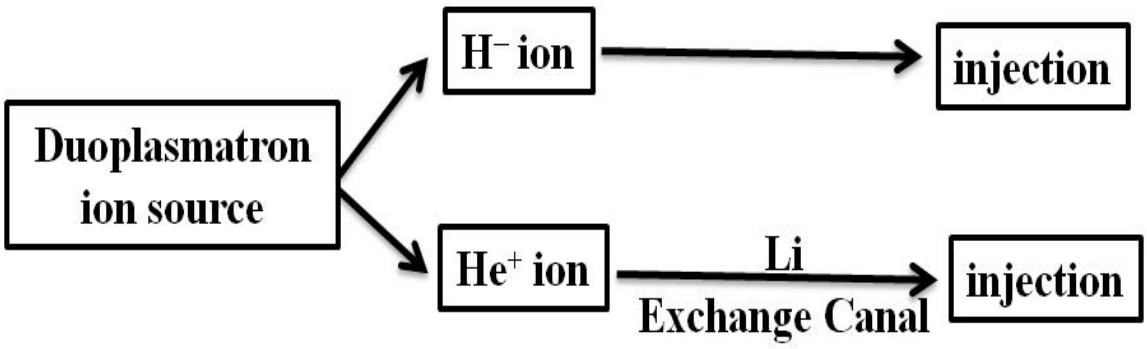

Figure 3.5.2 Flowchart for Duoplasmatron ion source for RBS study

(2) Low Energy Magnet

After the ion source to bend the beam 90^0 to get into accelerating tube

Parameter for $^{19}F^{-1}$ ion beam (before striper foil)

I (current)=18.59 amp

q=charge of F ion 1

m=18.99 (mass of F)

E=(3+15) keV

R= 0.4306 meter

(3) Accelerator tube

1×10^{-7}mbar

(4) Electrostatic Steerers

(5) Stripper

Nitrogen gas

(6) High Energy Magnet

Focus the beam into target

Parameter for $^{19}F^{3+}$ ion beam

I (current)= 29.3 amp

q=charge of F ion 3

m=18.99 (mass of F)

E=(6400+18) keV

R=1.489 meter

(7) Faraday Cup

Measure the current

The high energy side of the tandem is having four beam lines. Each of them is dedicated to Nuclear Reaction Analysis/Particle Induced Gamma Ray Emission study, Rutherford backscattering study, Particle Induced X-ray Emission study, and Activation/Channeling RBS applications.

The most multipurpose negative ion source currently available is the SNICS II type which is widely used on pelletron accelerator and many other accelerators worldwide. The SNICS source generates a negatively charged ion beam by 3KV cesium ion sputtering. The cesium (Melting point 28 ^{0}C, Boiling point 678 ^{0}C) vaporized from the cesium oven into the vapor and remains between the cathode and heated (1100-1200 ^{0}C) ionizing material called ionizer. The ionizer is heated by DC current to ~1100 ^{0}C. The cesium atoms get ionize on the hot surface of the ionizer, whereas some probability exists that cesium atoms may come closer to the cooled part of the cathode and condensed into a cesium layer. However, ionized cesium gets energized on acceleration towards cathode. The cathode is at -3 KV potential. The energized Cs will sputter more and more atoms which pick up electrons from the nearby surroundings. For studying the hydrogenated diamond like carbon thin films using nuclear

reaction analysis techniques fluorine ion beam was chosen. For this purpose, sodium fluoride salt mixed with the graphite powder and placed on the cathode. The cesium ion sputtering results fluoride ion (F^-) along with the other ions (C^-, Na^-, C_2^- etc). The negatively charged ions are extracted from the ion source with the potential of -15 KV (Extraction Voltage). They are analyzed and separated with a low energy magnet (90 degree bend) for selectively isolate the fluoride ions ($^{19}F^-$). The related parameters for low energy analytical magnet are, Charge and Mass of fluorine q =1, and m=18.99, respectively, Energy =-18 keV, Radius R=0.4306 met., k=0.433, Current I=18.59 ^{0}A. An upgrade of the systems is now available in the form of Multi-Cathode SNICS (MC-SNICS type).

We have a relatively inexpensive, direct extraction Duoplasmatron ion sources which is simple, reliable, and capable of performing routine operation. The system is useful in producing modest currents of negative ions from many molecular gases such as H^- and He^- with the help of sideways displacement of the intermediate (Zwischen) electrode. The H^- ion beam generated from this duoplasmatron ion source is used subsequently for Rutherford backscattering spectrometry study to measure the thickness of the HDLC films and carbon content different films. The ion source is cooled primarily by Freon and followed by water.

3.5.1 Nuclear Reaction Analysis

The synthesis of HDLC film in detailed is described in chapter 2. Four samples for which the CH_4 flow rates are 20, 30, 40 and 70 SCCM, thus grown with varying H_2 to CH_4 ratio during deposition at room temperature (RT), will be represented as samples A, B, C and D, respectively, in the rest of the article. The samples A–D, annealed at high temperatures 750 ^{0}C and 1050 ^{0}C in high vacuum (~1×10^{-7} torr) furnace, in order to study removal of hydrogen from the samples, will be represented as annealed (750 ^{0}C or 1050 ^{0}C) samples A–D in the rest of the article. Raman spectra of all these samples were recorded using a confocal micro-

Raman Spectrometer (LabRAM HR Vis. Horiba Jobin Yvon SAS France). The detailed description of operation is given in chapter 3 (section 2).

NRA has the ability to separate the respective contributions of surface and bulk in a non destructive way. The cross section for the off resonance is more than two orders of magnitude smaller than the peak, which provides a better depth profiling of the thin film. The sample is bombarded with more than 6.4 MeV $^{19}F^{3+}$ ion beam from the accelerator for depth profiling of hydrogen and the gamma rays produced from resonance reaction, were detected. When the incident energy of $^{19}F^{3+}$ ion bean is 6.4 MeV it provides the hydrogen content at the surface of sample. The incident ion energy is then increased above 6.4 MeV in order to determine the hydrogen within the sample. As the ion traverses the sample its energy decreases due to the coulombic interaction with the target material, and reaches the resonance energy only at a certain depth inside the surface. The corresponding γ-ray yield measured provides the hydrogen content at that depth, where it undergoes the reaction and produces those characteristic gamma rays. The difference of incident ion energy and resonance energy along with the stopping power data provides the depth scale as shown in Figure 3.5.1.1. Likewise the bombarding energy of the ion beam is increased at steps to measure hydrogen content as per depth for the entire thickness of the sample.

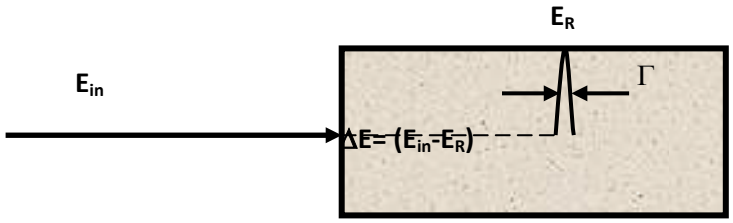

Figure 3.5.1.1 Schematic of depth profiling having resonance energy E_R and width Γ for the incident beam of energy E_{in}

NRA measurements were carried out by a 3 MV Tandetron accelerator at the surface and profile measurement laboratory of the National Centre for Compositional Characterisation of

Materials (CCCM), Hyderabad, India. Depth profiling of HDLC was accomplished by bombarding the specimens at normal incidence with a well-collimated (dia. 2 mm, current 2 nA) tripositive fluorine ion ($^{19}F^{3+}$) beam. The characteristic gamma rays for the reaction $^{1}H(^{19}F,\alpha\gamma)^{16}O$ were monitored by a 3″×3″ size Bismuth Germanate (BGO) semi-conductor detector. The characteristic gamma lines from the produced isotope ^{16}O are 6.1, 6.9 and 7.1 MeV. These gamma lines are detected by BGO detector at a distance of 2 cm behind the targets along the direction of the incident beam. The beam current was intergrated in the chamber, which is electrically insulated from the beam line. This gives total number of positive ions incident on the sample. The integrated counts between 4.8 and 6.3 MeV energy window of the PC-based multichannel analyzer, served as the yield of the reaction. This is found to give significant counts in the present experimental set. Due to poor electrical conductivity of the samples and backing semiconductor silicon material, small electrical conductor were attached at the top surface before putting in the beam line vacuum (better than 10^{-6} torr). A guard ring, with a bias of 900 V was positioned in front of the target to suppress secondary electrons. The beam current incident on the sample is measured by Faraday cup arrangement [56]. The experimental set up in the laboratory for depth profiling of hydrogen is given in Figure 3.5.1.2.

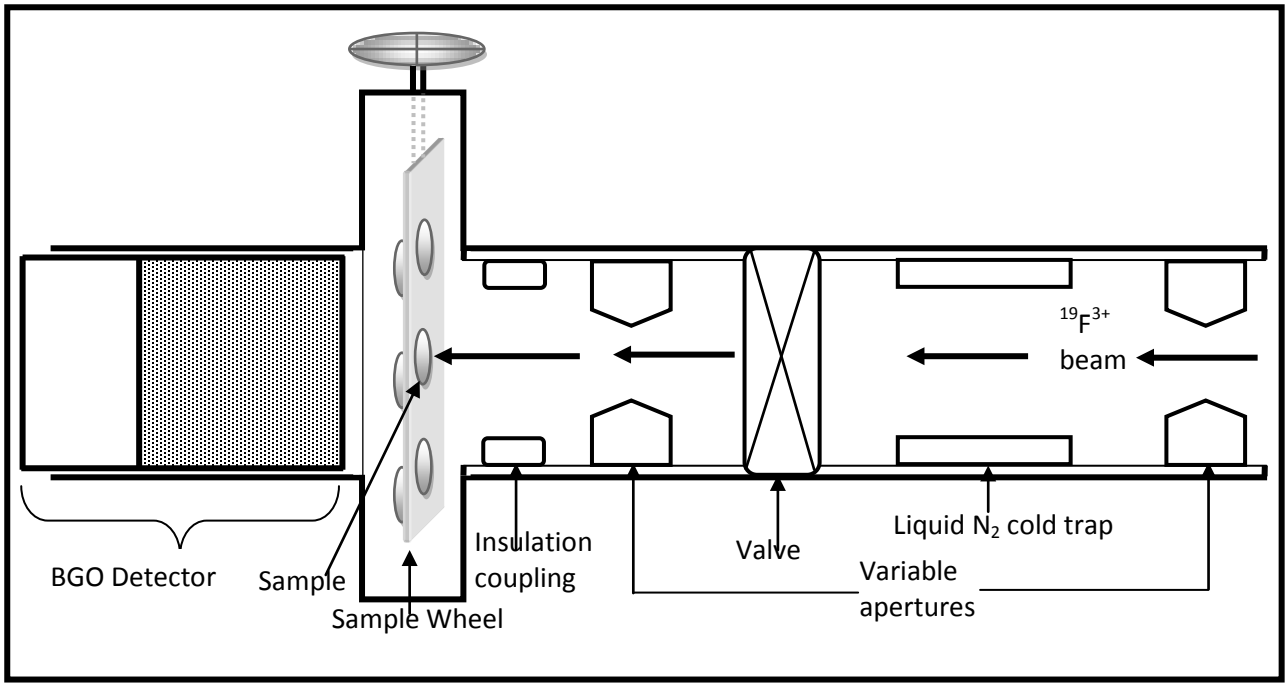

Figure 3.5.1.2 A schematic representation of the experimental system used to measure the hydrogen depth profiles. Sample viewing window and other complex parts are not shown here. A $^{19}F^{3+}$ beam from the accelerator bombards the sample mounted on a manual rotatable (X, Z, θ) sample wheel, and the characteristic gamma rays are measured with an BGO detector placed behind the sample.

Depth profiling of hydrogen was carried out by bombarding the targets with $^{19}F^{3+}$ ions. The measurements were also performed in the off-resonance region (beam energy below 6.4 MeV) to have the contribution of the background for each the samples as well as with silicon in all the measurements. The energy of the ion beam was increased in steps of 20 and 40 keV above the resonance energy, i.e. 6.4 MeV. The energy was increased until the integrated counts in the region of interest are equal or less than that of the off-resonance counts. The typical beam currents on the sample and standard were of the order of 2 and 3 nA over a ~ 2 mm diameter spot. Two sets of measurement (in steps of 20 and 40 keV) are carried out for each sample in the different regions to get the reproducibility of the results. The desorption phenomenon is studied for our specimen and standard which are treated at the same

conditions of the beam and the integrated counts in the multichannel analyzer are recorded in every 250 nC, until total charge in the Faraday cup is 5000 nC.

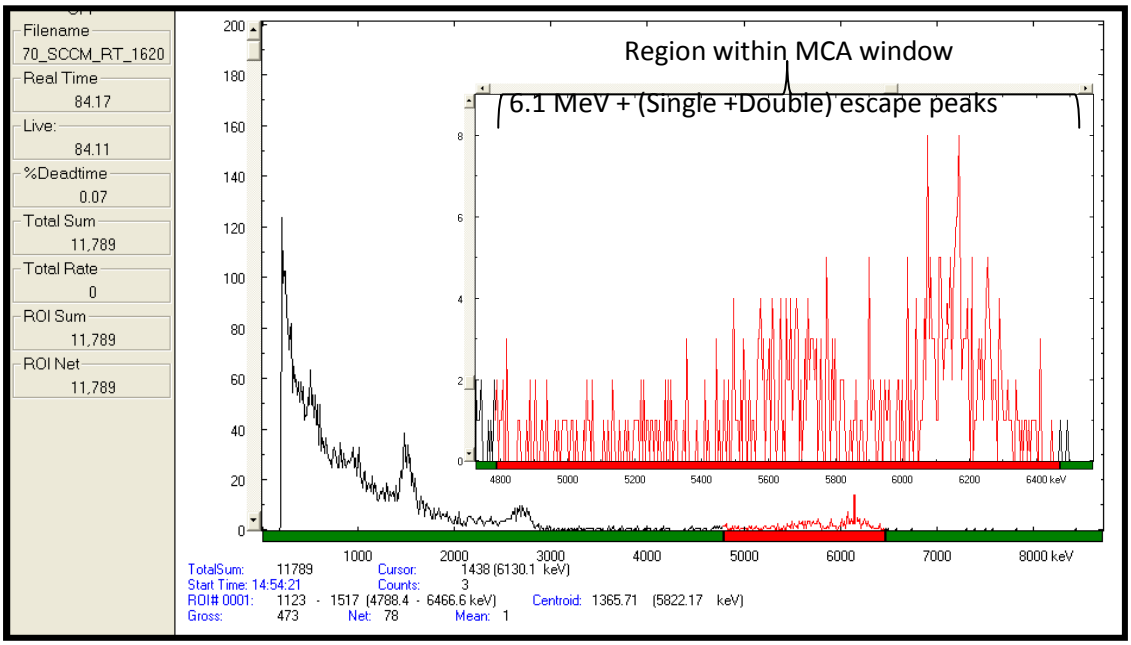

Figure 3.5.1.3 The pulse height spectrum recorded for 250 nC charge of $^{19}F^{3+}$ ion beam during hydrogen depth profiling of a typical as prepared HDLC film of 70 SCCM. The inset picture showing the peak of energy 6.1 MeV, and its single, and double escape peaks.

Three categories of samples are used for calibration purpose because of the long time stability of the composition under ultra-high vacuum (1) Chemical composite containing hydride in stoichiometric proportions, e.g., plastics and other organic compounds [119-120] (2) Hydrogen implanted targets viz. silicon [78], and (3) Metal hydrides [121].

3.5.1.1 Methodology and Technical Details :

Expression for Hydrogen content determination using NRA technique **:** The atomic fraction of Hydrogen in the HDLC film (considering as a binary film, C_xH_y) was estimated by the following equation [122]

$$f^{H}_{HDLC} = \frac{f^{H}_{Std}.\varepsilon^{C}_{HDLC}}{Y\varepsilon_{std} + f^{H}_{Std}.(\varepsilon^{C}_{HDLC} - \varepsilon^{H}_{HDLC})} \qquad (3.5.1.1)$$

where *Y* ratio of gamma yields for standard and sample, *f* atomic fraction of hydrogen in the film material given in subscript, ε_{Std} and ε^{i} stands for the stopping power for the standard and the i^{th} element having in the superscript. The ratio of yields, *Y* is obtained from the γ-ray yields in the NRA measurements. The stopping power and atomic fraction of hydrogen for the standard Mylar $C_{10}H_8O_4$ ε_{std} 1.841×10^2 eV/(10^{15} at/cm^2) and f^{H}_{std} 0.3636, respectively, are known. The stopping power data in this work is calculation using SRIM-2008.04 [123].

The depth χ_R is related to the incident beam energy E_i by the equation

$$\chi_R = \frac{E_i - E_R}{\varepsilon} \qquad (3.5.1.2)$$

where E_R is the resonance energy and ε is the stopping power.

The depth in at./cm^2 is converted into linear dimension using density (3.0 gm/cc [93]) of the film of known film thickness determined by other methods.

The stopping power of a multi-elemental film using Bragg's law of linear additively can be written as

$$\varepsilon = \sum_{i=1}^{N} f_i . \varepsilon_i \qquad (3.5.1.3)$$

where f_i and ε_i are the atomic fraction and the atomic stopping power of the i^{th} constituent, respectively and N is the total no of constituent in the film.

The depth resolution ($\Delta\chi_R$) was estimated from the equation given below [56]

$$\Delta\chi_R = \frac{[\Gamma^2 + (\Delta E)^2]^{\frac{1}{2}}}{\varepsilon} \qquad (3.5.1.4)$$

where Γ is the resonance width, ΔE = $\left(\Delta E_S^2 + \Delta E_B^2 + \Delta E_D^2\right)^{\frac{1}{2}}$ is the fluctuations in the energy of the bombarding ions at a depth of χ_R , ΔE_S is the energy straggling of the beam, ΔE_B is the energy spread of the incident ion beam, ΔE_D is the Doppler energy broadening in the thin film. The $\Delta\chi_R$ represents the measured FWHM of an infinitely thin spike of hydrogen at some depth. The depth resolution of $^{19}F^{3+}$ ion for hydrogen profiling techniques is ~ 20 nm (considering the $\Delta E_S \cong 0$; $\Delta E_B \cong 0.3$ keV, $\Delta E_D \cong 12$ keV), compound using stopping power from the elemental fraction of the film. To calculate the concentration the following values were used.

Stopping power for Hydrogen, $\varepsilon_H = 2.327 \times 10^2$ eV/(10^{15} at/cm^2)

Stopping power for Carbon, $\varepsilon_C = 7.82 \times 10$ eV/(10^{15} at/cm^2)

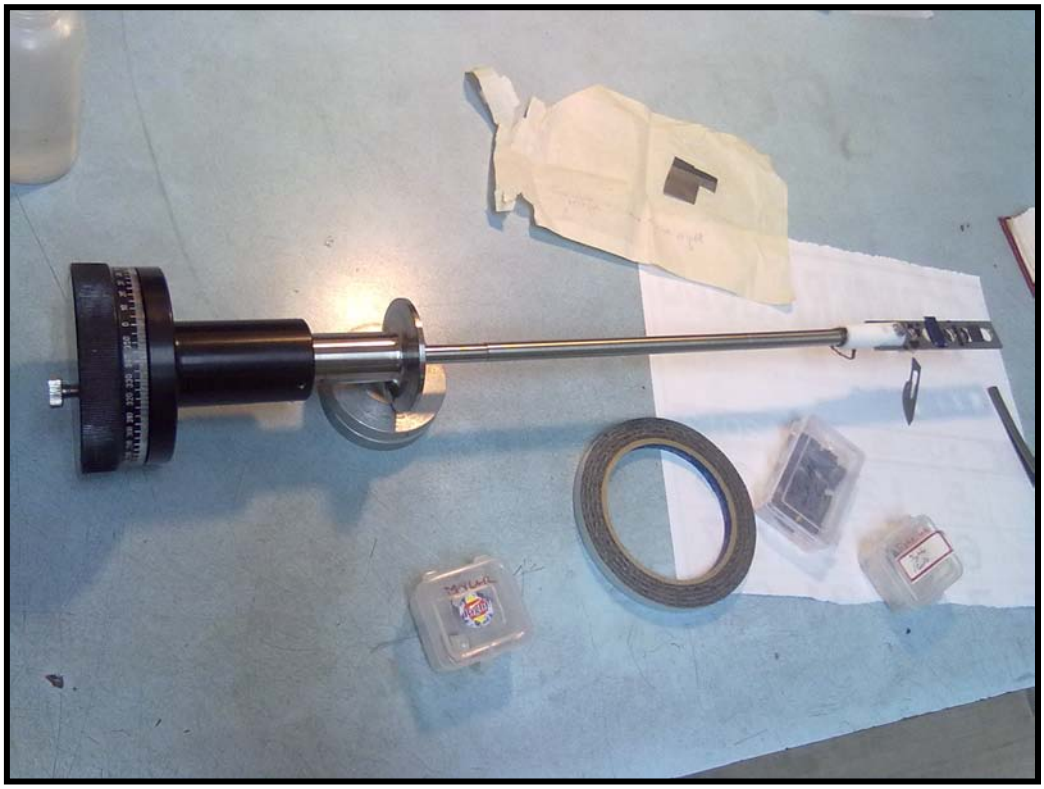

Figure 3.5.1.4 Picture of HDLC sample mounting holder

Figure 3.5.1.5 Picture of HDLC samples placed onto the holder

Figure 3.5.1.6 Picture of experimental arrangement for IBA study

(given in chapter 2 and also shown here for convenience)

3.5.2 Rutherford Backscattering Spectroscopy

RBS measurements on HDLC thin films (as prepared and annealed) are carried out with 1.0 MeV proton beam from the 3 MV Tandetron accelerator described earlier. The backscattered particles are detected by a silicon surface barrier (SSB) detector at an angle of 170^0. The scattering chamber is pumped down to ~5×10^{-6} mbar by turbo-molecular pump.

Expression for thickness determination using RBS technique **:** The energy loss of a 1.0 MeV proton beam in a thin film of thickness t is related to the stopping power of the material is given below [124-125].

$$t = \frac{\Delta E}{[\varepsilon_i]} \tag{3.5.2.1}$$

$$[\varepsilon_i] = \frac{K_i}{\cos\theta_1}\left[\frac{dE}{dX}\right]_{in} + \frac{1}{\cos\theta_2}\left[\frac{dE}{dX}\right]_{out} \tag{3.5.2.2}$$

where, t is the thickness, ΔE is the FWHM of the peak, ε_i is the stopping power of the i^{th} element and the subscripts ‘‘in’’ and ‘‘out’’ refer to the (constant) values of stopping power (dE/dX) along the inward and outward paths, θ_1 and θ_2 are the angles between the sample normal and the direction of the incident beam and of the scattered particle respectively. We have taken $\theta_1 = 0^0$; $\theta_2 = 10^0$; $\left[\frac{dE}{dX}\right]^C_{in,1.0MeV}$ =51.88 keV/μm and $\left[\frac{dE}{dX}\right]^C_{out,0.726MeV}$ =63.66 keV/μm; $[\varepsilon]_C$ = 102.29 keV/μm, FWHM for 70 SCCM RT sample 14.713 ± 0.20 keV, giving the thickness of the carbon thin film 144 ± 8 nm. The mass density of the film can be estimated using areal density and thickness obtained by RBS and NRA techniques, respectively.

3.6 Keithley Source Meter

The current–voltage (I-V) characteristics in ambient air, of the as-prepared HDLC and annealed HDLC films, were measured in the form of series current (I)-versus-voltage (V) measurement with a simple bias current using a Keithley 2635 single-channel current source meter.

The experimental data of Single Electron Transistor (SET) at room temperature, based upon diamond like carbon (DLC) is not reported in the literature [126-128]. The HDLC thin film grown onto a large area (12 cm×12 cm) substrate Si (100), behaves as a 2-D graphitic film, having both p-type and n-type surface conduction. A picture of ohmic contacts of Cu as source, and drain onto the HDLC surface [128-129] is shown in Figure 3.6.1a. The schematic layout of HDLC sample and ohmic contacts are shown in Figure 3.6.1b. Biswas et al. [130] have applied electrochemical method, in order to reduce the size of the domain of conducting (sp^2 C=C) carbons isolated by the domains of non-conducting (sp^3C-H) carbons, for hydrogenation of sp^2 C=C bond on the as-prepared HDLC surface, and thus produce electrochemically hydrogenated diamond like carbon (ECHDLC) surface. A confocal Micro-Raman spectrometer is used to measure Raman spectra of the HDLC samples to see any change of Raman spectra due to the electrochemical processes. The Keithley source meter (2635 Single Channel) instrument is shown below in Figure 3.6.2 and the experimental arrangement for I-V study using Keithley source meter is shown below in Figure 3.6.3. The typical results on HDLC films (as-prepared and annealed) obtained by current (I) vs. (V) characteristics onto the HDLC surface are displayed and critical discussion is made about the surface conductance mechanisms, based upon the results are given in chapter 4 (section 4).

3.6.1 Experimental arrangements for measuring I-V characteristics :

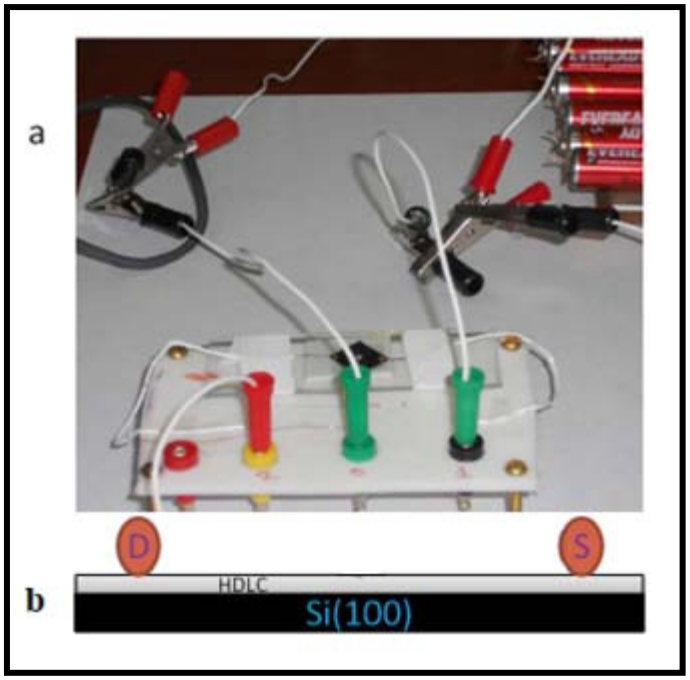

Figure 3.6.1 Picture and Schematic layout of sample. (a) A picture of three ohmic contacts on the surface of HDLC thin film and the connecting wires from these contacts. (b) A schematic view of layers of Si (100) substrate, thin film of HDLC and ohmic contacts: source (S), and drain (D), corresponding to contacts in the picture, onto the surface of HDLC sample.

Figure 3.6.2 Picture of Keithley source meter (2635 Single Channel)

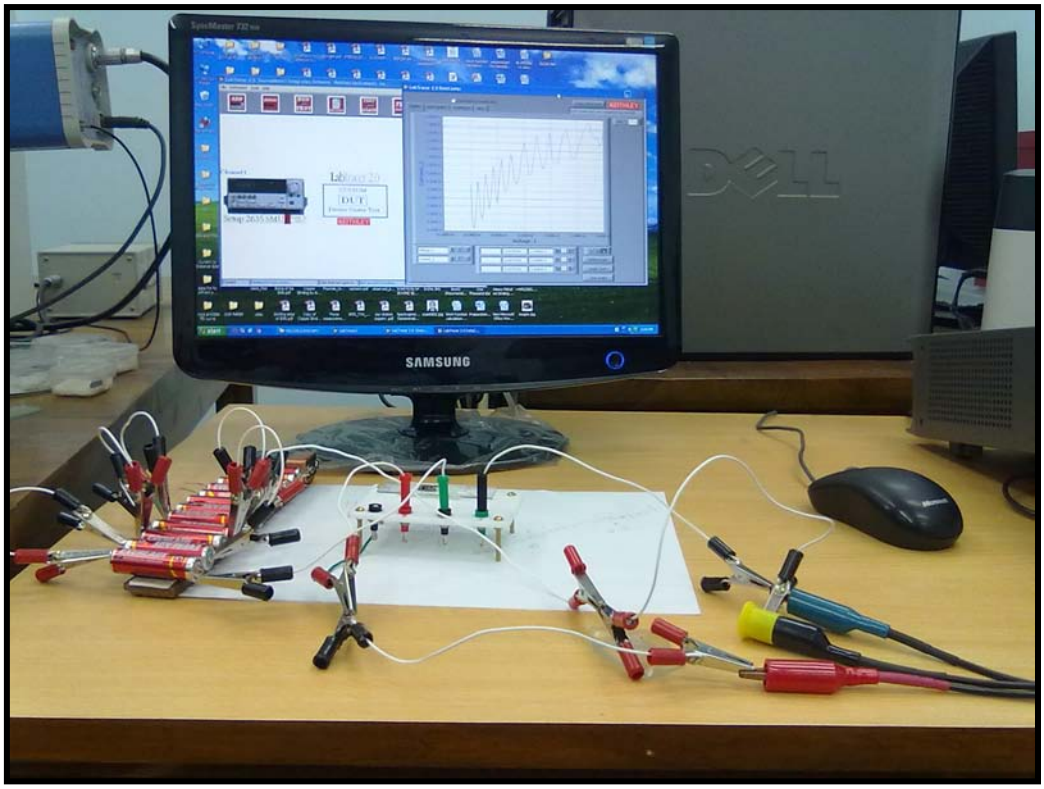

Figure 3.6.3 Picture of experimental arrangement I-V study using Keithley source meter

Specification conditions

The source and measurement accuracies are specified at the Source Meters® CHANNEL A 2635 terminals under the following conditions:

1. 23°C ± 5°C, < 70% relative humidity.

2. After two-hour warm-up.

3. Speed normal

4. A/D auto-zero enabled.

5. Remote sense operation or properly zeroed local operation.

6. Calibration period: one year.

3.7 Olympus Digital Camera

The parameters of the digital camera used for taking the photograph of the sp^2 C=C sites excited under visible light from a focused light source is given below

Equipment Make : Olypus Optical Co. Ltd.

Camera Model : C4040Z

Creation software : v552p-A78

Color representation : sRGB

Flash used : No

Focal length : 25.4 mm & 35.7 mm

F-number : F/6.3 & F/2.6

Exposure time : 1 sec

Metering mode : Spot and pattern

3.8 Dielectric measurement

Our HDLC as-prepared films have the properties of low conductivity (high impedance) and low loss. Therefore, our as-prepared HDLC films may be considered to a dielectric material. One important technique for analyzing such material is impedance spectroscopy, i.e. measuring the electrical impedance over a range of frequencies. The impedance is related to the conductivity and capacitance of the material and these parameters can easily determined using this technique. Dielectric characterizations were carried out over our HDLC samples as a function of frequency using an LCR meter (HIOKI) in the frequency range from below 1 Hz at room temperature. The instrument is shown in Figure 3.8.1 and the sample holder in Figure 3.8.2. The Solartron 1296 dielectric interface enhances its capabilities with Solartron 1260 frequency response analyzer (FRA) to cope with ultra-low current and capacitance levels experienced in analyzing dielectric materials.

Table 3.8.1 Dielectric Interface 1296 Specification

Parameter	Model (1296+1260)
Frequency Range	10 μ Hz to 10 MHz
Signal Amplitude up	to 7 Vrms
DC Bias	up to 40V

The 1296 software requires knowledge of the geometry of the sample. The thickness of the sample can be read from a micrometer digital display and the area of the sample is calculated manually. These dimensions are used in the 1296 PC software to calculate the permittivity of the material (which is independent of the size of the sample), using the formula:

$\varepsilon = C.d/A$

where ε = permittivity (F/m)

C = capacitance (F)

d = thickness (m)

A = area (m^2)

This allows results from materials of different sizes to be compared. Results can be displayed using the 1296 software as absolute or relative permittivity. Relative permittivity of the material, also known as the “dielectric constant” is calculated as:

$\varepsilon_r = \varepsilon / \varepsilon_0$

where: ε_r = relative permittivity

ε = permittivity of sample

ε_o = permittivity of free space (8.85419×10^{-12} F/m)

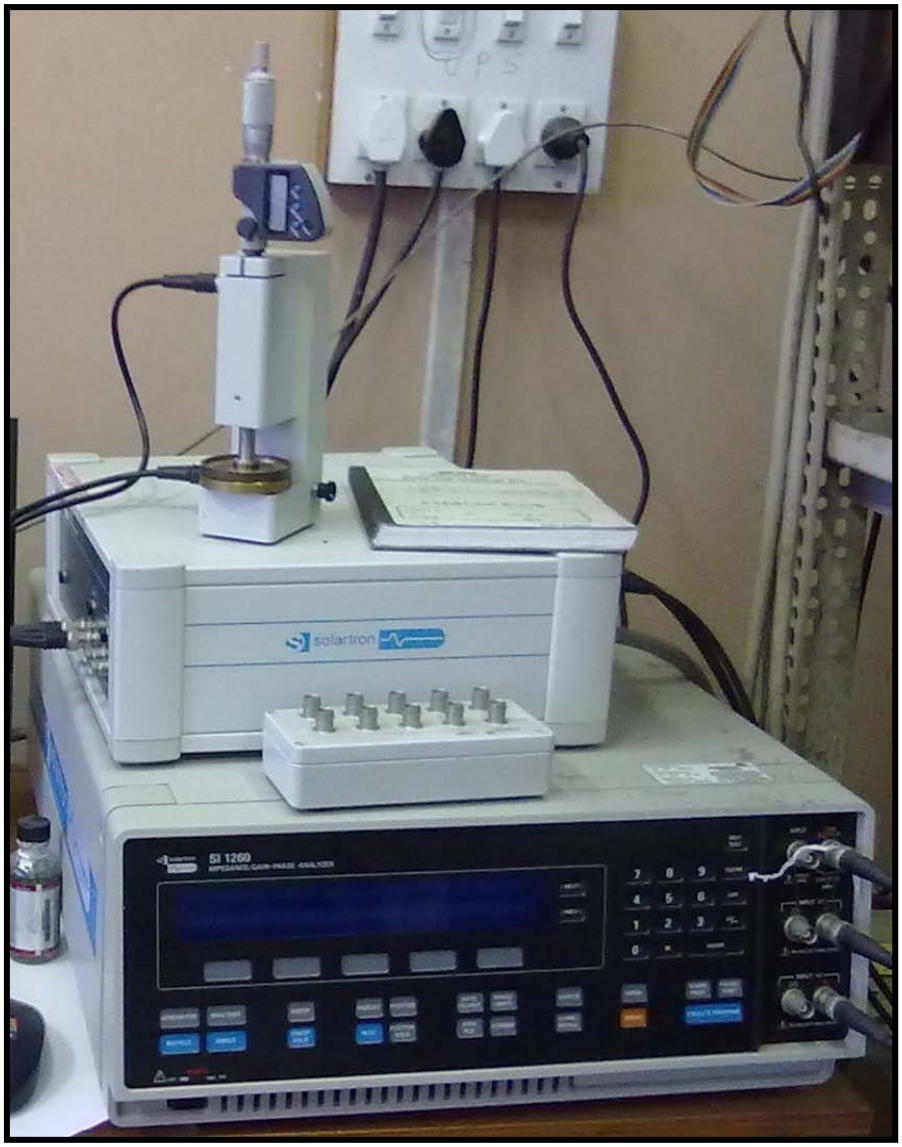

Figure 3.8.1 Dielectric Interface instrument (model 1296 and 1260)

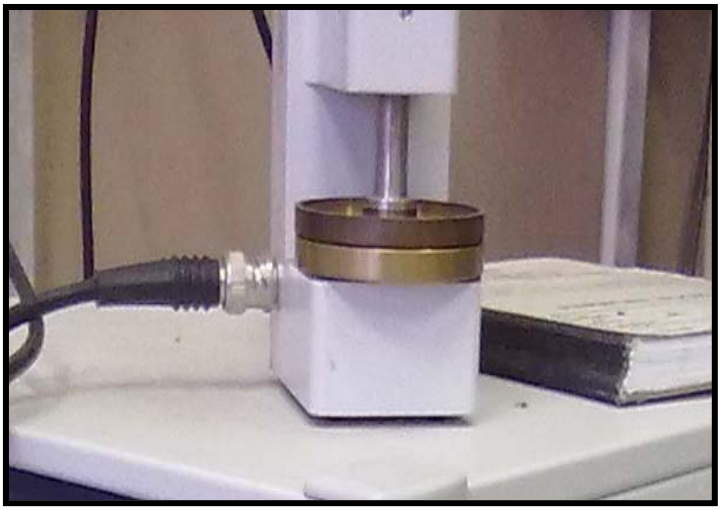

Figure 3.8.2 Sample holder of Dielectric Interface instrument

Chapter 4

Results and Discussions

4.0 Results and Discussions

The detail characterization of the HDLC sample is performed different spectroscopic and microscopic techniques viz. high resolution transmission electron microscopy (HRTEM), transmission electron energy loss spectroscopy (TEELS), atomic force microscopy (AFM), scanning tunneling microscopy (STM), scanning electron microscopy (SEM), micro Raman spectroscopy (mRS), nuclear reaction analysis (NRA), and Rutherford backscattering (RBS) measurements, current(I) vs voltage measurements etc.. The results of each of them are discussed below.

4.1 Results and discussion with HRTEM/TEELS, SEM, and AFM measurements

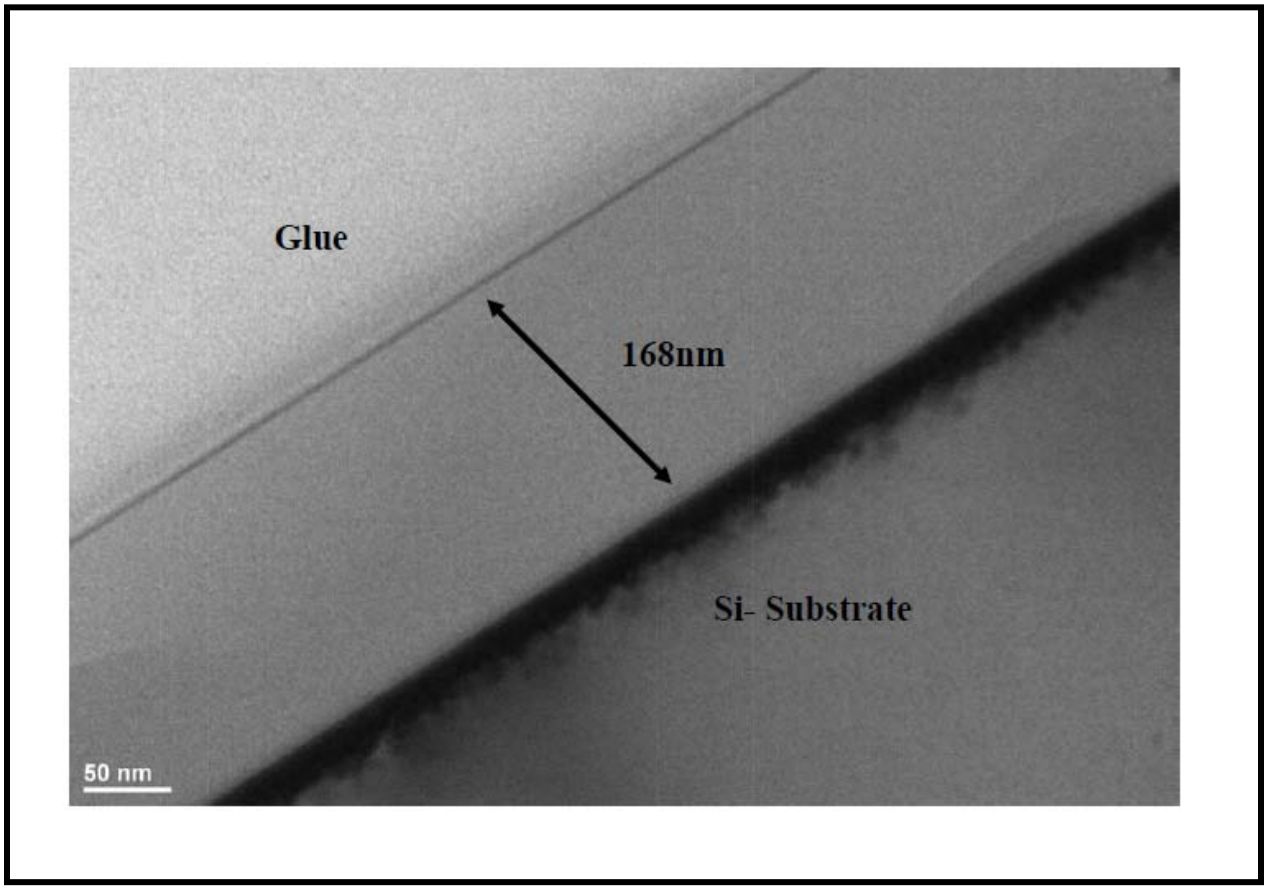

Figure 4.1.1 Typical HRTEM cross sectional view of the HDLC film

Typical cross-sectional view of HDLC sample is shown in Figure 4.1.1, which shows the typical thickness of the film is ~ 168 nm.

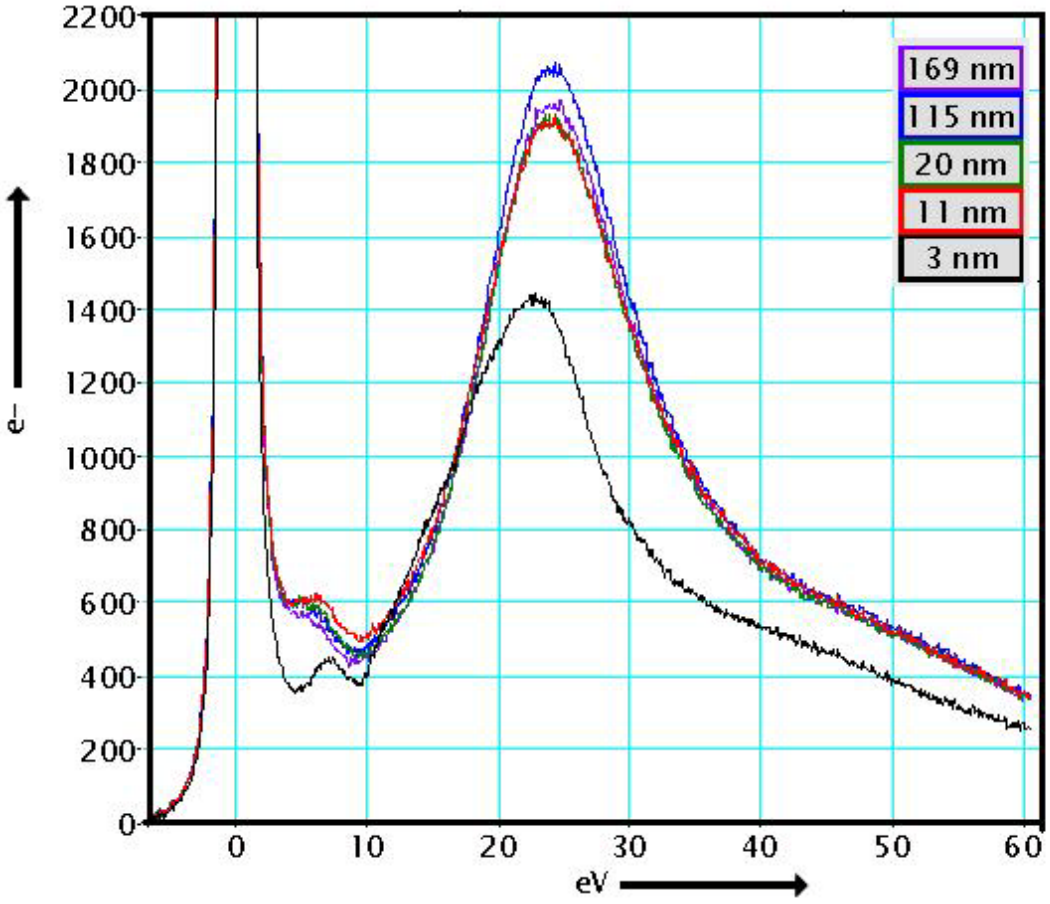

Figure 4.1.2 Typical TEELS spectra recorded for HDLC film. Numbers in the legend indicate approximate distance of the probe from the interface

Figure 4.1.2 describes typical TEELS spectra for HDLC film, showing the two characteristic peaks in low energy range (< 50 eV). Following the comparisons of TEELS spectra of graphitized carbon and amorphous carbon in the literatures [107, 109], we can explain our experimental results (Fig. 4.1.2). The broad peak at about 24 eV is the (π+σ) plasmon i.e. the bulk plasmon, which corresponds to collective excitation of all (π+σ) electrons; the other peak at ~ 6 to 7 eV is the π plasmon, which corresponds to collective excitation of all π electrons. All the

spectra were recorded at different distance of the probe from the interface. Except very close to the interface, there is no observed variation of the spectra. Above 3 nm from interface upto top of the HDLC film, the plasmon structures correspond to multilayered graphene i.e. hexagonal graphite structure and near the interface i.e. below 3 nm, the plasmon structure correspond to a few layer graphene, with slight red shift and reduced intensity of the plasmon peak of ($\pi+\sigma$) electrons [109]. Thus near the interface between Si(100) substrate and bulk graphitic structure we can assume a few layer graphene corresponding to sp^2 bonded C and this result supports the BEN model [89]. The density of valence electrons 'n' of a thin film can be measured from the low-loss spectrum through the measured value of plasmon energy $E_p = (4\pi n/\varepsilon_o m)^{1/2}$ from the low-loss spectra, where ε_o is dielectric constant of vacuum and m is effective mass of an electron. Thus we can say that the density of ($\pi+\sigma$) electrons is much higher in the bulk than in the interface of HDLC film which was measured to be of single crystalline nature different from the hexagonal graphene/graphite structure [93].

The morphology of the surface of the HDLC films has been analyzed by AFM and SEM respectively.

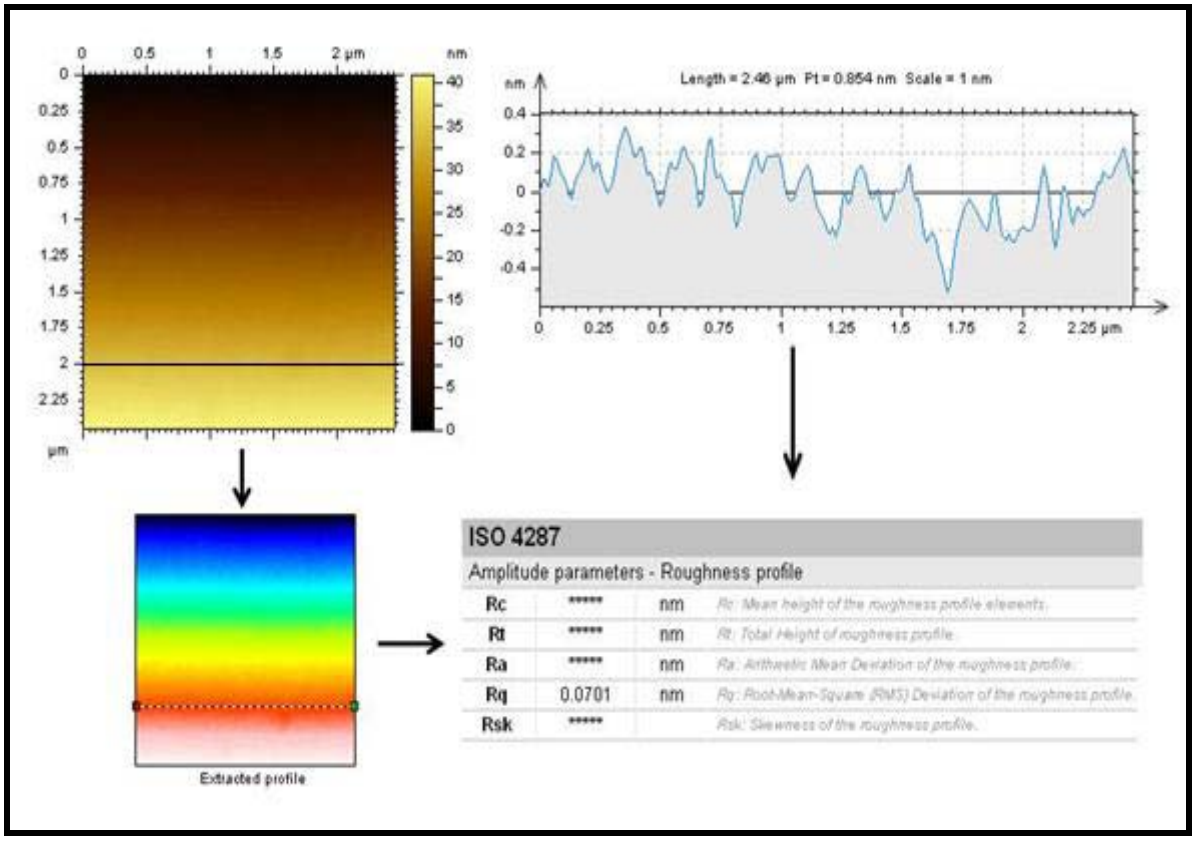

Figure 4.1.3 Non-contact mode AFM topography image of HDLC surface: scan size 2.5 µm × 2.5 µm

Figure 4.1.3 is a typical AFM topography image of the HDLC surface, giving its roughness value (~ 0.07 nm).

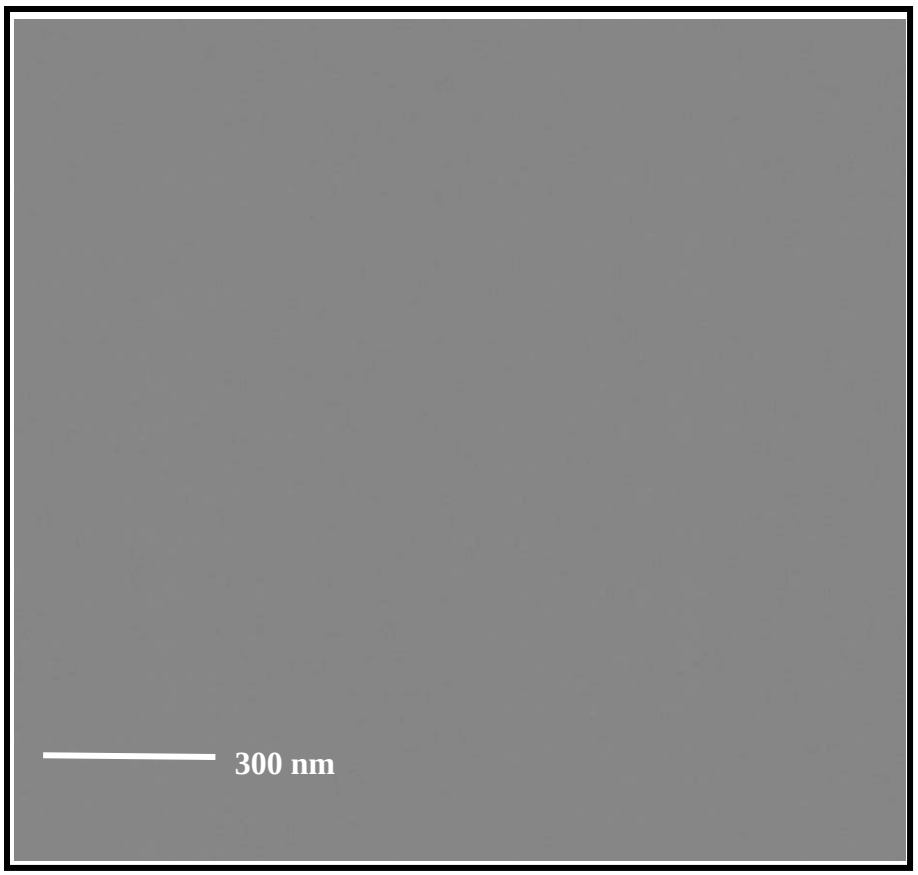

Figure 4.1.4 Typical FESEM image of HDLC film surface recorded at 80,000X

Figure 4.1.4 is a typical featureless secondary electron (SE) image of the HDLC surface. These results (Fig. 4.1.1, 4.1.2, 4.1.3, and 4.1.4) are consistent with an atomically smooth, non-porous continuous film. It may be referred [22] that ultra-nanocrystalline diamond of uniform grain size (3-5 nm) can produce continuous film having surface roughness ~ 7-15 nm only after achieving its thickness greater than 300 nm. Also, hydrogenated carbon films having hexagonal graphite and diamond as coherent domains were reported in earlier works [131]. Therefore our results seem to show that instead of discrete grains, coherent domains of σ bonded sp^3 C-H and π bonded sp^2 C=C carbons, can produce continuous, non-porous thin film having atomically smooth surface at lower thickness (~ 168 nm) of the film. This is a new result to the best of knowledge of author.

4.2 Results and discussion with micro-Raman spectroscopic measurements

Typical Raman spectrum of the as-prepared HDLC film is shown in Figure 4.2.1 over the 50-4000 cm^{-1}. The spectrum shows significant increase of photoluminescence background with the higher wave number along the abscissa due to the disorder carbon (sp^2) structures [132-133]. The single crystal silicon is characterized by a sharp peak at 512 cm^{-1} which is observed in most of our HDLC samples. Raman spectrum of HDLC film shows the Si peak (at 512 cm^{-1}) is downshifted by 8.7 cm^{-1} than that of standard silicon peak (Fig. 3.2.5). This may be attributed due to the stress generated between the Si(100) substrate and the interfacial graphitic layer [89].

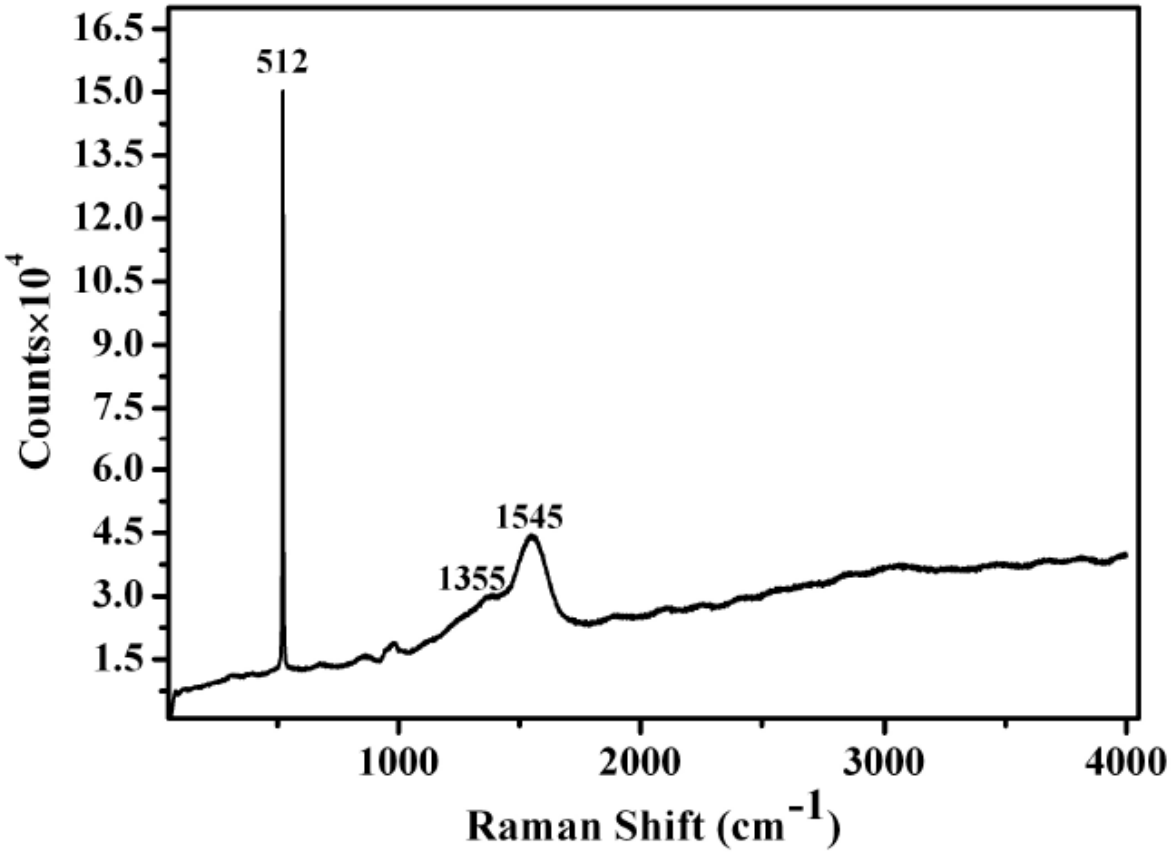

Figure 4.2.1 Typical Raman spectrum of HDLC film over the range 50-4000 cm^{-1}

Moreover, in the Raman spectra of HDLC samples, there is one broad peak at ~ 1000 cm^{-1}, which is due to the second order of silicon. These peaks are the signature of the backing silicon materials upon which the HDLC thin film was deposited.

4.2.1 First- , Second- and Higher-order Raman features

In general, the broad Raman spectra are the characteristics of different types of amorphous carbon thin films. The amorphous carbon can have sp^3 carbon (diamond-like) and sp^2 (graphite-like). In the case of a disordered hydrogenated carbon sample we can expect various effects on the position and broadening of G and D bands etc. [112, 133]. These two modes, namely G-band (sp^2 mode, commonly known as Graphitic band) and D-band (commonly known as disorder allowed zone edge mode of graphite) in the Raman spectrum of graphite are due to the zone center E_{2g} phonon mode at 1580 cm^{-1} and K-point phonons at 1350 cm^{-1}. Therefore first-, second- and higher order Raman spectra of HDLC are explored considering the effect of partial hydrogenation of hexagonal sp^2 (C=C) carbons on the characteristic G and D bands of graphitic materials. Thus as per our expectation, the broad peak envelops corresponding to first- , second- and higher-order Raman features after subtraction of the photoluminescence background are shown below in Figure 4.2.2, 4.2.3, and 4.2.4, respectively.

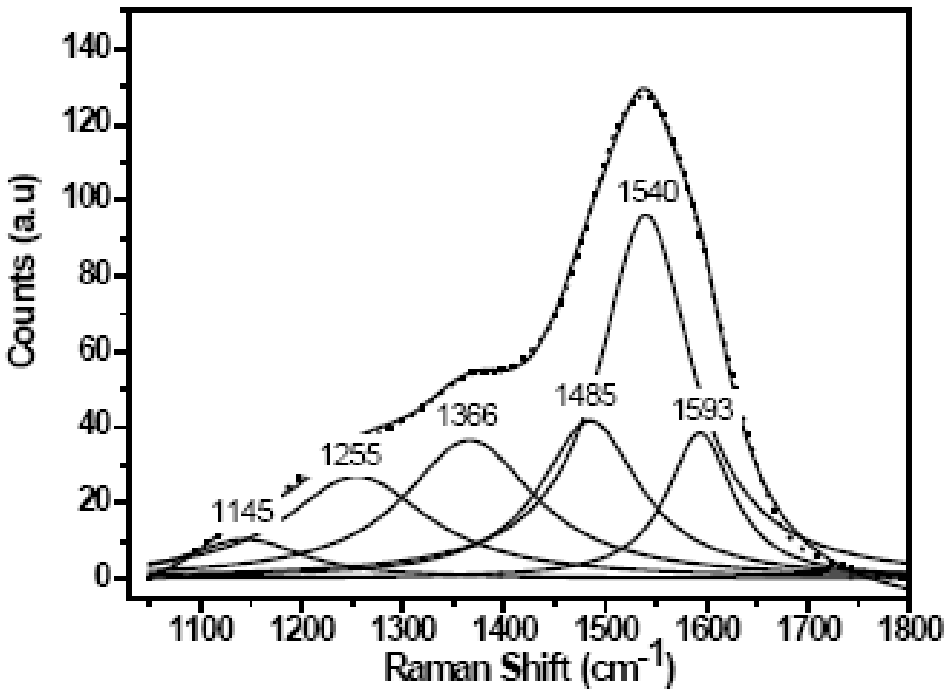

Figure 4.2.2 First-order Raman spectrum of HDLC film over the range 1000-1800 cm^{-1}

We have deconvoluted first order Raman spectrum using six Lorentzian functions (as shown in Fig. 4.2.2) keeping intensities, widths and peak positions as variable fitting parameters. The first order Raman spectra of the as-prepared HDLC film shows typical Raman modes of amorphous carbon having a broad asymmetric peak at ~1540 cm^{-1} (G-band), along with the other peaks at 1366 cm^{-1} (D-band) due to disorder in crystalline graphite, 1255 cm^{-1} (Nano crystalline diamond NCD line) due to hydrogenation of $sp^2C=C$ into sp^3C-H, 1145 cm^{-1} (trans poly acetylene mode) due to C-H wagging modes, 1593 cm^{-1} dumbbell defect in the NCD line. In the first-order Raman spectrum (Fig. 4.2.2) of HDLC, there is red-shifted G band (1540±1 cm^{-1}) to lower frequencies follows a 1/n dependence on the number of sp^2 carbon layers n [134] and is a signature of strained carbon-carbon bonds [135]; the D band (~ 1366±1 cm^{-1}) is a signature of lattice motion away from the center of the Brillouin zone lying between 1270 and 1450 cm^{-1}

depending upon the excitation wavelength and indicating symmetry breaking i.e. disorder induced in the hexagonal sp^2 carbons due to hydrogenation [136]; presence of nanocrystalline diamond (NCD) line (~ 1255 cm^{-1}) having significant downshift ($\Delta\nu$ ~ 77 cm^{-1}) with respect to pure diamond (sp^3 C-C) line (~ 1332 cm^{-1}) signifies the conversion of sp^2 C=C into sp^3 C-H (diamond like) due to hydrogenation and large broadening (full width at half maximum, FWHM ~173±16 cm^{-1}) of the Raman line interpreted as phonon confinement in NCD (sp^3 C-H) domains of less than 1 nm in size [137]; the estimated ratio of G and D band intensities (I_D/I_G) being less than 1 can be interpreted as size of defects should be less than 1 nm in size [133] i.e. if we assume sp^3 C-H domains as defects in the sp^2 C=C carbon matrix, then our above interpretations of broadening of Raman line and ratio of G and D band intensities seem to be plausible. The sum and difference in combinations of C=C chain stretching and C-H wagging modes [ν_1 and ν_3 modes of *trans*-polyacetylene (*trans*-PA)] appear at ~1145±4 cm^{-1} and ~1485±3 cm^{-1} respectively [137]. The dumbbell defect in NCD, called D′ appears at ~1593±1 cm^{-1} [70]. Thus the first-order Raman spectrum (Fig. 4.2.2) signifies effects of (i) strain in carbon-carbon bonds, (ii) multilayer of sp^3 C-H carbons embedded in sp^2 C=C carbon matrix and (iii) disorder induced in the sp^2 C=C carbon matrix by its hydrogenation.

All the above as described in earlier paragraph is “first order” scattering, i.e. the excitation of only one phonon. However, it can be also “second order” scattering, i.e. two phonons can be excited. The second order spectra of single crystals and highly oriented pyrolytic graphite are featureless continuous and exhibit several well defined bands which can enrich the features in the vibration states. For the second order Raman scattering, the sum of the phonon wave vectors must be equal to the wave vector transferred in the light scattering incident, but must be travelling in opposite directions. Second order scattering is usually weak, but can be

enhanced by various things. The second order spectrum broadens significantly with decreasing crystal size.

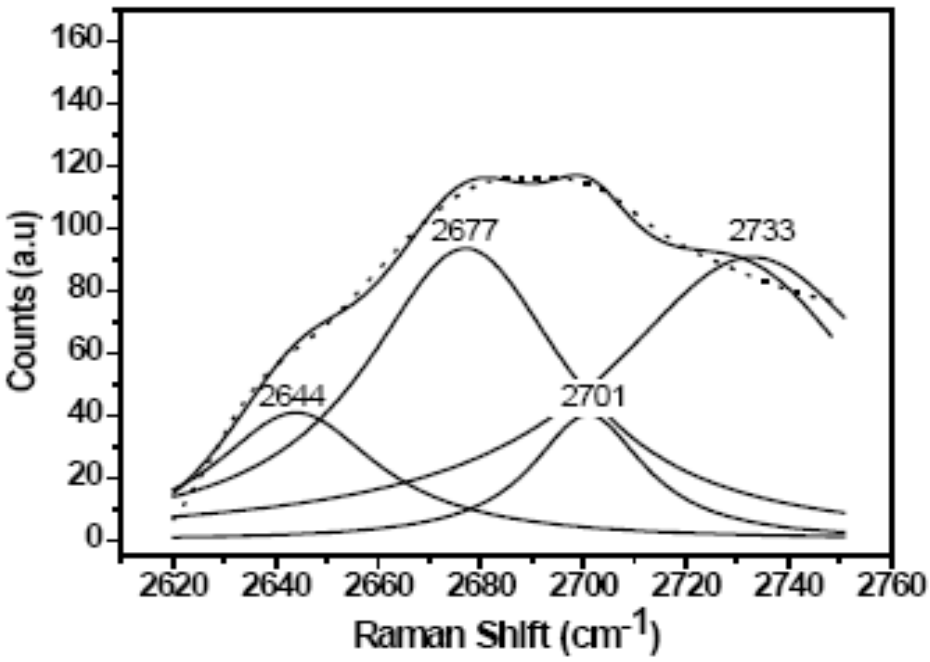

Figure 4.2.3 Second-order Raman spectrum of HDLC film over the range 2600-2750 cm^{-1}

We have deconvoluted second order Raman spectra after subtraction of photoluminescence background similar to the first order Raman spectrum using four Lorentzian functions (as shown in Fig. 4.2.3) keeping intensities, widths and peak positions as variables fitting parameters. The second-order Raman spectrum (Fig. 4.2.3) comprising of four overlapping Lorentzian peaks is a signature of four possible double resonance (DR) Raman scattering processes in the hexagonal sp^2 C=C carbon matrix [136]. The four bands 2701±4 cm^{-1}, 2644±3 cm^{-1}, 2677±2 cm^{-1} and 2733±4 cm^{-1} correspond to that for pristine monolayer of graphite (PMG), red-shifted 2D band due to high and low strain on PMG, and blue shifted 2D band of multilayer of sp^3 C-H carbons embedded in sp^2 C=C carbon matrix respectively [133, 135]. This result on second-order Raman

spectrum (Fig. 4.2.3) indicates double resonance Raman scattering process in the thin HDLC film as predicted for all kinds of sp^2 carbon materials [136].

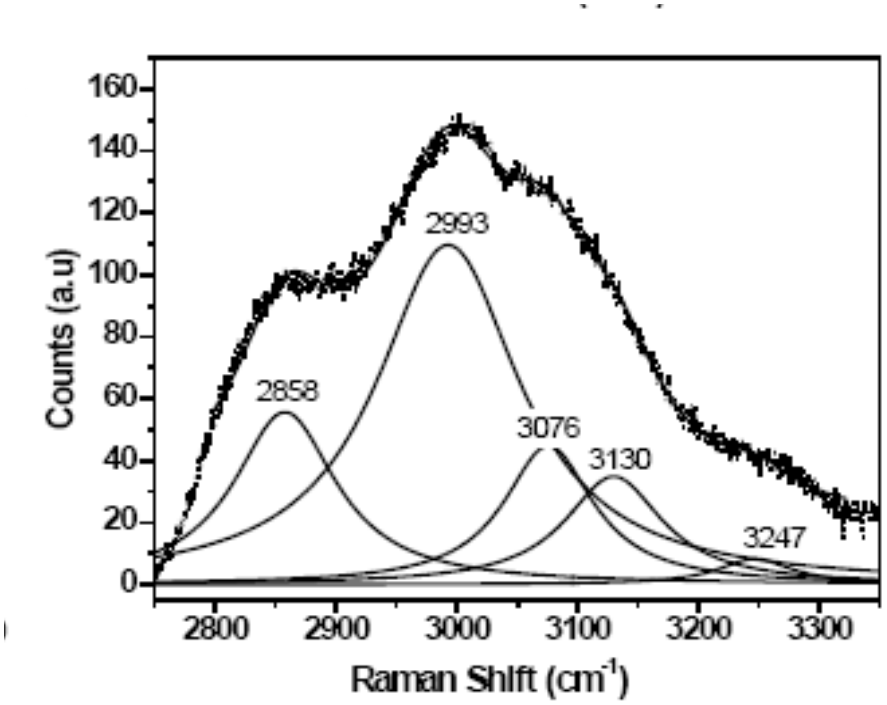

Figure 4.2.4 Higher-order Raman spectrum of HDLC film over the range 2800-3300 cm^{-1}

The higher-order Raman spectrum (Fig. 4.2.4) comprising of five peaks (2858±0.3 cm^{-1}, 2993±0.6 cm^{-1}, 3076±2 cm^{-1}, 3130±3 cm^{-1}, 3247±2 cm^{-1}) is a signature of stretch modes of sp^3 C-H, sp^2 =C-H bands [138], G+D′ band, due to defects induced by the hydrogenation of sp^2 (C=C) carbon matrix [133].

Table 4.2.1 Assignment of vibrational bands for HDLC Raman spectra

Spectral Region (cm^{-1})	Peak Position (cm^{-1})	FWHM (cm^{-1})	Comment/Interpretation (citation)
1030-1800	1145±4	140± 12	Trans-PA (ν_1 mode)

	1255±2	173±16	NC diamond
	1366±1	157±10	D band due to laser wavelength 488nm
	1485±3	119±8	Trans-PA (ν_3 mode)
	1540±1	110±7	Red-shifted G band for 2.8% strain
	1593±1	79±6	Dumbbell defect in NCD: D' band
2600-2750	2644±3	39±6	Red-shifted 2D band for 2% strain
	2677±2	48±7	Red-shifted 2D band for 0.8% strain
	2701±4	27±6	2D band for pristine graphene
	2733±4	69±17	Blue shifted 2D band
2800-3300	2858±0.3	103±2	Hydrogenated sp^3 carbon (graphane like): C-H stretch mode
	2993±0.6	145±2	Hydrogenated sp^3 carbon (graphane like): C-H stretch mode
	3076±2	90±5	sp^2 carbon, =C-H stretch mode
	3130±3	98±8	(G+D') band due to defects introduced into the graphene by hydrogenation
	3247±2	75±10	sp^1 carbon, ≡C-H stretch mode

Thus Raman spectroscopy suggests that our HDLC carbon film is made of multilayer of coherent domains of sp^3 C-H and sp^2 C=C carbons. From the position of G band in the Raman spectrum of HDLC film we can estimate, using an empirical relation sp^3 content = 0.24-

48.9(ω_G–0.1580), approximately 45% sp^3 and 55% sp^2 carbons in the film [61]. Our result is similar to the 40:60 ratio of sp^3/ sp^2 as observed in amorphous hydrogenated carbon films having hexagonal graphite and diamond as coherent domains [131].

4.2.2 Stress computation from Raman spectra

Bagilo et al. [139] exploited Raman spectroscopy and photoluminescence (PL) to examine systematically the sources and nature of stress and also investigated the effect with respect to the type and distribution of defects and impurities in thin diamond films grown on silicon substrates. The types of defects and even the impurities which were detected in the diamond films are the sp^2-type bonding of the graphitic phase and nitrogen, silicon respectively. Furthermore, the stress magnitude exhibits a strong mutual relation with the graphitic phase indicating that the sp^2 bonding creates a dominant compressive stress field. The stress produced during hydrogenation of hexagonal sp^2 carbon matrix deposited onto Si(100) substrate has been studied from the shape and width of Raman lines [140]. Accordingly, stress σ (GPa) within the HDLC film is estimated from the Raman shift $\Delta\nu$ (cm^{-1}) of the NCD line using the relationship given below in equation (4.2.1)

$$\Delta\nu = \nu - \nu_o = -\alpha\sigma \qquad (4.2.1)$$

Where α is pressure coefficient and ν_o is taken to be the Raman peak position (~ 1332 cm^{-1}) of natural diamond when no pressure is applied. The NCD line near ν ~ 1255 cm^{-1} is less than ν_o, indicating a positive tensile film stress. Net stress within a deposited film σ_{net} has been construed to arise from three potential contributions following the simple additivity relationship as given below in equation (4.2.2)

$$\sigma_{net} = \sigma_{TH} + \Sigma\sigma_{IN} + \sigma_{lm} \qquad (4.2.2)$$

Where σ_{TH} is thermal stress (TH), $\Sigma\sigma_{IN}$ is the sum of all internal stresses (IN), and σ_{lm} is stress due to lattice mismatch (lm). Raman spectra of HDLC are consistent with tensile stress, suggesting that σ_{TH} does not dominate σ_{net} and accordingly σ_{TH} can be neglected as a first-order approximation. Furthermore, we observe that the Raman shift associated with lattice stress is only 77 cm^{-1}, to be compared to 200 cm^{-1} anticipated for large lattice mismatches. Thus, it is apparent that σ_{lm} is small compared to σ_{net} and that σ_{lm} could be ignored as a first-order approximation. Collectively, these considerations led to the conclusion that total tensile stress in HDLC film is due primarily to $\Sigma\sigma_{IN.}$ Bagilo et al. [139] states that $\Sigma\sigma_{IN}$ is due to attractive forces across grain-boundaries and that $\Sigma\sigma_{IN}$ can rise to GPa proportions for nanometer-sized crystallites, sufficient to cause grain coalescence. In our case, sp^2 and sp^3 carbons exist coherently in the film as concluded from Raman analysis and thus the internal stress in the film should develop as a result of partial conversion of sp^2 C=C into sp^3 C-H. Indeed, using $\alpha \approx 1.9$ cm^{-1}/GPa and $\Delta\nu \approx 77$ cm^{-1}, we estimate the σ_{net} associated with the NCD line in HDLC to be tens of GPa. It implies that sp^3 C-H domains within HDLC must be nanometer in dimension, consistent with Raman analysis above [140]. Furthermore, FWHM of the 1255 cm^{-1} NCD line (~ 173±16 cm^{-1}) is consistent with phonon confinement in nanometer-sized regions [140]. All evidence taken together led us to conclude that internal tensile stress within HDLC film is caused due to partial hydrogenation of sp^2 C=C carbon matrix, to sp^3 C-H carbons.

4.2.3 Experimental signature of bilayer Graphene like and Graphane like structure in the Hydrogenated Diamond Like Carbon film

The signature of misoriented bilayer graphene like and graphene like structure in the HDLC film is described below, by studying Raman spectra of the as-deposited and annealed (1050 ^{0}C) HDLC films.

The results on the lattice parameters a=2.62 Å and C=6.752 Å of our HDLC film as described above, seem to correspond to hydrogenation of hexagonal structure of carbon atoms, called graphane [141]. Graphene is a crystalline allotrope of one-atom thick carbon with 2-dimensional characteristics. Technically, stability of graphene's is due to a tightly packed, periodic array of carbon atoms and a sp^2 orbital hybridization - a hybridization of orbitals s, p_x and p_y that constitute the σ-bond. The rest p_z electron forms π-bond, which is the key source that permits free-moving electrons. Although, there is strong σ-bonds in a particular layer, the weak bonding between the layers, which facilitates the easy removal of layers. The Raman spectroscopy is especially useful for our case because the Raman spectrum shows characteristic dependence of thickness of graphite film. Moreover, it is possible to identify and compare of single, bi, and multilayers of graphite from the Raman spectra. This possibility arises due to the fact that the evolution of Raman lines is directly related to the electronic structure. As it is known to us, that the most prominent line of graphite is G-band, at ~1580 cm^{-1}, and a very weak D-band at ~ 2700 cm^{-1}. The relative intensity of D-band enhances with the number of layers. Again, the line shape and position sensitive to the number of graphene layers for the 2D-band and is also sensitive to the chemical doping/defects. In bi-layer graphene, there are two inequivalent sub lattices which split into four bands [142-143] due to splitting in electronic bands. The motivation of this work is to explore the distinction between pure multilayered graphene film and HDLC film which is

composed of multilayer of coherent domains of sp^3 C-H (graphane-like) and sp^2 C=C carbons (graphene-like).

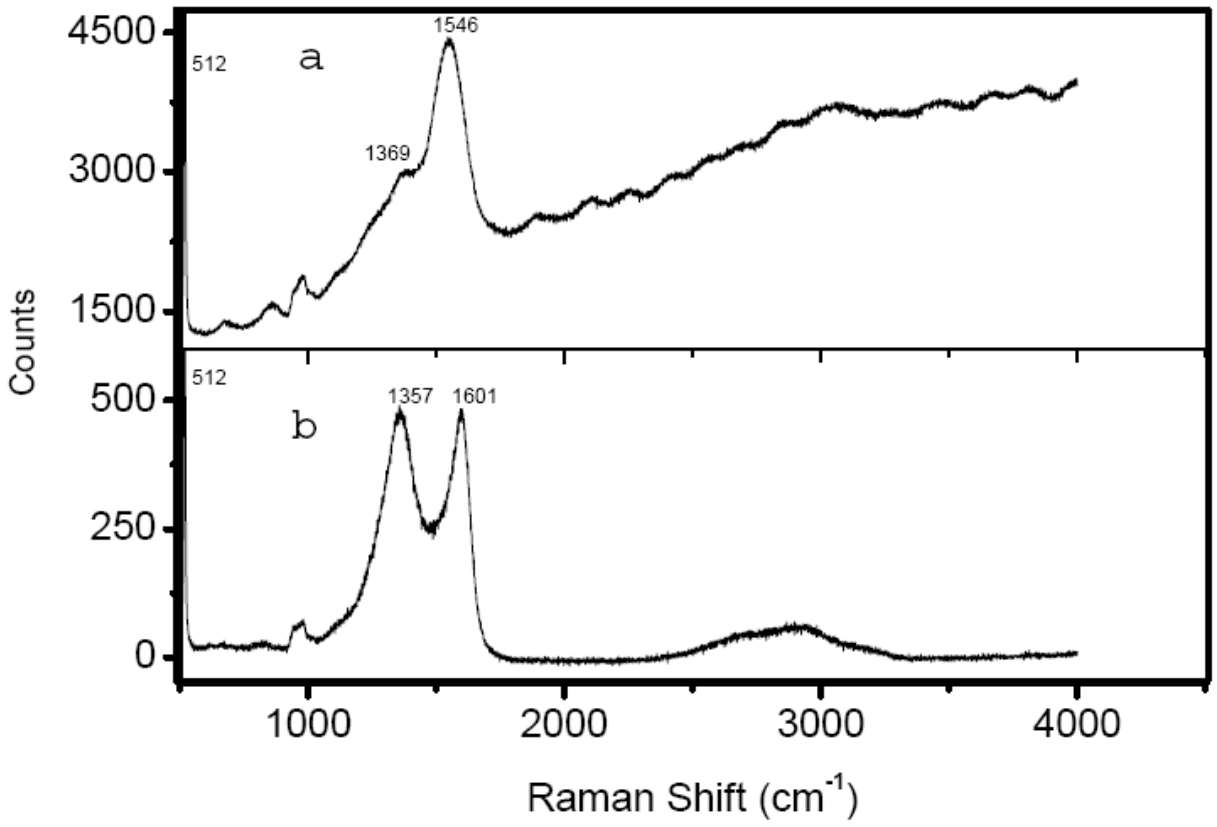

Figure 4.2.5 (a) Raman spectrum of as-prepared HDLC film. (b) Raman spectrum of annealed HDLC film

A typical comparison of Raman spectrum of the (a) as-prepared HDLC film and (b) annealed (at 1050 ^{0}C) HDLC film is shown in Figure 4.2.5 over the 500-4000 cm^{-1}. The significant difference is the presence of photoluminescence (PL) background in the former and the disappearance of PL background in the latter. Moreover, the PL spectrum (Fig. 4.2.5a) superimposes on the Raman spectrum (Fig. 4.2.5b) in the annealed HDLC samples. These observations clearly indicate the significant loss of bonded hydrogen atom from the as prepared

HDLC sample due to annealing effect at temperature 1050 ^{0}C and in high vacuum ~1×10^{-6} torr. It is known [132] showed that PL results from the recommbination of electron-hole pairs within sp^2 bonded clusters in a sp^3 bonded hydrogenated carbon matrix.

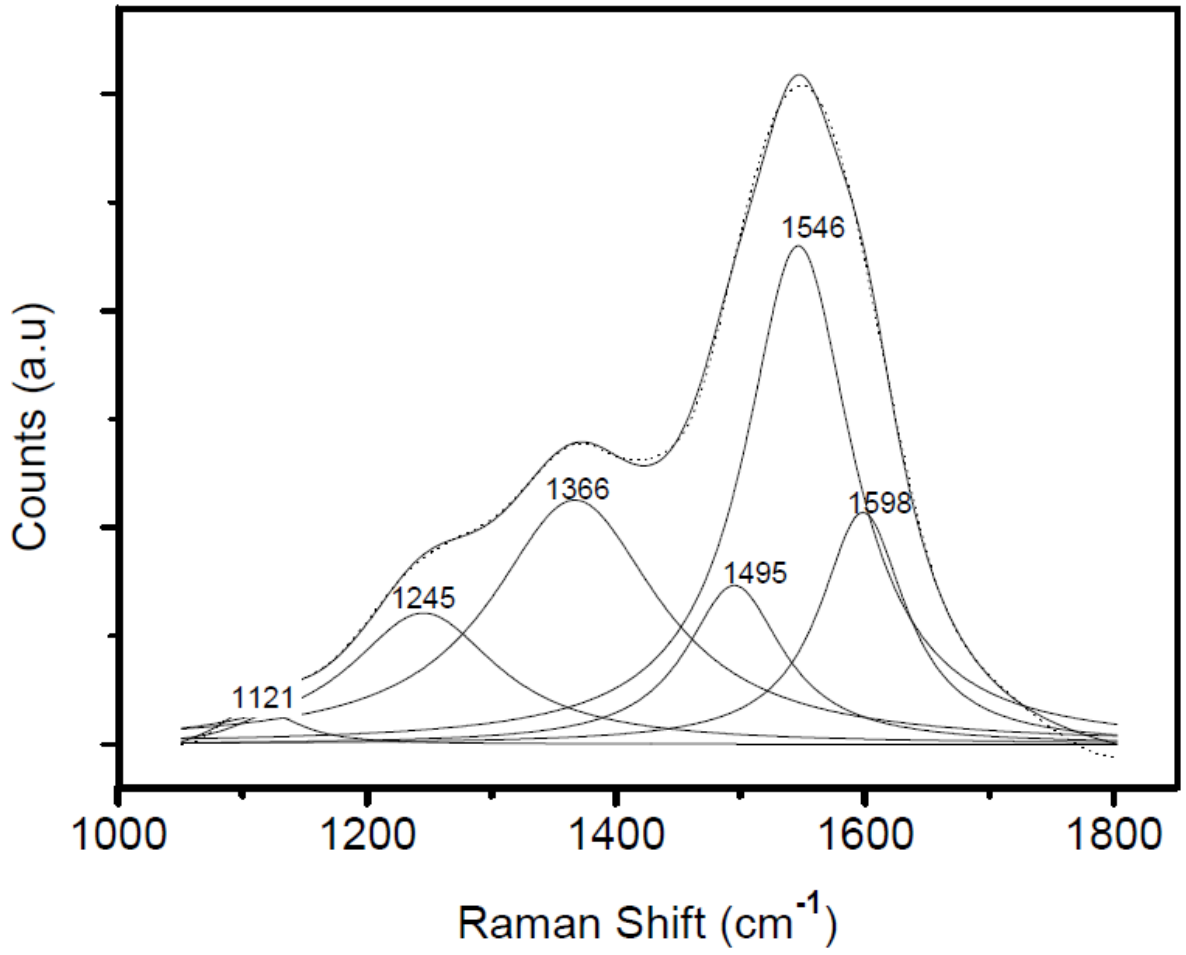

Figure 4.2.6 First-order Raman spectrum of as-prepared HDLC film over the region 1050-1800 cm^{-1}

We have deconvoluted first order Raman spectra after subtraction of photoluminescence background using six Lorentzian functions (as shown above) keeping intensities, widths and peak positions as variables fitting parameters for obtaining best fit results. On deconvolution, the first-order Raman spectrum (Fig. 4.2.6) is comprised of six overlapping Lorentzian peaks;

namely a broad asymmetric peak at 1546 ± 0.6 cm^{-1} known as G-band, a shoulder at 1366 ± 0.5 cm^{-1} known as D-peak, 1245 ± 0.9 cm^{-1} known as nanocrystalline diamond line (NCD line) [70]; features near 1121 ± 1 cm^{-1} and its companion mode 1450 ± 2.4 cm^{-1} appear due to sum and difference in combinations of C=C chain stretching and C-H wagging modes [v_1 and v_3 modes of trans polyacetylene (Trans-PA)] lying in the grain boundary [70]; and the dumbbell defect in NCD, appears at ~1598 ± 1.3 cm^{-1} [61].

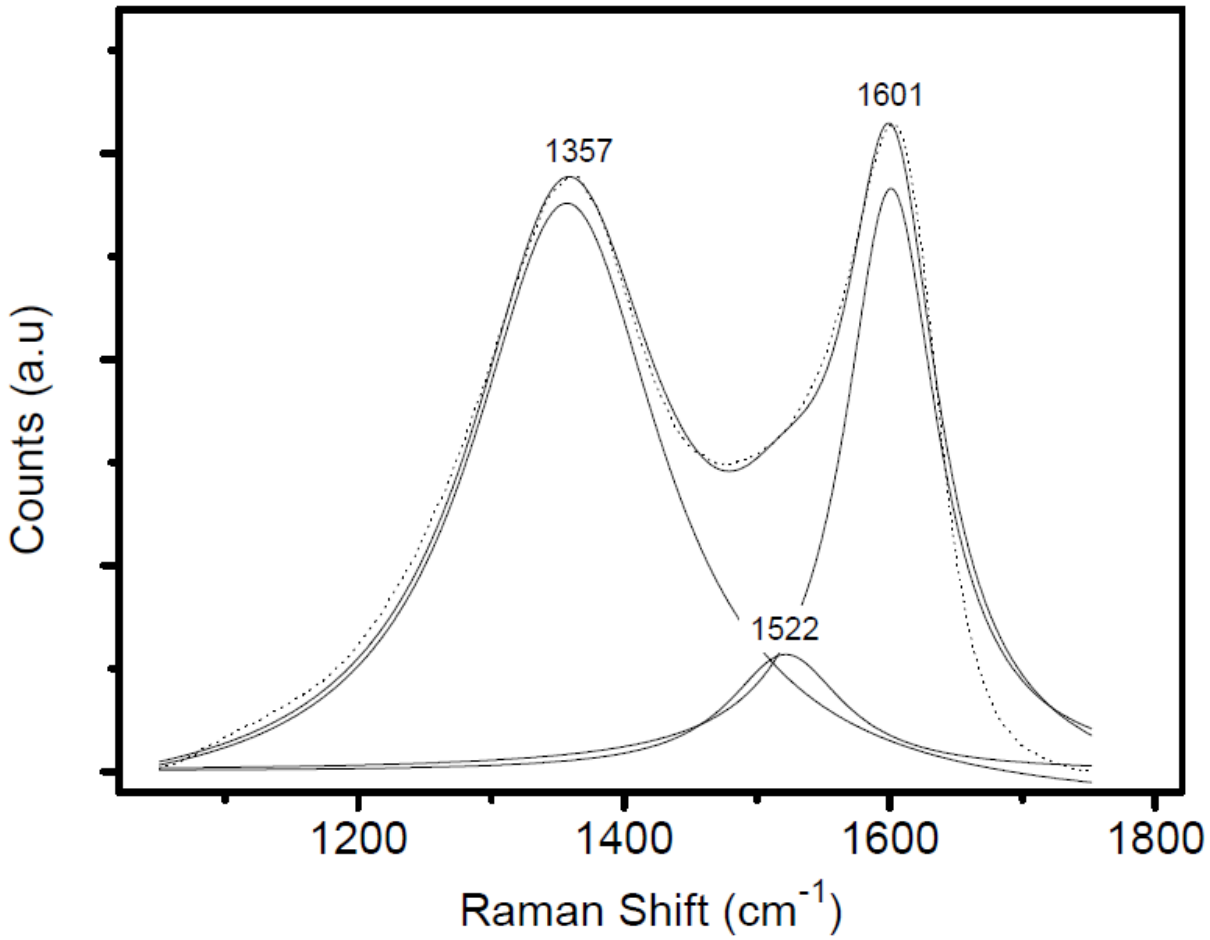

Figure 4.2.7 First-order Raman spectrum of annealed HDLC film over the region 1050-1800 cm^{-1}

The first order Raman spectra of the annealed HDLC film shows typical Raman modes at 1357 ± 0.5 cm^{-1} and 1601 ± 0.5 cm^{-1} which corresponds to the interlayer disorder mode, and characteristic G-band, respectively, in the turbostatic structure of graphitic material [67, 144-145]. These results in Figure 4.2.6 and 4.2.7 signify that the HDLC film, having been found to be a hydrogenated hexagonal crystal structure of carbon atoms, is composed of layers of graphite like crystalline structures which have parallel c-axes and which are connected to one another by disordered regions. In fact, the measured value of interlayer separation [93] $c/2$ ~ 3.376 Å for HDLC is larger than that for crystalline graphite which is 3.354 Å, signifying the existence of interlayer disorder regions in the HDLC sample. The interlayer disorder mode (D-band) and the G-band are active for crystallites of finite size in the nanometer range, and the ratio I_D/I_G inversely varies with their diameter; the D-band and G-band do not depend upon the mutual arrangement of graphite planes [67, 144-145]. Table 4.2.2 provides all parameters, which we have obtained in this analysis during the fittings of various annealed samples.

Table 4.2.2 Comparisons of the fitting data for annealed samples

Sample (Redχ^2, R^2)	**Peak**	**Error**	**Width**	**Error**	**Intensity**	**Error**	**I_D/I_G**
A50-25^{0}C (161, 0.9992)	1121	1.2	69.7	5.4	7495	779	
	1245	0.9	145	3.8	68948	3145	
	1366	**0.54**	**164**	**3.4**	**144929**	**4562**	**0.766**
	1495	2.4	95	5.1	54669	12474	

	1546	**0.66**	**104.6**	**6.46**	**189010**	**26121**	
	1598	1.27	84	4.7	70543	11327	
A50-750^{0}C (164, 0.99916)	1121	1.2	75	5.4	8372	840	
	1240	1.0	146	5.0	56854	3403	
	1368	**0.5**	**179**	**3.4**	**183646**	**5362**	1.067
	1496	2.3	97	5.1	48207	9141	
	1550.5	**0.6**	**97.5**	**4.7**	**172012**	**18692**	
	1597.6	0.8	74	3.2	74170	8756	
A50-1050^{0}C (1388, 0.998)	**1357**	**0.28**	**119.44**	**0.96**	**312646.8**	**3702.183**	1.93
	1601	**0.18**	**61.95**	**0.47**	**162303.6**	**2340.695**	
	1522	0.82	139.8	2.87	298050.2	8344.839	

A comparison between the results in Figure 4.2.6 and 4.2.7 shows the following: (1) The ratio I_D/I_G increases from 0.8 to 2.0 (approximately), indicating a reduction of size of the domain of crystallinity; (2) the intensities of the peaks at 1245 ± 0.9 cm^{-1}, 1121 ± 1.2 cm^{-1}, 1495 ± 2.4 cm^{-1}, and 1598 ±1.3 cm^{-1} in Figure 4.2.6 significantly disappeared in Figure 4.2.7, indicating loss of sp^3 C–H in the HDLC; and (3) the frequency shift ~57 cm^{-1} toward higher wave number is found for the G-band in Figure 4.2.7, indicating a reduction of size of the domain of

crystallinity. It has been observed that sp^2 C = C and sp^3 C–H carbons exist coherently, and the size of the sp^3 C–H domains in the HDLC is reduced due to the annealing effect, by the loss of bonded hydrogen atoms in the hydrogenated hexagonal crystal structure of carbon atoms. Hence, the aforementioned results (1)–(3) seem to be plausible for the annealed HDLC.

Analysis of second order Raman Spectra

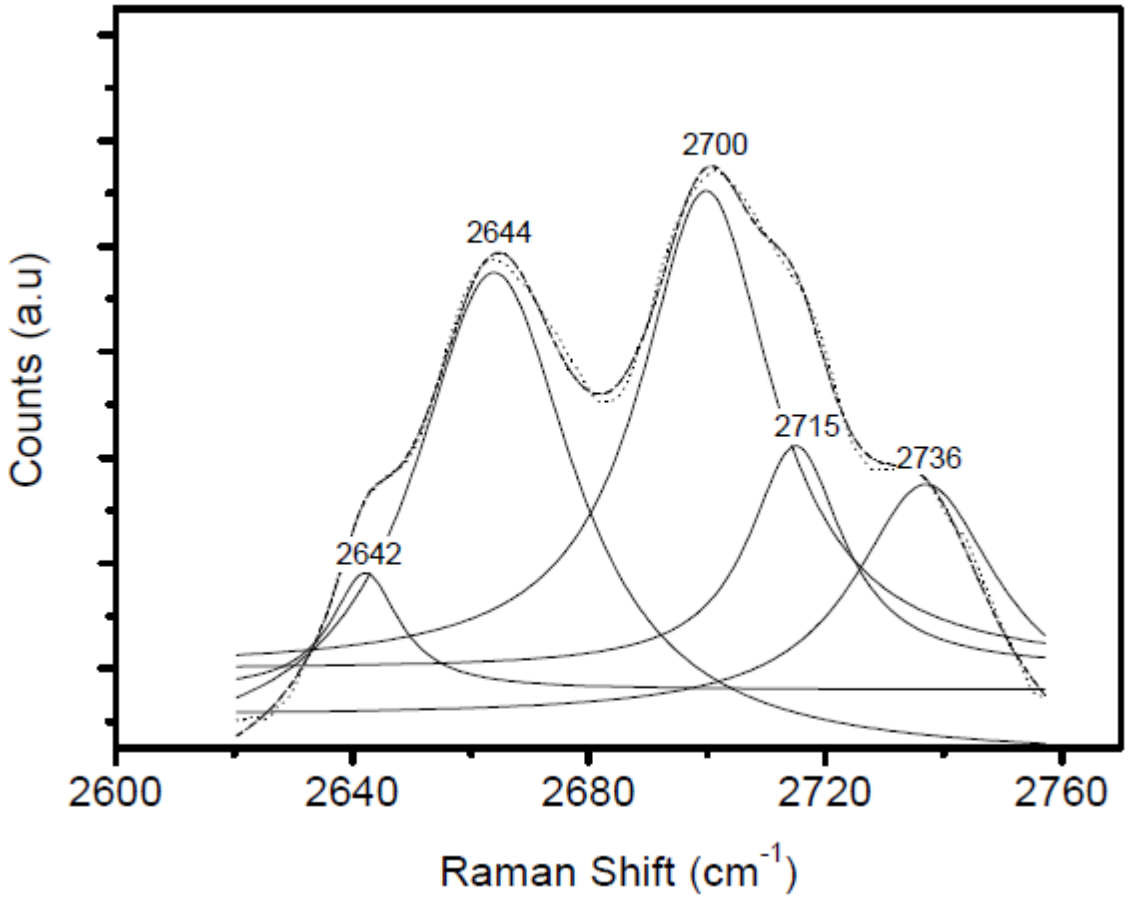

Figure 4.2.8 Second order Raman spectrum of as-prepared HDLC film

The second-order Raman spectrum of the as-prepared HDLC (Fig. 4.2.8), and that of the annealed sample at 1050 ^{0}C (Fig. 4.2.9), shows the presence of G'-band and the second order of the D-band, respectively [112]. The D- and G'-bands originate from a double-resonance Raman process in 2-D graphite [146]. Therefore, the present results, as shown in Figure 4.2.8 and 4.2.9,

signify the HDLC sample, having turbostatic behavior as found from the first-order Raman spectra, to behave as 2-D graphite due to interlayer disorder regions between the layers having been

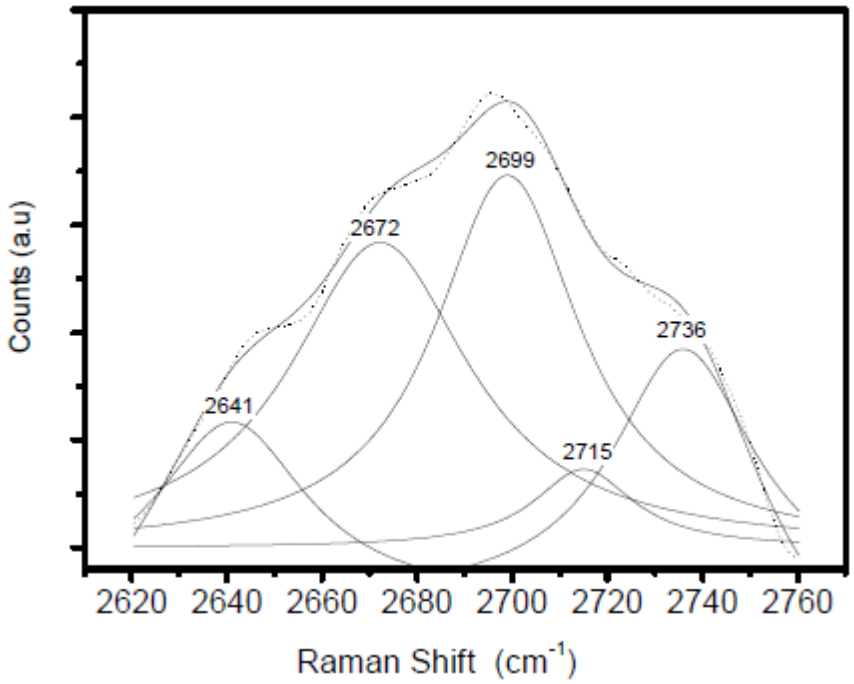

Figure 4.2.9 Second order Raman spectrum of annealed HDLC film

separated by 3.376 Å. Since the G'-band is very sensitive to the stacking order of the graphene layers along the c-axis and identification of the number of layers in the turbostatic graphite is done by the number of peaks in the G'-band [147], we have deconvoluted the G'-band with best fits by Lorentzian peaks. Both Figure 4.2.8 and Figure 4.2.9 show the following: 1) Four Raman modes aside from the peak at ~2700 cm^{-1} correspond to single-layer graphene; 2) full-width at half-maximum for all the five modes lies in the range of 15–40 cm^{-1}; and 3) $I_{G'}/I_G$ « 1. These results correspond to turbostatic multilayer graphene in general. According to the calculation of Latil et al. [148], a Bernal bilayer (AB) and a rotationally disordered graphene (A′) should

simply exhibit the sum of the spectra from a bilayer (i.e. a broadband with four components) plus the unique peak of graphene. Our experimental results, as shown in Figure 4.2.8 and 4.2.9, correspond to that theoretically predicted and experimentally confirmed for misoriented bilayer graphene [149]. Thus, from all evidences taken together from the first- and second-order Raman spectra [Fig. 4.2.8–4.2.9], we can say that the layers of the hexagonal structure of carbon atoms in the HDLC sample stay perfectly parallel but their mutual orientation along the c-axis is random (turbostatic) due to the existence of interlayer disorder; as a result, the 3-D crystallinity of the HDLC should be lost, while only the 2-D crystallinity should be preserved. Therefore, the as-prepared HDLC film can be assumed to have misoriented bilayer graphane like structure, and the annealed HDLC film can be assumed to have misoriented bilayer graphene like and graphane like structure within the coherent structure of the film. The Raman spectra [Fig. 4.2.8–4.2.9] do not tell us about why and how the interlayer disorder region is created in the HDLC film.

4.3. Results and discussion using NRA and RBS

4.3.1 Results of NRA measurements

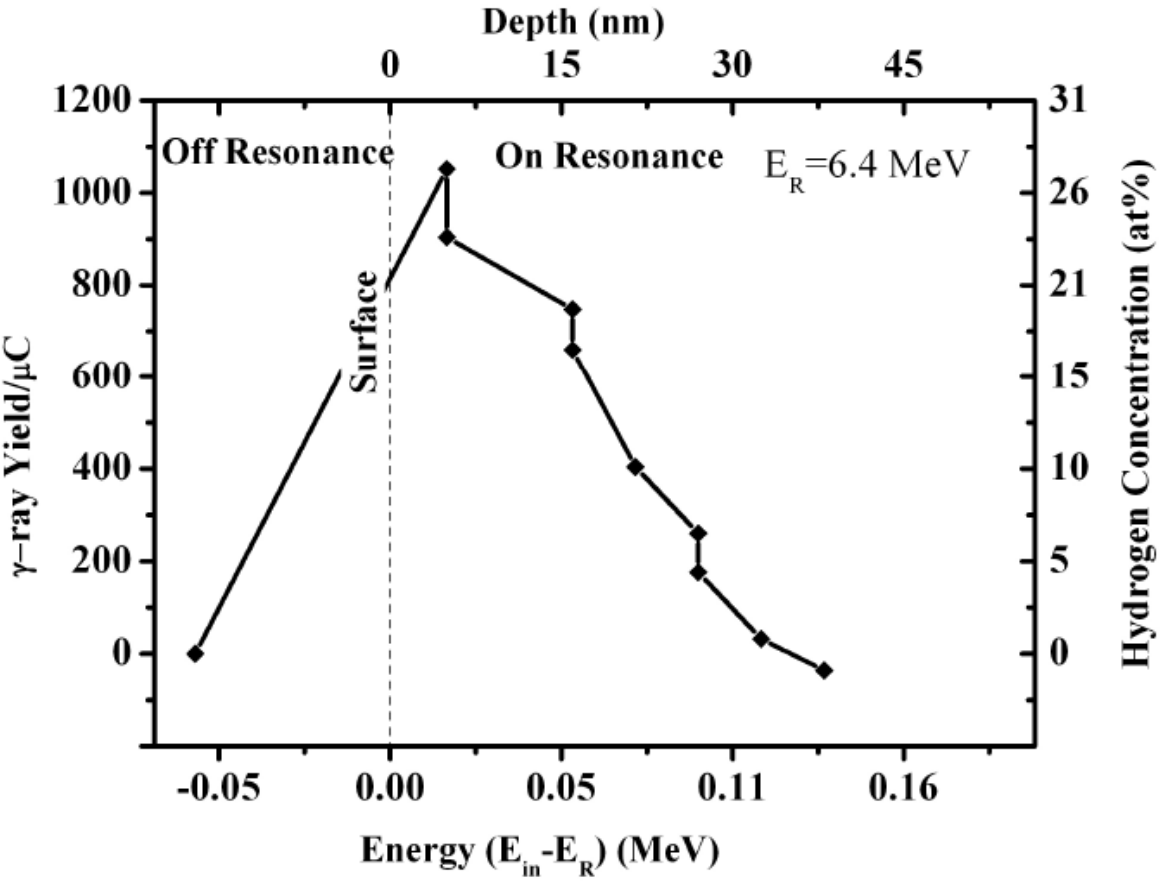

Figure 4.3.1 The typical NRA profile of as-prepared HDLC sample-A is shown. Both raw data of 6.1 MeV prompt γ-ray yields per μC of charge Vs. difference of incident beam energy and resonance energy (6.4 MeV), and corresponding hydrogen concentration (at.%) Vs. depth (nm) into HDLC sample are shown above

Figure 4.3.1 shows typical γ-ray yield (due to nuclear reaction $^{1}H(^{19}F,\alpha\gamma)^{16}O$), as a function of (i) energy difference between energy of incident ^{19}F ion beam (E_{in}) and the resonance energy (E_R) as recorded in a PC-based multichannel analyzer, (ii) hydrogen concentration at different depth of the film, estimated using stopping power value of HDLC. For $E_{in} < E_R$, the γ-ray yield

corresponds to 'background yield' and for $E_{in} = E_R$ the γ-ray yield corresponds to the presence of hydrogen atoms onto the surface of HDLC sample. With the increase of energy of the beam penetrating into the sample, the γ-ray yield starts decreasing from the surface of the target, as evident in Figure 4.3.1. The typical behavior of declining of γ-ray yield at different depth of as-prepared and annealed HDLC sample are observed to be similar. Figure 4.3.1 shows typical γ-ray yield (due to nuclear reaction $^{1}H(^{19}F,\alpha\gamma)^{16}O$), as a function of (i) energy difference between energy of incident ^{19}F ion beam (E_{in}) and the resonance energy (E_R) as recorded in a PC-based multichannel analyzer, (ii) hydrogen concentration at different depth of the film, estimated using stopping power value of HDLC. For $E_{in} < E_R$, the γ-ray yield corresponds to 'background yield' and for $E_{in} = E_R$ the γ-ray yield corresponds to the presence of hydrogen atoms onto the surface of HDLC sample. With the increase of energy of the beam penetrating into the sample, the γ-ray yield starts decreasing from the surface of the target, as evident in Figure 4.3.1. The typical behavior of declining of γ-ray yield at different depth of as-prepared and annealed HDLC sample are observed to be similar.

The as-prepared samples (A to D) when annealed at different temperatures 750 ^{0}C and 1050 ^{0}C in high vacuum, show that the yields, and hence the hydrogen content of the annealed films, in all the cases, are lower than that of the as-prepared samples. A typical result for the as-prepared sample B is shown in Figure 4.3.2. As expected, the hydrogen content should decrease with the increase of the annealing temperature. Therefore, the results in Figure 4.3.2 clearly indicate significant loss of bonded hydrogen atoms from the HDLC sample due to annealing effect. Since the decades, it has been well known that the heating of amorphous hydrogenated carbon above 300 ^{0}C will produce the exo-diffusion of hydrogen molecules through the recombination of small sized hydrogen atoms within the bulk of the materials. Such formation of H_2 molecules is

favorable due to the higher bond energy of H-H than that of the C-H bond. Therefore, annealing leads to the transformation of sp^3C-H sites into sp^2 sites. Consequently, there is the reduction of the photoluminescence background. It is also to be noted from the Figure 4.3.2 that the maximum depth at which the yields of hydrogen content are more or less equal to the background counts (210, 152 and 148 counts/μC for as-prepared and annealed sample at 750 and 1050 ^{0}C respectively) depends upon the annealing temperature; these depths are ~ 83 nm for the

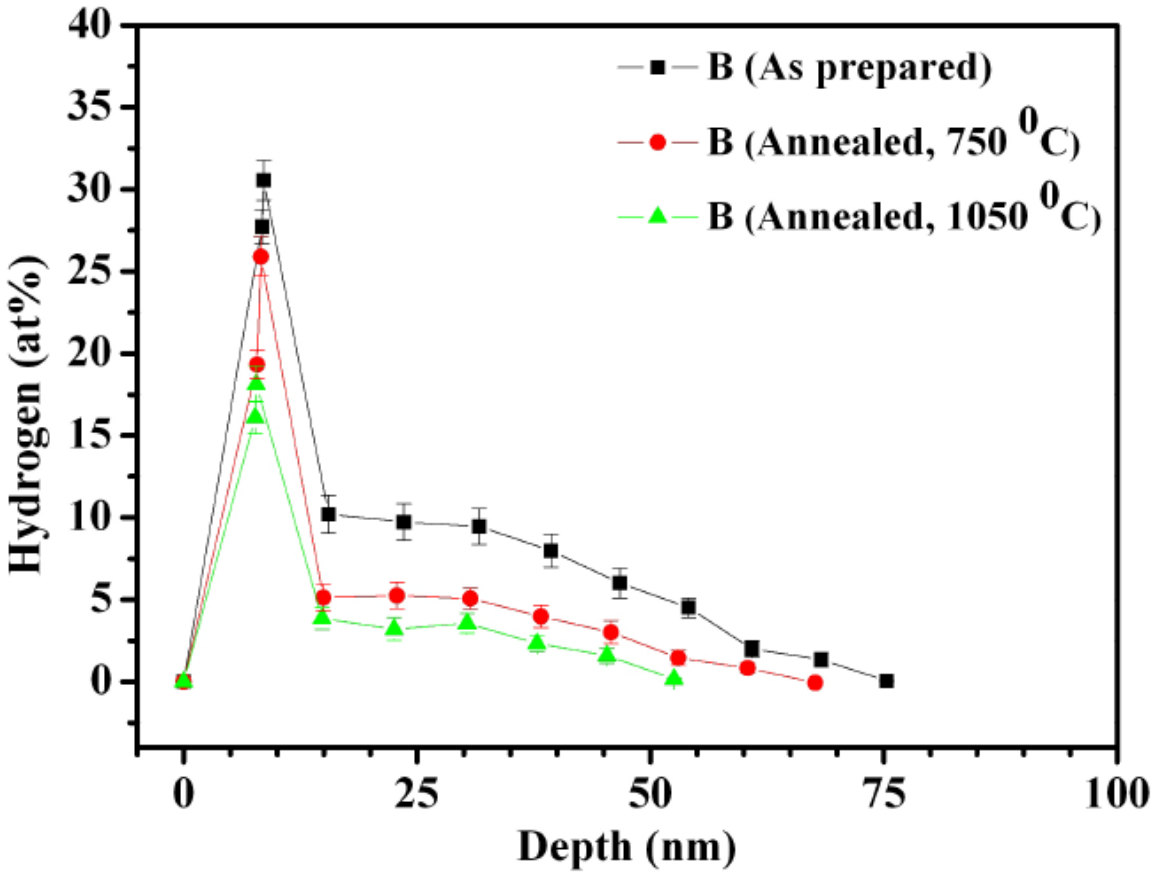

Figure 4.3.2 NRA measurements on HDLC sample-B thin films onto Si backing materials (30 SCCM, both as-prepared and annealed at 750 and 1050 ^{0}C) were carried out with $^{19}F^{3+}$ ion beam at beam current of 3 nA. For each of the above measurements fresh samples were annealed

as-prepared sample, ~ 68 nm for annealing temperature 750 ^{0}C and ~ 59 nm for annealing temperature 1050 ^{0}C. It is well established that the diamond is metastable and graphite is thermodynamically stable, and therefore, diamond and/ nano-crystalline Diamond (NCD) are converted into graphite when heated at elevated temperature ca 1300 ^{0}C [150-152]. Therefore, our results showing decreasing of depth of hydrogen content in the HDLC sample with increasing annealing temperature, may be attributed to conversion of sp^3 C-H (diamond like) to sp^2 C=C (graphite like) structure in the HDLC sample.

The variation of hydrogen content with the depth of the as-prepared samples (A-D) is shown in Figure 4.3.3. The hydrogen concentration is maximum just inside the surface which is approximately within 10 nm from the surface in most of the samples. This result may indicate that the unsaturated bonds of carbon are being terminated by hydrogen, thus leaving almost no unsaturated bonds in the samples at the end of their deposition. From the Figure 4.3.3, it is evident that at a given depth within the sample, the hydrogen content increases with the increase of flow rate of methane at a constant flow rate of hydrogen (500 SCCM) during deposition of samples (A-D). This result is in accordance with our earlier results as reported Singha et al. (2006) [61]. The continuing decrease of the hydrogen with depth of the samples (A-D) indicates that the films having higher graphitic nature towards the interface between the HDLC film and Si(100) substrate. This observation could be explained considering the fact that, in a bias enhanced nucleation of diamond on Si, there is always one intermediate buffer layer of SiC or graphite as shown in a model of diamond/graphite/Si(100) interface [89, 153]. This model provides the minimal lattice mismatch and minimal interfacial energy.

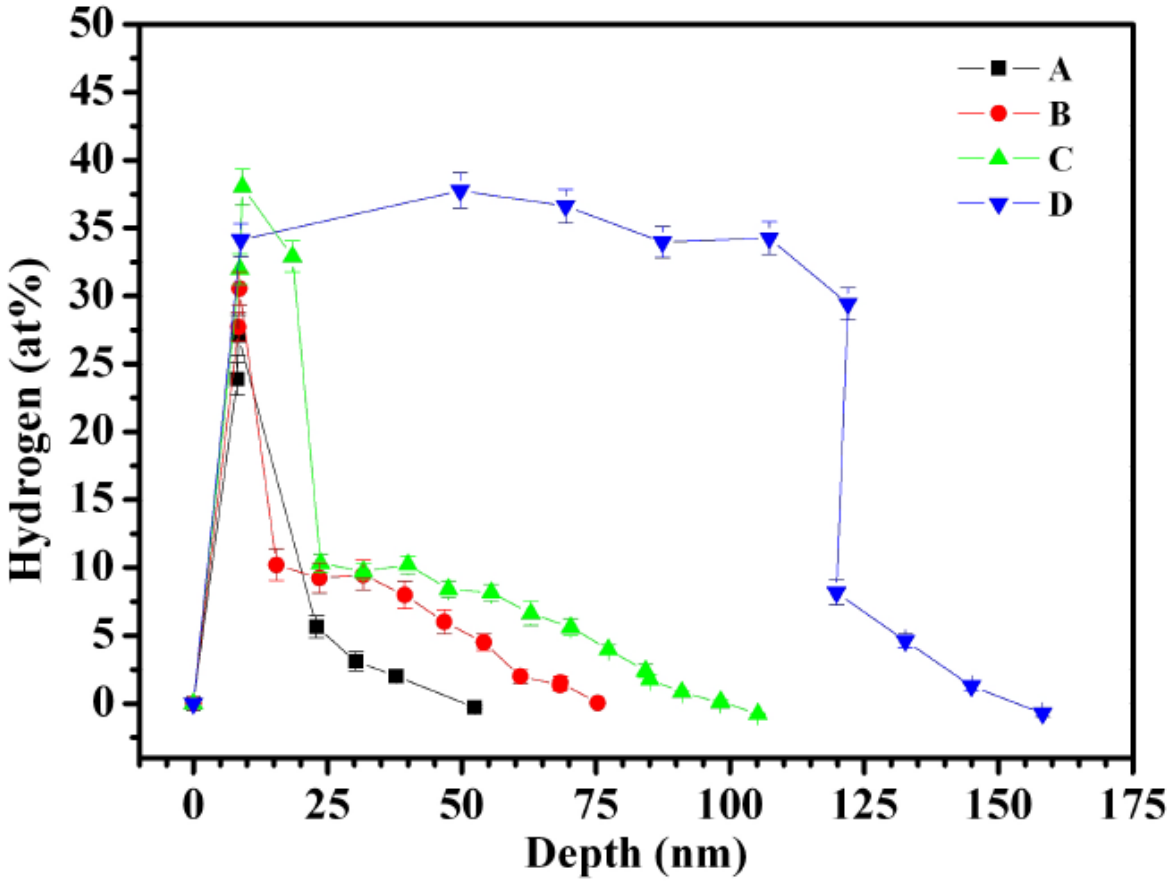

Figure 4.3.3 Hydrogen concentration distribution observed in NRA measurements for as-prepared HDLC samples (A-D) deposited in different flow rate (SCCM-standard cubic centimeter per minute) with $^{19}F^{3+}$ ion beam at beam current of 3 nA

The maximum depth of hydrogen content in the HDLC film depends upon flow rate of methane (Fig. 4.3.3) and for a given as-prepared HDLC film the maximum depth of hydrogen content decreases with increasing annealing temperature (Fig. 4.3.2). Therefore, the direction of flow out of hydrogen during annealing of HDLC sample is from the interface towards the surface. E. Vainonen-Ahlgren et al. (1997) [56] and Thomas et al. [154] have studied the migration of hydrogen in DLC films by NRA, RBS, and SIMS techniques and found migration of hydrogen towards the interface between the film and substrate and also release of hydrogen from the

surface region. On contrary to this observation, the migration of hydrogen towards surface from the interface in our HDLC sample seems to be plausible due to the fact that during the annealing process, the heat is transferred from the sample holder to the backing silicon material and then into the sample; hence, the interface of the sample and the Si is at higher temperature than the surface of the HDLC samples. Therefore, there might be a possible chance of little rearrangement of hydrogen bonds through the process of dehydrogenation and hydrogenation [155] within the sample. In some hydrogenous carbon materials loss of hydrogen under ion irradiation is reported earlier [156-157]. Due care, therefore, is to be taken while carried out the hydrogen determination. In such cases, the concentration of hydrogen should be measured as a function of ion dose and the initial hydrogen content can be obtained by extrapolation to the zero dose condition. This result is shown in Figure 4.3.4. The yields at zero dose condition are also shown along the dotted line for the as-prepared and annealed samples. These values were obtained from the polynomial fitting of the γ-ray yields vs. charge density. The stability of the standard samples under ion beam irradiation has already been studied [119]. This can be minimized by using the lower mass of the projectiles, which don't transfer large electronic energy as excitation energy in the sample. Nearly constant integrated counts (as shown in Fig. 4.3.4) for every 250 nC charge, were observed for the standards (Si_3N_4) for total 20 number of times exposure at primary beam energy of ~ 6.5 MeV. In contrary, the counts were slowly decreased for annealed samples and rapidly for the as-prepared samples as shown in Figure 4.3.4. This could be explained if we assume that the hydrogen is present in the film as bonded by chemical forces and also as non-bonded due to physical forces or weak Vander Wall forces. Therefore, the weakly bonded hydrogen readily desorbs from the thin films on heating. This desorption is maximum for the as-prepared films compared to annealed films.

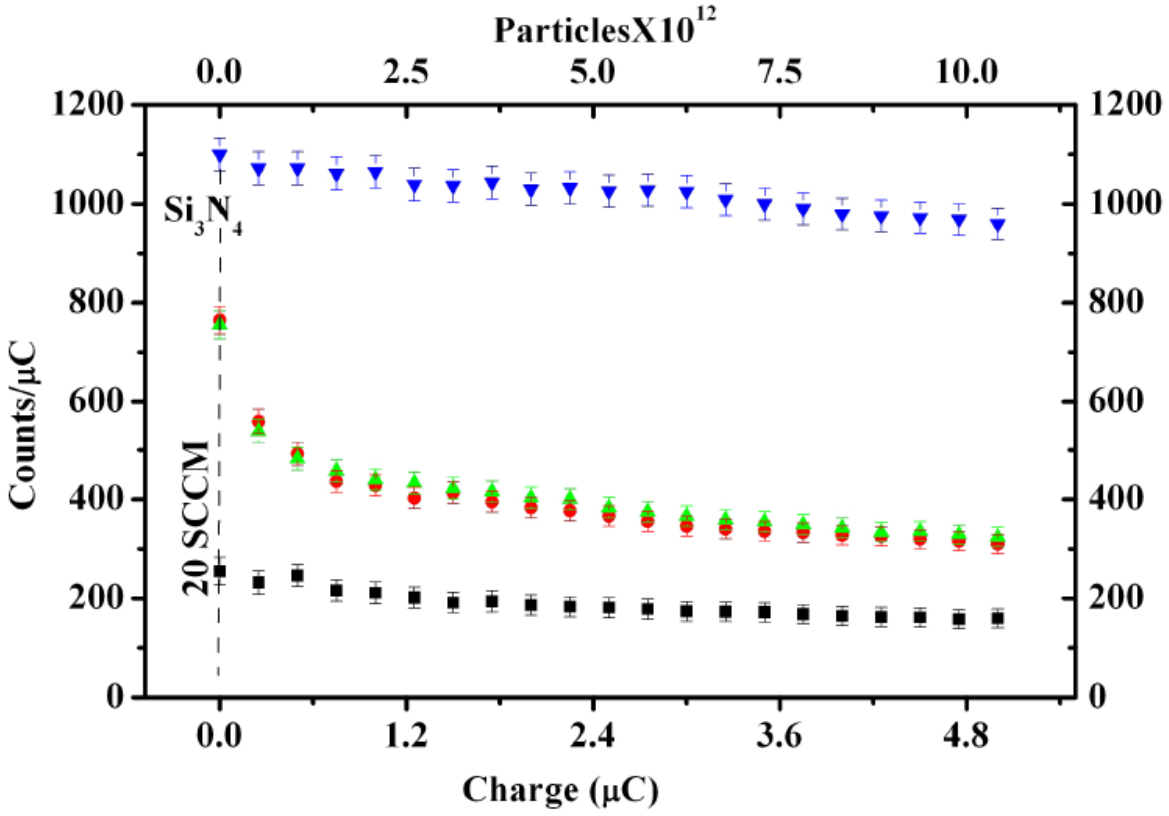

Figure 4.3.4 The γ-ray counts/μC vs. charge (μC) (Bottom) or fluence of $^{19}F^{3+}$ ion beam (Top) during hydrogen depth profiling for as-prepared (at two different regions of 5 mm apart) and annealed at 750 ^{0}C of HDLC samples-A at beam current of 3 nA and also Si_3N_4 standard at beam current of 3 nA observed in NRA technique

4.3.2 Results of RBS measurements

The backscattered spectra for as-prepared samples are recorded using 1.0 MeV proton beam and are shown in Figure 4.3.5. The higher channel number (i.e. higher energy) side of the RBS spectrum is due to the backing silicon materials (thickness ~0.5 mm). The Si-edge of sample A was different compared to sample B. There are two factors responsible, one is channeling and other is cross section which is even more non-Rutherford in this energy range. Again the cross section varies sharply at the Si-edge. The sharp peak is observed over the broad plateau of silicon

is due to the carbon. It is clear from the inset picture where there is no peak for the virgin silicon sample but sharp peaks for carbon onto silicon. The sharp peaks of carbon in the inset of Figure 4.3.5, show increase of peak area from 417±24 to 774±34 to 1936±65 counts/μC, and FWHM from 10.7±0.5 to 11.2±0.7 to 14.71±0.8 keV with the increase of flow rates of methane in the as-prepared samples viz., A, B, D respectively. Therefore, the thickness of the film increases with flow rates of methane.

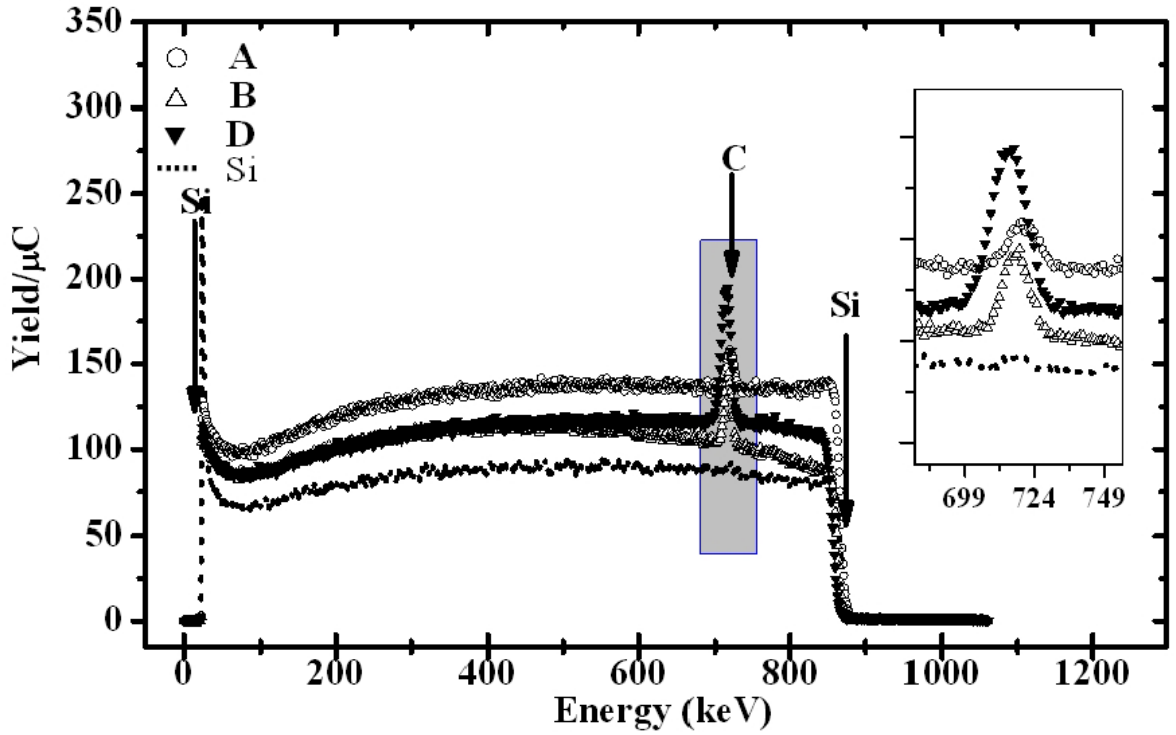

Figure 4.3.5 RBS measurements on as-prepared HDLC thin films onto Si backing materials prepared at different flow of methane were carried out with 1.0 MeV proton beam. The backscattered particles were detected by a silicon surface barrier (SSB) detector at an angle of 170^0

The RBS spectra for the as-prepared and annealed HDLC samples are measured. The FWHM for samples B (30 SCCM) both as-prepared and annealed at 750 and 1050 ^{0}C were 11.2±0.7,

11.1±0.5, 10.4±0.5 keV at 722±3 keV and the integrated area under the peaks are 813±46, 774±34, 670±27 counts/μC respectively. These values were obtained using Lorentzian fittings. It is observed that the as-prepared films have higher peak yields and higher FWHM compared to that of annealed one as shown in Figure 4.3.6. This result indicates thickness of as-prepared samples is larger than that for annealed one.

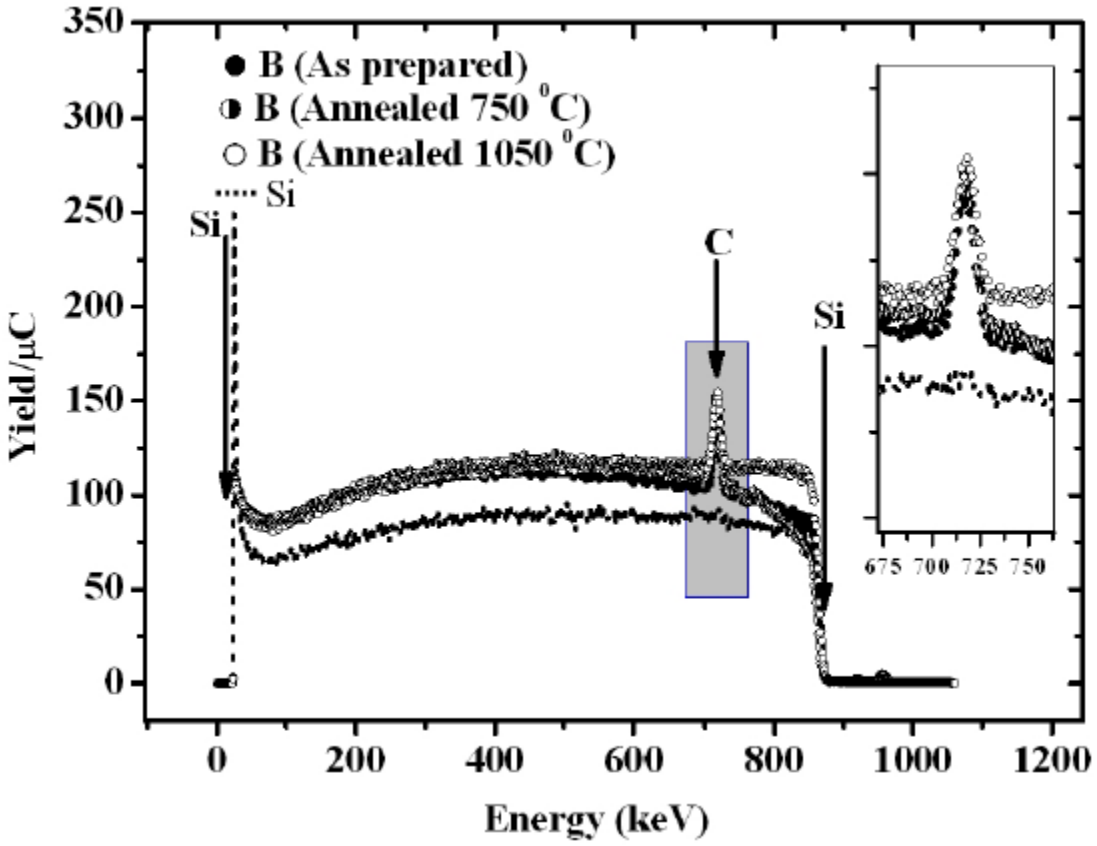

Figure 4.3.6 RBS measurements on HDLC thin films B onto Si backing materials (30 SCCM, both as-prepared and annealed at 750 and 1050 ^{0}C) were carried out with 1.0 MeV proton beam from Tandetron accelerator. The backscattered particles were detected by a silicon surface barrier (SSB) detector at an angle of 170^0. For each of the above measurements fresh samples were annealed

Kazunori et al. (1999) [158] and Wang et al. (1997) [159] have studied the erosion behavior of deuterated soft amorphous carbon thin film by heat treatment in air and vacuum, using elastic recoil detection (ERD) and proton enhanced scattering (PES) techniques. When the films are heated in air above 550K for 1 h, the film thickness, and the areal densities of carbon and deuterium both decrease. Moreover oxygen is incorporated into the films. Nevertheless, when annealed in vacuum, erosion starts at above 600K and decrease in thickness along with the decrease of all other components. Thermal desorption spectroscopy of the soft films reveals the evolution of hydrocarbon. They have also studied the thermal erosion behavior of hard a-C:H thin films under vacuum. This showed predominantly the release of hydrogen molecule to give semi-hard a-C:H films with very low hydrogen content. This implies that the soft films sublimate and hard film desorbs in vacuum during annealing. We have also observed the similar desorption and decrease in at% of hydrogen and that in thickness for HDLC thin film, when treated under vacuum at high temperature. The diagnosis by NRA measures the content of hydrogen whereas RBS techniques measures content of carbon. Therefore, the decrease of HDLC film thickness due to annealing (Fig. 4.3.6) should be caused by removal of carbon and hydrogen both.

Estimation of hydrogen content and thickness of HDLC sample

The atomic fraction of Hydrogen in the as-prepared HDLC film is estimated using equation (3.5.1.1) based upon NRA measurements. The results are given in Table 4.3.1.

The thickness of the as-prepared HDLC film along with their uncertainties is measured by NRA using equation (3.5.1.2) and by RBS using equation (3.5.2.1). These results are given in Table 4.3.2. The experimental detection limit of the sample has been estimated on the basis of three times standard deviation value (3s) of background counts in the region of a peak of the γ-ray spectrum of samples as per our experimental parameters and the value is ~ 3.0 at%.

Table 4.3.1 Atomic fraction of hydrogen in the HDLC films (A-D) as a function of flow rate of methane

Sample	Flow rate of methane (SCCM)	Hydrogen content At.%
A	20	30.1±3.2
B	30	30.5±3.4
C	40	32.9±3.5
D	70	34.1±3.9

Table 4.3.2 Comparison of depth of hydrogen by NRA and thickness of the as-prepared films (A-D) by RBS technique

Sample	Flow rate of CH_4 (SCCM)	Depth of hydrogen in the film by NRA (nm)	Thickness of the film by RBS (nm)
A	20	52±10	124±15
B	30	83±10	130±16
C	40	98±12	134±17
D	70	158±17	144±20

The overall error in the NRA and RBS measurement have been estimated by error propagation formula from the errors in counting statics of the gamma ray yields, stopping power, resonance width and fitting errors and it lies within 10-20%. Thickness of HDLC film by NRA is based upon maximum depth of hydrogen availability whereas that by RBS is based upon maximum depth of carbon availability in the film. Since toward interface between substrate and HDLC film, graphitic (sp^2 C=C) character is predominant than diamond (sp^3 C-H) character, it is obvious that the observed thickness by NRA smaller than that by RBS (Table 4.3.2) is reasonable.

Table 4.3.3 Effect of annealing on the thickness of the HDLC thin films

Sample	Flow rate of CH_4 (SCCM)	Depth of hydrogen in the film by NRA (nm)		
		RT (^{0}C)	750 (^{0}C)	1050 (^{0}C)
A	20	52±10	48±6	36±7
B	30	83±10	68±9	59±9
C	40	98±12	82±12	73±12
D	70	158±17	150±16	145±16

The structure of the modified films due to the annealing effect making a denser networking structure remained almost same even after further annealing at elevated temperatures. The

minute change in the thickness is due to removal of hydrogen (Table 4.3.3). Hence there are not significant different of thickness of the films when annealed at 750 and 1050 ^{0}C.

Investigation of as-prepared and annealed HDLC samples by ion beam analysis (IBA) techniques, comprised of NRA and RBS measurements, reveals the following : the hydrogen content decreases with the depth of the film i.e. there is predominant character of graphitic layer towards the interface between the substrate Si(100) and HDLC film.; this result matches with the BEN model [89] of diamond/graphite/Si(100) interface which minimizes the lattice mismatch and interfacial energy. Therefore our HDLC film may be considered a graphene/graphitic structure, sandwiched between the top diamond like structure (hydrogenated graphene: sp^3C–H) and silicon substrate. Hydrogenated graphenes (also called graphane) are expected to have a tunable band gap via the extent of hydrogenation [160].

4.4 Results and discussion with STM measurements

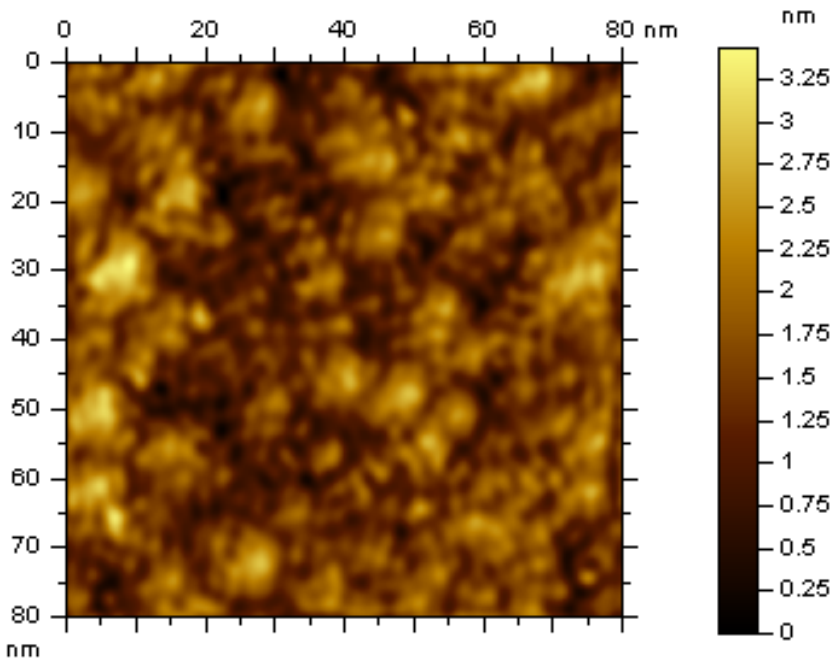

Figure 4.4.1 STM image of annealed HDLC film

It is observed that measurement of constant-current STM image of as-prepared sample is not possible but that of annealed one is possible as shown in Figure 4.4.1. These results support that as-prepared HDLC film is resistive but the annealed one is conductive at different places of it. Therefore we proposed the schematic structures of as-prepared sample and annealed one, described in Figure 4.4.2 (a&b). Figure 4.4.2a shows only the presence of σ bonded electrons, giving resistive nature of the as-prepared HDLC film whereas; Figure 4.4.2b shows primarily the presence of π bonded electrons, giving conductive nature of the annealed HDLC film at different places of it. The observed bright spots in Figure 4.4.1 seem to correspond the simulated constant-current STM image of the unoccupied states in the honeycomb lattice of the A' face of ABA' system [148]. Occupied states in the honeycomb lattice in the form of dark spots are also seen in

Figure 4.4.1. Bright spots are interconnected by dark spots indicating *the HDLC film comprising of coherent domains of sp^2 and sp^3 carbons.*

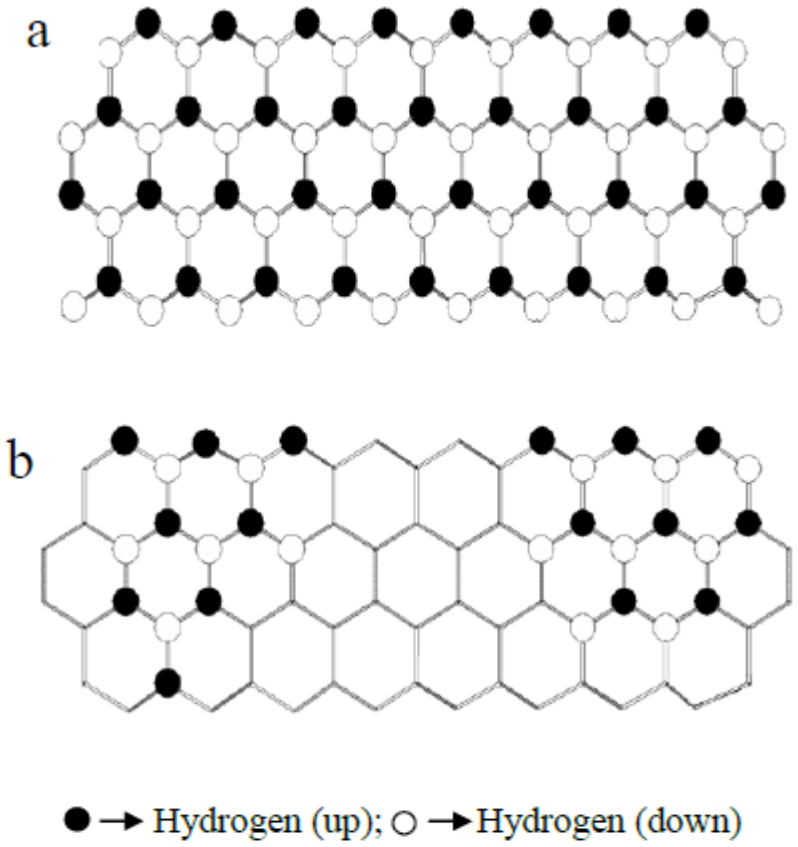

Figure 4.4.2 (a) Hydrogenated graphene layer, (b) partially removed hydrogen from the hydrogenated graphene layer

4.5 Results and discussion using I-V characteristics measurements

The typical I vs. V characteristic on the as-prepared HDLC surface (Fig. 4.5.1) shows step-like structures of non-uniform gaps. This result seems to describe the characteristic electron transport behavior in the HDLC surface, wherein conducting islands of sp^2C=C sites, (bright spots in Fig. 4.4.1) of different sizes in nm range are interconnected by the non-conducting sp^3 C-H sites (black spots in Fig. 4.4.1).

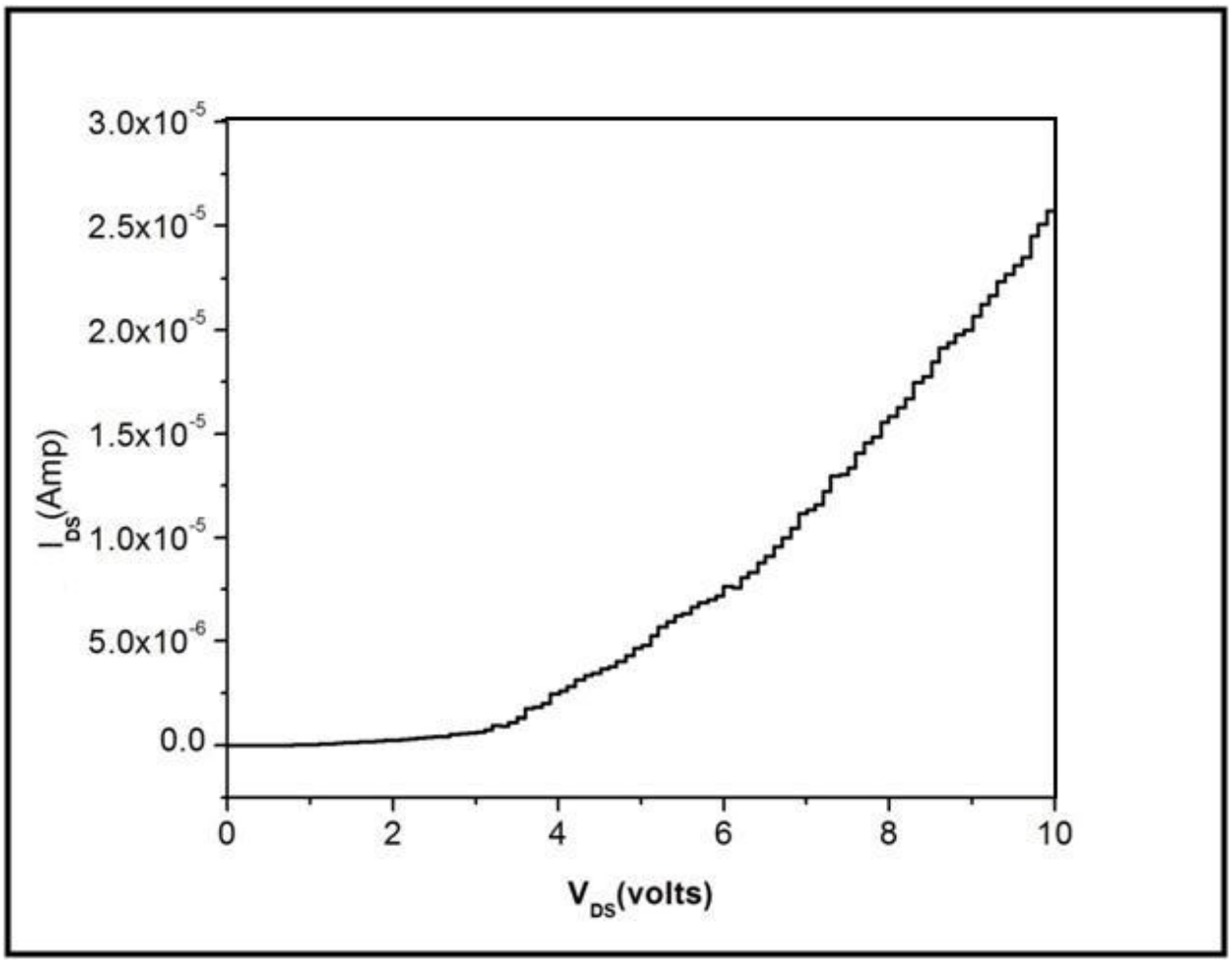

Figure 4.5.1 Multiple step current (I_{DS}) vs. voltage (V_{DS}) characteristic of the as-prepared HDLC sample on Si(100) substrate at 300 K

The step-like I-V characteristics were observed in diamond like carbon films [161] and it was suggested that the transport mechanism is tunneling between conducting nanoparticles ($sp^2C=C$ carbons) embedded in the insulating matrix of sp^3 carbons in the films [62] and thus the observation of step-like structures is a manifestation of Coulomb blockades [162] in these films. Our result (Fig. 4.5.1) and the earlier works [161] show the typical general form of the solid state structure in the form of *metal-barrier-particles-barrier-metal* , as required for observing coulomb blockade effect resulting in step-like structure in the I-V characteristics [163]. The

'Coulomb blockade' is evidenced in our experimental result (Fig. 4.5.1) from the observation of 'increment of current (ΔI)' due to 'break down of Coulomb blockade' and thus producing 'step-like' structure in the 'I-V characteristic'. Whether the charging of the conducting 'particle' i.e. 'sp^2 carbon' is due to 'single electron' in our result (Fig. 4.5.1) can be confirmed by estimating 'q' using the simple formula q/C = V, where C = 8 ε_r ε_0 r, if we assume the 'particles' to be spherical capacitors of radii r, embedded in 'insulating sp^3 carbon matrix' having dielectric constant ε_r and V is the required voltage for ΔI. There are sp^2 carbons of different sizes (Fig. 4 .4.1) in the range of few nm. The measured value of dielectric constant of HDLC film, for frequency less than 1 Hz, is typically $\varepsilon_r = 3\pm1$. The estimated value of C, for r = 1 to 10 nm, is ~ 10^{-18} F and typical measured value of ΔV required for current increment ΔI, is 425± 25 mV. Thus the estimated order of magnitude value of q is ~ 10^{-19} C, single electron's charge. Thus it is reasonable to belief that the result in Fig. 4.5.1 is a manifestation of Coulomb blockades in our HDLC films at room temperature (300 K).

4.6 Results and discussion with the optical photograph of HDLC surface

The typical image of the reflected light under the exposure of white light source onto the HDLC surface (Fig. 4.6.1) taken by Olympus digital camera, shows multiple colors from different points over the surface. This result seems to describe the characteristic behavior of confined conducting electrons in islands of sp^2C=C sites, (bright spots in Fig. 4.4.1) of different sizes in nm range, interconnected by the non-conducting sp^3 C-H sites (black spots in Fig. 4.4.1); here we may think of collective excitation of the conducting electrons in the nanostructured sp^2C=C sites of different sizes due to exposure of different wavelengths in white light, may result in emission of multiple colors. Such type of optical property was observed in noble metallic nanostructured particles, called 'particle plasmons' [164]. According to semi-classical model, collective

excitation of conducting electrons in noble metal nanoparticles, called particle Plasmon, occurs when the diameter of a nanoparticle is on the order of penetration depth of electromagnetic (EM) wave in the conducting material; the electric field of the interacting EM wave shifts the conduction electrons collectively with respect to the fixed positive charge of the

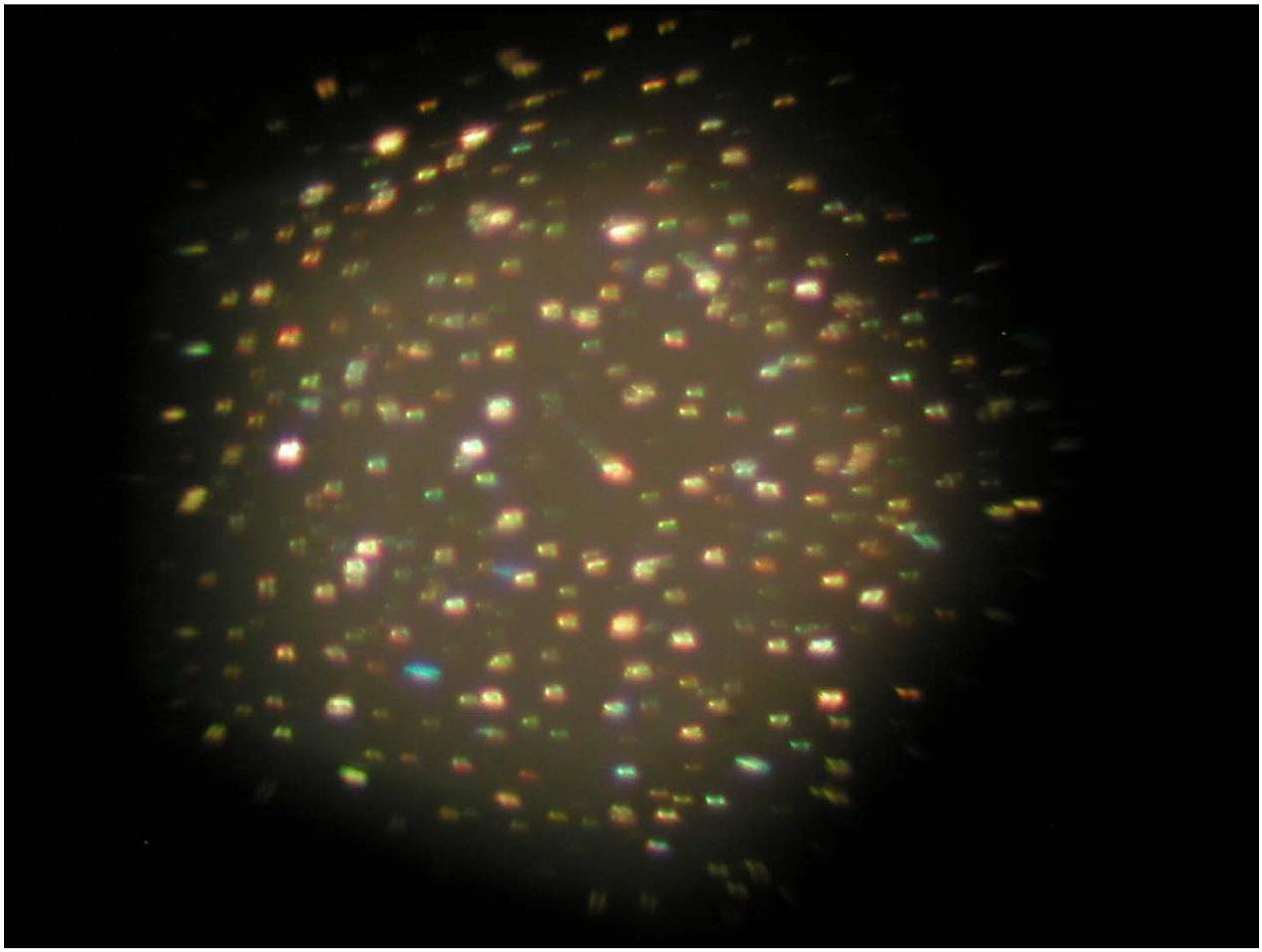

Figure 4.6.1 The image of the $sp^2C=C$ sites excited under visible light from a focused light source

lattice ions due to which separation of positive and negative charges occurs. Since the electrons are collectively under restoring force by the positive charges, therefore collective oscillation is produced. If the frequency of the excitation light field is in resonance with the eigen frequency of

this collective oscillation, even a small exciting field leads to a strong oscillation. An oscillating dipole radiates electromagnetic waves called plasmons. Therefore our result (Fig. 4.6.1.) is well understood by this semi-classical model.

4.7 Reminiscence of investigations of HDLC film by HRTEM, SEM, AFM, mRS, STM, IBA, I vs. V measurements and optical imaging measurements

Coherency of σ bonded sp^3 C-H and π bonded sp^2 C=C carbons of sub nanometer sizes of the domains of each, can produce a continuous, non-porous multilayered HDLC thin film (thickness ~ 50 – 168 nm) having atomically smooth surface, instead of discrete uniform grains (sizes 5-10 nm) as in the case of ultra-nanocrystalline diamond film of thickness greater than 300 nm. From the attempts of depositing HDLC films onto various substrates like Si(100), quartz, steel etc., it is found that synthesis of coherently coupled σ bonded sp^3 C-H and π bonded sp^2 C=C carbon film according to BEN model [89], as described above, should be possible for the single crystalline Si(100) type substrate. These multilayered HHDLC film may be considered a graphene/graphitic structure, sandwiched between the top diamond like structure (hydrogenated graphene: sp^3 C–H) and silicon substrate. Due to existence of interlayer disorder between the layers, the 3-D crystallinity of the HHDLC film should be lost, while only the 2-D crystallinity should be preserved. As a result, our HHDLC film onto Si(100) should behave as 2-D material composed of coherently coupled sp^3 C-H and sp^2 C=C carbons at different ratio under different deposition conditions. As a new characteristic behavior on the electron transport and optical property of our 2-D HHDLC film onto large area Si(100) substrate we observed respectively: (i) step-like I vs. V characteristic, indicating manifestation of Coulomb blockade effect, and (ii) different colors in the optical image, indicating existence of particle plasmons, as observed in the case of noble metallic nanostructures.

4.8 Typical Raman spectrum of HDLC film onto different substrates

The deposition conditions of HDLC thin film onto stainless steel substrate is given in chapter 2. The detiled analysis of the HDLC film is reported by Kumari et al. [91].Therefore, i have not carried out any further study for the characterization of HDLC film onto stainless steel substrate. A typical Raman spectrum of HDLC film onto stainless steel substrate is shown in Figure 4.8.1.

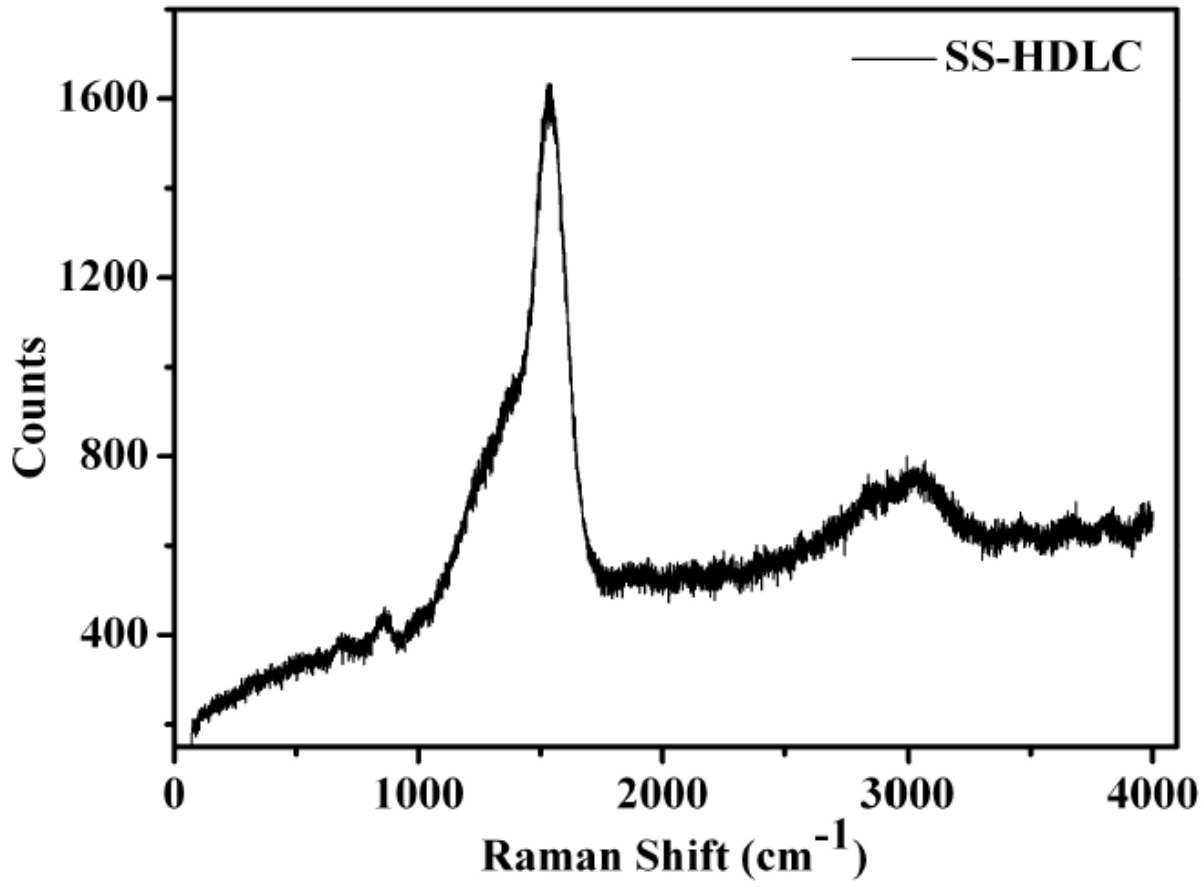

Figure 4.8.1 Typical Raman spectrum of HDLC film onto stainless steel substrate over the range 50-4000 cm^{-1}

It has been observed that our HDLC thin films are typically uniform, smooth, scratch resistant, hard, continuous surface with no-observable porosity, and gold-coloured thin films over stainless

steel substrate. Kumari et al. [91] reported the presence of much higher content of carbon in the HDLC film than that of in the bare stainless steel, as observed from the energy dispersive X-ray (EDX) analysis of bare stainless steel and HDLC coated stainless steel. Gowri et al. [165] demonstrated the synthesis of diamond film onto various steel substrates using a three-stage growth process. In the first stage, a high substrate temperature and a high CH_4 percent were used to achieve faster accumulation critical carbon content. Secondly, the substrate was made to undergo ultrasonic scratching in diamond slurry outside reactor chamber, and finally deposition of diamond film was carried out under conventional HFCVD process. In contrast to that, we have deposited directly HDLC films onto stainless steel substrate without the need for an extra ex-situ pre-treatment step or interfacial layer(s) [91].

Typical Raman spectrum of HDLC film onto quartz substrate is shown in Figure 4.8.2a and that of bare quartz is shown in Figure 4.8.2b. Yang et al. [167] and Joseph [168] et al. studied the growth of highly transparent NCD and UNCD films coatings on quartz-glass substrates using conventional MWECVD method by CH_4 and H_2 or Ar gas mixtures. Although, they have used two stage pre-treatment before depositing the required films via with diamond powder (ex-situ) and pure H_2 plasma. But, we have used single stage pre-treatment method for the depositing the thin film. Raman spectra is used to differentiate the nanocrystalline diamond (via. 1140 cm^{-1}), a broad peak at ~1350 cm^{-1} for NCD/UNCD as the crystalline size decreases and also non-diamond carbon. It has been observed that increased content of non-diamond carbon was responsible for the poor transmittance of the deposit. The control of optimum quantity of CH_4 makes the film as protective coating for optical components due to the very smooth surface characteristics, good averaged transmittance, and hardness. Our low temperature growth process

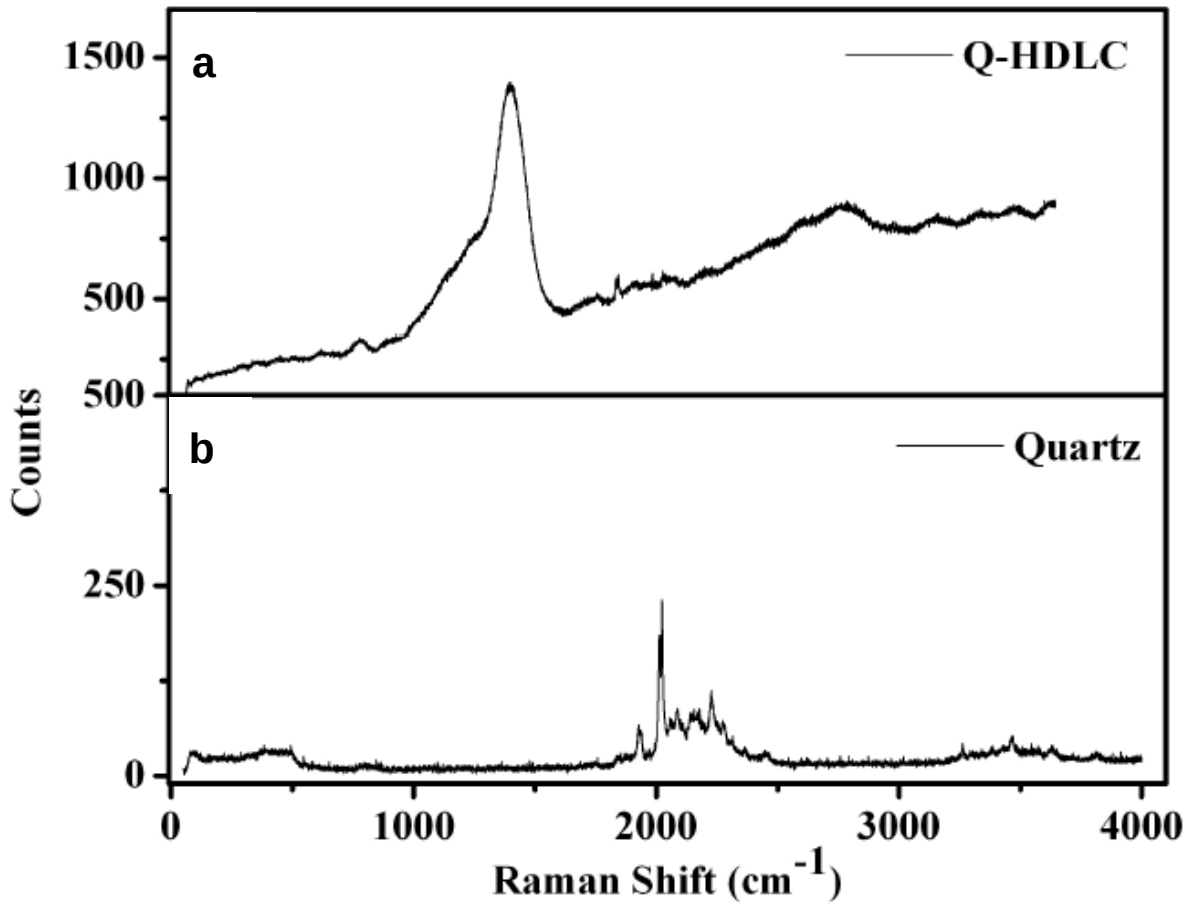

Figure 4.8.2 Typical Raman spectrum of (a) HDLC film onto quartz substrate (b) bare quartz over the range 50-4000 cm^{-1}

of NCD/UNCD films on quartz using PECVD method provides a new successful method to grow transparent NCD/UNCD films through heating the substrate or pre-treatment [167, 168]. Moreover, the grain size of UNCD/NCD films critically controls the higher transmission properties of UNCD as compared to that of NCD and Micro-crystalline diamond (MCD). This opens up new directions for the preparation of NCD or UNCD film for the applications of transparent window. Typical transmittance spectra of quartz and HDLC films deposited on

quartz over the 200 – 2500 nm are shown in Figure 4.8.3. These measurements were carried out in PerkinElmer UV/VIS/NIR Spectrometer (Model Lambda 950) at Variable Energy Cyclotron Centre, Kolkata, India.

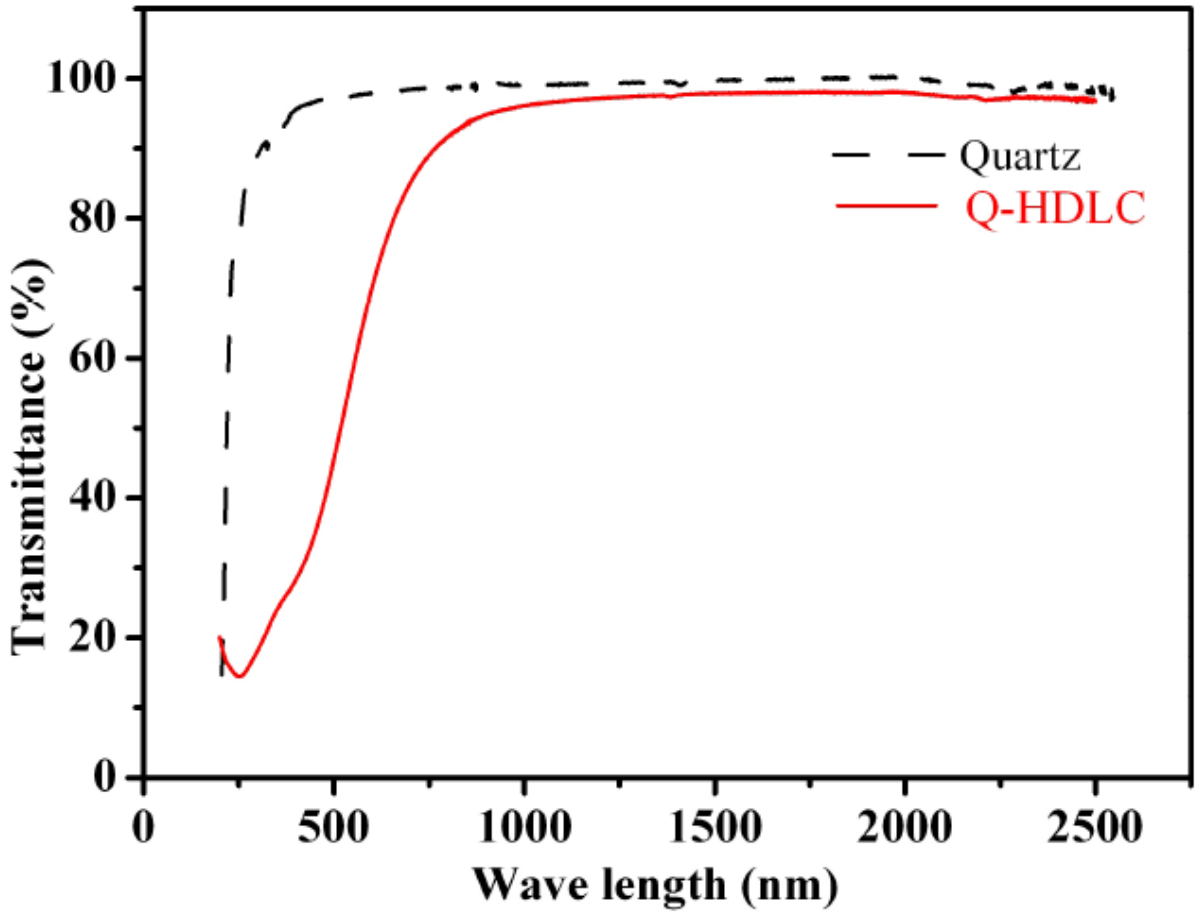

Figure 4.8.3 Typical transmittance spectra of quartz and HDLC films deposited on quartz over the 200 – 2500 nm

Typical Raman spectrum of HDLC film onto carbon foam substrate is shown Figure 4.8.4a and that of bare carbon foam is shown in Figure 4.8.4b.

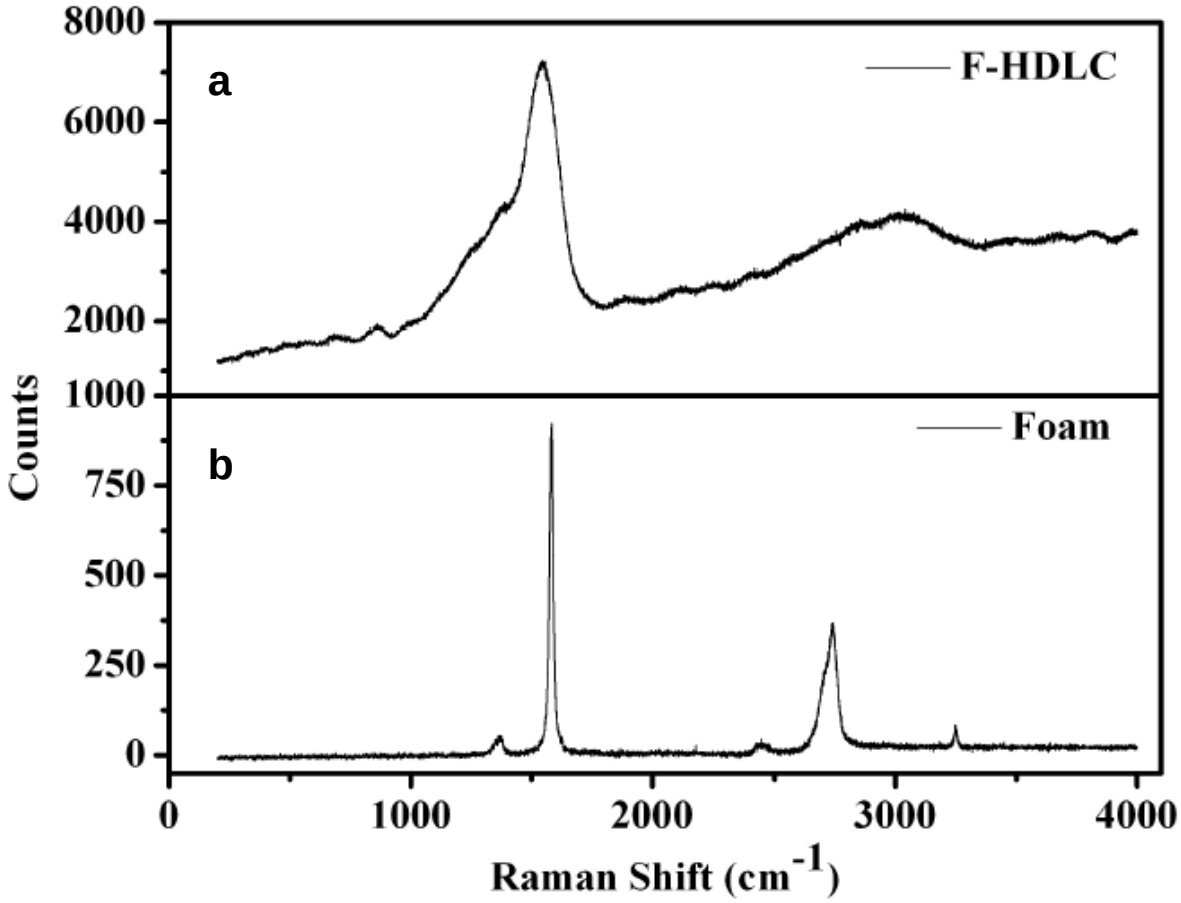

Figure 4.8.4 Typical Raman spectrum of (a) HDLC film onto carbon foam substrate (b) bare carbon foam over the range 50-4000 cm^{-1}

Comparative analysis between HDLC films on various substrates

NCD/UNCD/Diamond thin films have been deposited on a variety of substrates. However the dominant substrate has been single crystal silicon onto which the films was made for the present work. The diamond nucleation rates and adhesions vary with the tendency to form intermediate carbide layers. Gracio et al. [25] has classified the various substrates for CVD diamond

deposition into three major groups based on the interaction of carbon with various substrates. According to these interactions, the substrates have been classified as having (a) strong tendency towards carbide formation, (b) poor or no carbon solubility or reaction, (c) weak carbide formation, but strong carbon dissolving substrate. Consequently, the above carbide-substrate interaction may lead to different adhesion behaviors which may be attributed due to the different film structures in carbide-substrate interface.

The class (a) substrates with strong carbide formation include Si, Ti, Nb, Ta, Cr, Mo, W and rare earth metals. Si is widely used as a substrate for growing diamond for different uses. Silicon has sufficiently high melting point (1683 K), and hence it forms a localized carbide layer which has a relatively low thermal expansion coefficient. The other silicon compounds commonly used include SiO_2, quartz, and Si_3N_4 that also form strong carbide layers. Hence, due to this strong carbide layer (SiC, TiC, WC etc.), the NCD/UNCD coating on these materials is expected to exhibit good adhesion. Consequently, it causes the stress in the film and substrate, which is evident by the Raman shift when we compare standard silicon sample and coated thin films. As an extension of the formation of strong carbon layers, Si and Ti are commonly used as interlayer's for obtaining adherent coatings on substrate of class (b) (for example Copper), and class (c) (for example stainless steel). The class (b) substrates include Cu, Sn, Pb, Ag, and Au. They render the category of substrates for making free-standing films. They have very low carbon affinity and consequently adhesions of UNCD/NCD coatings are expected to be very weak. In fact, the films can be easily removed from Copper surface after deposition and become free-standing. There are significant variations of grain size along the film depth profile. The grain size generally increases from the interface towards the surface. This is due to the fact that initially smaller nucleation particles grow on the substrate surface directly, latter as the growth

continues the particle grains coalesce each other to become bigger in size in perpendicular direction. As a result of growth competition, some preferential grains become larger and larger. Consequently the Raman spectra of backside are higher graphitic nature then that of top surface side. The class (c) includes substrates viz. Pt, Pd, Rh, Fe and Ni, which act as carbon dissolving leading to a significant amount of carbon diffusion in the substrate during UNCD/NCD film growth process. There is the delay of nucleation due to transport of carbon to the bulk from surface. One has to remember the above processes during the growth of typical diamond films on steel. The weak adhesion of the films to steel substrates may lead to the delamination of the grown films. Nevertheless, the characteristics of steel may be changed due to heavy carbon diffusion. Again, there is large difference in thermal properties of substrate and film may cause residue stress in the film. Buijnsters et al. [166] studied the direct deposition of diamond on steel substrate, and showed that without any pre-treatment procedure, the formation of interlayer consists of a mixture of graphite, amorphous carbon (a-C), and iron carbide prior to diamond film growth. The competitive growth of non-diamond phase leads to the partial embedding of the formed diamond grains of the deposited films.

The deposition conditions of HDLC thin film onto quartz substrate is given in chapter 2. The Raman spectrum of HDLC film onto quartz and carbon foam substrates are shown in Figure 4.8.2a and 4.8.4a. The Raman spectrums are found to be similar in nature. Therefore, it is expected that nature of these films are also to be similar to that of HDLC films onto silicon. In this small space of thesis work, i have not wished to analyze in detailed the HDLC film onto these substrates. Nevertheless, this can be taken as future directions of research.

Chapter 5

Summary and Conclusions

5.1 Summary and Conclusions:

Hexagonal HDLC (HHDLC) thin films onto different substrates (Si(100), quartz, steel, carbon foam) were synthesized using an asymmetric capacitively coupled RF (13.56 MHz) discharge at room temperature (RT) for 30 min. deposition time with a flow of helium, methane, and hydrogen and different combination of processing parameters were used to vary the composition of the elements (C, H) in the HHDLC thin films. We have established that our HHDLC films synthesized on silicon substrate are basically UNCD/NCD film. We have demonstrated that the films having large specific surface area ~10^{12} nm^2/g. It has been reported in earlier works that the ultra-nanocrystalline diamond (grain size ~ 3-5 nm, roughness ~ 7-15 nm) can produce continuous film having thickness > 300 nm. Our observation show that coherent domains of sub-nanometer sizes of sp^3C-H and sp^2C=C can produce continuous, non-porous HHDLC thin film having atomically smooth surface and this is a new result. This result was published in SCI journal and is given in ref [169]. The non-uniform depth distribution of hydrogen in the as prepared films is observed and it decreases with depth. A significant desorption of hydrogen has been found from the films during annealing in vacuum. The films also experience a mild loss of carbon during high vacuum annealing. The depth profiles of hydrogen in the annealed films are indicative of the prevalence of graphitic carbon near film – substrate interface. Thus I have established this work as an experimental verification of the BEN model [89] for the first time. This work was published in SCI journal [170]. The typical result on the measurement of TEELS of HHDLC film is described in the present thesis work. The nature of two peaks in the low-energy region of the TEELS spectrum corresponds to hexagonal character of our HDLC film. This observation corresponds to the new experimental signature [171] of misoriented bilayer graphene like and graphane like structure in the film having interlayer disorder regions. Due to existence of interlayer disorder between the layers, the 3-D crystallinity of the HHDLC

film should be lost, while only the 2-D crystallinity should be preserved. As a result, our HHDLC film onto Si(100) should behave as 2-D material composed of coherently coupled sp^3 C-H and sp^2 C=C carbons at different ratio under different deposition conditions. The signature of HHDLC as 2-D material is observed in the measurement of I vs. V characteristic which shows 'step-like' behavior indicating manifestation of Coulomb blockade effect. In conformity with the TEELS spectrum of HHDLC, different colors in the optical image is also reported in the present work. This result indicates existence of particle plasmons, as observed in the case of noble metallic nanostructures. Deposition of HDLC film onto quartz, steel, carbon foam with characteristic Raman spectra is also described in the present thesis works.

Based upon above mentioned summary of my thesis works, I may conclude the following:

- That coherency of sp^3 C-H and sp^2 C=C carbons can produce continuous, non-porous, atomically smooth hexagonal HDLC thin film onto large area Si(100) substrate at room temperature, has been shown in my thesis works.
- That HHDLC behaves as a 2-D material has been shown in my thesis works.
- Electron transport property of the 2-D HHDLC implies 'coulomb blockade' effect, indicating application as single electron transistor (SET) device at room temperature.
- Optical property of the 2-D HHDLC implies that this material can be used as 'photonic material'
- As a future course of research and development, I propose to use the 2-D HHDLC material in application to SET device as well as 'plasmonic device'

−: END :−

References

References

1. D. Zhang, and R. Q. Zhang. "Signature of nanodiamond in Raman spectra: a density functional theoretical study." *J. Phys. Chem. B.* 109 (18) (2005): 9006-9013.

2. Y. Zhu, et al. "The Biocompatibility of Nanodiamonds and Their Application in Drug Delivery Systems." *Theranostics* 2 (3) (2012): 302-312.

3. V. N. Mochalin, O. Shenderova, D. Ho, and Y. Gogotsi. "The properties and applications of nanodiamonds." *Nat. Nanotechnol.* 7 (2012): 11-23.

4. K. Panda, et al. "Tribological properties of ultrananocrystalline diamond and diamond nanorod films." *Surf. Coatings Technol.* 207 (2012): 535-545.

5. Q. Liang, A. Stanishevsky, and A. K. Vohra. "Tribological properties of undoped and boron-doped nanocrystalline diamond films." *Thin Solid Films* 517 (2008): 800-804.

6. A. V. Sumant, O. Auciellllo, M. Liao, and O. A. Williams. "MEMS/NEMS based on mono-, nano-, and ultrananocrystalline diamond films." *MRS Bulletin* 39 (2014): 511-516.

7. A. V. Sumant, O. Auciellllo, R. W. Carpick, S. Srinivasan, and J. E. Butler. "Ultrananocrystalline and Nanocrystalline Diamond Thin Films for MEMS/NEMS Applications." *MRS Bulletin* 35 (2010): 281-288.

8. O. Auciello, et al. "Materials science and fabrication processes for a new MEMS technology based on ultrananocrystalline diamond thin films." *J. Phys.: Condens. Matter* 16 (2004): R539-R552.

9. A. R. Krauss, et al. "Ultrananocrystalline diamond thin films for MEMS and moving mechanical assembly devices." *Diamond Relat. Mater.* 10 (2001): 1952-1961.

10. F. Buja, A. V. Sumant, J. Kokorian, and W. M. van Spengena. "Electrically conducting ultrananocrystalline diamond for the development of a next generation of micro-actuators." *Sensors and Actuators A* 214 (2014): 259-266.

11. W. Yang, et al. "DNA-modified nanocrystalline diamond thin films as stable, biologically active substrates." *Nat. Mater.* 1 (2002): 253-257.

12. W. Yang, J. E. Butler, J. N. Russell, and R. J. Hamers. "Direct electrical detection of antigen–antibody binding on diamond and silicon substrates using electrical impedance spectroscopy." *Analyst* 132 (2007): 296-306.

13. W. Yang, J. E. Butler, J. N. Russell, and R. J. Hamers. "Interfacial Electrical Properties of DNA-Modified Diamond Thin Films: Intrinsic Response and Hybridization-Induced Field Effects." *Langmuir* 20 (16) (2004): 6778-6787.

14. S. Rotter, and J. C. Madaleno. "Diamond CVD by a combined plasma pretreatment and seeding procedure." *Chem. Vap. Deposition* 15 (2009): 209-216.

15. R. S. Edelstein, I. Gouzman, M. Folman, S. Rotter, and A. Hoffman. "Surface carbon saturation as a means of CVD diamond nucleation enhancement." *Diamond Relat. Mater.* 8 (1999): 139-145.

16. T. Sharda, T. Soga, T. Jimbo, and M. Umeno. "Highly stressed carbon film coatings on silicon: Potential applications." *Appl. Phys. Lett.* 80 (2002): 2880-2882.

17. T. Sharda, M. Umeno, T. Soga, and T. Jimbo. "Growth of nanocrystalline diamond films by biased enhanced microwave chemical vapor deposition: A different regime of growth." *Appl. Phys. Lett.* 77 (26) (2000): 4304-4306.

18. J. E. Butler, and A. V. Sumant. "The CVD of Nanodiamond Materials." *J. Chem. Vapor Depos.* 14 (2008): 145-160.

19. J. Philip, et al. "Elastic, mechanical, and thermal properties of nanocrystalline diamond films." *J. Appl. Phys.* 93 (4) (2003): 2164-2171.

20. R. B. Corvin, J. G. Harrison, S. A. Catledge, and Y. K. Vohra. "Gas-phase thermodynamic models of nitrogen-induced nanocrystallinity in chemical vapor-deposited diamond." *Appl. Phys. Lett.* 80 (14) (2002): 2550-2552.

21. W. J. Zhang, et al. "Diamond nucleation enhancement by direct low-energy ion-beam deposition." *Phys. Rev. B* 61 (8) (2000): 5579-5586.

22. Y. C. Chen, et al. "Synthesis and characterization of smooth ultrananocrystalline diamond films via low pressure bias-enhanced nucleation and growth." *App. Phys. Lett.* 92 (2008): 133113-3.

23. W. Zhu, F. R. Sivazlian, B. R. Stoner, and J. T. Glass. "Nucleation and selected area deposition of diamond by biased hot filament chemical vapor deposition." *J. Mater. Res.* 10 (2) (1995): 425-430.

24. J. C. Angus, et al. "Chemical Vapour Deposition of Diamond." *Philos. Trans. R. Soc. London Ser. A* 342 (1993): 195 - 208.

25. J. J. Gracio, Q. H. Fan, and J. C. Madalenol. "Diamond growth by chemical vapour deposition." *J. Phys. D: Appl. Phys.*43 (2010): 374017-22.

26. D. M. Gruen, "Nanocrystalline Diamond Films." *Annu. Rev. Mater. Sci.* 29 (1999): 211-259.

27. P. John, J. R. Rabeau, and J. I. B. Wilson. "The cavity ring-down spectroscopy of C_2 in a microwave plasma." *Diamond Relat. Mater.* 11 (2002): 806-811.

28. K. E. Spear, "Diamond-Ceramic coating of the future." *J. Am. Ceram. Soc.* 72 (2) (1989): 171-191.

29. A. K. Gangopadhyay, and M. A. Tamor. "Friction and wear behavior of diamond films against steel and ceramics." *Wear* 169 (1993): 221-229.

30. http://www.azom.com/article.aspx?ArticleID=1630.

31. http://www.azom.com/article.aspx?ArticleID=516.

32. P. J. Gielisse, V. I. Ivanov-Omskii, G. Popovici, and M. Prelas. *Diamond and Diamond-Like Film Applications.* Pennsylvania, USA: Technomic publication, 1998, p 495.

33. Z. H. Shen, et al. "Mechanical properties of nanocrystalline diamond films." *J. Appl. Phys.* 99 (2006): 124302-6.

34. V. P. Adiga, "Mechanical stiffness and dissipation in ultrananocrystalline diamond films. " Publicly accessible Penn Dissertations, 2010, p 413.

35. X. Peng, L, Z. H. Barber, and T. W. Clyne. "Surface roughness of diamond-like carbon films prepared using various techniques." *Surf. Coating Technol.* 138 (2001): 23-32.

36. T. A. Yoshitake, Nagano, M. Itakura, N. Kuwano, T. Hara, and K. Nagayama. "Spectral Absorption Properties of Ultrananocrystalline Diamond/Amorphous Carbon Composite Thin Films Prepared by Pulsed Laser Deposition." *Jpn. J. Appl. Phys.* 46 (10L) (2007): L936-L938.

37. http://www.thinfilmsblog.com.

38. S. Wang, Y. Zhang, N. Abidi, and L. Cabrales. "Wettability and surface free energy of graphene films." *Langmuir* 25 (18) (2009): 11078-11081.

39. L. Wang, J. Liu, L. Ren, Q. Su, W. Shi, and Xia Y. "Effect of carbon concentration on the optical properties of nanocrystalline diamond films deposited by hot-filament chemical vapor deposition method." *J. Nanosci. Nanotechnol.* 8 (5) (2008): 2534-2539.

40. K. Jonnalagadda, S. W. Cho, I. Chasiotis, T. Friedmann, and J. Sullivan. "Effect of intrinsic stress gradient on the effective mode-I fracture toughness of amorphous diamond-like carbon films for MEMS." *J. Mech. Phys. Solids* 56 (2) (2009): 388-401.

41. M. Nastasi, P. Kodali, K. C. Walter, J. D. Embury, R. Raj, and Y. Nakamura. "Fracture toughness of diamondlike carbon coatings." *J. Mater. Res.* 14 (5) (1999): 2173-2180.

42. S. J. Cho, K. R. Lee, K. Yong Eun, J. Hee Hahn, and D. H. Ko. "Determination of elastic modulus and Poisson's ratio of diamond-like carbon films." *Thin Solid Films* 341 (1) (1999): 207-210.

43. C. Donnet, and A. Grill. "Friction control of diamond-like carbon coatings." *Surf. Coatings Technol.* 94 (1997): 456-462.

44. J. A. Heimberg, K. J. Wahl, I. L. Singer, and A. Erdemir. "Superlow friction behavior of diamond-like carbon coatings: Time and speed effects." *Appl. Phys. Lett.* 78 (17) (2001): 2449-2451.

45. Ilan A. Blech, and P. Wood. "Linear thermal expansion coefficient and biaxial elastic modulus of diamondlike carbon films." *J. Vac. Sci. Technol. A* 11 (3) (1993): 728-729.

46. F. C. Marques, R. G. Lacerda, A. Champi, V. Stolojan, D. C. Cox, and S. R. P. Silva. "Thermal expansion coefficient of hydrogenated amorphous carbon." *Appl. Phys. Lett.* 83 (15) (2003): 3099-3101.

47. M. Shamsa, W. L. Liu, A. A. Balandina, C. Casiraghi, W. I. Milne, and A. C. Ferrari. "Thermal conductivity of diamond-like carbon films." *Appl. Phys. Lett.* 89 (16) (2006): 161921-3.

48. N. Woehrl, T. Hirte, O. Posth, and V. Buck. "Investigation of the coefficient of thermal expansion in nanocrystalline diamond films." *Diam. Rel. Mater.* 18 (2009): 224-228.

49. X. Xiao, B.W. Sheldon, E. Konca, L. C. Lev, and M. J. Lukitsch. "The failure mechanism of chromium as the interlayer to enhance the adhesion of nanocrystalline diamond coatings on cemented carbide." *Diam. Rel. Mater.* 18 (2009): 1114–1117.

50. M. J. Mirtich, J. S. Sovey, and A. B. Banks. "Deposition of diamondlike carbon films." U.S. Patent 4.490.229. Dec. 1984.

51. K. K. Chan, S. R. P. Silva, and G. A. J. Amaratunga. "Electronic properties of semiconducting diamond-like carbon-diamond." *Thin Solid Films* 212 (1992): 232-239.

52. M. Björling, R. Larsson, and P. Marklund. "The Effect of DLC Coating Thickness on Elstohydrodynamic Friction." *Tribol. Lett.* 55 (2014): 353-362.

53. M. Shamsa, S. Ghosh, I. Calizo, V. Ralchenko, A. Popovich, and A. A. Balandin. "Thermal conductivity of nitrogenated ultrananocrystalline diamond films on silicon." *J. Appl. Phys.* 103 (8) (2008): 083538-8.

54. F. J. H. Guillén, K. Janischowsky, J. Kusterer, W. Ebert, and E. Kohn. "Mechanical characterization and stress engineering of nanocrystalline diamonds films for MEMS applications." *Diamond Rel. Mater.* 14 (2005): 411-415.

55. A. V. Sumant, D. S. Grierson, J. E. Gerbi, J. A. Carlisle, O. Auciello, and R. W. Carpick. "Surface chemistry and bonding configuration of ultrananocrystalline diamond surfaces and their effects on nanotribological properties." *Phys. Rev. B* 76 (23) (2007): 235429-11.

56. W. A. Lanford, "Use of nuclear reaction analysis to characterize the elemental composition and density of thin film amorphous silicon." *Solar Cells* 2 (1980): 351-363.

57. E. Vainonen, J. Likonen, T. Ahlgren, P. Haussalo, J. Keinonen, and C. H. Wu. "Hydrogen migration in diamond-like carbon films." *J. Appl. Phys.* 82 (8) (1997): 3791-3796.

58. J. W. Zou, K. Reiehelt, K. Schmidt, and B. Dischler. "The deposition and study of hard carbon films." *J. Appl. Phys.* 65 (10) (1989): 3914-3918.

59. S. Kaplan, F. Jansen, and J. Machonkin. "Characterization of amorphous carbon-hydrogen films by solid-state nuclear magnetic resonance." *Appl. Phys. Lett. 47* (7) (1985): 750-753.

60. A. C. Ferrari, and J. Robertson. "Interpretation of Raman spectra of disordered and amorphous carbon." *Phys. Rev. B* 60 (20) (2000): 14095-14107

61. A. Singha, A. Ghosh, N. R. Ray, and A. Roy, "Quantitative Analysis of Hydrogenated DLC Films by Visible Raman Spectroscopy." *J. Appl. Phys.* 100 (4) (2006): 044910-8.

62. J. Robertson, "Diamond like amorphous carbon." *Mater. Sci. Eng. Rep.* 37 (2002): 129-281.

63. C. Casiraghi, A. C. Ferrari, and J. Robertson. "Raman spectroscopy of hydrogenated amorphous carbons." *Phys. Rev. B* 72 (8) (2005): 085401-14.

64. F. R. McFeely, S. P. Kowalczyk, L. Ley, R. G. Cavell, R. A. Pollak, and D. A. Shirley. "X-ray photoemission studies of diamond, graphite, and glassy carbon valence bands." *Phys. Rev. B* 9 (12) (1974): 5268-5278.

65. B. B. Pate, "The diamond surface: atomic and electronic structure." *Surf. Sci.* 165 (1) (1986): 83-142.

66. K. W. Nebesny, B. L. Maschhoff, and N. R. Armstrong. "Quantitation of Auger and X-ray Photoelectron Spectroscopies." *Anal. Chem.* 61 (1989): 469A-477A.

67. R. J. Nemanich, and S. A. Solin. "First- and second-order Raman scattering from finite-size crystals of graphite." *Phys. Rev. B, Condens. Matter Mater. Phys.* 20 (2) (1979): 392-401.

67. R. J. Nemanich, and S. A. Solin. "First- and second-order Raman scattering from finite-size crystals of graphite." *Phys. Rev. B, Condens. Matter Mater. Phys.* 20 (2) (1979): 392-401.

68. J. R. Nemanich, J. T. Glass, G. Lucovsky, and R. E. Shroder. "Raman scattering characterization of carbon bonding in diamond and diamondlike thin films." *J. Vac. Sci. Technol. A* 6 (3) (1988): 1783-1787.

69. J. Schwan, S. Ulrich, V. Batori, H. Ehrhardt, and S. R. P. Silva. "Raman spectroscopy on amorphous carbon films." *J. Appl. Phys.* 440 (1) (1996): 440-447

70. A. C. Ferrari, and J. Robertson. "Origin of the 1150 cm^{-1} Raman mode in the nanocrystalline diamond." *Phys. Rev. B* 63 (2001): 121405-1-4.

71. J. M. Calleja, J. Kuhl, and M. Cardona. "Resonant Raman scattering in diamond." *Phys. Rev. B* 17 (2) (1978): 876-883.

72. S. A. Solin, and A. K. Ramdas. "Raman Spectrum of Diamond." *Phys. Rev. B* 1 (4) (1970): 1687-1698.

73. M. A. Washington, and H. Z. Cummins. "Linewidth of the sharp two-phonon Raman peak in diamond." *Phys. Rev. B* 15 (12) (1977): 5840-5842.

74. R. B. Wright, R. Varma, and D. M. Gruen. "Raman scattering and SEM studies of graphite and silicon carbide surfaces bombarded with energetic protons, deuterons and helium ions." *J. Nucl. Mater.* 63 (1976): 415-421.

75. R. Tsu, J. H. González, and C. I. Hernández, "Observation of splitting of the E2g mode and two-phonon spectrum in graphites." *Solid State Commun.* 27 (5) (1978): 507-510.

76. B. L. Doyle, and P. S. Peercy. "Technique for profiling ^{1}H with 2.5-MeV Van de Graaff accelerators." *Appl. Phys. Lett.* 34 (11) (1979): 811-813.

77. H. Liebl, "Beam optics in secondary ion mass spectrometry." *Nucl. Instrum. Meth. Phys. Res.* 187 (1) (1981): 143-151.

78. W. Magee, and C. P. Wu. "Hydrogen ion implantation profiles as determined by SIMS." *Nucl. Instrum Meth.* 149 (1978): 529-533.

79. D. A. Liech, and T. A. Tombrello. "A technique for measuring hydrogen concentration versus depth in solid samples." *Nucl. Inst. Meth.* 108 (1973): 67-71.

80. J. L'ecuyer, C. Brassard, C. Cardinal, and B. Terreault. "The use of ^{6}Li and ^{35}Cl ion beams in surface analysis." *Nucl. Instrum. Meth.* 149 (1978): 271-277.

81. M. A. Kastner, "The single electron transistor and artificial atoms." *Ann. Phys. (Leipzig)* 9 (2000): 885-894.

82. K. Matsumoto, M. Ishii, K. Segawa, Y. Oka, B. J. Vartanian, and J. S. Harris. "Room temperature operation of a single electron transistor made by the scanning tunneling microscope nanooxidation process for the TiOx/Ti system." *Appl. Phys. Lett.* 68 (1) (1996): 34-36.

83. P. S. K. Karre, P. L. Bergstrom, G. Mallick, and S. P. Karna. "Room temperature operational single electron transistor fabricated by focused ion beam deposition." *J. Appl. Phys.* 102 (2007): 024316-1-4.

84. M. V. Hauf, P. Simon, M. Seifert, A. W. Holleitner, M. Stutzmann, and J. A. Garrido. "Low dimensionality of the surface conductivity of diamond." *Phys. Rev. B.* 89 (11) (2014): 115426-5.

85. S. Matsumoto, Y. Sato, M. Kamo, and N. Setaka. "Vapor Deposition of Diamond Particles from Methane." *Jpn. J. Appl. Phys.* 21 (4) (1982): L183-L185.

86. S. Matsumoto, Y. Sato, M. Tsutsumi, and N. Setaka. "Growth of diamond particles from methane-hydrogen gas." *J. Mater. Sci.* 17 (1982): 3106-3112.

87. H. Yoshikawa, C. Morel, and Y. Koga. "Synthesis of nanocrystalline diamond films using microwave plasma CVD." *Diam. Relat. Mater.* 10 (2001): 1588-1591.

88. S. Matsumoto, "Chemical vapour deposition of diamond in RF glow discharge." *J. Mater. Sci. Lett.* 4 (1985): 600-602.

89. J. Robertson, J. Gerber, S. Sattel, M. Weiler, K. Jung, and H. Ehrhardt. "Mechanism of bias-enhanced nucleation of diamond on Si." *Appl. Phys. Lett.* 64 (24) (1995): 3287-3289.

90. N. R. Ray, and A. N. S. Iyengar. Edited by R. Hatakeyama and S. Samukawa. *Proceedings of the Sixth International Conference on Reactive Plasmas and 23rd Symposium on Plasma Processing.* Matshushima/Sendai, Japan, 24-27 Jan. 2006. 583.

91. K. Kumari, S. Benerjee, T. K. Chini, and N. R. Ray. "Preparation of diamond like carbon thin film on stainless steel and its SEM characterization." *Bull. Mater. Sci.* 32 (6) (2009): 563-567.

92. S. Mathew, U. M. Bhatta, A. K. M. M. Islam, M. Mukherjee, N. R. Ray, and B. N. Dev. "Structural modifications of diamond like carbon films induced by MeV nitrogen ion irradiation." *Appl. Surf. Sci.* 225 (9) (2009): 4796-4800.

93. H. S. Biswas, et al. "Covalent Immobilization of Protein onto a functionalized Hydrogenated Diamond-like Carbon Substrate." *Langmuir* 26 (22) (2010): 17413–17418.

94. J. Asmussen, and D.K. Reinhard, *Diamond Films Handbook.* New York: Marcel Dekker, Inc., 2002.

95. F. P. Bundy, H. T. Hall, H. M. Strong, and R. H. Wentorf Jr. "Man-made Diamonds." *Nature* 176 (1955): 51-55.

96. G. N. Lewis, and M. Randall. "The free energy of some carbon compounds." *J. Am. Chem. Soc.* 37 (3) (1915): 458-470.

97. W. G. Eversole, Synthesis of diamond. U.S. Patent 3030,188. Apr. 1962.

98. J. J. Lander, and J. Morrison. "Low energy electron diffraction study of the (111) diamond surface." *Surf. Sci* 4 (3) (1966): 241-246.

99. S. P. Chauhan, J. C. Angus, and N. C. Gardner. "Kinetics of carbon deposition on diamond powder." *J. Appl. Phys.* 47 (11) (1976): 4746-4754.

100. W. A. Yarbrough, and R. Messier. "Current Issues and Problems in the Chemical Vapor Deposition of Diamond." *Science* 247 (1990): 688-696.

101. M. Kamo, Y. Sato, S. Matsumoto, and N. Setaka. "Diamond synthesis from gas phase in microwave plasma." *J. Cryst. Growth* 62 (1983): 642-644.

102. A. V. Crewe, J. Wall, and J. Langmore. "Visibility of a single atom." *Science* 168 (3937) (1970): 1338-1340.

103. J. C. Meyer, C. O. Dirit, M. F. Crommie, and A. Zettl. "Imaging and dynamics of light atoms and molecules on graphene." *Nature* 454 (7202) (2008): 319-322.

104. C. Kisielowski, et al. "Detection of single atoms and buried defects in three dimensions by aberration-corrected electron microscopy with 0.5 Å information limit." *Microscopy and Microanalysis* 14 (2008): 469–477.

105. J. Nebesářová, and M. Vancová. "How to Observe Small Biological Objects in Low-Voltage Electron Microscope." *Microscopy and Microanalysis* 13 (3) (2007): 248–249.

106. L. F. Drummy, J. Yang, and D. C. Martin. "Low-voltage electron microscopy of polymer and organic molecular thin films." *Ultramicroscopy* 99 (4) (2004): 247-256.

107. Y. Murooka, N. Tanaka, S. Hirono, and M. Hibino. "Electron energy loss spectroscopy of carbon films prepared by electron cyclotron resonance plasma sputtering." *Mater. Trans.* 43 (8) (2002): 2092-2096.

108. R. F. Egerton, "Electron energy-loss spectroscopy in TEM." *Rep. Prog. Phys.* 72 (2009): 016502-25.

109. T. Eberlein, et al. "Plasmon spectroscopy of free-standing graphene films." *Phys. Rev. B.* 77 (2008): 233406-4.

110. P. K. Chu, and L. Liuhe. "Characterization of amorphous and nanocrystalline carbon films." *Mater. Chem. Phys.* 96 (2006): 253-277.

111. S. Prawer, et al. "Systematic variation of the Raman spectra of DLC films as a function of sp^2:sp^3 composition." *Diamond Relat. Mater.* 5 (1996): 433-438.

112. M. A. Pimenta, G Dresselhaus, M S Dresselhaus, L G Cancado, A Jorio, and R Saito. "Studying disorder in graphite-based systems by Raman spectroscopy." *Phys. Chem. Chem. Phys.* 9 (2007): 1276-1291.

113. P. K. Hansma, and J. Tersoff. "Scanning tunneling microscopy." *J. Appl. Phys.* 61 (2) (1987): R1-R23.

114. G. Binnig, and H. Rohrer. "Scanning tunneling microscopy." *Surf. Sci.* 126 (1983): 236-244.

115. G. Binnig, C. F. Quate, and Ch. Gerber. "Atomic Force Microscope." *Phys. Rev. Lett.* 56 (9) (1986): 930-933.

116. E. Meyer, "Atomic force microscopy." *Prog. Surf. Sci.* 41 (1992): 3-49.

117. H. Todokoro, and M. Ezumi. Scanning electron microscope. United States Patent 5,872,358. Feb. 1999.

118. D. A. Skoog, F. J. Holler, and S. R. Crouch. "Surface characterization by spectroscopy and microscopy." In *Instrumental Analysis*, by D. A. Skoog, F. J. Holler and S. R. Crouch, 647-684. Delhi: Cengage Learning, 2007.

119. S. Kumar, J. V. Ramana, C. David, V. S. Raju, and S. Gangadharan. "Polyaniline, a conducting polymer, as a standard for hydrogen profiling on material surfaces." *Nucl. Inst. Meth. Phys. Res. B* 142 (1998): 549-554.

120. L. Westerberg, L. E. Svensson, E. Karlsson, M. W. Richardson, and K. Lundstrom. "Stable absolute calibration standards for hydrogen profile analysis using nuclear resonance techniques." *Nucl. Inst. Meth. Phys. Res. B* 9 (1985): 49-54.

121. B. Hjörvarsson, J. Rydén, T. Ericsson, and E. Karlsson. "Hydrogenated tantalum: A convenient calibration substance for hydrogen profile analysis using nuclear resonance reactions." *Nucl. Inst. and Meth. in Phys. Res. B* 42 (1989): 257-263.

122. S. Kumar, J. V. Ramana, C. David, V. S. Raju, and S. Gangadharan. "Ion beam analysis of porous silicon layers." *Nucl. Inst. Meth. Phys. Res. B* 179 (2001): 113-120.

123. J. F. Ziegler, M. D. Ziegler, and J. P. Biersack. *The Stopping and Range of Ions in Matter, SRIM – Version 2008.04.* 2008. www.SRIM.org.

124. W. K. Chu, J. W. Mayer, and M. A. Nicolet. *Backscattering spectrometry.* New York: Academic Press, 1978.

125. J. F. Ziegler, et al. "Profiling hydrogen in materials using ion beams." *Nucl. Inst. and Meth.* 149 (1978): 19-39.

126. Y. Wu, et al. "High-frequency, scaled graphene transistors on diamond like carbon." *Nature* 472 (2011): 74-78.

127. J. C. Angus, and C. C. Hayman. "Low-Pressure, Metastable Growth of Diamond and "Diamondlike" Phases." Science 241 (1988): 913-921.

128. K. Tsugawa, et al. "High-performance diamond surface-channel field-effect transistors and their operation mechanism." *Diamond Relat. Mater.* 8 (1999): 927-933.

129. N. R. Ray, J. Datta, H. S. Biswas, P. Sen, and K. Bagani. "Room temperature operational single electron transistor on the macroscopic surface of hydrogenated diamond like carbon." arXiv preprint arXiv:1306.6477, 2013.

130. H. S. Biswas, J. Datta, P. Sen, U. C. Ghosh, and N. R. Ray. "Raman spectra of electrochemically hydrogenated diamond like carbon surface." *Chem. Phys. Lett. 600* (2014): 10-14.

131. N. Yoshizawa, Y. Yamada, and M. Shiraishi. "Structure of amorphous carbon film prepared from RF plasma deposition." *Carbon* 31 (7) (1993): 1049–1055.

132. B. Marchon, J Gui, Grannen K, C, Rauch G, J W AgerIII, and S R P Silva. "Photoluminescence and Raman spectroscopy in hydrogenated carbon films." *IEEE Trans. Magn.* 33 (5) (1997): 3148-3150.

133. M. S. Dresselhaus, A. Jorio, M. Hofmann, G. Dresselhaus, and R. Saito. "Perspectives on carbon nanotubes and graphene Raman spectroscopy." *Nano Lett.* 10 (3) (2010): 751-758.

134. M. S. Dresselhaus, A. Jorio, and M. Hofmann. "Raman spectroscopy as a probe of graphene and carbon nanotubes." *Phil. Trans. R. Soc. A* 366 (2008): 231-236.

135. Z. H. Ni, T. Yu, Y.H. Lu, Y.Y. Wang, Y.P. Feng, and Z.X. Shan. "Uniaxial strain on graphene: Raman spectroscopy study and band gap opening." *ACS Nano* 2 (2008): 2301-2305.

136. C. Thomson, and S. Reich. "Double resonance Raman scattering in graphite." *Phys. Rev. Lett.* 85 (2000): 5214-5217.

137. J. Robertson, "Hard amorphous (diamond like) carbons." *Prog. Solid State Chem.* 21 (1991): 199-333.

138. C. William, "Organic Spectroscopy." 58-88. New York: Palgrave, 2005.

139. J. A. Bagilo, B. C. Farnsworth, S. Hankin, G. Hamill, and D. O'Nill. "Studies of stress related issues in microwave CVD diamond on <100> silicon substrates." *Thin Solid Films* 212 (1992): 180-185.

140. L. Bergman, and R. J. Nemanich. "Raman and photoluminescence analysis of stress state and impurity distribution in diamond thin films." *J. Appl. Phys.* 78 (11) (1995): 6709-6719.

141. M. Z. S. Flores, R.S. Autreto P, B, Legoas S, and S, Galvao D. "Graphene to graphane-a theoretical study." *Nanotechnol.* 20 (2009): 465704-465709.

142. A. C. Ferrari, et al. "Raman Spectrum of Graphene and Graphene Layers." *Phys. Rev. Lett.* 97 (2006): 187401-4.

143. I. Childres, L. A. Jauregui, W. Park, H. Cao, and Y.P. Chen. "Raman spectroscopy of graphene and related materials." Chap. 19 in *New Developments in Photon and Materials Research*, edited by J.I. Jang. Binghamton, NY, USA: Nova Science Publishers, 2013.

144. F. Tuinstra, and J. L. Koenig. "Raman spectrum of graphite." *J. Chem. Phys.* 53 (1970): 1126-1130.

145. M. I. Nathan, J. E. Smith Jr., and K. N. Tu. "Raman spectra of glassy carbon." *J. Appl. Phys.* 45 (5) (1974): 2370.

146. V. Zólyomi, J. Koltai, and J. Kürti. "Resonance Raman spectroscopy of graphite and graphene." *Phys. Stat. Sol. B* 248 (11) (2011): 2435–2444.

147. L. M. Malard, M. A. Pimenta, G. Dresselhaus, and M. S. Dresselhaus. "Raman spectroscopy in graphene." *Phys. Rep.* 473 (5/6) (2009): 51–87.

148. S. Latil, V. Meunier, and L. Henrard. "Massless fermions in multilayer graphitic systems with misoriented layers: Ab initio calculations and experimental fingerprints." *Phys. Rev. B, Condens. Matter Mater. Phys.* 76 (20) (2007): 201402-4.

149. P. Poncharal, A. Ayari, T. Michel, and J. L. Sauvajol. "Raman spectra of misoriented bilayer graphene." *Phys. Rev. B, Condens. Matter Mater.* 78 (11) (2008): 113407-4.

150. http://en.wikipedia.org/wiki/Man-made diamond.

151. F. P. Bundy, and J. S. Kasper. "Hexagonal Diamond—A New Form of Carbon." *J. Chem. Phys.* 46 (1967): 3437-3446.

152. T. Yagi, and W. Utsumi. "High-pressure in situ x-ray-diffraction study of the phase transformation from graphite to hexagonal diamond at room temperature." *Phys. Rev. B* 46 (1992): 6031-6039.

153. X. Jiang, and C. L. Jia. "Direct Local Epitaxy of Diamond on Si(100) and Surface-Roughening-Induced Crystal Misorientation." *Phys. Rev. Lett.* 84 (2000): 3658-3661.

154. J. P. Thomas, M. Fallavier, and J. Tousset. "Hydrogen mobility under beam impact when using the $^{1}H(^{15}N, \alpha\gamma)^{12}C$ nuclear reaction for material analysis." *Nucl. Inst. Meth.* 187 (1981): 573-580.

155. J. Biener, A. Schenk, B. Winter, C. Lutterloh, U. A. Schubert, and J. Küppers. "Hydrogenation of amorphous C : H surfaces by thermal H (D) atoms." *Surf. Sci.* 307-309 (1994): 228-234.

156. V. D. Vankar, and N. Dilawar. "Ion irradiation effects in diamond and diamond like carbon thin films." *Vacuum* 41 (11) (1996): 1275-1280.

157. D. C. Ingram, and A. W. McCormick. "The effect of Mev ion irradiation on the hydrogen content and resistivity of direct ion beam deposited diamondlike carbon." *Nucl. Inst. Meth. Phys. Res. B* 34 (1988): 68-73.

158. K. Maruyama, W. Jacob, and J. Roth. "Erosion behavior of soft, amorphous deuterated carbon films by heat treatment in air and under vacuum." *J. Nucl. Mater.* 264 (1999): 56-70.

159. W. Wang, W. Jacob, and J. Roth. "Oxidation and hydrogen isotope exchange in amorphous, deuterated carbon films." *J. Nucl. Mater.* 245 (1997): 66-71.

160. M. Pumera, and C. H. A. Wong. "Graphane and hydrogenated graphene." *Chem. Soc. Rev.* 42 (2013): 5987-5995.

161. S. S. Tinchev, S. Alexandrova, and E. Valcheva. "Single electron tunneling as a plausible mechanism in diamond like carbon films." eprint arXiv 2008: 0804.2164.

162. K. K. Likharev, "Single-electron devices and their applications." *Proc. IEEE* 87 (1999): 606-632.

163. J. B. Barner, and S. T. Ruggiero. "Observation of the incremental charging of Ag particles by single electrons." *Phys. Rev. Lett.* 59 (7) (1987): 807-810.

164. Carsten Sönnichsen. "Plasmons in metal nanostructures." dissertation, physics dept., Ludwig-Maximilians-University of Munich, 2001.

165. M. Gowri, H. Li, J. J. Schermer, W. J. P. van Enckevort, and J. J. ter Meulen. "Direct deposition of diamond films on steel using a three-step process.″ *Diamond Relat. Mater*. 15 (2006): 498 – 501.

166. J. G. Buijnsters, P. Shankar, and J. J. Ter Meulen. "Direct deposition of polycrystalline diamond onto steel substrates.″ *Surf. Coatings Technol.* 201 (2007): 8955–8960.

167. W. B. Yang, F. X. Lu, and Z. X. Cao. "Growth of nanocrystalline diamond protective coatings on quartz glass. ″ *Appl. Phys. Lett.* 91 (12) (2002): 10068-10073

168. P. T. Joseph, Nyan-Hwa Tai, Yi-Chun Chen, Hsiu-Fung Cheng, and I-Nan Lin. "Transparent ultrananocrystalline diamond films on quartz substrate.″ *Diamond Relat. Mater*. 17 (2008): 476–480.

169. J. Datta, N. R. Ray, P. Sen, H. S. Biswas, and E. A. Vogler. "Structure of Hydrogenated diamond like carbon by Micro-Raman Spectroscopy." *Mater. Lett.* 71 (2012): 131-133.

170. J. Datta, et al. "Study of depth profile of hydrogen in hydrogenated diamond like carbon thin film by ion beam analysis techniques." *Nucl. Instr. Meth. Phys. Res. B* 328 (2014): 27-32.

171. N. R. Ray, J. Datta, H. S. Biswas, and S. Datta. "Signature of Misoriented Bilayer Graphenelike and Graphanelike Structure in the Hydrogenated Diamond-Like Carbon Film." *IEEE Trans. Plasma Sci.* 40 (7) (2012): 1789-1793.

Materials Letters 71 (2012) 131–133

Contents lists available at SciVerse ScienceDirect

Materials Letters

journal homepage: www.elsevier.com/locate/matlet

Structure of hydrogenated diamond like carbon by Micro-Raman spectroscopy

Jagannath Datta [a], Nihar R. Ray [a,*], Pintu Sen [b], Hari S. Biswas [a], Erwin A. Vogler [c]

[a] Nanocrystalline Diamond like Carbon Synthesis Laboratory, Plasma Physics Division, Saha Institute of Nuclear Physics, 1/AF, Bidhannagar, Kolkata-700 064, India
[b] Physics Department, Variable Energy Cyclotron Center, 1/AF, Bidhannagar, Kolkata-700 064, India
[c] Department of Materials Science and Engineering, The Pennsylvania State University, University Park, PA, 16802, USA

ARTICLE INFO

Article history:
Received 20 June 2011
Accepted 9 December 2011
Available online 16 December 2011

Keywords:
Atomically thin carbon film
Hydrogenated diamond like carbon film
Ultrananocrystalline diamond film
Coherent domains

ABSTRACT

The first-, second- and higher order Raman spectra of hydrogenated diamond like carbon (HDLC) are analyzed considering the effect of partial hydrogenation of hexagonal sp^2 (C═C) carbons on the characteristic G and D bands of graphitic materials. That coherency of sp^3 C–H and sp^2 C═C carbons in HDLC can produce a continuous, non-porous thin film having atomically smooth surface is reported as a new result.

1. Introduction

The reactive chemical groups (C═C, C–H) present in the hydrogenated diamond like carbon (HDLC) film, provide a model substrate for protein immobilization onto it and its biosensing properties [1]. These unique characteristics of HDLC have been characterized by Micro Raman spectroscopy in the present work.

2. Experimental

The synthesis of HDLC film is described elsewhere [1]. The cross sectional view and also the morphology of the surface of the HDLC film have been analyzed by transmission electron microscopy (TEM), and atomic force microscopy (AFM), scanning electron microscopy (SEM) respectively. Raman spectra were obtained using a confocal Micro Raman spectrometer (LabRAM *HR* Vis. Horiba Jobin Yvon SAS France). For the excitation wavelength 488 nm, grating 1800 g/mm, 100× objective having numerical aperture (NA) 0.9 giving the best confocality i.e. the depth of focus ~2 μm, there is no loss of Raman signal with the confocal hole size 100 ± 5 μm. Since the maximum diameter of the illuminated spot (~1.22 × λ/NA) on the HDLC sample is less than 1 μm, there is hardly any loss of Raman signal from the sample under the above mentioned operating conditions of the spectrometer. Also the depth of focus (~2 μm) being much larger than the thickness (~168 nm) of the sample as shown in the TEM cross-sectional view (Fig. 1), the Raman spectrum measures bulk of the sample. The observed Raman spectrum (Fig. 2A), recorded at exposure 10 s and repetitions 10, extends over a range of frequencies with a non-zero line width. In addition, it's center shifted from its well defined central frequency (~1580 cm^{-1}). A Gaussian profile describes broadening effect due to randomly distributed Raman signals from the sample, with no associated shift, while a Lorentzian profile describes both effects — broadening and shift, due to the structure of the sample interacting coherently. Raman spectra are deconvolved in expectation of multiple chemical environments within the HDLC film, a graphite-based system [2]. Lorentzian peak shapes are used for all Raman modes, resulting in best fits of the broad spectral envelope.

3. Results and discussion

Typical Raman spectrum of HDLC film over the 1000–4000 cm^{-1} range (Fig. 2A) exhibits an increasing photoluminescence background which is typical of disordered sp^2 carbon structure [3,4]. In the case of a disordered hydrogenated carbon sample we can expect various effects on the position and broadening of G and D bands etc. [2,4]. Thus as per our expectation, the broad peak envelops corresponding to first-, second- and higher-order Raman features after subtraction of the photoluminescence background are shown in Fig. 2B–D respectively.

The first-order Raman spectrum (Fig. 2B) is comprised of six overlapping Lorentzian peaks; the red-shifted G band (~1540 ± 1 cm^{-1}) to lower frequencies follows a 1/n dependence on the number of sp^2 carbon layers n [5] and is a signature of strained carbon–carbon bonds [6]; the D band (~1366 ± 1 cm^{-1}) is a signature of lattice motion away from the center of the Brillouin zone lying between 1270 and 1450 cm^{-1} depending upon the excitation wavelength and indicating symmetry breaking i.e. disorder induced in the hexagonal sp^2 carbons due to hydrogenation [7]; presence of nanocrystalline diamond (NCD) line (~1255 cm^{-1}) having significant downshift ($\Delta\nu$~77 cm^{-1}) w.r.t

* Corresponding author. Fax: +91 33 23374637.
E-mail address: niharranjan.ray@saha.ac.in (N.R. Ray).

0167-577X/$ – see front matter © 2011 Elsevier B.V. All rights reserved.
doi:10.1016/j.matlet.2011.12.041

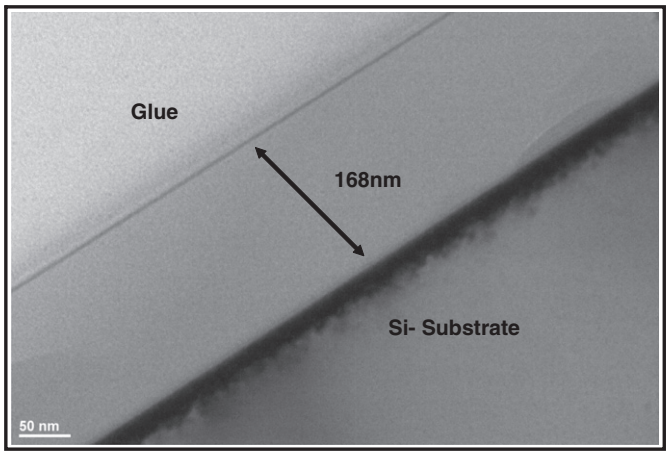

Fig. 1. Typical TEM cross sectional view of the HDLC film measured with a Philips CM 200 kV TEM machine operated at 200 kV with LaB_6 filament; the cross sectional sample was prepared by the TEM sample preparation equipments of Gatan, USA.

pure diamond (sp^3 C–C) line (~1332 cm^{-1}) signifies conversion of sp^2 C═C into sp^3 C–H due to hydrogenation and large broadening (full width at half maximum, FWHM ~173 ± 16 cm^{-1}) of the Raman line is interpreted as phonon confinement in NCD (sp^3 C–H) domains of less than 1 nm in size [8]; the estimated ratio of G and D band intensities (I_D/I_G) being less than 1 can be interpreted as size of defects should be less than 1 nm in size [4] i.e. if we assume sp^3 C–H domains as defects in the sp^2 C═C carbon matrix, then our above interpretations from broadening of Raman line and ratio of G and D band intensities seem to be plausible. The sum and difference in combinations of C═C chain stretching and C–H wagging modes [ν_1 and ν_2 modes of *trans*-polyacetylene (*trans*-PA)] appear at ~1145 ± 4 cm^{-1} and ~1485 ± 3 cm^{-1} respectively [9]. The dumbbell defect in NCD, called D′ appears at ~1593 ± 1 cm^{-1} [8]. Thus the first-order Raman spectrum (Fig. 2B) signifies effects of (i) strain in carbon–carbon bonds, (ii) multilayer of sp^3 C–H carbons embedded in sp^2 C═C carbon matrix and (iii) disorder induced in the sp^2 C═C carbon matrix by its hydrogenation.

The second-order Raman spectrum (Fig. 2C) comprising of 4 overlapping Lorentzian peaks is a signature of four possible double resonance (DR) Raman scattering processes in the hexagonal sp^2 C═C carbon matrix [7]. The four bands 2701 ± 4 cm^{-1}, 2644 ± 3 cm^{-1}, 2677 ± 2 cm^{-1} and 2733 ± 4 cm^{-1} correspond to that for pristine monolayer of graphite (PMG), red-shifted 2D band due to high and low strain on PMG, and blue shifted 2D band of multilayer of sp^3 C–H carbons embedded in sp^2 C═C carbon matrix respectively [4,6]. This result on second-order Raman spectrum (Fig. 2C) indicates double resonance Raman scattering process in the thin HDLC film as predicted for all kinds of sp^2 carbon materials [7].

The higher-order Raman spectrum (Fig. 2D) comprising of five peaks (2858 ± 0.3 cm^{-1}, 2993 ± 0.6 cm^{-1}, 3076 ± 2 cm^{-1}, 3130 ± 3 cm^{-1}, 3247 ± 2 cm^{-1}) is a signature of stretch modes of sp^3 C–H, sp^2 = C═H bands [10], G + D′ band, due to defects introduced by the hydrogenation of sp^2 (C═C) carbon matrix [4].

Thus Raman spectroscopy suggests that HDLC carbon film is made of multilayer of coherent domains of sp^3 C–H and sp^2 C═C carbons.

From the position of G band in the Raman spectrum of HDLC film we can estimate, using an empirical relation sp^3 content = 0.24–48.9 (ω_G–0.1580), approximately 45% sp^3 and 55% sp^2 carbons in the film [11]. Our result is similar to the 40:60 ratio observed in amorphous hydrogenated carbon films having hexagonal graphite and diamond as coherent domains [12].

Hydrogenation of hexagonal sp^2 carbon matrix deposited onto Si (1 0 0) substrate should produce stress in the film, which can be studied from the shape and width of Raman lines [13]. Accordingly, stress

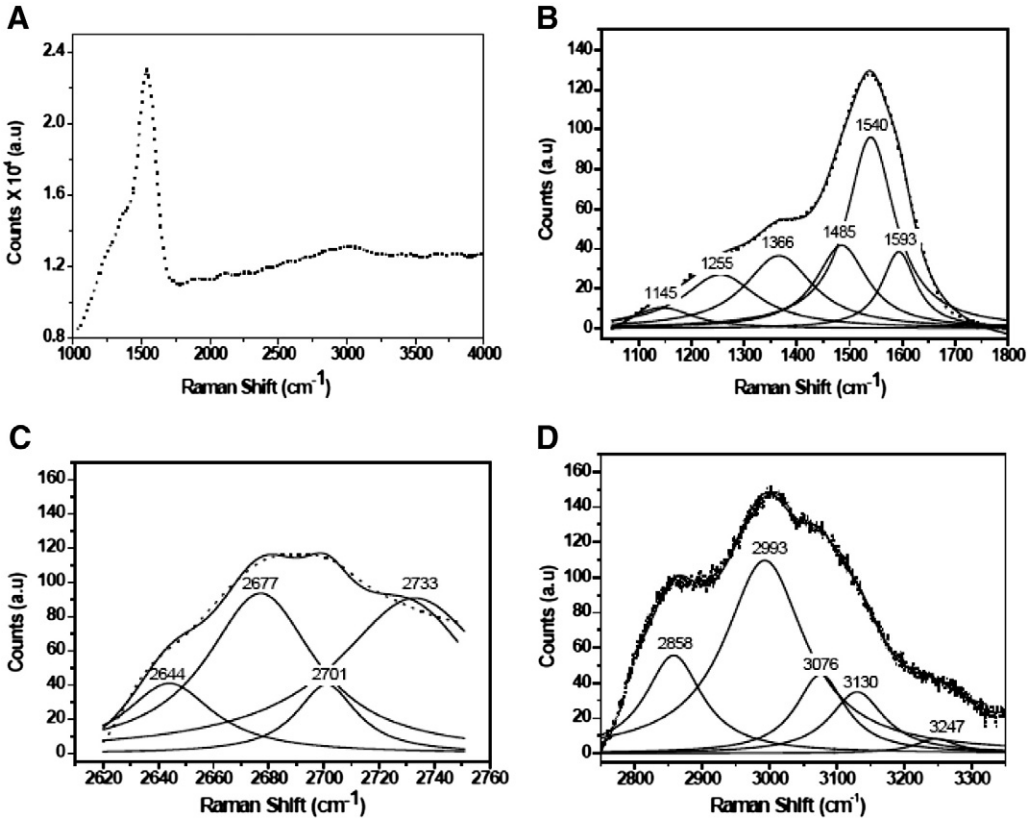

Fig. 2. A. Typical Raman spectrum of HDLC film over the range 1000–4000 cm^{-1}. B. First-order Raman spectrum of HDLC film over the range 1030–1800 cm^{-1}. C. Second-order Raman spectrum of HDLC film over the range2600–2750 cm^{-1}. D. Higher-order Raman spectrum of HDLC film over the range 2800–3300 cm^{-1}.

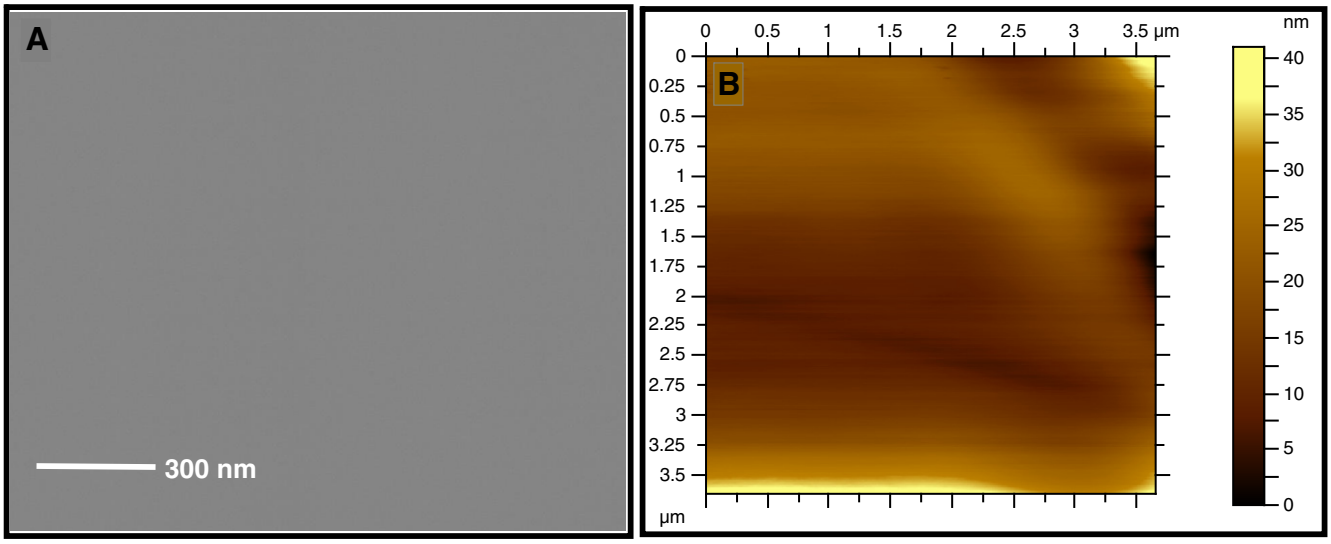

Fig.3. A. SEM image of HDLC film recorded with an FEI Quanta 200f operating at 10 kV in low-vacuum mode to avoid sample charging of the un-coated specimen. The HDLC surface is smooth and contiguous at 80,000× by SEM. B. Non-contact mode AFM topography image of HDLC surface: scan size 3.5 µm×3.5 µm.

σ (GPa) within the HDLC film is estimated from the Raman shift $\Delta\nu$ (cm^{-1}) of the NCD line using the relationship $\Delta\nu = \nu - \nu_o = -\alpha\sigma$, where α is pressure coefficient and ν_o is taken to be the Raman peak position (~1332 cm^{-1}) of natural diamond when no pressure is applied. The NCD line near ν~1255 cm^{-1} is less than ν_o, indicating a positive tensile film stress. Net stress within a deposited film σ_{net} has been construed to arise from three potential contributions following the simple additivity relationship $\sigma_{net} = \sigma_{TH} + \Sigma\sigma_{IN} + \sigma_{lm}$; where σ_{TH} is thermal stress, $\Sigma\sigma_{IN}$ is the sum of all internal stresses, and σ_{lm} is stress due to lattice mismatch. HDLC Raman spectra are consistent with tensile stress, suggesting that σ_{TH} does not dominate σ_{net} and we have consequently assumed that σ_{TH} can be neglected as a first-order approximation. Furthermore, we observe that the Raman shift associated with lattice stress is only 77 cm^{-1}, to be compared to 200 cm^{-1} anticipated for large lattice mismatches. Thus, it is apparent that σ_{lm} is small compared to σ_{net} and that σ_{lm} could be ignored as a first-order approximation. Collectively, these considerations led to the conclusion that total tensile stress in HDLC film is due primarily to $\Sigma\sigma_{IN}$. Bagilo et al. [14] states that $\Sigma\sigma_{IN}$ is due to attractive forces across grain-boundaries and that $\Sigma\sigma_{IN}$ can rise to GPa proportions for nanometer-sized crystallites, sufficient to cause grain coalescence. In our case, sp^2 and sp^3 carbons exist coherently in the film as concluded from Raman analysis above and thus the internal stress in the film should develop as a result of partial conversion of sp^2 C═C into sp^3 C–H. Indeed, using $\alpha \approx 1.9$ cm^{-1}/GPa and $\Delta\nu \approx 77$ cm^{-1}, we estimate the σ_{net} associated with the NCD line in HDLC to be tens of GPa, implying that sp^3 C–H domains within HDLC must be nanometer in dimension, consistent with Raman analysis above [13]. Furthermore, FWHM of the 1255 cm^{-1} NCD line (~173 ± 16 cm^{-1}) is consistent with phonon confinement in nanometer-sized regions [13]. All evidence taken together led us to conclude that internal tensile stress within HDLC film is caused due to partial hydrogenation of sp^2 C═C carbon matrix, resulting in sp^3 C–H carbons.

Fig. 3A is typical featureless secondary electron (SE) image of the HDLC surface and Fig. 3B is typical AFM topography image of the HDLC surface, giving its roughness value (~0.01 nm). These results (Fig. 3A and B) are consistent with an atomically smooth, non-porous continuous film. It may be referred [15] that ultrananocrystalline diamond of uniform grain size (3–5 nm) can produce continuous film having surface roughness ~7–15 nm only after achieving its thickness greater than 300 nm. Therefore our results show that instead of discrete grains, coherent domains of sp^3 C–H and sp^2 C–C carbons can produce continuous, non-porous thin film having atomically smooth surface.

4. Conclusions

In conclusion, that coherency of sp^3 C–H and sp^2 C═C carbons in the HDLC can produce a continuous, non-porous thin film having atomically smooth surface, instead of discrete uniform grains as in the case of ultrananocrystalline diamond film, is a new result.

Acknowledgments

NRR thanks the Department of Atomic Energy, Govt. of India, for funding XI plan project Diamond Nanotechnology for Bioapplications. We thank Prof. T. K. Chini and Mr. S. Banerjee for recording SEM images, Dr. A K Srivastava for recording cross-sectional TEM view and Mr. S. S. Sil and U. S. Sil for technical help.

References

[1] Biswas HS, Datta J, Chowdhury DP, Reddy AVR, Ghosh UC, Srivastava AK, et al. Covalent immobilization of protein onto a functionalized hydrogenated diamond-like carbon substrate. Langmuir 2010;26(12):17413–8.
[2] Pimenta MA, Dresselhaus G, Dresselhaus MS, Cancado LG, Jorio A, Saito R. Studying disorder in graphite-based systems by Raman spectroscopy. Phys Chem Chem Phys 2007;9:1276–91.
[3] Marchon B, Gui J, Grannen K, Rauch GC, AgerIII JW, Silva SRP, et al. Photoluminescence and Raman spectroscopy in hydrogenated carbon films. IEEE Trans Magn 1997;33(5):3148–50.
[4] Dresselhaus MS, Jorio A, Hofmann M, Dresselhaus G, Saito R. Perspectives on carbon nanotubes and graphene Raman spectroscopy. Nano Lett 2010;10:751–8.
[5] Dresselhaus MS, Dresselhaus G, Hofmann. Raman spectroscopy as a probe of graphene and carbon nanotubes. Philos Trans R Soc A 2008;366:231–6.
[6] Ni ZH, Yu T, Lu YH, Wang YY, Feng YP, Shan ZX. Uniaxial strain on graphene: Raman spectroscopy study and band gap opening. ACS Nano 2008;2(11):2301–5.
[7] Thomson C, Reich S. Double resonance Raman scattering in graphite. Phys Rev Lett 2000;85:5214–7.
[8] Ferrari AC, Robertson J. Origin of the 1150 cm^{-1} Raman mode in nanocrystalline diamond. Phys Rev B 2001;63(12):121405-1-4.
[9] Robertson J. Hard amorphous (diamond like) carbons. Prog Solid State Chem 1981;21(4):199–333.
[10] Camp William. Organic Spectroscopy. New York: Palgrave; 2005. p. 58–88.
[11] Singha A, Ghosh A, Roy A, Ray NR. Quantative analysis of hydrogenated diamondlike carbon films by visible Raman spectroscopy. J Appl Phys 2006;100:044910-1-8.
[12] Yoshizawa N, Yamada Y, Shiraishi M. Structure of amorphous carbon film prepared from RF plasma deposition. Carbon 1993;31(7):1049–55.
[13] Bergman L, Nemanich RJ. Raman and photoluminescence analysis of stress state and impurity distribution in diamond thin films. J Appl Phys 1995;78(11):6709–19.
[14] Bagilo JA, Farnsworth BC, Hankin S, Hamill G, O'Nill D. Studies of stress related issues in microwave CVD diamond on <100> silicon substrates. Thin Solid Films 1992;212:180–5.
[15] Chen YC, Zhong XY, Konicek AR, Grierson DS, Tai NH, Lin IN, et al. Synthesis and characterization of smooth ultrananocrystalline diamond films via low pressure bias-enhanced nucleation and growth. Appl Phys Lett 2008;92:133113-1-3.

Nuclear Instruments and Methods in Physics Research B 328 (2014) 27–32

Contents lists available at ScienceDirect

Nuclear Instruments and Methods in Physics Research B

journal homepage: www.elsevier.com/locate/nimb

Study of depth profile of hydrogen in hydrogenated diamond like carbon thin film using ion beam analysis techniques

J. Datta [a], H.S. Biswas [b], P. Rao [c], G.L.N. Reddy [c], S. Kumar [c], N.R. Ray [d,*], D.P. Chowdhury [a], A.V.R. Reddy [e]

[a] Analytical Chemistry Division, BARC, Variable Energy Cyclotron Centre, 1/AF, Bidhan Nagar, Kolkata 700064, India
[b] Dept. of Chemistry, Surendranath College, Kolkata 700009, India
[c] National Centre for Compositional Characterization of Materials, BARC, ECIL Post, Hyderabad 500062, India
[d] Surface Physics Material Science Division, Saha Institute of Nuclear Physics, 1/AF, Bidhan Nagar, Kolkata 700064, India
[e] Analytical Chemistry Division, Bhabha Atomic Research Centre, Trombay, Mumbai 400085, India

ARTICLE INFO

Article history:
Received 28 November 2013
Received in revised form 24 February 2014
Accepted 24 February 2014

Keywords:
Hydrogen
Depth profile
Diamond like carbon
Thin film
Ion beam analysis

ABSTRACT

The Hydrogenated Diamond Like Carbon (HDLC) thin films are deposited on Silicon substrate at room temperature using asymmetric capacitively coupled RF plasma with varying flow rates of methane. These films are undergone annealing at high vacuum ($\sim 10^{-7}$ torr) and high temperature (750 and 1050 °C) furnace. The as-prepared and annealed HDLC films have been depth profiled for hydrogen using the resonance at 6.44 MeV in $^{1}H(^{19}F,\alpha\gamma)^{16}O$ nuclear reaction. The as prepared films exhibit non-uniform depth distribution of hydrogen: it decreases with depth. Annealing in vacuum brings about is a significant desorption of hydrogen from the films. Loss of hydrogen, albeit in much lower proportions, is also induced by the bombarding beam. The films also experience a mild loss of carbon, as shown by proton backscattering spectrometry, during high vacuum annealing. The depth profiles of hydrogen in the annealed films are indicative of the prevalence of graphitic carbon near film–substrate interface.

1. Introduction

In recent years, diamond like carbon (DLC) films has attracted a great deal of research interest as they have enormous possibility for technological applications [1,2]. Depending upon atomic structure of DLC films, the behavior of the film is diamond like. For example, opaque samples with hardness one-fifth of that of diamond and the transparent ones nearly as dense and hard as diamond [3] have considered as DLC films. The films with 20–40% of hydrogen content are commonly known as hydrogenated DLC (HDLC) films. In general, the physical and chemical properties of carbon materials, having sp^3 (diamond like) and sp^2 (graphite like) bonds in different ratio in the carbon matrix, may be different compared to pure graphite or diamond. We have demonstrated earlier [4,5] that HDLC films, deposited onto Si (100) substrate by reactive gas-plasma process, are composed of an ordered hexagonal structure of carbon atoms with lattice parameters $a = 2.62$ Å and $c = 6.752$ Å different to those present in a hexagonal graphite structure. Further structural investigation by confocal micro Raman spectroscopy [5,6] shows that coherency of sp^3 C–H and sp^2 C=C carbons in the HDLC can produce a continuous nonporous thin film (thickness ≈ 168 nm) having atomically smooth surface. Recently, the signature of interlayer disorder region in the HDLC film has been observed when Raman spectra of as-prepared HDLC and annealed HDLC samples are compared [5,6]. Due to existence of interlayer disorder, the 3D crystallinity of the HDLC should be lost, while only the 2D crystallinity should be preserved [7]. The Raman spectra do not tell us about why and how the interlayer disorder region is created in the HDLC film. The main effect of hydrogen in HDLC films is to modify its C–C network at different depth of the film. How these modifications occur at various depth of the HDLC film during its synthesis onto Si(100) substrate cannot be studied by Raman spectroscopy or X-ray photoelectron (XP) spectroscopy method, because (i) the skin depth of the 488 nm excitation source, which we have used in Raman measurements, is ~6 μm and using this technique we get information for the whole material rather than at different depth of the thin film having thickness ~168 nm (ii) XP spectroscopy [8,9] is a surface sensitive probe in our case, because here the skin depth for X-rays is ~5 nm. These earlier works [5–7] motivate us to explore the distribution of hydrogen in the film along its depth by ion beam analysis (IBA) techniques, viz., nuclear reaction analysis (NRA), Rutherford backscattering (RBS) techniques, in order to know how hydrogen modify C–C network in the HDLC film onto Si(100) substrate.

* Corresponding author. Tel.: +91 9836645969; fax: +91 3323374637.

http://dx.doi.org/10.1016/j.nimb.2014.02.127
0168-583X/

2. Experimental

The HDLC thin films are deposited on mirror-polished Si (1 0 0) substrate at room temperature using asymmetric capacitively coupled RF 13.56 MHz plasma system. The depositions are made systematically as follows: a pretreatment of the bare mirror-polished Si(1 0 0) substrate has been done for 15 min using pure hydrogen plasma at pressure of 0.2 mbar and dc self-bias of −200 V. The deposition has been made for 30 min at pressure of 0.7 mbar keeping the flow rate of helium (He) at 1500 SCCM (SCCM denotes cubic centimeter per minute at STP), hydrogen (H_2) at 500 SCCM, and varying the flow rate of methane (CH_4).

Four samples for which the CH_4 flow rates are 20, 30, 40 and 70 SCCM, thus grown with varying H_2 to CH_4 ratio during deposition at room temperature (RT), will be represented as samples A, B, C and D, respectively, in the rest of the article. The samples A–D, annealed at high temperatures 750 °C and 1050 °C in high vacuum ($\sim 1 \times 10^{-7}$ torr) furnace, in order to study removal of hydrogen from the samples, will be represented as annealed (750 °C/1050 °C) samples A–D in the rest of the article.

Nuclear reaction analysis (NRA) [10,11], a non-destructive nuclear method for depth profiling, has been applied for the quantitative determination of hydrogen at different depths of the as-prepared and annealed samples A–D, using the resonance at 6.44 MeV for the reaction $^1H(^{19}F,\alpha\gamma)^{16}O$ in the present experiment. The Rutherford backscattering (RBS) [12–14] on the as-prepared and annealed samples A–D, with 1.0 MeV proton beam is carried out to measure the thickness of HDLC films. Both NRA and RBS measurements are carried out by a 3 MV Tandetron accelerator at the surface and profile measurement laboratory of the National Center for Compositional Characterization of Materials (NCCCM), Hyderabad, India.

2.1. NRA measurements

Depth profiling of hydrogen in the samples A–D are accomplished by bombarding the sample at normal incidence with a well-collimated (dia. 2 mm, current 3 nA) tripositive fluorine ion ($^{19}F^{3+}$) beam in the scattering chamber under vacuum 10^{-6} mbar. The characteristic gamma rays for the reaction $^1H(^{19}F,\alpha\gamma)^{16}O$ are monitored using a bismuth germanate (BGO) semi-conductor detector having efficiency ~10% and placed at a distance of 2 cm behind the sample along the direction of the incident beam. The characteristic gamma rays from the produced isotope ^{16}O are 6.1, 6.9 and 7.1 MeV. A guard ring, with a bias of −900 V is positioned in front of the sample to suppress secondary electrons. The beam current incident on the sample is measured by Faraday cup arrangement [15]. The γ-ray yield of the reaction was obtained from the integrated counts between 4.8 and 7.1 MeV energy window of the PC-based multichannel analyzer, and this is found to give significant counts in the present experimental set.

The measurements for depth profiling in the sample and standard (viz., mylar) [16–18] are performed in the following steps: (i) γ-yield is measured at off-resonance region (beam energy below 6.44 MeV) to have the contribution of the background for each sample (ii) energy of the incident ion beam is increased in steps of 20 keV/40 keV above the resonance energy 6.44 MeV till the integrated counts in the region of interest are equal or less than that of the off-resonance counts. In the above two steps, the typical beam currents for both sample and standard are of the order of 3 and 2 nA over a ~2 mm diameter spot. Two sets of measurement (in steps of 20 and 40 keV) are carried out for each sample in the different regions to get the reproducibility of the results. The desorption phenomenomenon is studied for our specimen and standard which are treated at the same conditions of the beam and the integrated counts in the multichannel analyzer are recorded in every 250 nC, until total charge in the Faraday cup is 5000 nC.

2.2. RBS measurements

RBS measurements on HDLC thin films (as prepared and annealed) are carried out in the scattering chamber under vacuum $\sim 5 \times 10^{-6}$ mbar by with 1.0 MeV proton beam from the same Tandetron accelerator. The backscattered particles are detected by a silicon surface barrier (SSB) detector at an angle of 170°.

2.3. Methodology and technical details

2.3.1. Expression for hydrogen content determination using NRA technique

The atomic fraction of hydrogen in the HDLC film (considering as a binary film, C_xH_y) is estimated by the following equation [19]

$$f^{H}_{HDLC} = \frac{f^{H}_{Std} \cdot \varepsilon^{C}_{HDLC}}{Y\varepsilon_{Std} + f^{H}_{Std} \cdot (\varepsilon^{C}_{HDLC} - \varepsilon^{H}_{HDLC})} \quad (1)$$

where Y is the ratio of gamma yields for standard and sample, f is the atomic fraction of hydrogen in the film material given in subscript, ε_{Std} and ε^i are the stopping power for the standard and the ith element having in the superscript. The ratio of yields, Y is obtained from the γ-ray yields in the NRA measurements. The stopping power and atomic fraction of hydrogen for the standard Mylar ε_{std} 1.841×10^2 eV/(10^{15} at./cm^2) and f^{H}_{Std} 0.3636, respectively, are known. The stopping power data in this work is calculated using SRIM-2008.04 [20].

The depth χ_R is related to the incident beam energy E_i by the equation

$$\chi_R = \frac{E_i - E_R}{\varepsilon} \quad (2)$$

where E_R is the resonance energy and ε is the stopping power. The depth in at./cm^2 is converted into linear dimension using density (3.0 gm/cc [4]) of the film of known film thickness determined by other methods.

The stopping power of a multi-elemental film using Bragg's law of linear additively can be written as

$$\varepsilon = \sum_{i=1}^{N} f_i.\varepsilon_i \quad (3)$$

where f_i and ε_i are the atomic fraction and the atomic stopping power of the ith constituent, respectively and N is the total no. of constituents in the film.

2.3.2. Expression for thickness determination using RBS technique

The energy loss of a 1.0 MeV proton beam in a thin film of thickness t, related to the stopping power of the material is given below [13–14]

$$t = \frac{\Delta E}{[\varepsilon_i]} \quad (4)$$

$$[\varepsilon_i] = \frac{K_i}{\cos\theta_1}\left[\frac{dE}{dX}\right]_{in} + \frac{1}{\cos\theta_2}\left[\frac{dE}{dX}\right]_{out} \quad (5)$$

where t is the thickness, ΔE is the FWHM of the peak, ε_i is the stopping power of the ith element and the subscripts "in" and "out" refer to the (constant) values of stopping power (dE/dX) along the inward and outward paths, θ_1 and θ_2 are the angles between the sample normal and the direction of the incident beam and of the scattered particle respectively.

3. Results and discussions

3.1. NRA measurements

Fig. 1 shows typical γ-ray yield (due to nuclear reaction $^{1}H(^{19}F,\alpha\gamma)^{16}O$), as a function of (i) energy difference between energy of incident ^{19}F ion beam (E_{in}) and the resonance energy (E_R) as recorded in a PC-based multichannel analyzer, (ii) hydrogen concentration at different depth of the film, estimated using stopping power value of HDLC. For $E_{in} < E_R$, the γ-ray yield corresponds to 'background yield' and for $E_{in} = E_R$ the γ-ray yield corresponds to the presence of hydrogen atoms onto the surface of HDLC sample. With the increase of energy of the beam penetrating into the sample, the γ-ray yield starts decreasing from the surface of the target, as evident in Fig. 1. The typical behavior of declining of γ-ray yield at different depth of as prepared and annealed HDLC sample are observed to be similar.

The as-prepared samples (A–D) when annealed at different temperatures 750 °C and 1050 °C in high vacuum, show that the yields, and hence the hydrogen content of the annealed films, in all the cases, are lower than that of the as-prepared samples. A typical result for the as-prepared sample B is shown in Fig. 2. As expected, the hydrogen content should decrease with the increase of the annealing temperature. Therefore, the results in Fig. 2 clearly indicate significant loss of bonded hydrogen atoms from the HDLC sample due to annealing effect. Since the decades, it has been well known that the heating of amorphous hydrogenated carbon above 300 °C will produce the exo-diffusion of hydrogen molecules through the recombination of small sized hydrogen atoms within the bulk of the materials. Such formation of H_2 molecules is favorable due to the higher bond energy of H–H than that of the C–H bond. Therefore, annealing leads to the transformation of sp^3C–H sites into sp^2 sites. Consequently, there is the reduction of the photoluminescence background, validated in our earlier results [5]. It is also to be noted from the Fig. 2 that the maximum depth at which the yields of hydrogen content are more or less equal to the background counts (210, 152 and 148 counts/μC for as prepared and annealed sample at 750 and 1050 °C, respectively) depends upon the annealing temperature; these depths are ~83 nm for the as prepared sample, ~68 nm for annealing temperature 750 °C and ~59 nm for annealing temperature 1050 °C. It is well established that the diamond is metastable and graphite is thermodynamically stable, and therefore, diamond and/nano-crystalline Diamond (NCD) are converted into graphite when heated at elevated temperature ca 1300 °C [21–23]. Therefore, our results

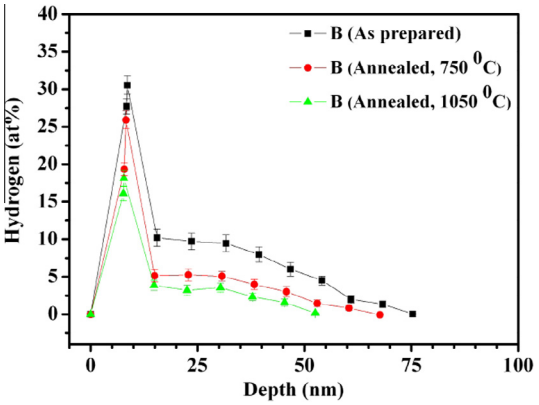

Fig. 2. NRA measurements on HDLC sample-B thin films onto Si backing materials (30 SCCM, both as prepared and annealed at 750 and 1050 °C) were carried out with $^{19}F^{3+}$ ion beam at beam current of 3 nA. For each of the above measurements fresh samples were annealed.

showing decreasing of depth of hydrogen content in the HDLC sample with increasing annealing temperature, may be attributed to conversion of sp^3 C–H (diamond like) to sp^2 C=C (graphite like) structure in the HDLC sample.

The variation of hydrogen content with the depth of the as-prepared samples (A–D) is shown in Fig. 3. The hydrogen concentration is maximum just inside the surface which is approximately within 10 nm from the surface in most of the samples. This result may indicate that the unsaturated bonds of carbon are being terminated by hydrogen, thus leaving almost no unsaturated bonds in the samples at the end of their deposition. From the Fig. 3, it is evident that at a given depth within the sample, the hydrogen content increases with the increase of flow rate of methane at a constant flow rate of hydrogen (500 SCCM) during deposition of samples (A–D). This result is in accordance with our earlier results as reported Singha et al. [24]. The continuing decrease of the hydrogen with depth of the samples (A–D) indicates that the films having higher graphitic nature towards the interface between the HDLC film and Si(100) substrate. This observation could be explained considering the fact that, in a bias enhanced nucleation of diamond on Si, there is always one intermediate buffer layer of SiC or graphite as shown in a model of diamond/graphite/Si(100) interface [25,26]. This model provides the minimal lattice mismatch and minimal interfacial energy.

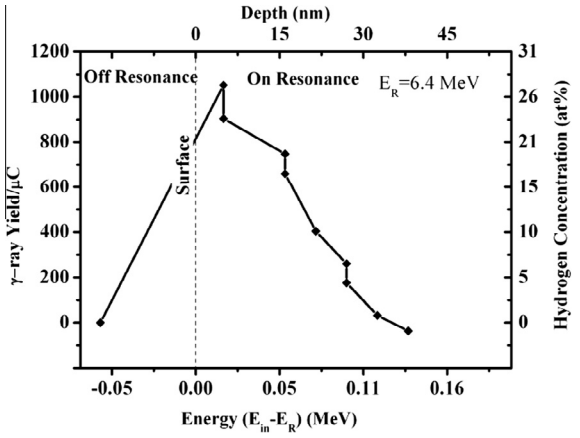

Fig. 1. The typical NRA profile of as prepared HDLC sample-A is shown. Both raw data of 6.1 MeV prompt γ-ray yields per μC of charge vs. difference of incident beam energy and resonance energy (6.4 MeV), and corresponding hydrogen concentration (at%) vs. depth (nm) into HDLC sample are shown above.

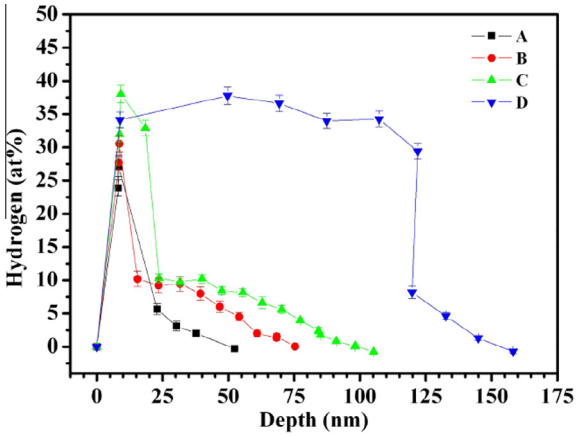

Fig. 3. Hydrogen concentration distribution observed in NRA measurements for as prepared HDLC samples (A–D) deposited in different flow rate (SCCM-standard cubic centimeter per minute) with $^{19}F^{3+}$ ion beam at beam current of 3 nA.

The maximum depth of hydrogen content in the HDLC film depends upon flow rate of methane (Fig. 3) and for a given as-prepared HDLC film the maximum depth of hydrogen content decreases with increasing annealing temperature (Fig. 2). Therefore, the direction of flow out of hydrogen during annealing of HDLC sample is from the interface towards the surface. Vainonen et al. [27,28] and Thomas et al. [29] have studied the migration of hydrogen in DLC films by NRA, RBS, and SIMS techniques and found migration of hydrogen towards the interface between the film and substrate and also release of hydrogen from the surface region. On contrary to this observation, the migration of hydrogen towards surface from the interface in our HDLC sample seems to be plausible due to the fact that during the annealing process, the heat is transferred from the sample holder to the backing silicon material and then into the sample; hence, the interface of the sample and the Si is at higher temperature than the surface of the HDLC samples. Therefore, there might be a possible chance of little rearrangement of hydrogen bonds through the process of dehydrogenation and hydrogenation [30] within the sample. In some hydrogenous carbon materials loss of hydrogen under ion irradiation is reported earlier [31,32]. Due care, therefore, is to be taken while carried out the hydrogen determination. In such cases, the concentration of hydrogen should be measured as a function of ion dose and the initial hydrogen content can be obtained by extrapolation to the zero dose condition. This result is shown in Fig. 4. The yields at zero dose condition are also shown along the dotted line for the as-prepared and annealed samples. These values were obtained from the polynomial fitting of the γ-ray yields vs. charge density. The stability of the standard samples under ion beam irradiation has already been studied [16]. This can be minimized by using the lower mass of the projectiles, which don't transfer large electronic energy as excitation energy in the sample. Nearly constant integrated counts (as shown in Fig. 4) for every 250 nC charge, were observed for the standards (Si_3N_4) for total 20 number of times exposure at primary beam energy of ~6.5 MeV. In contrary, the counts were slowly decreased for annealed samples and rapidly for the as-prepared samples as shown in Fig. 4. This could be explained if we assume that the hydrogen is present in the film as bonded by chemical forces and also as non-bonded due to physical forces or weak Vander Wall forces. Therefore, the weakly bonded hydrogen readily desorbs from the thin films on heating. This desorption is maximum for the as-prepared films compared to annealed films.

3.2. RBS measurements

The backscattered spectra for as prepared and annealed samples are recorded using 1.0 MeV proton beam and are shown in Fig. 5. The higher channel number (i.e., higher energy) side of the RBS spectrum is due to the backing silicon materials (thickness ~2000 nm). The Si-edge of sample A was different compared to sample B. There are two factors responsible, one is channeling and other is cross section which is even more non-Rutherford in this energy range. Again the cross section varies sharply at the Si-edge. The sharp peak is observed over the broad plateau of silicon is due to the carbon. It is clear from the inset picture where there is no peak for the virgin silicon sample but sharp peaks for carbon onto silicon. The sharp peaks of carbon in the inset of Fig. 5, show increase of peak area from 417 ± 24 to 774 ± 34 to 1936 ± 65 counts/μC, and FWHM from 10.7 ± 0.5 to 11.2 ± 0.7 to 14.71 ± 0.8 keV with the increase of flow rates of methane in the as-prepared samples viz., A, B, D, respectively. Therefore, the thickness of the film increases with flow rates of methane.

The RBS spectra for the as prepared and annealed HDLC samples are measured. The FWHM for samples B (30 SCCM) both as prepared and annealed at 750 and 1050 °C were 11.2 ± 0.7, 11.1 ± 0.5, 10.4 ± 0.5 keV at 722 ± 3 keV and the integrated area under the peaks are 813 ± 46, 774 ± 34, 670 ± 27 counts/μC respectively. These values were obtained using Lorentzian fittings. It is observed that the as prepared films have higher peak yields and higher FWHM compared to that of annealed one as shown in Fig. 6. This result indicates thickness of as-prepared samples is larger than that for annealed one.

Kazunori et al. [33] and Wang et al. [34] have studied the erosion behavior of deuterated soft amorphous carbon thin film by heat treatment in air and vacuum, using elastic recoil detection (ERD) and proton enhanced scattering (PES) techniques. When the films are heated in air above 550 K for 1 h, the film thickness, and the areal densities of carbon and deuterium both decrease. Moreover oxygen is incorporated into the films. But when annealed in vacuum, erosion starts at above 600 K and decrease in thickness along with the decrease of all other components. Thermal desorption spectroscopy of the soft films reveals the evolution of hydrocarbon. They have also studied the thermal erosion behavior of hard a-C:H thin films under vacuum. This showed predominantly the release of hydrogen molecule to give semi-hard a-C:H films with very low hydrogen content. This implies that the soft films sublimate and hard film desorbs in vacuum during annealing. We have also observed the similar desorption and decrease in at.% of

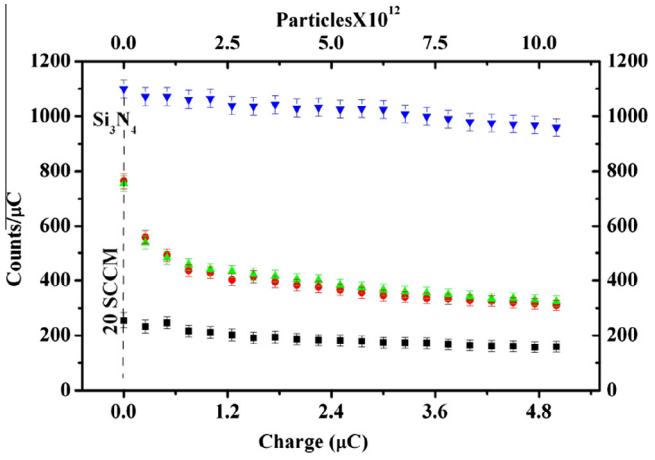

Fig. 4. The γ-ray counts/μC vs. charge (μC) (Bottom) or fluence of $^{19}F^{3+}$ ion beam (Top) during hydrogen depth profiling for as prepared (at two different regions of 5 mm apart) and annealed at 750 °C of HDLC samples-A at beam current of 3 nA and also Si_3N_4 standard at beam current of 3 nA observed in NRA technique.

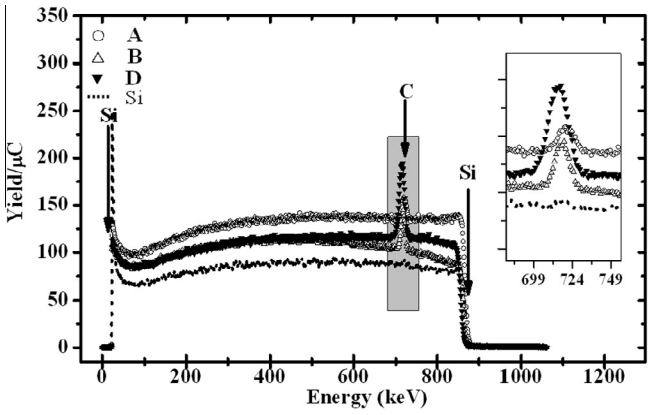

Fig. 5. RBS measurements on as prepared HDLC thin films onto Si backing materials prepared at different flow of methane were carried out with 1.0 MeV proton beam. The backscattered particles were detected by a silicon surface barrier (SSB) detector at an angle of 170°.

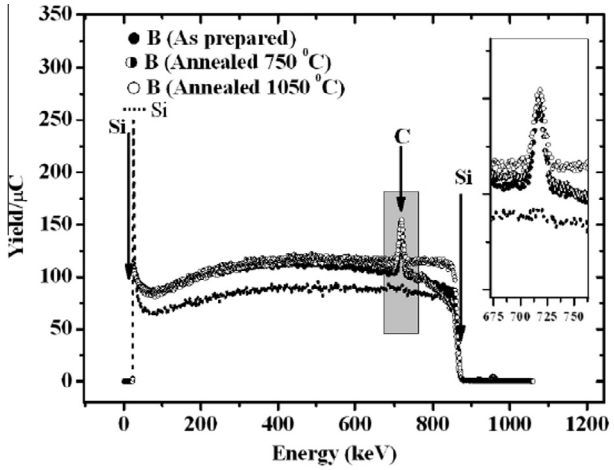

Fig. 6. RBS measurements on HDLC thin films B onto Si backing materials (30 SCCM, both as prepared and annealed at 750 and 1050 °C) were carried out with 1.0 MeV proton beam from Tandetron accelerator. The backscattered particles were detected by a silicon surface barrier (SSB) detector at an angle of 170°. For each of the above measurements fresh samples were annealed.

hydrogen and that in thickness for HDLC thin film, when treated under vacuum at high temperature. The diagnosis by NRA measures the content of hydrogen whereas RBS techniques measures content of carbon. Therefore, the decrease of HDLC film thickness due to annealing (Fig. 6) should be caused by removal of carbon and hydrogen both.

3.3. Estimation of hydrogen content and thickness of HDLC sample

The atomic fraction of hydrogen in the as prepared HDLC film is estimated using Eq. (1) based upon NRA measurements. The results are given in Table 1.

The thickness of the as prepared HDLC film along with their uncertainties is measured by NRA using Eq. (2) and by RBS using Eq. (5). These results are given in Table 2. The experimental detection limit of the sample has been estimated on the basis of three times standard deviation value (3s) of background counts in the region of a peak of the γ-ray spectrum of samples as per our experimental parameters and the value is ~3.0 at.%.

The overall error in the NRA and RBS measurement have been estimated by error propagation formula from the errors in counting statics of the gamma ray yields, stopping power, resonance width and fitting errors and it lies within 10–20%. Thickness of HDLC film by NRA is based upon maximum depth of hydrogen availability whereas that by RBS is based upon maximum depth of carbon availability in the film. Since toward interface between substrate and HDLC film, graphitic (sp^2 C=C) character is predominant than diamond (sp^3 C–H) character, it is obvious that the observed thickness by NRA smaller than that by RBS (Table 2) is reasonable.

The structure of the modified films due to the annealing effect making a denser networking structure remained almost same even after further annealing at elevated temperatures. The minute change in the thickness is due to removal of hydrogen (Table 3). Hence there are not significant different of thickness of the films when annealed at 750 and 1050 °C.

Table 1
Atomic fraction of hydrogen in the HDLC films (A–D) as a function of flow rate of methane.

Sample	Flow rate of methane (SCCM)	Hydrogen content (at.%)
A	20	30.1 ± 3.2
B	30	30.5 ± 3.4
C	40	32.9 ± 3.5
D	70	34.1 ± 3.9

Table 2
Comparison of depth of hydrogen by NRA and thickness of the as prepared films (A–D) by RBS technique.

Sample	Flow rate of CH_4 (SCCM)	Depth of hydrogen in the film by NRA (nm)	Thickness of the film by RBS (nm)
A	20	52 ± 10	124 ± 15
B	30	83 ± 10	130 ± 16
C	40	98 ± 12	134 ± 17
D	70	158 ± 17	144 ± 20

Table 3
Effect of annealing on the thickness of the HDLC thin films.

Sample	Flow rate of CH_4 (SCCM)	Depth of hydrogen in the film by NRA (nm)		
		RT (°C)	750 (°C)	1050 (°C)
A	20	52 ± 10	48 ± 6	36 ± 7
B	30	83 ± 10	68 ± 9	59 ± 9
C	40	98 ± 12	82 ± 12	73 ± 12
D	70	158 ± 17	150 ± 16	145 ± 16

4. Conclusions

We conclude that HDLC is composed of coherently coupled sp^3C–H and sp^2C=C carbons producing a continuous non-porous atomically smooth surface [5,6]. As prepared and annealed HDLC films, have been investigated by IBA techniques as described above by determining the depth profiling of hydrogen of the films and its thickness. This study reveals the nature of attachment of hydrogen atom to the carbon network of the film and also shows that the hydrogen content is maximum at the surface of the films. This hydrogen terminates the unsaturated bonds of carbon in the film surface at the end of their deposition. The hydrogen content increases with the increase of flow rate of methane at a constant flow rate of hydrogen and helium. The predominant character of graphitic layer towards the interface between the substrate and HDLC film have been substantiated from the thickness measurements by IBA techniques having high depth resolution of ~10 nm. The hydrogen content decreases with the depth of the films. This result matches with the Robertson model [25] of diamond/graphite/Si(100) interface which minimizes the lattice mismatch and interfacial energy. Therefore our HDLC film may be considered a graphene/graphitic structure, sandwich between the top diamond like structure (hydrogenated graphene: sp^3C–H) and silicon substrate. Hydrogenated graphenes (also called graphane) are expected to have a tunable band gap via the extent of hydrogenation [35]. This material has been predicted to be a semiconductor in contrast to metallic graphene, thus finding applications in electronic devices such as transistors [36]. The studies described above, satisfactorily corroborate the expected variation in thicknesses of the film, both as prepared and annealed. These studies also exhibit the chemical phenomena like desorption of hydrogen from the film during both annealing process and bombardment with ion beams. Thus IBA techniques are very useful tools for the characterization of HDLC thin film. The denser networking structure, composed of carbon and hydrogen, remained almost the same even after the irradiation. This property should be useful for their application as protective coatings in the construction of radiation detectors.

Acknowledgement

NRR thanks the Department of Atomic Energy, Govt. of India, for financial assistance. We thank Mr. S.S. Sil and Mr. U.S. Sil, SINP for their technical help in this work.

References

[1] J. Robertson, Diamond like amorphous carbon, Mater. Sci. Eng. Rep. 37 (2002) 129–281.
[2] Y. Wu, Yu-Ming Lin, A.A. Bol, K.A. Jenkins, F. Xia, D.B. Farmer, Yu Zhu, P. Avouris, High-frequency scaled graphene transistors on diamond like carbon, Nature 472 (2011) 74–78.
[3] M.A. Tamor, W.C. Vassell, Raman "fingerprinting" of amorphous carbon films, J. Appl. Phys. 76 (6) (1994) 3823–3830.
[4] H.S. Biswas, J. Datta, D.P. Chowdhury, A.V.R. Reddy, U.C. Ghosh, A.K. Srivastava, N.R. Ray, Covalent immobilization of protein onto a functionalized hydrogenated diamond-like carbon substrate, Langmuir 26 (22) (2010) 17413–17418.
[5] J. Datta, N.R. Ray, P. Sen, H.S. Biswas, E.A. Vogler, Structure of hydrogenated diamond like carbon by micro-Raman spectroscopy, Mater. Lett. 71 (2012) 131–133.
[6] N.R. Ray, J. Datta, H.S. Biswas, S. Datta, Signature of misoriented bilayer graphenelike and graphane like structure in the hydrogenated diamond-like carbon film, IEEE Trans. Plasma Sci. 40 (7) (2012) 1789–1793.
[7] F. Tuinstra, J.L. Koenig, Raman spectrum of graphite, J. Chem. Phys. 53 (1970) 1126–1130.
[8] K.W. Nebesny, B.L. Maschhoff, N.R. Armstrong, Quantitation of Auger and X-ray photoelectron spectroscopies, Anal. Chem. 61 (1989) 469A–477A.
[9] D.A. Skoog, F.J. Holler, T.A. Nieman, Principles of Instrumental Analysis, fifth ed., Thomson, Singapore, 2005. 535–562.
[10] D.A. Liech, T.A. Tombrello, A technique for measuring hydrogen concentration versus depth in solid samples, Nucl. Inst. Meth. 108 (1973) 67–71.
[11] W.A. Lanford, H.P. Trantvetter, J.F. Ziegler, Keller, New precision technique for measuring the concentration versus depth of hydrogen in solids, J. Appl. Phys. Lett. 28 (9) (1976) 566–568.
[12] E. Rauhala, Proton elastic scattering cross sections of carbon, nitrogen and silicon for backscattering analysis in the energy range 0.7–2.5 MeV, Nucl. Inst. Meth. Phys. Res. B 12 (1985) 447–452.
[13] W.K. Chu, J.W. Mayer, M.A. Nicolet, Backscattering Spectrometry, Academic Press, New York, 1978.
[14] J.F. Ziegler, C.P. Wu, P. Williams, C.W. White, B. Terreault, B.M.U. Scherzer, R.L. Schulte, E.J. Schneid, C.W. Magee, E. Ligeon, J.L. 'Ecuyer, W.A. Lanford, F.J. Kuehne, E.A. Kamykowski, W.O. Hofer, A. Guivarc'h, Profiling hydrogen in materials using ion beams, Nucl. Inst. Meth. 149 (1978) 19–39.
[15] W.A. Lanford, Use of nuclear reaction analysis to characterize the elemental composition and density of thin film amorphous silicon, Solar Cells 2 (1980) 351–363.
[16] S. Kumar, J.V. Ramana, C. David, V.S. Raju, S. Gangadharan, Polyaniline, a conducting polymer, as a standard for hydrogen profiling on material surfaces, Nucl. Inst. Meth. Phys. Res. B 142 (1998) 549–554.
[17] L. Westerberg, L.E. Svensson, E. Karlsson, M.W. Richardson, K. Lundstrom, Stable absolute calibration standards for hydrogen profile analysis using nuclear resonance techniques, Nucl. Inst. Meth. Phys. Res. B 9 (1985) 49–54.
[18] B. Hjörvarsson, J. Rydén, T. Ericsson, E. Karlsson, Hydrogenated tantalum: a convenient calibration substance for hydrogen profile analysis using nuclear resonance reactions, Nucl. Inst. Meth. Phys. Res. B 42 (1989) 257–263.
[19] S. Kumar, J.V. Ramana, C. David, V.S. Raju, Ion beam analysis of porous silicon layers, Nucl. Inst. Meth. Phys. Res. B 179 (2001) 113–120.
[20] J.F. Ziegler, M.D. Ziegler, J.P. Biersack, The Stopping and Range of Ions in Matter, SRIM – Version 2008.04 (2008) <www.SRIM.org>.
[21] <http://en.wikipedia.org/wiki/Man-made diamond>.
[22] F.P. Bundy, J.S. Kasper, Hexagonal diamond—a new form of carbon, J. Chem. Phys. 46 (1967) 3437–3446.
[23] T. Yagi, W. Utsumi, High-pressure in situ X-ray-diffraction study of the phase transformation from graphite to hexagonal diamond at room temperature, Phys. Rev. B 46 (1992) 6031–6039.
[24] A. Singha, A. Ghosh, N.R. Ray, A. Roy, Quantitative analysis of hydrogenated DLC films by visible Raman spectroscopy, J. Appl. Phys. 100 (4) (2006) 044910–044918.
[25] J. Robertson, J. Gerber, S. Sattel, M. Weiler, K. Jung, H. Ehrhardt, Mechanism of bias-enhanced nucleation of diamond on Si, Appl. Phys. Lett. 66 (1995) 3287–3289.
[26] X. Jiang, C.L. Jia, Direct local epitaxy of diamond on Si(100) and surface-roughening-induced crystal misorientation, Phys. Rev. Lett. 84 (2000) 3658–3661.
[27] E. Vainonen, J. Likonen, T. Ahlgren, P. Haussalo, J. Keinonen, C.H. Wu, Hydrogen migration in diamond-like carbon films, J. Appl. Phys. 82 (8) (1997) 3791–3796.
[28] E. Vainonen-Ahlgren, P. Tikkanen, J. Likonen, E. Rauhala, J. Keinonen, Hydrogen in diamondlike carbon films, J. Nucl. Mater. 266–269 (1999) 975–979.
[29] J.P. Thomas, M. Fallavier, J. Tousset, Hydrogen mobility under beam impact when using the $^{1}H(^{15}N, \alpha\gamma)^{12}C$ nuclear reaction for material analysis, Nucl. Inst. Meth. 187 (1981) 573–580.
[30] J. Biener, A. Schenk, B. Winter, C. Lutterloh, U.A. Schubert, J. Küppers, Hydrogenation of amorphous C:H surfaces by thermal H (D) atoms, Surf Sci. 307–309 (1994) 228–234.
[31] V.D. Vankar, N. Dilawar, Ion irradiation effects in diamond and diamond like carbon thin films, Vacuum 47 (11) (1996) 1275–1280.
[32] D.C. Ingram, A.W. McCormick, The effect of MeV ion irradiation on the hydrogen content and resistivity of direct ion beam deposited diamond like carbon, Nucl. Inst. Meth. Phys. Res. B 34 (1988) 68–73.
[33] K. Maruyama, W. Jacob, J. Roth, Erosion behavior of soft, amorphous deuterated carbon films by heat treatment in air and under vacuum, J. Nucl. Mater. 264 (1999) 56–70.
[34] W. Wang, W. Jacob, J. Roth, Oxidation and hydrogen isotope exchange in amorphous, deuterated carbon films, J. Nucl. Mater. 245 (1997) 66–71.
[35] M. Pumera, C.H.A. Wong, Graphane and hydrogenated graphene, Chem. Soc. Rev. 42 (2013) 5987.
[36] A. Savchenko, Transforming graphene, Science 323 (2009) 589.

Signature of Misoriented Bilayer Graphenelike and Graphanelike Structure in the Hydrogenated Diamond-Like Carbon Film

Nihar R. Ray, Jagannath Datta, Hari S. Biswas, and Someswar Datta

***Abstract*—In the present experimental work, we have described the signature of misoriented bilayer graphenelike and graphanelike structure in the hydrogenated diamond-like carbon film having interlayer disorder region and high specific surface area. Our new results have implications for bilayer graphene/graphane electronic devices.**

***Index Terms*—Graphane, graphite, high-field-effect mobility, hydrogenated diamond-like carbon (HDLC), interlayer disorder, misoriented bilayer graphene, Raman spectroscopy.**

I. Introduction

GRAPHENE IS a promising material for future electronic applications, due to its high-field-effect mobility and optical transparency [1]. The highest performing graphene samples produced by mechanical exfoliation of graphite [2] seem to be not very good for device applications, because of very low specific surface area on the order of few tens of square nanometers per gram. We have demonstrated earlier [3] that hydrogenated diamond-like carbon (HDLC) films, having large specific surface area $\sim 10^{12}$ nm^2/g deposited onto a Si (100) substrate and produced by reactive gas–plasma process, are composed of an ordered hexagonal structure of carbon atoms with lattice parameters $a = 2.62$ Å and $c = 6.752$ Å different to those present in a hexagonal graphite structure. These lattice parameters are similar under different orientations of the sample. These results seem to correspond to hydrogenation of the hexagonal structure of carbon atoms, called graphane [4]. Further structural investigation by micro Raman spectroscopy [5] shows that coherency of sp^3 C–H and sp^2 C = C carbons in the HDLC can produce a continuous nonporous thin film (thickness $\sim$168 nm) having atomically smooth surface. These earlier works [3], [5] motivate us to explore the structure of HDLC films, in order to address the issues related to graphene-based materials. In this paper, we report the experimental signatures of misoriented bilayer graphanelike and graphenelike structure in the as-deposited HDLC film, having some interesting electronic properties.

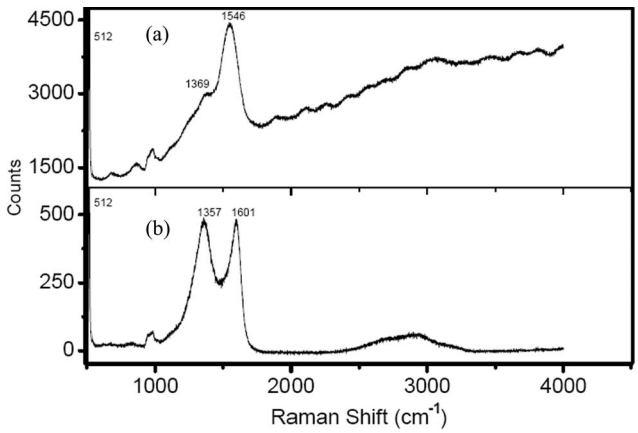

Fig. 1. (a) Raman spectrum of as-prepared HDLC film. (b) Raman spectrum of annealed HDLC film.

II. Experiment

The HDLC film [3], [5] was heated at a fixed temperature of 1050 °C for 30 min in high vacuum $\sim 1 \times 10^{-6}$ torr and cooled to room temperature after heating. Raman spectra were obtained using a confocal micro Raman spectrometer (LabRAM *HR* Vis., Horiba Jobin Yvon S.A.S., France). Under the operating conditions of the spectrometer as described elsewhere [5], the Raman spectrum measures bulk of the sample. The current–voltage ($I-V$) characteristics in ambient air, of the as-prepared HDLC and annealed HDLC films, were measured in the form of series current (I)-versus-voltage (V) measurement with a simple bias current using a Keithley 2635 single-channel current source meter. Using scanning tunneling microscopy (STM) under the constant-tunneling-current mode, a topographic image of the sample was obtained by a multimode scanning probe microscope (Agilent AFM 5500 series system, USA) having a multipurpose small scanner with a scan range Z of 0–2 mm and a noise level Z of < 0.02 nm rms. In this instrument, a feedback loop maintains a constant tunneling current during scanning by vertically moving the scanner at each ($X-Y$) data point until reaching a given set-point value (0.5 nA). The computer stores the vertical position of the scanner at each ($X - Y$) data point to form the topographic

Manuscript received February 7, 2012; revised April 13, 2012; accepted May 17, 2012. Date of publication June 13, 2012; date of current version July 5, 2012. The work of N. R. Ray was supported by the Department of Atomic Energy, Government of India, through XI plan project Diamond Nanotechnology for Bioapplications.

N. R. Ray is with the Plasma Physics Division, Saha Institute of Nuclear Physics, Kolkata 700 064, India (e-mail: niharranjan.ray@saha.ac.in).

J. Datta is with the Analytical Chemistry Division, BARC, Variable Energy Cyclotron Center, Kolkata 700 064, India (e-mail: jdatta@vecc.gov.in).

H. S. Biswas is with the Department of Chemistry, Surendranath College, Kolkata 700 009, India (e-mail: harishankar.biswas@saha.ac.in).

S. Datta is with the Bioceramic and Coating Division, CGCRI, Kolkata 700 032, India (e-mail: sdatta@cgcri.res.in).

Color versions of one or more of the figures in this paper are available online at http://ieeexplore.ieee.org.

Digital Object Identifier 10.1109/TPS.2012.2201176

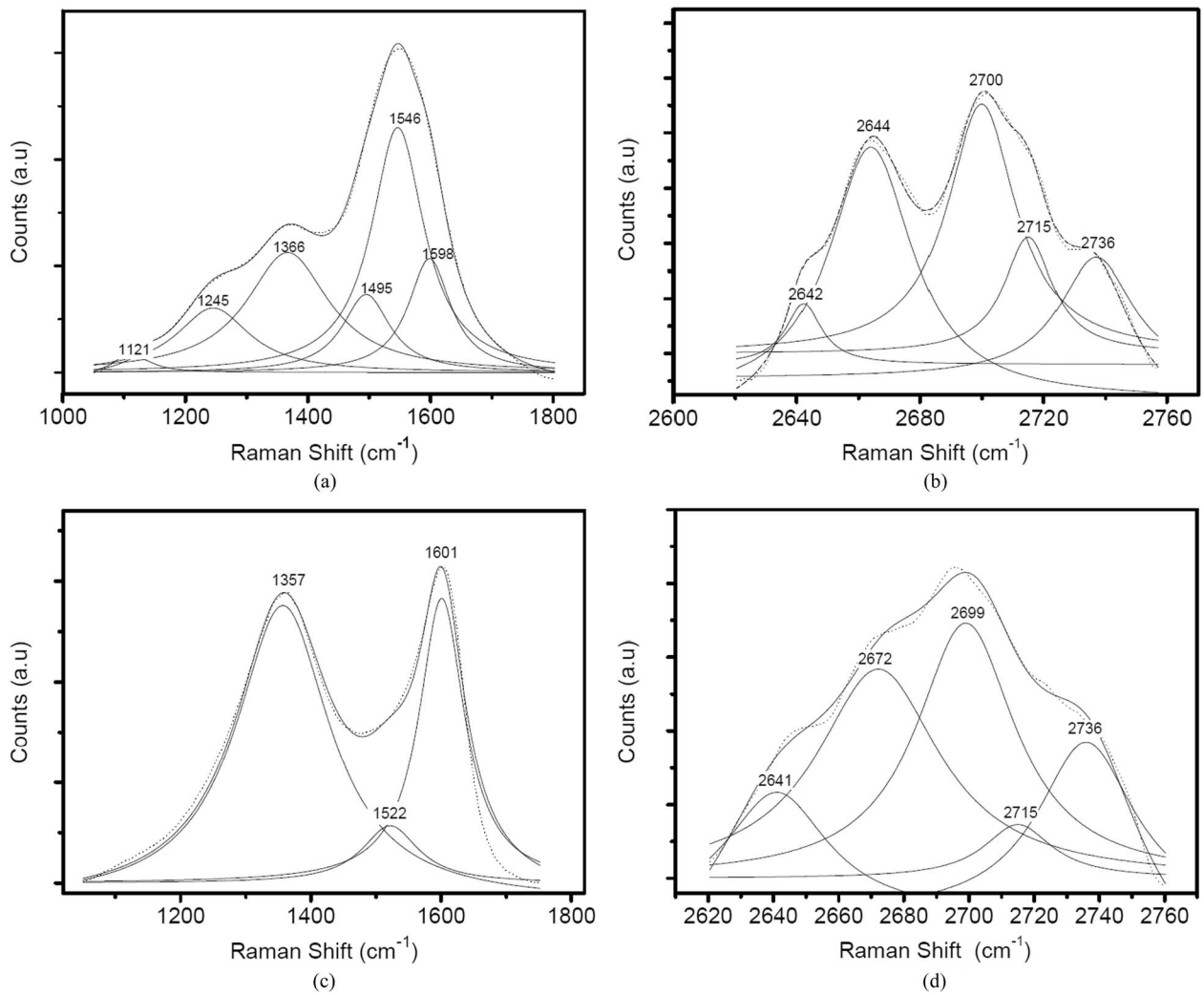

Fig. 2. (a) First-order Raman spectrum of as-prepared HDLC film. (b) Second-order Raman spectrum of as-prepared HDLC film. (c) First-order Raman spectrum of annealed HDLC film. (d) Second-order Raman spectrum of annealed HDLC film.

image of the sample surface which is to be conductive or semiconductive.

III. Results and Discussion

A typical Raman spectrum of the as-prepared HDLC film [Fig. 1(a)] and that of the annealed sample at 1050 °C [Fig. 1(b)] clearly show the presence of photoluminescence (PL) background and the disappearance of PL background, respectively, superimposed upon the Raman scattering spectrum. These results clearly indicate significant loss of bonded hydrogen atoms from the HDLC sample due to annealing effect, since it is thought that PL is due to recombination of electron–hole pairs within sp^2-bonded clusters in an sp^3-bonded hydrogenated carbon matrix [6].

The first-order Raman spectrum [Fig. 2(a)] of the as-prepared HDLC film shows typical Raman modes of amorphous carbon having a broad asymmetric peak at $\sim 1546 \pm 0.66$ cm^{-1} (G-band [5], [7]) along with other peaks at 1366 ± 0.54 cm^{-1} (D-band [8]), 1245 ± 0.9 cm^{-1} (nanocrystalline diamond (NCD) line [5], [9] due to hydrogenation of sp^2 C = C into sp^3 C–H), 1121 ± 1 cm^{-1} and 1495 ± 2.4 cm^{-1} (*trans*-PA modes [5], [10] due to C–H wagging modes), and 1598 ± 1.3 cm^{-1} (dumbbell defect in the NCD line [5], [11]). The first-order Raman spectrum [Fig. 2(c)] of the annealed HDLC film shows typical Raman modes at 1357 ± 0.57 cm^{-1} and 1601 ± 0.57 cm^{-1} which correspond to interlayer "disorder mode" and characteristic G-band, respectively, in the turbostatic structure of graphitic material [12]–[14]. These results in Fig. 2(a) and (c) signify that the HDLC film, having been found to be a hydrogenated hexagonal crystal structure of carbon atoms [3], [4], is composed of layers of graphitelike crystalline structures which have parallel c-axes and which are connected to one another by disordered regions. In fact, the measured value of interlayer separation [3] $c/2 \sim 3.376$ Å for HDLC is larger than that for crystalline graphite which is 3.354 Å, signifying the existence of interlayer disorder regions in the HDLC sample. The interlayer disorder mode (D-band) and the G-band are active for crystallites of finite size in the nanometer range, and the ratio I_D/I_G inversely varies with their diameter; the D-band and G-band do not depend upon the mutual arrangement of graphite planes [12]–[14].

A comparison between the results in Fig. 2(a) and (c) shows the following: 1) The ratio I_D/I_G increases from 0.8 to 2.0

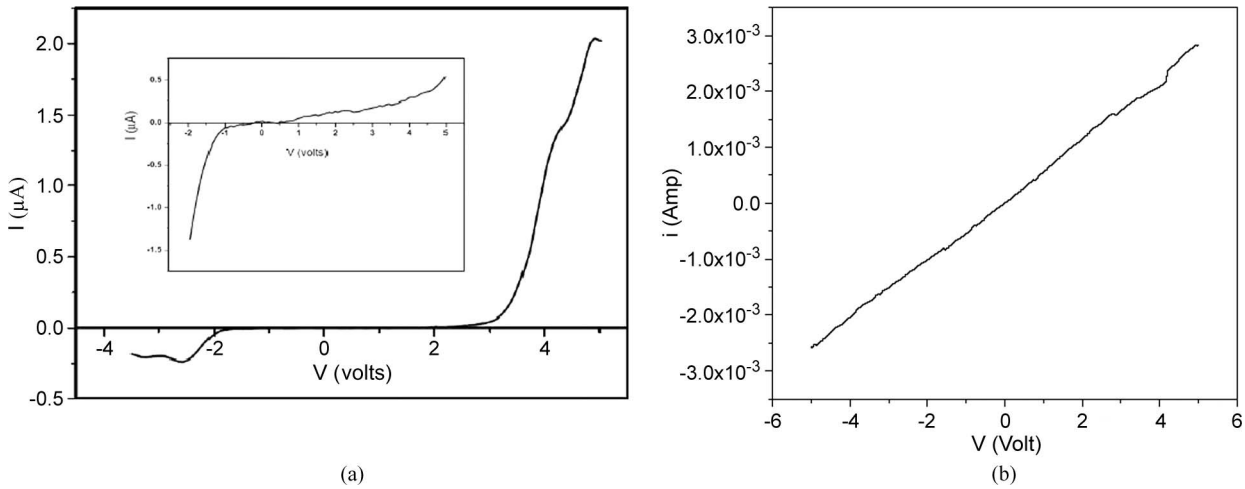

Fig. 3. (a) Current (I)-versus-voltage (V) curve for the as-prepared HDLC film. (b) Current (I)-versus-voltage (V) curve for the annealed HDLC film.

(approximately), indicating a reduction of size of the domain of crystallinity [12]; 2) the intensities of the peaks at 1245 ± 0.9 cm^{-1}, 1121 ± 1.2 cm^{-1}, 1495 ± 2.4 cm^{-1}, and 1598 ± 1.3 cm^{-1} in Fig. 2(a) significantly disappeared in Fig. 2(c), indicating loss of sp^3 C–H in the HDLC [9]–[11]; and 3) the frequency shift $\sim$54 cm^{-1} toward higher wavenumber is found for the G-band in Fig. 2(c), indicating a reduction of size of the domain of crystallinity [12]. In our earlier studies [5], it is seen that sp^2 C = C and sp^3 C–H carbons exist coherently, and due to the annealing effect, in the present work, the size of the sp^3 C–H domains in the HDLC is reduced by the loss of bonded hydrogen atoms in the hydrogenated hexagonal crystal structure of carbon atoms. Hence, the aforementioned results 1)–3) seem to be plausible for the annealed HDLC.

The second-order Raman spectrum of the as-prepared HDLC film [Fig. 2(b)] and that of the annealed sample at 1050 °C [Fig. 2(d)] show the presence of G′-band and the second order of the D-band, respectively [15]. The D- and G′-bands originate from a double-resonance Raman process [16] in 2-D graphite. Therefore, the present results, as shown in Fig. 2(b) and (d), signify the HDLC sample, having turbostatic behavior as found from the first-order Raman spectra, to behave as 2-D graphite due to interlayer disorder regions between the layers having been separated by 3.376 Å. Since the G′-band is very sensitive to the stacking order of the graphene layers along the c-axis [13]–[15] and identification of the number of layers in the turbostatic graphite is done by the number of peaks in the G′-band [17], we have deconvoluted the G′-band with best fits by Lorentzian peaks. Both Fig. 2(b) and Fig. 2(d) show the following: 1) Four Raman modes aside from the peak at $\sim$2700 cm^{-1} correspond to single-layer graphene; 2) full-width at half-maximum for all the five modes lies in the range of 15–40 cm^{-1}; and 3) $I'_G/I_G \ll 1$. These results correspond to turbostatic multilayer graphene in general [17]. According to the calculation of Latil *et al.* [19], a Bernal bilayer (AB) and a rotationally disordered graphene (A′) should simply exhibit the sum of the spectra from a bilayer (i.e., a broadband with four components) plus the unique peak of graphene. Our experimental results, as shown in Fig. 2(b) and (d), correspond

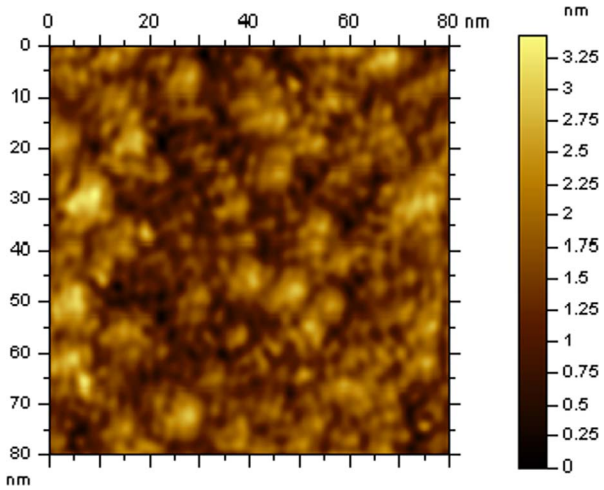

Fig. 4. STM image of annealed HDLC film.

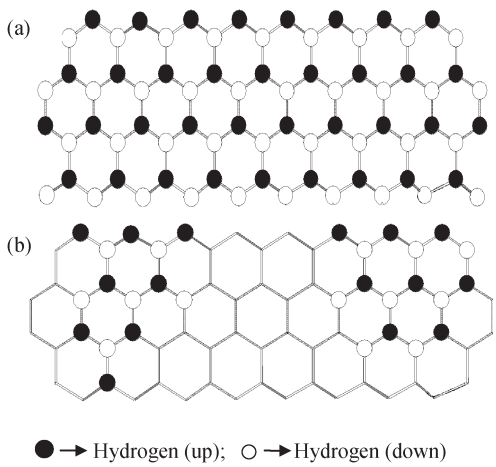

Fig. 5. (a) Schematic drawing of hydrogenated graphene layer. (b) Schematic drawing of partially removed hydrogen from the hydrogenated graphene layer.

to that theoretically predicted and experimentally confirmed for misoriented bilayer graphene [18], [19].

Thus, from all evidences taken together from the first- and second-order Raman spectra [Fig. 2(a)–(d)], we can say that

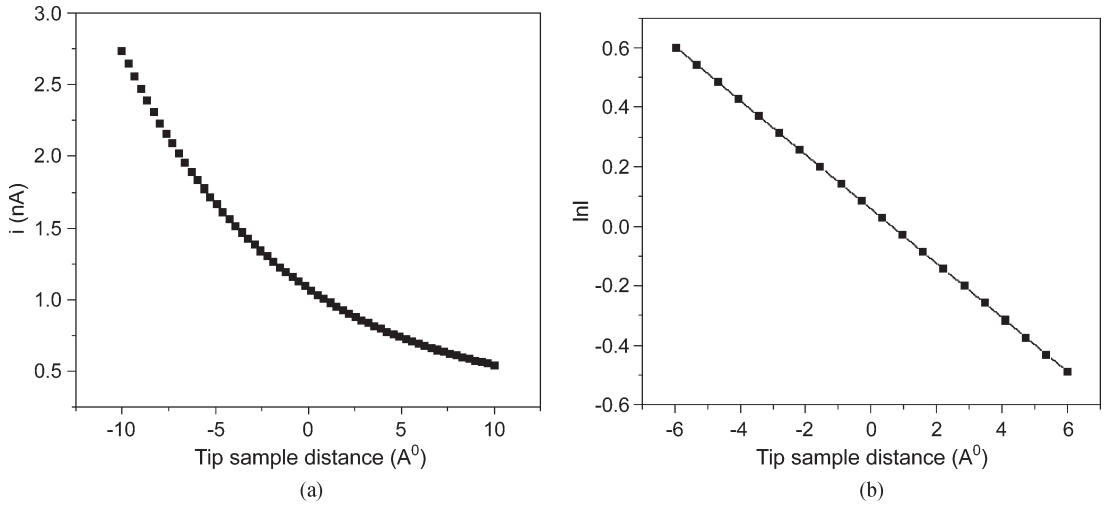

Fig. 6. (a) Tunneling current versus distance for the annealed HDLC film. (b) Semilogarithmic plot of tunneling current versus distance for the annealed HDLC film.

the layers of the hexagonal structure of carbon atoms in the HDLC sample [3]–[5] stay perfectly parallel but their mutual orientation along the c-axis is random (turbostatic) due to the existence of interlayer disorder; as a result, the 3-D crystallinity of the HDLC should be lost, while only the 2-D crystallinity should be preserved [12]. Therefore, the as-prepared HDLC film can be assumed to have misoriented bilayer graphanelike structure, and the annealed HDLC film can be assumed to have misoriented bilayer graphenelike and graphanelike structure within the coherent structure of the film. The Raman spectra [Fig. 2(a)–(d)] do not tell us about why and how the interlayer disorder region is created in the HDLC film.

The typical $I-V$ characteristic of the as-prepared HDLC film, as shown in Fig. 3(a), shows the following: 1) Ambipolar conductance with wide bandgap ($\sim$4.5 eV) indicates a typical wide-bandgap semiconductor property, and 2) the ratio of negative current (due to sp^3 C–H as electron acceptor) to positive current (due to sp^2 C–H as electron donor) is $\sim$0.13. Comparing these results 1) and 2) to the $I-V$ characteristic of a p-doped Si (100) substrate having a bandgap less than 1 eV, as shown in the inset of Fig. 3(a), it may be said that majority carriers of current in the as-prepared HDLC film are electrons and those in the p-doped Si (100) substrate are holes. The typical $I-V$ characteristic of the annealed HDLC film, as shown in Fig. 3(b), shows correspondence to an ohmic curve of a conductor having zero bandgap. From the observed results on the $I-V$ characteristics of the as-prepared HDLC film and annealed HDLC film, it is plausible that the former one should behave as an n-type wide-bandgap semiconductor and the latter one should behave as a metallic conductor.

The constant-current STM image of the as-prepared sample cannot be measured, but that of the annealed one is possible, as shown in Fig. 4. These results support that the as-prepared HDLC film is resistive but the annealed one is conductive. A structure to understand schematically the resistive nature of the as-prepared HDLC film is shown in Fig. 5(a), where, primarily, the presence of σ-bonded electrons is shown, and similarly, that to understand the conductive nature of the annealed HDLC film is shown in Fig. 5(b), where, primarily, the presence of π-bonded electrons is shown. The observed bright spots in Fig. 4 seem to correspond to the simulated constant-current STM image of the unoccupied states in the honeycomb lattice of the A$'$ face of the ABA$'$ system [19]. Occupied states in the honeycomb lattice in the form of dark spots are also seen in Fig. 4. Bright spots are interconnected by dark spots indicating the HDLC film [5] comprising coherent domains of sp^2 and sp^3 carbons.

A typical tunneling-current-versus-distance characteristic and a semilogarithmic plot of this characteristic for the annealed HDLC film are shown in Fig. 6(a) and (b), respectively. This result corresponds to a typical current-versus-height relation, in the absence of a condensate on the surface of electrodes in STM measurements, indicating approximately an exponential decay with a characteristic length of a few angstroms [20]. The estimated work function of the film from the slope of the curve [Fig. 6(b)] $\sim$0.013 eV is about 350 times less than the work function of a free-standing graphene film which is $\sim$4.5 eV [21]. Reduction of the work function of free-standing graphene by several orders of magnitude is predicted to be due to the presence of adsorbate in the electrodes [20]. Recently, it has been found that interaction of graphene with a metallic or insulating substrate may shift the Fermi energy level, causing significant change of work function [21], [22]. The work function of the annealed HDLC film seems to be less than 4.5 eV. The estimated value of tunnel-current density in air $\sim$100 μA/cm^2, using constant-current value $\sim$0.5 nA and STM probe diameter $\sim$0.25 mm, and the observed value of work function of the annealed HDLC film tell us that the annealed HDLC can be expected to be a good high-field-effect electron current emitter in high vacuum.

IV. Conclusion

That the HDLC thin film grown onto large substrate area $\sim$25 mm $\times$ 25 mm behaves as a 2-D graphitic film has been demonstrated in the present experimental work. The new experimental signatures of misoriented bilayer graphenelike and graphanelike structures in the HDLC film having thickness

$\sim$168 nm and their properties as mentioned previously create scientific interest for their electronic applications. Knowledge of electronic properties like temperature-dependent Hall effect, carrier mobilities, and change of work function due to different kinds of substrates will tell us the possible unique applications of our 2-D graphitic film in electronic devices. We have planned to measure these electronic properties in the future.

ACKNOWLEDGMENT

The authors would like to thank S. S. Sil and U. S. Sil for their technical help in the present work.

REFERENCES

[1] M. S. Fuhrer, C. N. Lau, and A. H. MacDonald, "Graphene: Materially better carbon," *MRS Bull.*, vol. 35, no. 4, pp. 289–295, Apr. 2010.
[2] K. S. Novoselov, D. Jiang, F. Schedin, T. J. Booth, V. V. Khotkevich, S. V. Morozov, and A. K. Geim, "Two-dimensional atomic crystals," *Proc. Nat. Acad. Sci. USA*, vol. 102, no. 30, pp. 10 451–10 453, Jul. 2005.
[3] H. S. Biswas, J. Datta, D. P. Chowdhury, A. V. R. Reddy, U. C. Ghosh, A. K. Srivastava, and N. R. Ray, "Covalent immobilization of protein onto a functionalized hydrogenated diamond-like carbon substrate," *Langmuir*, vol. 26, no. 22, pp. 17 413–17 418, Nov. 2010.
[4] M. Z. S. Flores, P. R. S. Autreto, S. B. Legoas, and D. S. Galvao, "Graphene to graphane—A theoretical study," *Nanotechnology*, vol. 20, no. 46, pp. 465 704–465 709, Nov. 2009.
[5] J. Datta, N. R. Ray, P. Sen, H. S. Biswas, and E. A. Vogler, "Structure of hydrogenated diamond like carbon by micro-Raman spectroscopy," *Mater. Lett.*, vol. 71, pp. 131–133, Mar. 2012.
[6] B. Marchon, J. Gui, K. Grannen, G. C. Rauch, J. W. Ager, S. R. P. Silva, and J. Robertson, "Photoluminescence and Raman spectroscopy in hydrogenated carbon films," *IEEE Trans. Magn.*, vol. 33, no. 5, pp. 3148–3150, Sep. 1997.
[7] Z. H. Ni, T. Yu, Y. H. Lu, Y. Y. Wang, Y. P. Feng, and Z. X. Shan, "Uniaxial strain on graphene: Raman spectroscopy study and band gap opening," *ACS Nano*, vol. 2, no. 11, pp. 2301–2305, Nov. 2008.
[8] C. Thomson and S. Reich, "Double resonance Raman scattering in graphite," *Phys. Rev. Lett.*, vol. 85, no. 24, pp. 5214–5217, Dec. 2000.
[9] A. C. Ferrari and J. Robertson, "Origin of the 1150 cm^{-1} Raman mode in the nanocrystalline diamond," *Phys. Rev. B*, vol. 63, no. 12, pp. 121405-1–121405-4, Mar. 2001.
[10] J. Robertson, "Hard amorphous (diamond like) carbons," *Prog. Solid State Chem.*, vol. 21, no. 4, pp. 199–333, 1991.
[11] A. Singha, A. Ghosh, A. Roy, and N. R. Ray, "Quantitative analysis of hydrogenated diamond like carbon films by visible Raman spectroscopy," *J. Appl. Phys.*, vol. 100, no. 4, pp. 044910-1–044910-8, Aug. 2006.
[12] F. Tuinstra and J. L. Koenig, "Raman spectrum of graphite," *J. Chem. Phys.*, vol. 53, pp. 1126–1130, Aug. 1970.
[13] R. J. Nemanich and S. A. Solin, "First- and second-order Raman scattering from finite-size crystals of graphite," *Phys. Rev. B, Condens. Matter Mater. Phys.*, vol. 20, no. 2, pp. 392–401, Jul. 1979.
[14] M. I. Nathan, J. E. Smith, Jr., and K. N. Tu, "Raman spectra of glassy carbon," *J. Appl. Phys.*, vol. 45, no. 5, p. 2370, May 1974.
[15] M. A. Pimenta, G. Dresselhaus, M. S. Dresselhaus, L. G. Cancado, A. Jorio, and R. Saito, "Studying disorder in graphite-based systems by Raman spectroscopy," *Phys. Chem. Chem. Phys.*, vol. 9, no. 11, pp. 1276–1291, Jan. 2007.
[16] V. Zólyomi, J. Koltai, and J. Kürti, "Resonance Raman spectroscopy of graphite and graphene," *Phys. Stat. Sol. (B)*, vol. 248, no. 11, pp. 2435–2444, Nov. 2011.
[17] L. M. Malard, M. A. Pimenta, G. Dresselhaus, and M. S. Dresselhaus, "Raman spectroscopy in graphene," *Phys. Rep.*, vol. 473, no. 5/6, pp. 51–87, Apr. 2009.
[18] P. Poncharal, A. Ayari, T. Michel, and J. L. Sauvajol, "Raman spectra of misoriented bilayer graphene," *Phys. Rev. B, Condens. Matter Mater. Phys.* , vol. 78, no. 11, pp. 113407-1–113407-4, Sep. 2008.
[19] S. Latil, V. Meunier, and L. Henrard, "Massless fermions in multilayer graphitic systems with misoriented layers: *Ab initio* calculations and experimental fingerprints," *Phys. Rev. B, Condens. Matter Mater. Phys.*, vol. 76, no. 20, pp. 201402-1–201402-4, Nov. 2007.
[20] [Online]. Available: http://www.ntmdt.com/spm-basics/view/current-distance-characteristic
[21] Y. J. Yu, Y. Zhao, S. Ryu, L. E. Brau, K. S. Kim, and P. Kim, "Tuning the graphene work function by electric field," *Nano Lett.*, vol. 9, no. 10, pp. 3430–3434, Aug. 2009.
[22] G. Giovannetti, P. A. Khomyakov, G. Brocks, V. M. Karpan, J. van den Brink, and P. J. Kelly, "Doping graphene with metal clusters," *Phys. Rev. Lett.*, vol. 101, pp. 026803-1–026803-4, Jul. 2008.

Nihar R. Ray was born in Burdwan, India, on April 24, 1952. He received the B.Sc.(Hons.) degree in physics, the M.Sc. degree in physics with spectroscopy as special paper, and the Ph.D.(Sc.) degree from the University of Calcutta, Kolkata, India, in 1973, 1975, and 1989, respectively.

He is currently a Professor with the Plasma Physics Division, Saha Institute of Nuclear Physics, Kolkata. His current research project is Diamond Nanotechnology for Bioapplications.

Jagannath Datta, photograph and biography not available at the time of publication.

Hari S. Biswas, photograph and biography not available at the time of publication.

Someswar Datta, photograph and biography not available at the time of publication.